UNIVERSITY OF CALIFORNIA

Los Angeles

The Influence of Symptom Presentation, Spinal Cord Compression, and Sex on Supraspinal Structure and Function in Patients with Degenerative Cervical Myelopathy

A dissertation submitted in partial satisfaction

of the requirements for the degree

Doctor of Philosophy in Neuroscience

by

Talia Christelle Oughourlian

2023

ABSTRACT OF THE DISSERTATION

The Influence of Symptom Presentation, Spinal Cord Compression, and Sex on Supraspinal Structure and Function in Patients with Degenerative Cervical Myelopathy

by

Talia Christelle Oughourlian

Doctor of Philosophy in Neuroscience

University of California, Los Angeles, 2023

Professor Benjamin M. Ellingson, Chair

Degenerative cervical myelopathy (DCM) is a chronic, progressive disorder characterized by the age-related degeneration of osseocartilaginous structures within the cervical spine resulting in narrowing of the spinal canal and chronic compression of the spinal cord. Chronic spinal cord compression can result in persisting neck pain and neurological deficits including loss of fine motor skills, weakness or numbness in the upper limbs, and gait abnormalities and imbalance, ultimately requiring surgical intervention to relieve cord compression. DCM is the most common form of spinal cord injury in adults and as the elderly population continues to grow, incidence of DCM will rise alongside an increased demand on healthcare resources. Further investigation into the neural response to chronic spinal cord compression may not only inform disease progression and prognosis but may benefit patient monitoring and treatment planning.

This dissertation aims to elucidate how symptom presentation, degree of spinal compression, microstructural and cellular integrity of the affected cord, and sex impact supraspinal structure and function in patients with DCM. To address the goals of the dissertation, we implemented a multimodal neuroimaging approach including anatomical, functional, and diffusion imaging of the brain and T2-weighted, diffusion, and metabolic imaging of the spine. First, we characterized and compared spinal cord compression induced alterations in cerebral morphometry and functional connectivity between symptomatic DCM and asymptomatic spinal cord compression (ASCC) patients to further uncover potential compensatory neural mechanisms driving symptom presentation and disease progression. Because the degree of cervical cord compression is not strongly linked to symptom severity, we investigated whether macrostructural, microstructural, and metabolic properties of the cervical spinal cord result in conventional anatomical and functional alterations within the brains of patients with DCM. Lastly, we identified sex-specific differences on cerebral structure and functional connectivity in patients with DCM.

In summary, the dissertation revealed unique cerebral signatures between symptomatic and asymptomatic patients, novel insights into the interrelationship between spinal and supraspinal alterations, and sex-specific supraspinal reorganization in patients with DCM. Findings from this work contribute to our knowledge of disease characteristics and compensatory neural mechanisms; and may benefit future development of non-invasive imaging biomarkers, more precise predicative models to inform disease progression, and novel pharmacological strategies to enhance neuroprotective mechanisms and functional recovery in patients with DCM.

The dissertation of Talia Christelle Oughourlian is approved.

Langston T. Holly

Juan P. Villablanca

Jennifer S. Labus

Benjamin M. Ellingson, Committee Chair

University of California, Los Angeles

2023

To my father who taught me unwavering determination and to my mother who bestowed creativity and art into my life, and who both remind me see the beauty and adventure in life. Thank you for your unconditional love and support.

TABLE OF CONTENTS

LIST OF FIGURES

LIST OF TABLES

ACKNOWLEDGEMENTS

I would like to express my deepest gratitude to all the individuals who supported me throughout my academic journey. This dissertation would not have been possible without their guidance and encouragement.

First and foremost, I would like to thank my parents for their constant love, support, and encouragement. Their unwavering belief in my abilities and their endless sacrifices have played a significant role in helping me reach this milestone. From a young age, they inspired me through their quiet examples of hard work, dedication, and respect. Their willingness to explore new ideas and experiences has instilled a sense open-mindedness, curiosity, and adventure in me.

I am grateful to my brothers for their patience and guidance. Thank you for sharing your experiences and giving me the courage to explore new opportunities and pursue my passions. Thank you to Mila, who constantly reminded me to enjoy the little moments that make our short time on Earth truly beautiful. I would also like to thank my extended family for their presence and encouragement, especially during the challenging times. Thank you to my aunt, Justine, whose bright memory continues to inspire and motivate me to do this work.

I would like to express my deepest appreciation to my mentor and PhD advisor, Professor Benjamin Ellingson, for his instrumental guidance, expertise, and support throughout my doctoral studies. Thank you for teaching me to think like a scientist and to constantly push the boundaries of my research. Your dedication to biomedical research and your pursuit to improve the lives of patients profoundly inspires me. Thank you for believing in me and encouraging me to do my best work.

I would like to thank the members of my dissertation committee, Drs. Benjamin Ellingson, Langston Holly, Pablo Villablanca, and Jennifer Labus, for their valuable feedback and guidance.

Thank you for your insightful comments and for sharing your wealth of experience in research and medicine. Your expertise and support have not only improved my research and expanded my knowledge but have helped me grow as a scientist.

My sincerest thanks to my lab mates in the UCLA Brain Tumor Imaging Laboratory (BTIL). I am grateful to have been part of such a dedicated, supportive, and multidisciplinary team. Thank you for always being willing to help me and share your advice. I would like to express my gratitude to the scientists, graduate students, visiting scholars and clinicians, volunteers, and research associates who were an instrumental part in the completion of this research. Special thanks to Dr. Chencai Wang for his expertise, mentorship, and support throughout the preparation of this dissertation. Thank you all for being such a wonderful group of people, both inside and outside the lab.

I would like to thank my department and the people who make the UCLA Neuroscience Interdepartmental Program so special. Thank you to Dr. Felix Schweizer, Jenny Lee, and the neuroscience faculty for building a wonderful, supportive program and for always making time for your students. Thank you for always ensuring we had the resources to succeed and thrive. I would like to express my gratitude to my friends and cohort mates whose friendship, encouragement, and laughter made this challenging journey enjoyable. A very special thanks to Cassandra Klune whose kindheartedness, patience, and integrity have been a consistent source of inspiration and comfort. I feel very fortunate to have shared this journey with you, thank you for making it a memorable and enriching experience.

I would like to express my appreciation to all the patients and their families who generously gave their time and effort to take part in this research. Your courage and willingness to participate in these studies have been invaluable in advancing our understanding of DCM. I would also like to thank the Parkinson’s Progression Markers Initiative (PPMI) data repository and the UCLA Center for Neurobiology of Stress and Resilience (CNSR) for contributing healthy control neuroimaging data that was critical for the analyses presented in this dissertation.

VITA

2018 **Bachelors of Science** University of Southern California, Los Angeles, CA

Computational Neuroscience with Honors

SELECTED PUBLICATIONS

ORCID: 0000-0001-8133-2928

Google Scholar Profile: Talia C. Oughourlian

- **Oughourlian, T.**, Tun, G., Antony, K., Gupta, A., Mays, V., Mayer, E., Rapkin, A., & Labus, J. (2022). Symptom-associated alterations in functional connectivity in primary and secondary provoked vestibulodynia. *Pain, 10.1097*.
- **Oughourlian, T.**, Yao, J., Hagiwara, A., Nathanson, D., Raymond, C., Pope, W., Salamon, N., Lai, A., Ji, M., Nghiemphu, P., Liau, L., Cloughesy, T., & Ellingson, B. (2021). Relative oxygen extraction fraction (rOEF) MR imaging reveals higher hypoxia in human epidermal growth factor receptor (EGFR) amplified compared with non-amplified gliomas. *Neuroradiology, 63(6), 857-868.*
- **Oughourlian, T.**, Wang, C., Salamon, N., Holly, L., & Ellingson, B. (2021). Sex-dependent cortical volume changes in patients with degenerative cervical myelopathy. *Journal of Clinical Medicine, 10(17).*
- **Oughourlian, T.**, Yao, J., Schlossman, J., Raymond, C., Ji, M., Tatekawa, H., Salamon, N., Pope, W., Czernin, J., Nghiemphu, P., Lai, A., Cloughesy, T., & Ellingson, B. (2020). Rate of change in maximum ^{18}F-FDOPA PET uptake and non-enhancing tumor volume

predict malignant transformation and overall survival in low-grade gliomas. *Journal of Neuro-Oncology, 147(1), 135-145.*

SELECT PRESENTATIONS

2021, 2022	UCLA Specialized Center of Research and Education (SCORE) Symposium, *Poster Presentation*
2021	Society for Neuroscience (SfN) Annual Conference, *Poster Presentation*
2020	International Society for Magnetic Resonance in Medicine (ISMRM) Annual Conference, *Oral Presentation*
2020	American Society of Neuroradiology (ASNR) Annual Conference, *Oral Presentation*

AWARDS & FELLOWSHIPS

2019 – 2022	Advancing Science in America (ARCS) Foundation Fellowship
2022	Graduate Student Association's Presidential Service Award, *University of California, Los Angeles*
2017	Provost Research Fellowship, *University of Southern California*
2017	Provost Summer Undergraduate Research Fellowship, *University of Southern California*
2016, 2017	Student Opportunity for Undergraduate Research Fellowship, *University of Southern California*

CHAPTER 1

Degenerative Cervical Myelopathy

1.1 Introduction

Degenerative cervical myelopathy (DCM) is a progressive condition characterized by the deterioration of osseocartilaginous structures within the cervical spine resulting in chronic compression and injury to the spinal cord [1,2]. Degeneration of spinal vertebrae, ligaments, and soft tissues can cause persisting neck pain, while spinal canal narrowing and cord compression can induce neurological symptoms including loss of fine motor skills, weakness and/or numbness of the upper extremities, and limb dyscoordination [1,3]. DCM is the most common cause of spinal cord dysfunction in people over the age of 55 [4,5] and with a growing elderly population, the incidence of DCM is expected to rise. In some cases, chronic spinal cord compression and worsening of symptoms ultimately requires surgical intervention to relieve compression on the spinal cord [6]. Management and treatment of DCM can further benefit from a more comprehensive understanding of the neuropathological mechanisms driving symptom presentation, disease progression, and functional recovery. The present chapter will provide a review of DCM epidemiology, pathophysiology, and natural history, as well as an overview of previous neuroimaging findings within the brains and spinal cords of patients with DCM.

1.2 Epidemiology

Although DCM is considered the leading cause of spinal cord impairment in the elderly, estimation of disease prevalence and incidence remains challenging. The term DCM was recently introduced to encompasses both cervical spondylotic myelopathy (CSM) and ossification of the posterior longitudinal ligament (OPLL) [7,8]. As a result, previous epidemiological studies reported incidence of CSM and OPLL as separate clinical entities [9]. Additionally, disease prevalence is difficult to capture due a portion of patients with DCM who may experience subtle or no symptoms and thus are not presented in the clinical setting. Further, evaluation of DCM incidence rate is problematic and often underestimated because it is challenging to measure disease onset, particularly prior to symptom presentation. In combination with the disorder being relatively understudied, most epidemiological investigations are often conducted in specific geographical locations and therefore do not represent more general populations.

In North America, the estimated incidence and prevalence of DCM was reported to be a minimum of 41 and 605 per million, respectively [8]. However, non-myelopathic spinal cord compression is prevalent in about 24% of the healthy population and about 35% in people over the age of 60 [10]. Progression of osteoarthritis of the cervical spine to DCM was reported in 8 to 13% of individuals between the ages of 60 to 79 with a higher rate of progression in males compared to females [11]. Additionally, cervical myelopathy is more prevalent in males than females with a reported incidence ratio as high as 2.7-to-1 [12]. With the overall aging of the global population, we can anticipate an increase in DCM prevalence, related healthcare costs, and strain on respective healthcare systems.

1.3 Pathology

Primary and progressive pathophysiological alterations within the cervical spine contribute to spinal stenosis and chronic spinal cord compression. Thus, initiating a cascade of secondary pathobiological events and neural injury within the spinal cord and white matter tracks resulting in neurological symptoms [5].

1.3.1 Pathophysiology

The pathoaetiology of DCM is initiated by degenerative alterations of the osseocartilaginous structures of the spine. Such contributing alterations are categorized as either static or dynamic factors [13]. Static factors are characterized as structural abnormalities that result in degeneration of the spinal column and canal narrowing [13]. Canal narrowing can occur from age-related alterations and/or congenital pathologies. In most cases, age-related intervertebral disc degeneration initiates redistribution of the axial load on the spinal column and causes canal narrowing [3]. Intervertebral discs are composed of the annulus fibrosus, a collagen-rich outer layer, and the nucleus pulposus, a gelatinous inner layer that provides structural integrity to the intervertebral disc [8]. With advancing age, the nucleus pulposus becomes less turgid and less effective at bearing vertical load resulting in reduced disc height and disc bulging [5]. Due to the imbalanced pressure forces and increased stress on cartilage endplates produced by disc bulging and/or herniation, formation of osteophytic spur can occur and further contribute to canal stenosis [8]. Additionally, spinal canal ligaments can experience ossification, calcification, and/or hypertrophy, specifically along the posterior longitudinal ligament (PLL) and the ligament flavum (LF). Abnormal spine biomechanics can lead to ossification of the PLL, thickening of the LF, and laxity of the facet joints [8]. Static pathophysiological alterations characteristic of DCM are illustrated in **Figure 1.1**.

In addition to mechanical compression, dynamic factors may further compress and damage the spinal cord. Physiological cervical motion, such as flexion or extension, may result in additional, but transient cord compression [13]. For example, hyperextension of the neck causes buckling of the LF and narrowing of the canal, also known as the “pincer effect” [14]. Neck flexion and extension contribute to axial cord stretch and strain which may induce further cellular damage to the cord [14]. Overall, static and dynamic mechanical pathologies narrow the spinal canal and result in chronic, progressive spinal cord compression.

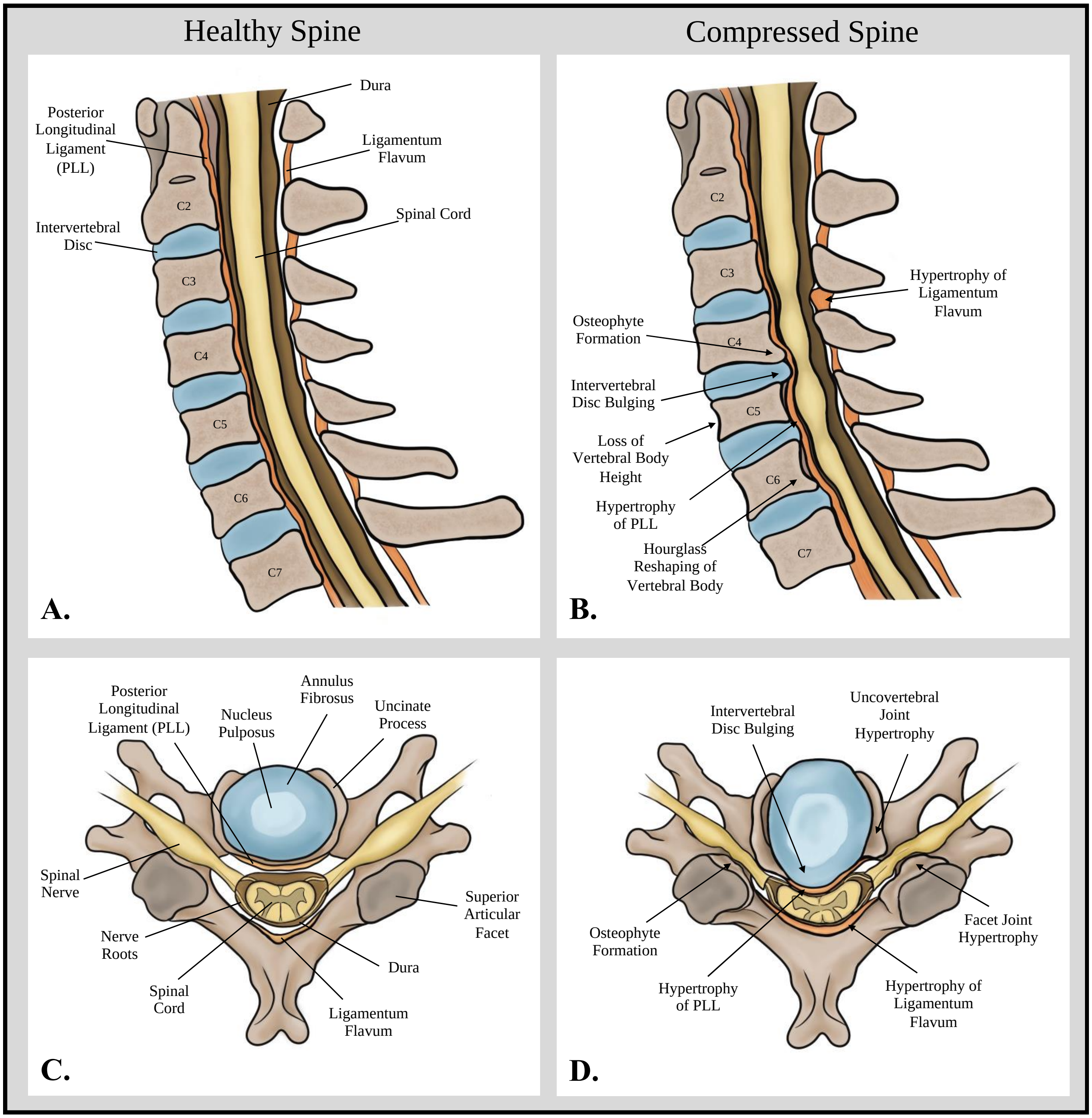

Figure 1.1: Pathophysiological alterations occurring in the cervical spine in DCM.

(A) Sagittal diagram of the healthy cervical spine. (**B)** Sagittal diagram of the compressed cervical spine in degenerative cervical myelopathy. C. Axial diagram of the healthy cervical spine at an intervertebral cross-section. D. Axial diagram of the compressed cervical spine in degenerative cervical myelopathy.

1.3.2 Pathobiology

Primary mechanical alterations resulting in cervical canal narrowing and chronic spinal cord compression are accompanied by secondary pathobiological changes and neural injury. Extrinsic compression on the spinal cord causes impaired spinal cord perfusion and local blood vessel deformation, subsequently reducing regional intraparenchymal spinal cord blood flow and ischemia [13]. Chronic ischemic conditions result in a dysfunction and reduction of endothelial cells, the cells lining the interior surface of the blood vessels and essential for proper blood circulation [15]. Endothelial cell dysfunction and hypoxic cell death prompt disruption of the blood spinal cord barrier (BSCB) and trigger a unique neuroinflammatory response [3]. Chronic compression induced BSCB damage precipitates spinal cord parenchyma edema formation, while increased BSCB permeability alters the spinal cord microenvironment by permitting entrance of peripheral inflammatory cell types within the spinal cord parenchyma [15]. Unlike in acute spinal cord injury, the BSCB remains compromised under chronic compressive forces in DCM [15]. Malperfusion and disrupted blood flow impact axonal pathways, particularly the corticospinal tracts, and affect the lower cervical spinal cord, a cervical region with the most vulnerable blood supply and most commonly affect by compression in DCM [14]. Ischemic injury to the corticospinal tracts is consistent with the clinical presentation of DCM [5].

Conformational remodeling of the spinal cord and BSCB permeability potentiate neuroinflammatory activation of microglia and recruitment of macrophages near the sites of compression [15]. Inflammatory cells release pro-inflammatory cytokines within the spinal cord which facilitate neuronal loss and axonal demyelination [8]. Furthermore, fluctuations in neuronal activity and metabolism prompt glutamatergic excitotoxicity and contribute to neuronal and oligodendrocyte apoptosis [14]. Due to under expression of glutamate receptors and calcium binding proteins, motor neurons are particularly susceptible to glutamate and calcium mediated toxicity and neurodegeneration [14]. Chronic ischemia and inflammatory activate pro-apoptotic pathways prompting neuronal and oligodendrocyte death within the spinal cord [14]. Axonal degeneration and subsequent oligodendrocyte apoptosis are implicated in demyelination of corticospinal tracts and other white matter tracts outside the site of compression [15]. Such cellular degeneration and death contribute to the progressive nature of DCM symptoms. In DCM, chronic spinal cord compression induced ischemia triggers a cascade of biochemical reactions responsible for neural injury and symptom presentation. An overview of pathophysiological and pathobiological processes contributing to DCM are illustrated in **Figure 1.2**.

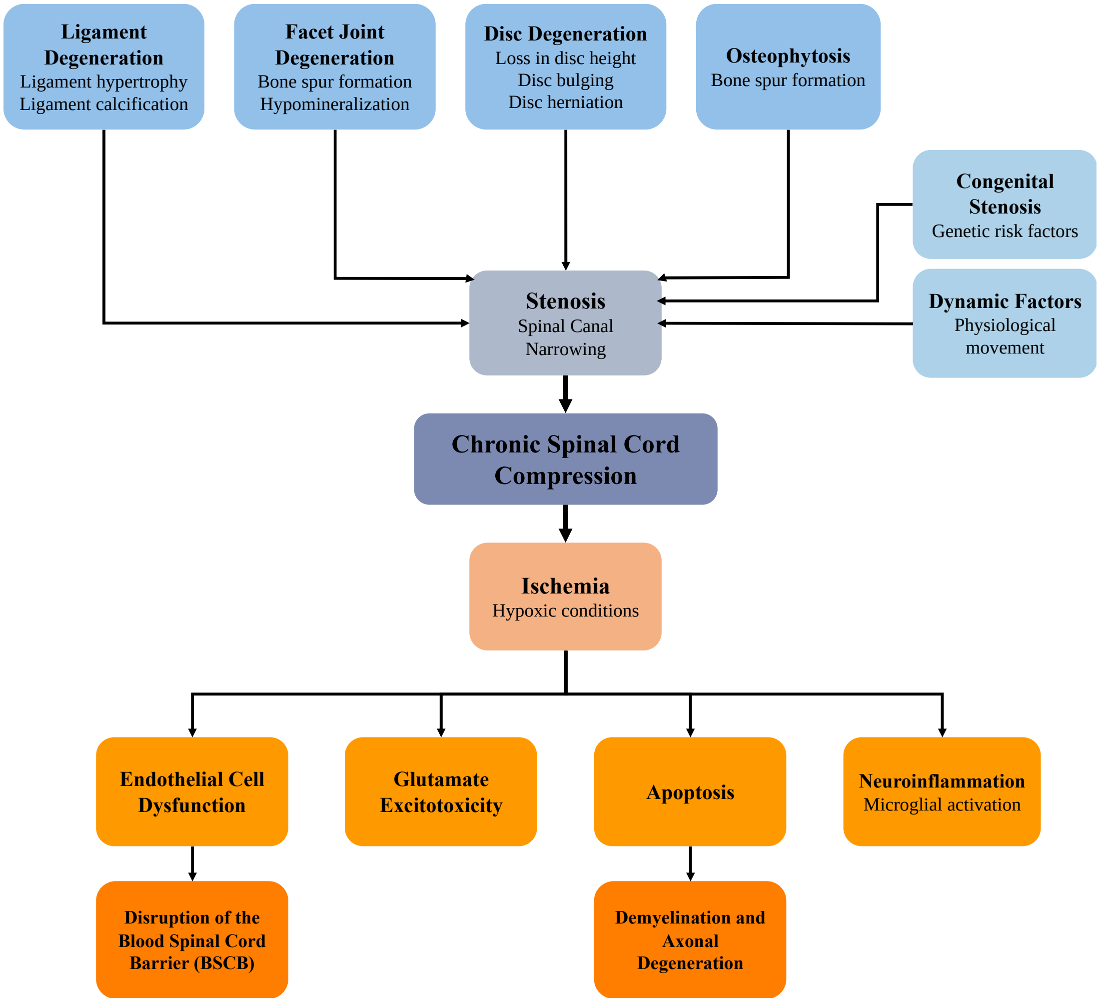

Figure 1.2: Mechanical and Cellular Pathological Alterations in Degenerative Cervical Myelopathy.

1.4 Natural History

1.4.1 Assessment and Diagnosis

Diagnosis of DCM requires both a clinical and radiographical patient assessment. Generally, patients present to clinic with symptoms including neck pain and/or stiffness, paresthesia and/or weakness in the upper and/or lower limbs, loss of fine motor skills and/or dexterity, gait imbalances, and/or urge incontinence [5]. Symptom onset is usually between the ages of 40 and 70 years [2]. Following a clinical assessment, patients will undergo anatomical MR imaging of the cervical spine to confirm the diagnosis and determine the location and extent of stenosis [2]. In some cases, cervical compression and DCM are detected when patients undergo spinal imaging for other reasons, for example in the case of a motor-vehicle accident. Additionally, evidence demonstrates a genetic heritability and susceptibility for the development of DCM, as well as an effect on pathological severity and treatment response [16-18]. Thus, in some instances patients may present with a family history of cervical myelopathy. Additional risk factors associated with DCM development include a congenitally narrow spinal canal [8,19], sex with a higher incidence in males [20], and ethnic background with higher disease frequency in Asian populations [8].

Symptom severity and neurological impairment in DCM are assessed with clinician-administered scales including the modified Japanese Orthopedic Association (mJOA) score, the Neck Disability Index (NDI), and the Nurick grading scale [21-23]. The mJOA scoring system is widely administered in this patient population and utilized to measure both motor and sensory impairments associated with DCM. As depicted in **Table 1.1**, the mJOA questionnaire is comprised of an 18-point scale that addresses upper extremity motor function (5 points), lower extremity motor function (7 points), sensation (3 points), and micturition (3 points) [21]. An mJOA score of 18 reflects no neurological deficit or asymptomatic spinal cord compression, while a score of 17 to 15 reflects mild myelopathy. An mJOA score of 14 to 12 represents moderate myelopathy and a score of 11 to 0 is categorized as severe myelopathy [21]. Such scoring systems are important in evaluating neurological deficits, monitoring patient progression, and determining treatment strategies.

It is important to note that a subset of patients present with cervical stenosis and spinal cord compression but do not exhibit symptoms associated with DCM, this subset is referred to as patients with asymptomatic spinal cord compression (ASCC). It is estimated the prevalence of symptomatic DCM to be about 2% of the population, while ASCC is prevalent in about 24% in the healthy population and about 35% in people over the age of 60 [24]. However, it is important to monitor ASCC patients because an estimated 10% to 22.6% with develop symptoms of myelopathy [25]. Additionally, ASCC patients are at an elevated risk of developing acute spinal cord injury and further complications following a fall or head/neck injury [26].

Modified Japanese Orthopaedic Association (mJOA) Score

Category	Score	Description
Motor Dysfunction of Upper Extremities (/5)	5	No dysfunction in upper extremities
	4	Able to button shirt with slight difficulty
	3	Able to button shirt with great difficulty
	2	Inability to button shirt, but able to eat with a spoon
	1	Inability to eat with a spoon, but able to move hands
	0	Inability to move hands
Motor Dysfunction of Lower Extremities (/7)	7	No dysfunction in lower extremities
	6	Mild lack of stability, but ability to walk with unaided, smooth reciprocation
	5	Moderate to severe lack of stability, but able to walk up/down stairs without hand rail
	4	Able to walk up/down stairs with hand rail
	3	Able to walk on flat surface with a walking aid
	2	Able to move legs, but unable to walk
	1	Inability to move legs, but sensory preservation in lower extremities
	0	Complete loss of motor and sensory functionin lower extremities
Sensory Dysfunction (/3)	3	No sensory loss
	2	Mild sensory loss
	1	Severe sensory loss or pain
	0	Complete loss of hand sensation
Sphincter Dysfunction (/3)	3	Normal micturition
	2	Mild to moderate difficulty with micturition
	1	Severe difficulty with micturition
	0	Inability to micturate voluntarily
Asymptomatic		mJOA Score of 18
Mild Myelopathy		mJOA Score of 17 to 15
Moderate Myelopathy		mJOA Score of 14 to 12
Severe Myelopathy		mJOA Score of 11 to 0

Table 1.1: The modified Japanese Orthopedic Association (mJOA) score scale.

The modified Japanese Orthopedic Association (mJOA) score scale. mJOA scale is used to evaluate neurological dysfunction in patients with DCM. Table adapted from Fehlings et al. (2018).

1.4.2 Management and Treatment

The disease course of DCM is highly variable among patients. Some patients exhibit years of stable neurological status while others experience progressive neurological decline [27]. Studies have reported that 20% to 62% of patients with DCM will deteriorate neurologically over 3 to 6 years after initial assessment [3]. Prediction of which patients will experience disease progression and identification of prognostic imaging biomarkers remains an active area of research. Non-operative management of DCM include physical therapy, cervical traction, bracing/immobilization neck collars, and analgesics [5,7]. However, few studies support the efficacy of such non-operative treatments [5]. It is estimated that between 23% and 54% of patients who initially receive non-surgical treatments will eventually require surgical intervention [5]. Therefore, surgical intervention is increasingly recommended for patients with DCM, especially for patients with moderate to severe neurological symptoms [28]. Surgical treatments for DCM aim to decompress the spinal cord and stabilize the cervical spine. Surgical strategies, including cervical laminoplasty, arthroplasty, discectomy, corpectomy, and fusion, vary among patients depending on anatomical and pathophysiological factors [28,29]. In most cases, operative treatment effectively impedes neurological decline and improves functional and disability-related symptoms of DCM one year following treatment [6]. DCM diagnosis and treatment courses are summarized in **Figure 1.3**.

In addition, adjuvant therapies are currently under investigation to provide neuroprotective benefits [7]. For example, Riluzole, a sodium-channel/glutamate blocker, was effective in protecting spinal cord tissue and reducing neurological symptoms in animal models of DCM [30,31]. Although the phase 3, multicenter, double-blinded, randomized control clinical trial reported no significant impact of Riluzole treatment on mJOA following surgical intervention in

DCM, results did show a reduction in neuropathic and neck pain [32]. Use of corticosteroids are also under investigation as adjunct treatment in DCM [33]. The present standard of care for DCM includes patient monitoring for signs of neurological deterioration and determining optimal treatment based on disease progression.

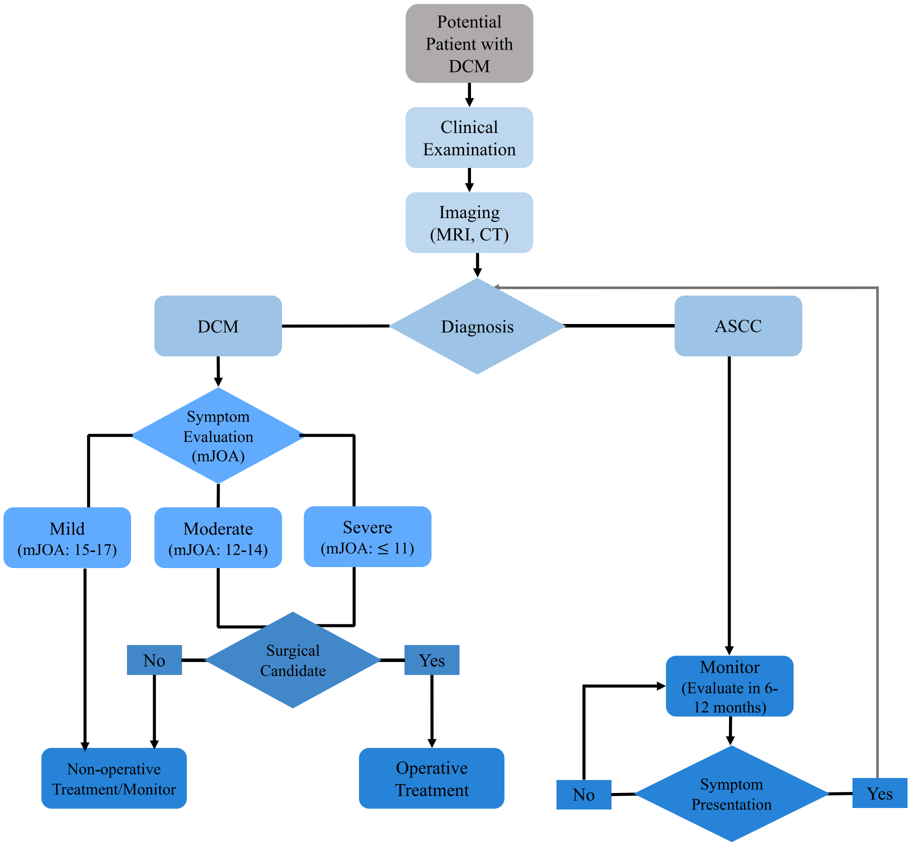

Figure 1.3: Degenerative cervical myelopathy diagnosis and treatment flow chart.

1.5 Neuroimaging of the Spine in DCM

In the setting of DCM, conventional MRI for diagnosis and standard of care is typically performed using T2-weighted and T1-weighted MRI [34]. Intramedullary signal changes or T2-weighted hyperintensity in the compressed spinal cord are reported in 58% to 85% of patients with DCM [35] and are linked to pathological disease features including edema, myelomalacia, gliosis, and ischemia [36]. The presence of cervical spinal cord T2 hyperintensity and T1 hypointensity have been correlated with worse neurological symptoms in DCM [37,38]. Additionally, multilevel T1 hyperintensity, as well as the combined presence of T2 hyperintensity and T1 hypointensity, have been associated with worse surgical outcomes [39-41]. Whereas a reduction in T2 hyperintensity following surgical intervention has been associated with more favorable prognosis [41,42]. In cases in which MRI is contraindicated, CT myelography can be used in patients with DCM and is particularly advantageous in visualizing the extent of ligament ossification and for surgical planning [34].

Beyond conventional MRI, advanced MRI techniques have been employed to measure spinal cord microstructure and to further characterize cord injury. Particularly, quantitative parameters of diffusion tensor imaging (DTI) of the cervical spinal cord, including fractional anisotropy (FA) and apparent diffusion coefficient (ADC), have been investigated as imaging and prognostic biomarkers in DCM. Diffusion-weighted imaging measures the random movement of water molecules (directional diffusion) and in the context of the spinal cord can elucidate white matter integrity and degree of axonal degeneration [36]. Such DTI measurements have been demonstrated to be more indicative of spinal cord damage than T2-weighted imaging [43]. Specifically, in patients with chronic spinal cord compression, FA of the compressed cord was decreased compared to HCs [44], and has been demonstrated to be correlated with symptom severity measures including mJOA [45], pain assessment survey [46], and the Nurick score [47]. In addition, studies have revealed the prognostic value of FA, in which a higher preoperative FA value at the site of maximum compression was associated with post-operative improvement of symptoms measured via JOA [48] and NDI [47]. Furthermore, symptomatic DCM patients exhibit significantly lower FA and higher ADC compared to ASCC patients [49,50].

In DCM, mean ADC of the effected spinal cord, or the average magnitude or rate of water diffusion, was significantly alternated throughout disease stages and indicative of cellular events including ischemia, edema, and axonal degeneration [36]. In early stages of compression, ADC was lower at the maximum site of compression [51], but higher during later stages of chronic spinal cord compression [44,52]. Furthermore, higher ADC was associated with worse neurological symptoms, measured using mJOA scores [53]. Spinal cord ADC at the maximum site of compression was shown to decreased following surgical intervention [53].

In addition to diffusion imaging, metabolic imaging of the spinal cord using magnetic resonance spectroscopy (MRS) has further uncovered alterations in cellular biochemistry and function during DCM pathogenesis. The MRS technique provides a measure of molecular concentrations of metabolites including *N*-acetyl aspartate (NAA), myo-inositol (Myo-I), choline (Cho), creatine (Cr), and lactate [54]. The metabolite NAA is only found in neurons and axons and is considered to indicate axonal integrity, while lactate concentration is postulated to be related to mitochondrial dysfunction and ischemia following neural injury [55]. Compared to HCs, patients with DCM exhibited lower NAA/Cr ratio and elevated lactate concentration at C2, indicative of axonal and neuronal loss and ischemia, respectively [56]. In early stages of spinal cord compression, patients demonstrated slightly elevated Myo-I, glutamine-glutamate complex, and NAA concentrations at C2, suggesting early biomarkers of spinal inflammation and demyelination

[57,58]. While patients in later DCM disease stages exhibited higher Cho/Cr ratio and a Cho peak at C2 suggesting more extensive demyelination and gliosis [57,58]. Furthermore, Cho/NAA concentration at C2 was significantly correlated with neurological function, as measured by mJOA score, and in combination with DTI-based fiber density and mean diffusivity (MD) was an accurate predictor of mJOA in patients with DCM [57,58]. Such advanced imaging modalities have provided novel insights into DCM and have the potential to benefit patient management and overall outcome.

1.6 Neuroimaging of the Brain in DCM

In DCM, chronic narrowing of the spinal canal not only induces structural and functional alterations within the spinal cord, but also leads to supraspinal reorganization within the brain [1]. Previous studies have demonstrated characteristic and symptom-related gray and white matter changes within the brains of patients with DCM. Specifically, significant cortical atrophy in patients with DCM has been observed in sensorimotor regions including the primary motor cortex, primary sensory cortex, and the supplementary motor area, and cerebellum compared to HCs [59-65]. However, patients did demonstrate increased cortical volume in occipital and vision related cortices [61]. Furthermore, gray matter atrophy of sensorimotor, cerebellar, and pain-related cortices was positively correlated with patient symptom severity [59,60,62]. Degeneration of such cortical regions are consistent with the spinal cord injury, corticospinal tract damage, and clinical symptoms present in DCM.

Similarly, DCM patients exhibited significant reductions in white matter fiber density and integrity along the corticospinal tract compared to HCs [66,67]. Patients also demonstrated reduced white matter integrity along pathways associated with sensorimotor and pain perception and modulation including the corpus callosum, thalamic radiation, internal capsule, and corona radiata [67,68]. Moreover, reductions in white matter fiber density along tracts involved in sensory and motor functions were positively correlated with worsening symptom severity [66,68]. In addition, DCM patients exhibited recovery of microstructural integrity along the corticospinal tract and decreased structural connectivity between frontal and motor regions following surgical decompression of the cervical spine [69]. Although fairly understudied in DCM, MR spectroscopy within the brain revealed a significant decrease in NAA/Cr metabolite levels in the sensorimotor cortex in DCM patients compared to HCs, further providing evidence of neuronal damage and dysfunction within primary sensorimotor cortices and upstream of the principal spinal cord injury in DCM [67,70].

Complementary to macro- and micro-structural alterations, DCM patients experience functional cerebral reorganization postulated to be critical when compensating for motor and sensory deficits. Using resting-state fMRI, several studies have demonstrated altered intrinsic functional connectivity (FC) within the sensorimotor cortices, as well as between motor, thalamic, and cerebellar regions compared to healthy individuals [71-73]. Particularly, increased FC within sensorimotor areas, including the pre- and post-central gyri and supplemental motor area (SMA), and between thalamic and cerebellar regions was associated with increased severity of patient neck disability and neurological impairment in patients with DCM [72-74]. Decreased functional connectivity between motor and thalamic regions, as well as between frontal regions and the putamen, thalamus, and cerebellum, were associated with decreasing neurological status [73]. Similarly, during a finger tapping paradigm, patients with DCM demonstrated greater functional activation in the contralateral primary motor cortex [75], but decreased activation in the cerebellar hemispheres compared with HCs [67]. Increased motor cortex activation was correlated with worse spinal cord compression severity [71,76]. Furthermore, one study revealed characteristic alterations in FC throughout disease progression and reported a decrease in FC between cerebellar and thalamic, frontal, and motor regions in earlier stages of myelopathy but an increase in FC during more severe disease stages [77]. However, FC within the cerebellum and between the cerebellum and brainstem initially increased and then decreased as the disease progressed. Following surgical intervention, studies have demonstrated patients with DCM experience increased FC between cerebellar and frontal regions, as well as between the thalamus, frontal, and cingulate cortices, but decreased FC between thalamic, motor, and cerebellar regions [59,78].

1.7 Motivation and Dissertation Aims

As the elderly population continues to grow, incidence of DCM will rise alongside increasing demand on our healthcare systems and costs associated with disease management and treatment. By investigating chronic compression induced alterations in the brain and spinal cord, we may better understand predictors of disease development and the neuroprotective mechanisms driving favorable disease prognosis. This dissertation aims to elucidate how patient symptoms or lack thereof, degree of spinal cord compression, microstructural integrity of the affected cord, and sex impact supraspinal structure and function. Findings from this work will expand our knowledge on disease characteristics, progression, and compensatory mechanisms; and will benefit the further development of imaging biomarkers, predictive models, and novel pharmacological strategies for DCM.

AIM 1: Characterize and compare spinal cord compression induced alterations in brain structure and function in symptomatic and asymptomatic patients.

Utilizing a multimodal brain imaging approach, I will characterize alterations in supraspinal morphometry and connectivity and determine how such alterations reflect symptom presentation in patients with DCM compared to patient with asymptomatic spinal cord compression (ASCC). Findings from this aim will further elucidate compensatory neural mechanisms and disease progression.

AIM 2: Correlate macro- and micro-structural cervical spinal cord measurements with supraspinal alterations in patients with DCM.

With anatomical, diffusion-weighted, and MR spectroscopic imaging of the cervical spinal cord, I will determine how macroscopic, microstructural, and metabolic properties of compression result in conventional anatomical and functional alterations within the brains of patients with DCM. Such analyses will reveal the interrelationship between cord compression and upstream supraspinal alterations.

AIM 3: Identify sex-dependent alterations in brain structure and connectivity in DCM patients.

Using anatomical and functional imaging modalities, I will assess the role of sex differences on cerebral morphometry and intrinsic functional connectivity in patients with DCM. Differences in sex hormones may influence a patient's response to neurotrauma and the pathological mechanisms driving DCM, consequently affecting changes within the brain and neurological symptom presentation.

CHAPTER 2

Characterizing Supraspinal Structural and Functional Differences between Patients with Asymptomatic Spinal Cord Compression and Symptomatic Degenerative Cervical Myelopathy

2.1 Introduction

In DCM, degenerative alterations within the cervical spine result in chronic spinal cord compression and possible presentation of symptoms including persisting neck pain and stiffness, loss of fine motor skills, weakness in the hands and arms, as well as changes in gait [1,4]. As symptoms of DCM worsen, a subset of patients will require surgical intervention to decompress the affected spinal regions, relieve symptoms, and cease disease progression [3]. Interestingly, patients can present radiographic evidence of spinal degeneration and significant spinal cord compression, but experience no symptoms commonly associated with DCM. This subset of patients is often referred to as having asymptomatic spinal cord compression (ASCC) [79].

A 2021 review article estimated the prevalence of symptomatic DCM to be 2.3% of the population while the prevalence of ASCC to be 24.2% in the healthy population and 35.3% in the those over the age of 60 [24]. Between 10 and 22.6% of ASCC patients will develop symptoms of myelopathy [24,25]. Although symptomatic and asymptomatic patients may exhibit similar degree of stenosis and/or spinal cord compression, it remains largely unknown what factors drive symptom presentation and disease progression in DCM.

The role of genetic factors has been investigated in DCM, with one large scale genealogical study demonstrating the genetic predisposition and heritability of DCM [18]. However, to the best of our knowledge no studies have assessed the role of genetics on disease progression and differentiation between symptomatic and asymptomatic prognosis. In addition to a genetic component, we hypothesize differing supraspinal compensatory and neuroprotective mechanisms to significantly influence symptom presentation and disease progression in DCM. Altered structural and functional connectivity of the brain may not only act in response to chronic spinal cord compression but may provide adaptive strategies to compensate for neurological deficits associated with DCM.

The present study aimed to investigate differences in cerebral morphometry, functional connectivity (FC), and white matter microstructure between symptomatic DCM and ASCC patients. Using a multimodal imaging approach, cerebral gray matter volume (GMV), whole-brain functional connectivity, white matter fiber density (FD), fractional anisotropy (FA), and mean diffusivity (MD) were measured and compared between symptomatic DCM, ASCC, and healthy control subjects. I hypothesize that ASCC patients will exhibit more refined cerebral reorganization specifically recruiting visual pathways and related cortical regions, while symptomatic DCM patients will display widespread cerebral alterations involving cerebellar and subcortical recruitment. Investigation of the influence of symptomatic and asymptomatic DCM on supraspinal structure and connectivity can potentially elucidate effective cerebral compensatory mechanisms and is necessary to further develop more successful, personalized treatments for DCM.

2.2 Material and Methods

2.2.1 Patient Population

A total of 102 patients were prospectively enrolled from 2015 to 2022 in a cross-sectional study including brain and spinal cord imaging as well as a neurological examination. Patients were recruited from the UCLA outpatient neurosurgery clinic and exhibited spinal cord compression with evidence of spinal cord deformation, mass effect, and no visible cerebrospinal fluid signal around the spinal cord at the site of maximal compression on MRI. Patients included in this study had not undergone surgical intervention for cervical spinal cord compression at the time of brain imaging. All patients signed Institutional Review Board-approved consent forms, and all analyses were performed in compliance with the Health Insurance Portability and Accountability Act (HIPAA). The modified Japanese Orthopedic Association (mJOA) score was used as a measure of neurological function [80]. The mJOA scoring scale ranges from 0 to 18, where lower scores represent a worse neurological impairment and an mJOA score of 18 represents no impairment of neurological function. Patients with an mJOA score of 18 were categorized as ASCC, while patients with an mJOA between 17 and 0 were categorized as symptomatic DCM. The patient cohort consisted of 67 symptomatic and 35 asymptomatic patients. The symptomatic cohort consisted of 46 males and 21 females with ranging in age from 37 to 81 years with a mean age of 57.7 years with a standard deviation of 10.2 years. The mean body mass index (BMI) for symptomatic patients was 26.6 with a standard deviation of 4.0. The ASCC cohort consisted of 19 males and 16 females with ranging in age from 31 to 80 years with a mean age of 58.6 years with a standard deviation of 13.3 years. The mean BMI for ASCC patients was 25.2 with a standard deviation of 4.0. All patients underwent brain and spinal cord imaging at UCLA. All 102 patients underwent anatomical and resting-state fMRI imaging of the brain, while 48 symptomatic DCM patients and 23 ASCC patients also underwent diffusion-weighted brain imaging. Patient demographic data was summarized in **Table 2.1**.

	Number of Subject (Male/Female)	**Age** (Median ± SD) [min, max]	**mJOA** (Median ± SD) [min, max]	**BMI** (Median ± SD) [min, max]
Symptomatic DCM Patients (T1, fMRI)	**67** (46/21)	(57.7 ± 10.2) [37, 81]	(14.6 ± 2.3) [10, 17]	(26.6 ± 4.0) [18.9, 38.4]
DCM DTI Sub-cohort	**48** (31/17)	(57.9 ± 9.8) [37, 87]	(14.3 ± 2.3) [10, 17]	(26.5 ± 4.4) [18.9, 38.4]
ASCC Patients (T1, fMRI)	**35** (19/16)	(58.6 ± 13.3) [31, 80]	18	(25.2 ± 4.0) [19.4, 39.5]
ASCC DTI Sub-cohort	**23** (11/12)	(57.7 ± 12.4) [31, 75]	18	(25.1 ± 4.5) [20.2, 39.5]

Table 2.1: Patient demographics.

Age is provided in mean years ± the standard deviation and minimum and maximum years. The modified Japanese Orthopedic Association (mJOA) score is provided in mean score ± the standard deviation with the minimum and maximum scores. The mean body mass index (BMI) is provided in mean score ± the standard deviation with the minimum and maximum scores.

2.2.2 Healthy Control Population

For cortical morphometry and functional connectivity analyses 59 age-matched healthy control (HC) volunteers were included from the UCLA Center for Neurobiology of Stress and Resilience (CNSR). The HC cohort consisted of 28 males and 31 females ranging in age from 45 to 73 years with a mean age of 49.9 years with a standard deviation of 4.2 years. The mean BMI for HCs was 26.7 with a standard deviation of 4.8. Exclusion criteria implemented by the CNSR investigators consisted of 1) significant neurological or psychiatric disorder, 2) chronic gastrointestinal disorder, 3) chronic pain disorder, 4) active autoimmune or infectious disorder, 5) history of cancer, and 6) women who are pregnant or planning to become pregnant at time of study. Due to the above exclusion criteria, the healthy control subjects included in this study were categorized as neurologically asymptotic and assigned a mJOA score of 18. All healthy controls underwent anatomical and resting-state functional brain imaging at UCLA. Of the 59 HCs, 17 subjects underwent diffusion-weighted brain imaging at UCLA. Healthy participant demographic data was summarized in **Table 2.2**.

	Number of Subject (Male/Female)	**Age** (Median ± SD) [min, max]	**BMI** (Median ± SD) [min, max]
Healthy Controls (T1, fMRI)	**59** (28/31)	(49.9 ± 4.2) [45, 73]	(26.7 ± 4.8) [19.2, 40.7]
DTI Sub-cohort	**17** (13/4)	(53.3 ± 8.2) [44, 73]	(25.0 ± 3.7) [20.4, 30.0]

Table 2.2: Healthy control demographics.

Age is provided in mean years ± the standard deviation and minimum and maximum years. The mean body mass index (BMI) is provided in mean score ± the standard deviation with the minimum and maximum scores.

2.2.3 MR Imaging Acquisition, Processing, and Statistical Analysis

Structural Magnetic Resonance Imaging

High-resolution 1 mm isotropic 3-dimensional (3D) T1-weighted structural MRIs of the brain were acquired on a 3T MR scanner (Siemens Prisma or Trio; Siemens Healthcare, Erlangen, Germany) using a 3D magnetization-prepared rapid gradient-echo (MPRAGE) sequence in either the coronal, sagittal, or axial orientation, with a repetition time (TR) of 2300 to 2500 ms, a minimum echo time (TE) between 2 to 3 ms, an inversion time (TI) of 900 to 945 ms, a flip angle of 9^o to 20^o, slice thickness of 1 mm with no interslice gap, and field of view (FOV) of 240 x 320 mm and matrix size of 240 x 320 (in the patient cohort) or FOV of 220 x 220 mm and matrix size of 256 x 256 (in the healthy cohort).

Cortical parcellation and computation of gray matter volume of the brain were conducted using the FreeSurfer software package (https://surfer.nmr.mgh.harvard.edu/fswiki) on the T1-weighted images described above [81]. Brain surfaces were preprocessed, smoothed with a full-width half-maximum of 10 mm, and registered to the standard space as defined by Desikan-Killiany-Tourville (DKT) atlas [82]. Whole-brain cortical volume analysis was completed using FreeSurfer. A general linear model (GLM) was used to determine vertex-level significant differences in GMV between the following groups: 1) symptomatic DCM patients and HCs, 2) ASCC patients and HCs, and 3) symptomatic DCM and ASCC patients. To control for the influence of age and BMI on GMV, age and BMI were included as covariates in morphometric analyses. Previous studies have demonstrated relationships between BMI and altered cerebral morphometry [83,84], therefore BMI was included as a covariate in the present study. The vertex-wise level of significance was set at $p < 0.05$, with multiple comparisons correction performed using Monte Carlo permutations with a significance level of $p < 0.05$.

Resting-state Functional Magnetic Resonance Imaging (rs-fMRI)

To assess functional connectivity, resting state functional MRIs were acquired on a 3T MR scanner (Siemens Prisma; Siemens Healthcare, Erlangen, Germany) with a TR of 1500 to 2200 ms, TE of 28 to 30 ms, flip angle of 77^{o}, FOV of 220 to 245 mm with an acquisition matrix of 64 x 64 for an in-plane resolution of 3.4 to 3.8 mm, interleaved acquisition, slice thickness of 4 mm with no interslice gap, parallel imaging via CAIPIRNHA with a factor of 2, and multi-band acceleration with a factor of 2.

Functional MR images were processed using the CONN toolbox (https://www.nitrc.org/projects/conn) [85], which utilizes functions from the Statistic Parametric Mapping (SPM) toolbox (http://www.fil.ion.ucl.ac.uk/spm/). Functional and structural images were processed using the standard built-in preprocessing pipeline provided in the CONN toolbox. The default pipeline performs the following steps: 1) realignment of functional images including motion correction based on 12 degrees of freedom and unwarping, 2) slice-timing correction to correct for difference in acquisition time between slices, 3) registration of functional images to structural images, 4) registration of structural images to the Montreal Neurological Institute (MNI) defined standardized space, 5) removal of signal intensity spikes and functional volumes with excessive motion (threshold set at 2 mm translation and 2° rotation in any direction) using the Artifacts Detection Tool (ART) from SPM, 6) segmentation and normalization of functional images based on tissue type (gray matter, white matter, and cerebrospinal fluid) in MNI space, and 7) spatial smoothing of functional data using 8 mm, full width at half maximum (FWHM) Gaussian kernel. Additionally, signals from the white matter, CSF, and motion parameters were regressed from the functional data and signal filtering was performed using a band-pass filter of 0.008–0.10 Hz to reduce noise caused by scanner drift and physiological effects (i.e., pulsation and respiration).

Functional connectivity (FC) of the brain was assessed using whole brain ROI-to-ROI (also termed seed-to-seed) and ROI-to-voxel (also termed seed-to-voxel) analyses. Regions of interest (ROIs) were selected from the Harvard-Oxford Automated Anatomical Labeling (AAL) atlases [86]. Whole-brain ROI-to-ROI analyses used 132 cerebral ROIs. ROIs for seed-to-voxel analyses were generated by extracting significant regions from GMV analyses to create binary masks and then imported into the CONN toolbox as ROIs. GLMs were used to evaluate significant group differences in functional connectivity between the whole-brain and corresponding significant GMV mask while accounting for the influence of age and BMI. Previous studies have demonstrated relationships between BMI and altered functional brain connectivity [87-89], therefore BMI was included as a covariate in the present study. For ROI-to-ROI analyses the connection-level significance was set at $p < 0.01$ and cluster-level significance was set at a false discovery rate (FDR) corrected $p < 0.05$. For seed-to-voxel analyses the voxel-level significance was set at $p < 0.001$ and cluster-level significance was set at a false discovery rate (FDR) corrected $p < 0.05$. Statistical analyses were performed using the CONN toolbox [85], MATLAB (Release 2018a, MathWorks, Natick, MA) and GraphPad Prism software (Version 7.0c GraphPad Software, San Diego, California).

Diffusion Tensor Imaging (DTI)

Diffusion-weighted images of the brain were collected using standard spin-echo echo planar imaging on a Siemens Prisma 3T MR scanner (Siemens Prisma; Siemens Healthcare, Erlangen, Germany) with a TR of 9500 to 11400 ms, TE of 82 to 88 ms, flip angle of 90°, FOV of 256 by 256 mm with an acquisition matrix of 128 by 128 for voxel size of 2 mm x 2 mm x 2 mm. Diffusion weighting was distributed along 65 directions using *b* values of 0 s/mm^2 and 1000 s/mm^2. Subject space data was resampled to 1 mm isotropic resolution for analyses in standard MNI space.

The following steps were used to preprocess diffusion weighted images: 1) image denoising using the MRtrix3 software package (Brain Research Institute, Melbourne, Australia, http://www.brain.org.au/software/mrtrix) [90], 2) eddy current and motion correction using the FMRIB's Diffusion Toolbox (FDT) (www.fmrib.ox.ac.uk/fsl), 3) b zero image registration

(registration to subject's first non-diffusion weighed images), and 4) skull extraction using the Brain Extraction Tool (BET) from FSL. The MRtrix3 software was then used to perform fixel-based analysis via probabilistic tractography by seeding 10 million random voxels throughout the brain and counting the number of fiber tracts passing through each voxel resulting in fiber density (FD) maps for each subject. Fractional anisotropy (FA) and mean diffusivity (MD) values were calculated from the diffusion tensor and registered to the Johns Hopkins University DTI atlas (ICBM-DTI-81 1mm FA atlas) using the linear (FLIRT) and nonlinear (FNIRT) commands in FSL. The AFNI (Analysis of Functional NeuroImages) software and *3dttest++* and *3dClustSim* commands were used to implement a GLM to evaluate voxel-wise differences in FD, FA, and MD between cohorts while accounting subject age and BMI. Cluster significance was set at $p < 0.05$ (two-sided) with a false discovery rate (FDR) < 0.05.

2.3 Results

2.3.1 Subject Characteristics

As summarized in **Table 2.1**, the symptomatic DCM patient cohort consisted of 67 patients with a mean age of 57.7 ± 10.2 years, mean mJOA score of 14.6 ± 2.3, and mean BMI of 26.6 ± 4.0. Of the 67 symptomatic patients, 9 patients were categorized with severe myelopathy (mJOA ≤ 11), 19 patients exhibited moderate myelopathy ($12 \leq$ mJOA ≤ 14), and 39 patients presented with mild myelopathy ($15 \leq$ mJOA ≤ 17) at the time of the brain scan. The ASCC cohort consisted of 35 patients with a mean age of 58.6 ± 13.3 years and a mean BMI of 25.2 ± 4.0. No significant difference in age or BMI between the symptomatic DCM and ASCC patient cohorts was observed (Wilcoxon-Mann-Whitney test, age: $p = 0.6269$, BMI: $p = 0.0719$). A sub-cohort of patients was included for diffusion-based analyses. The sub-cohort of symptomatic DCM with diffusion-weighted imaging consisted of 48 patients with a mean age of 57.9 ± 9.8 years, mean mJOA score of 14.3 ± 2.3, and mean BMI of 26.5 ± 4.4. The sub-cohort of ASCC patients with diffusion-weighted imaging consisted of 23 patients with a mean age of 57.7 ± 12.4 years and a mean BMI of 25.1 ± 4.5. No significant difference in age or BMI between the symptomatic DCM and ASCC sub-cohorts was observed (Wilcoxon-Mann-Whitney test, age: $p = 0.8571$, BMI: $p = 0.1489$).

The HC cohort consisted of 59 subjects with a mean age of 49.9 ± 4.2 years and a mean BMI of 26.7 ± 4.8. The sub-cohort of HCs with diffusion-weighted imaging consisted of 17 subjects with a mean age of 53.3 ± 8.2 years and a mean BMI of 25.0 ± 3.7. A significant difference in age was observed between the HCs and symptomatic DCM patient cohorts (Wilcoxon-Mann-Whitney test, $p < 0.0001$) and between the HCs and ASCC patient cohorts (Wilcoxon-Mann-Whitney test, $p = 0.0028$). No significant differences in BMI were observed between HCs and symptomatic DCM patient cohorts (Wilcoxon-Mann-Whitney test, $p = 0.9777$) nor between HCs and ASCC patient cohorts (Wilcoxon-Mann-Whitney test, $p = 0.1036$). In addition, no significant differences were in age or BMI were observed between HCs and symptomatic DCM sub-cohorts (Wilcoxon-Mann-Whitney test, age: $p = 0.0686$, BMI: $p = 0.2093$) nor between HCs and ASCC patient sub-cohorts (Wilcoxon-Mann-Whitney test, age: $p = 0.1979$, BMI: $p = 0.8925$).

2.3.2 Disease-specific Differences in Cortical Morphometry

Results from whole-brain cortical volume analysis revealed significant differences in gray matter volume (GMV) between symptomatic DCM patients, ASCC patients, and HCs. Specifically, symptomatic patients exhibited significantly larger GMV in the left and right lateral occipital cortices compared to HCs (**Fig. 2.1 A**). When comparing cortical volume between ASCC patients and HCs, asymptomatic patients exhibited significantly smaller GMV in the left postcentral and right precentral gyri (**Fig. 2.1 B**). In addition, significant differences in GMV were observed between symptomatic DCM and ASCC patients. Specifically, symptomatic DCM patients demonstrated larger GMV compared to ASCC patients in various regions including the left cuneus, left precentral gyrus, right supramarginal gyrus, right superior parietal gyrus, and right superior temporal gyrus (**Figure 2.1 C**).

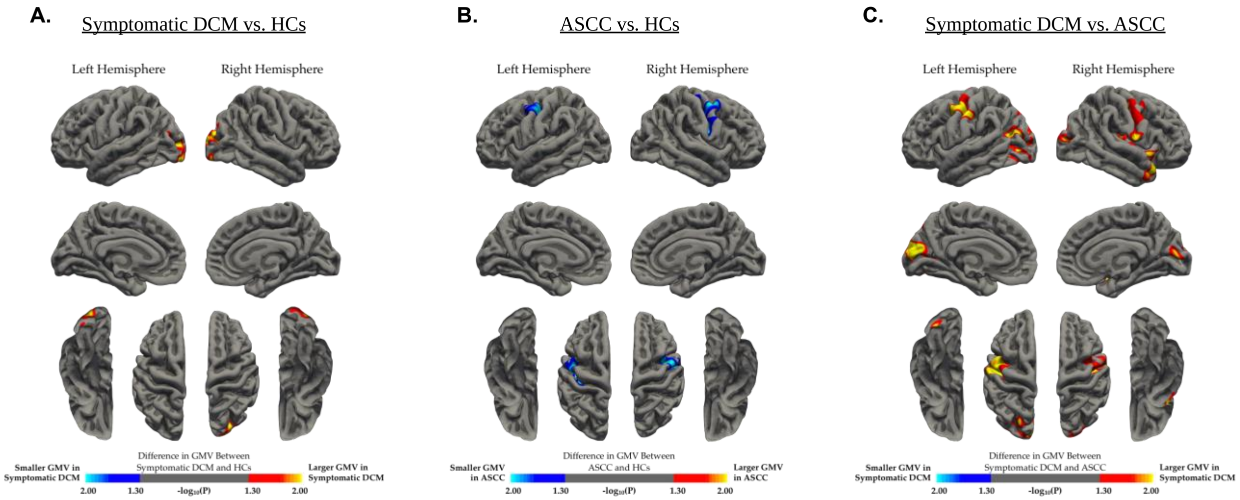

Figure 2.1: Cortical morphometry analysis between symptomatic DCM, ASCC, and HCs. Whole-brain correlation analysis comparing gray matter volume (GMV) between (**A**) symptomatic DCM patients and healthy controls (HCs), (**B**) ASCC patients and HCs, and (**C**) symptomatic DCM and ASCC patients while regressing out the effects of age and BMI. (**A**) Red-yellow color denotes larger GMV in symptomatic DCM patients, while blue-light blue color denotes smaller GMV in symptomatic patients compared to HCs. (**B**) Red-yellow color denotes larger GMV in ASCC patients, while blue-light blue color denotes smaller GMV in ASCC patients compared to HCs. (**C**) Red-yellow color denotes larger GMV in symptomatic DCM patients, while blue-light blue color denotes smaller GMV in symptomatic DCM patients compared to ASCC patients. Significant clusters were determined by thresholding based on statistical significance of $p < 0.05$.

2.3.3 Disease-specific Differences in Cerebral Functional Connectivity

To evaluate functional alterations associated with symptomatic DCM and ASCC, whole-brain ROI-to-ROI functional connectivity analyses were performed between patient and HC cohorts while accounting for the effects of subject age and BMI on FC. When compared to HCs, symptomatic DCM patients displayed widespread significant differences in FC (**Fig. 2.2 A**). Largely, symptomatic DCM patients exhibited higher FC between primary visual regions and thalamic, brainstem, and cerebellar regions compared to HCs (**Fig. 2.2 A, B**). Specifically, symptomatic patients demonstrated higher FC between bilateral primary and secondary visual regions including the intracalcarine cortex (ICC), supracalcarine cortex (SCC), lateral occipital cortex (LOC), lingual gyrus, and fusiform gyrus, and the bilateral thalamus, brainstem, and various cerebellar regions including both hemisphere and vermis regions (**Fig. 2.2 A, B**). When compared to HCs, symptomatic patients also displayed increased FC between the thalamus and the pre- and post-central gyri.

Additionally, symptomatic patients displayed decreased FC compared to HCs between sensorimotor and visual regions, as well as between frontal and cerebellar regions (**Fig. 2.2 A, B**). Bilateral sensorimotor regions including the pre- and post-central gyri, supramarginal gyri, and supplementary motor area (SMA), demonstrated reduced FC with the bilateral ICC, bilateral SCC, fusiform gyri, lingual gyri, and brainstem in symptomatic patients compared to HCs (**Fig. 2.2 A, B**). Symptomatic patients also demonstrated decreased FC between the cingulate cortex and thalamus and cerebellum. Furthermore, the significant GMV mask between symptomatic DCM patients and HCs (**Fig. 2.1 A**) was extracted and utilized as a ROI for seed-to-voxel based analyses. The GMV mask, primarily encompassing the lateral occipital cortices, displayed higher functional connectivity with voxels in regions including the bilateral postcentral gyrus, right precentral gyrus, bilateral thalamus, bilateral supramarginal gyrus, cingulate cortex, left superior frontal gyrus, and right superior parietal lobule in symptomatic patients compared to HCs (**Fig. 2.2 C**).

Symptomatic DCM vs. HCs

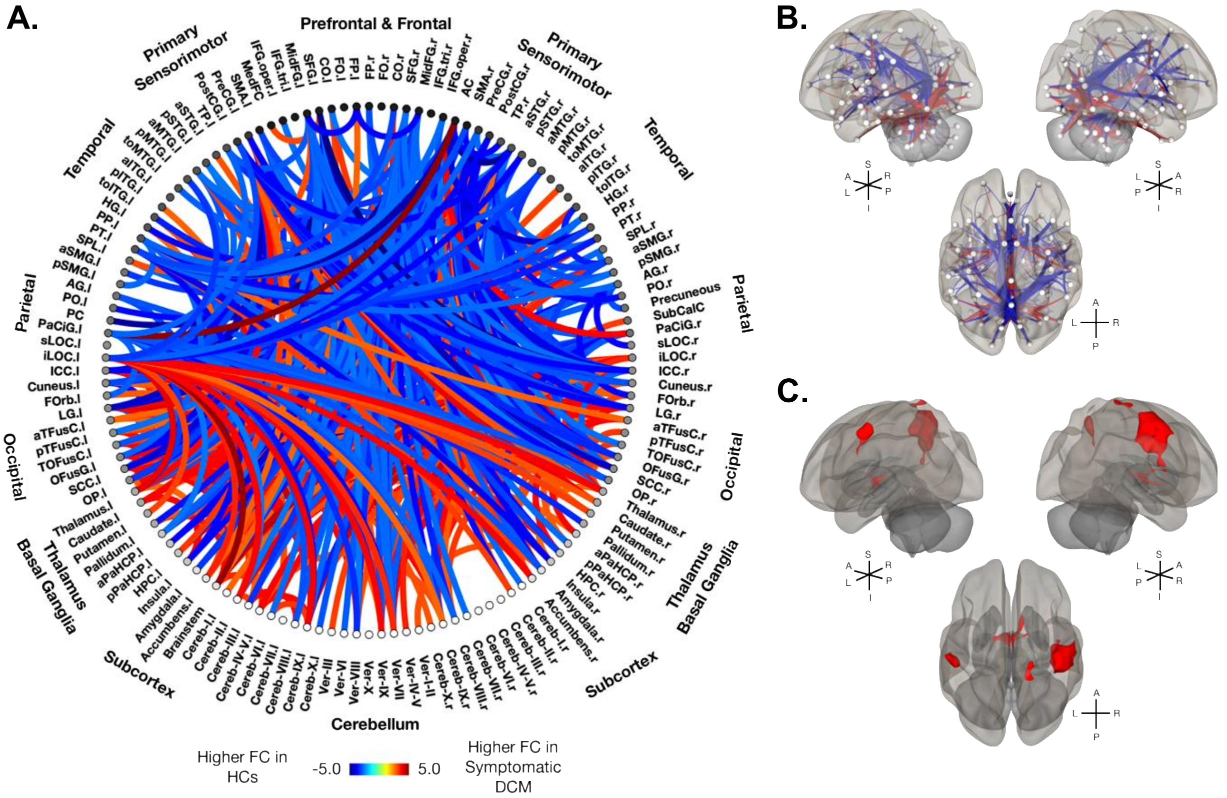

Figure 2.2: Whole-brain functional connectivity (FC) analysis between symptomatic DCM patients and HCs.

Whole-brain functional connectivity (FC) analysis between symptomatic DCM patients and healthy controls (HCs). **(A)** ROI-to-ROI functional connectome diagrams using 132 Harvard-Oxford Automated Anatomical Labeling (AAL) atlas defined ROIs. Colors on the connectome denote the value of the T-statistic in which red-orange color denotes higher FC in symptomatic DCM patients compared to HCs, while blue-light blue denotes higher FC in HCs compared to symptomatic DCM patients while regressing out the effects of age and BMI. ROIs are labeled with l = left hemisphere and r = right hemisphere. **(B)** Left, right, and superiors views of a 3D brain rendering illustrating significant ROIs as spheres and significant differences in FC between the ROIs as lines with red denoting higher FC in symptomatic DCM patients compared to HCs and blue denoting higher FC in HCs compared to symptomatic DCM patients. Lighter spheres represent more superficial ROIs relative to the viewer, while darker sphere represent ROIs deeper within the brain. Significant connection-level threshold was set at p-value < 0.01 and ROI-level threshold was set at FDR-corrected p-value < 0.05. **(C)** Left, right, and superiors views of a 3D brain rendering illustrating significant voxels from seed-to-voxel FC analysis using significant symptomatic DCM vs. HCs GMV clusters as seeds. The red color denotes significant voxels with increased FC with the GMV mask seed in symptomatic DCM compared to HCs, while the blue color denotes significant voxels with decreased FC in symptomatic DCM compared to HCs. Significant clusters were determined by thresholding based on voxel-level significance of $p < 0.001$ and cluster-level FDR corrected $p < 0.05$.

Like the symptomatic cohort, ASCC patients exhibited altered FC throughout the brain compared to HCs albeit less widespread (**Fig. 2.3**). Generally, ASCC patients displayed higher FC primarily within occipital brain regions, and between occipital and thalamic, temporal, and cerebellar regions (**Fig. 2.3 A, B**). Asymptomatic patients demonstrated higher FC between the thalamus and visual regions including the LOC, ICC, and lingual gyrus, temporal regions including the middle and inferior temporal gyri, and hippocampal regions. In addition, higher FC was observed in ASCC patients compared to HCs between the cingulate cortices and the thalamus, cerebellum, brainstem, and hippocampal regions (**Fig. 2.3 A, B**).

In contrast, lower FC in ASCC patients compared to HCs was observed within sensorimotor regions, as well as between sensorimotor and temporal, visual, and subcortical regions (**Fig. 2.3**). Particularly, asymptomatic patients exhibited lower FC between the precentral gyri and the bilateral ICC and parahippocampal cortices compared to HCs (**Fig. 2.3 A, B**). Additionally, ASCC patients demonstrated lower FC between cingulate cortices and the thalamus, brainstem, and cerebellar regions. ASCC patients also displayed lower FC compared to HCs between the insular cortices and parietal and motor regions including the left precentral gyrus, bilateral SMA, bilateral supramarginal gyri (**Fig. 2.3 A, B**). When seeding the significant GMV mask, primarily encompassing the left postcentral and right precentral gyri, ASCC patients exhibited higher FC with voxels in the left angular gyrus and lower FC with voxels in the occipital cortex including the lingual gyri, ICC, occipital pole and fusiform gyri compared to HCs (**Fig. 2.3 C**).

No statistically significant differences were observed in whole-brain ROI-to-ROI functional connectivity between symptomatic DCM and ASCC patients after correction for multiple comparisons.

ASCC vs. HCs

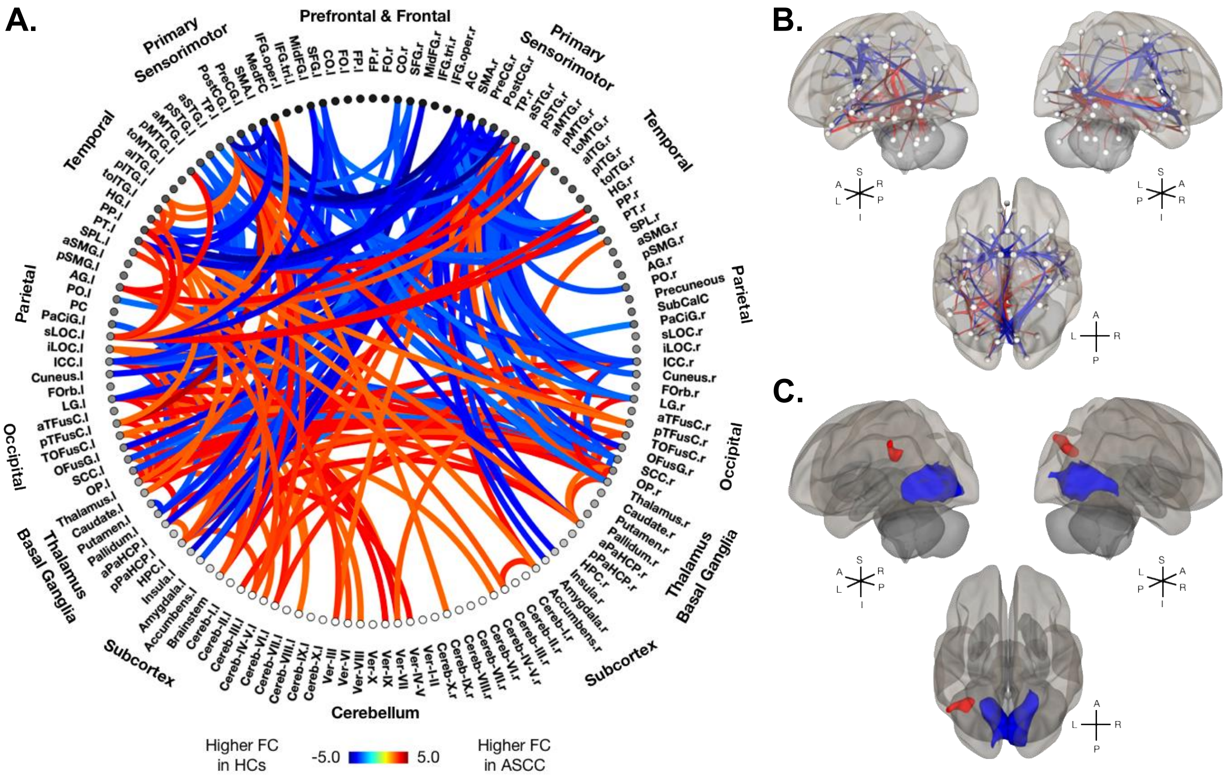

Figure 2.3: Whole-brain functional connectivity (FC) analysis between ASCC patients and healthy controls (HCs).

Whole-brain functional connectivity (FC) analysis between ASCC patients and healthy controls (HCs). **(A)** ROI-to-ROI functional connectome diagrams using 132 Harvard-Oxford Automated Anatomical

Labeling (AAL) atlas defined ROIs. Colors on the connectome denote the value of the T-statistic in which red-orange color denotes higher FC in ASCC patients compared to HCs, while blue-light blue denotes higher FC in HCs compared to ASCC patients while regressing out the effects of age and BMI. ROIs are labeled with l = left hemisphere and r = right hemisphere. **(B)** Left, right, and superiors views of a 3D brain rendering illustrating significant ROIs as spheres and significant differences in FC between the ROIs as lines with red denoting higher FC in ASCC patients compared to HCs and blue denoting higher FC in HCs compared to ASCC patients. Lighter spheres represent more superficial ROIs relative to the viewer, while darker sphere represent ROIs deeper within the brain. Significant connection-level threshold was set at p-value < 0.01 and ROI-level threshold was set at FDR-corrected p-value < 0.05. **(C)** Left, right, and superiors views of a 3D brain rendering illustrating significant voxels from seed-to-voxel FC analysis using significant ASCC vs. HCs GMV clusters as seeds. The red color denotes significant voxels with increased FC with the GMV mask seed in ASCC compared to HCs, while the blue color denotes significant voxels with decreased FC in ASCC compared to HCs. Significant clusters were determined by thresholding based on voxel-level significance of $p < 0.001$ and cluster-level FDR corrected $p < 0.05$.

2.3.4 Disease-specific Differences in Cerebral Microstructure

Compared with healthy controls (HCs), symptomatic DCM patients exhibited differences in fiber density (FD), fractional anisotropy (FA), and mean diffusivity (MD) along various white matter pathways. Specifically, symptomatic DCM patients demonstrated higher FD in voxels located along the internal and external capsules, cingulate, middle and inferior cerebellar peduncle, corona radiata (anterior, posterior, and superior regions), and the superior longitudinal fasciculi (**Fig. 2.4 A**). Symptomatic DCM patients also displayed higher FD compared to HCs in voxels located at the thalamus, but lower FD in voxels along the body and splenium of the corpus callosum (**Fig. 2.4 A**). When compared to HCs, symptomatic patients exhibited lower FA in voxels located in various white matter tracts including the superior longitudinal fasciculi, superior fronto-occipital fasciculi, corticospinal tracts, fornix, cingulum, corpus callosum, and thalamic radiations (**Fig. 2.4 B**). Additionally, symptomatic DCM patients experienced lower FA in voxels located in the internal and external capsules, cerebral peduncles, and cerebellar peduncles compared to HCs (**Fig. 2.4 B**). Similarly, albeit across fewer white matter structures, symptomatic DCM patients demonstrated lower MD compared to HCs in voxels located along the corticospinal tracts, fornix, corpus callosum, corona radiata, cerebral peduncles, and cerebellar peduncles (**Fig. 2.4 C**). Significant anatomical locations, cluster sizes, and T-statistics are listed in **Table 2.3**.

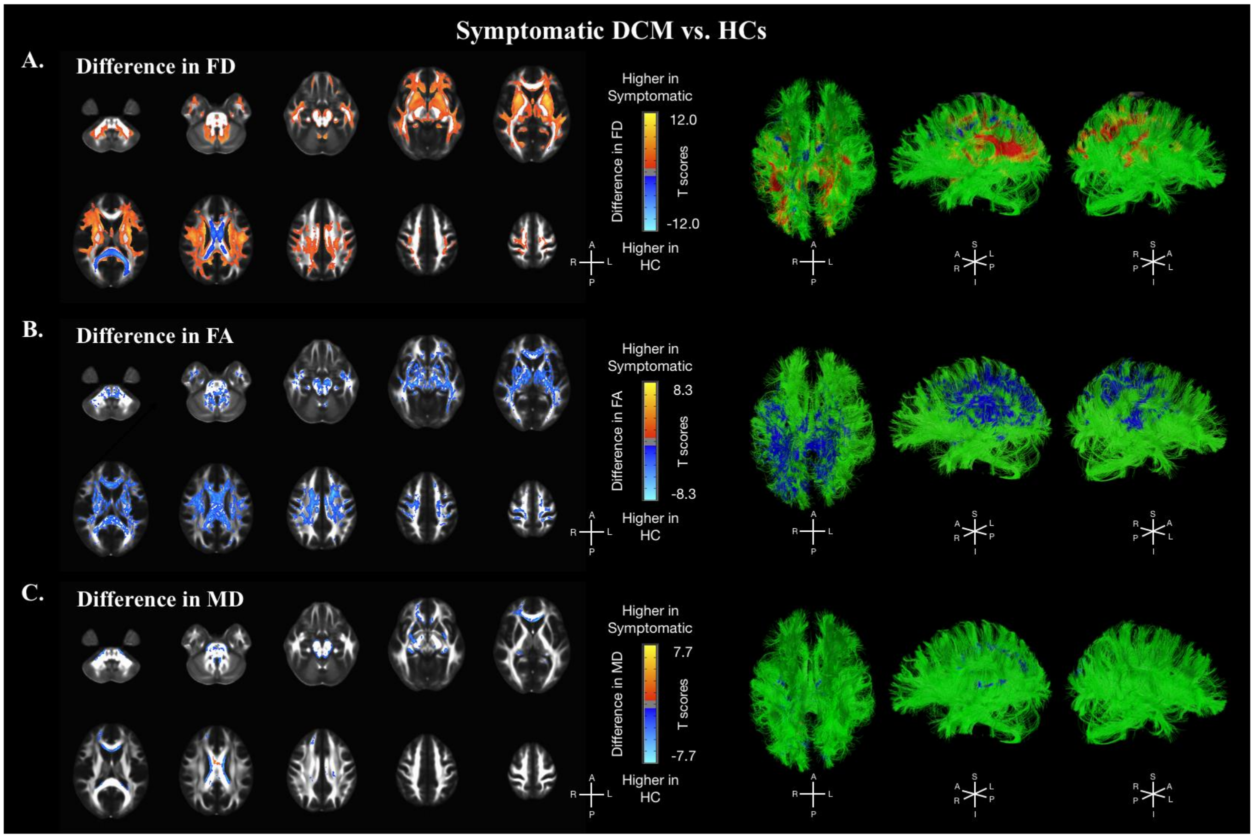

Figure 2.4: Voxel-wise diffusion tenor imaging (DTI) analysis between symptomatic DCM and HCs.

Anatomical localization of clusters with significantly different **(A)** fiber density (FD), **(B)** fractional anisotropy (FA), and **(C)** mean diffusivity (MD) between symptomatic DCM patients and healthy controls (HCs), while controlling for subject age and BMI. **(Left)** Colors on axial brain white matter tract template denote the value of the corresponding T-statistic in which red-orange color denotes higher values in symptomatic DCM patients compared to HCs, while blue-light blue denotes higher values in HCs compared to symptomatic DCM patients. **(Right)** 3-dimensional representation of fiber tracts and corresponding significant clusters. Significant clusters were determined by thresholding based on level of statistical significance of $p < 0.05$ and cluster-based corrections using permutation test.

When compared to HCs, ASCC patients demonstrated significant differences in FD, FA, and MD measurements across various cerebral white matter regions (**Fig. 2.4**). Asymptomatic patients exhibited higher FD in voxels located in white matter region throughout the brain; although largely along the superior longitudinal fasciculi, corpus callosum, internal and external capsules, corona radiata, cingulum, cerebellar peduncles, thalamic radiations, and thalamus compared to HCs (**Fig. 2.5 A**). In contrast, ASCC patients demonstrated significantly lower FA compared to HCs throughout the brain. Specifically, ASCC patients displayed lower FA in voxels located at the superior longitudinal fasciculi, corpus callosum, internal and external capsules, corona radiata, cingulum, cerebellar peduncles, and thalamus (**Fig. 2.5 B**). Asymptomatic patients also displayed significantly lower MD compared to HCs in voxels located along the corona radiata, cingulum, cerebral peduncles, superior and middle cerebellar peduncles, and corpus callosum (**Fig. 2.5 C**). Significant anatomical locations, cluster sizes, and T-statistics are listed in **Table 2.3**.

No statistically significant differences in FD, FA, nor MD were observed between the symptomatic DCM and ASCC patient cohorts.

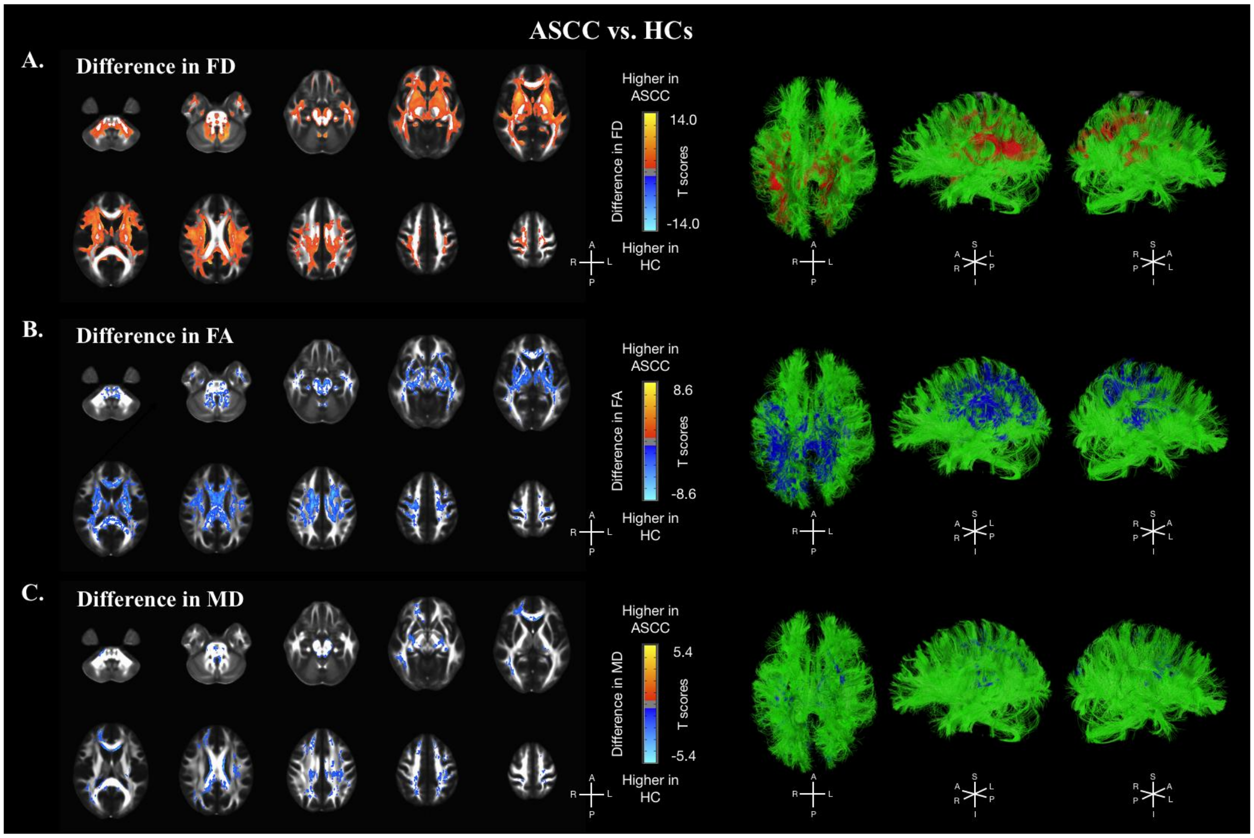

Figure 2.5: Voxel-wise diffusion tenor imaging (DTI) analysis between ASCC and HCs.

Anatomical localization of clusters with significantly different **(A)** fiber density (FD), **(B)** fractional anisotropy (FA), and **(C)** mean diffusivity (MD) between ASCC patients and healthy controls (HCs), while controlling for subject age and BMI. **(Left)** Colors on axial brain white matter tract template denote the value of the corresponding T-statistic in which red-orange color denotes higher values in ASCC patients compared to HCs, while blue-light blue denotes higher values in HCs compared to ASCC patients. **(Right)** 3-dimensional representation of fiber tracts and corresponding significant clusters. Significant clusters were determined by thresholding based on level of statistical significance of $p < 0.05$ and cluster-based corrections using permutation test.

Anatomical Region	Symtomatic DCM vs. HCs						ASCC vs. HCs					
	FD		FA		MD		FD		FA		MD	
	T-statistic	Cluster Volume (µL)	T-statistic	Cluster Volume (µL)	T-statistic	Cluster Volume (µL)	T-statistic	Cluster Volume (µL)	T-statistic	Cluster Volume (µL)	T-statistic	Cluster Volume (µL)
Anterior Limb of Internal Capsule Left	3.81718	2018	-3.06205	1486	-	-	3.91756	2516	-3.02815	1275	-	-
Anterior Limb of Internal Capsule Right	3.91683	2257	-3.06333	1226	-	-	4.02094	2552	-3.0052	1144	-	-
Anterior Corona Radiata Left	3.96171	4364	-2.83586	2061	-2.70674	1191	3.96099	5071	-2.76549	1353	-2.57095	1665
Anterior Corona Radiata Right	3.76022	4979	-2.937	3069	-2.63932	101	4.00544	5284	-2.94491	2472	-2.49629	64
Body of Corpus Callosum	-1.66716	5838	-3.48714	10506	-1.96076	2676	3.31725	1567	-3.35683	9791	-2.85077	2757
Cerebral Peduncle Left	2.49562	172	-3.42732	1273	-2.5257	169	2.94887	452	-2.89123	923	-2.5256	158
Cerebral Peduncle Right	2.77571	261	-3.30893	1466	-2.54836	215	3.2249	512	-3.13739	1109	-2.71701	209
Cingulum (Cingulate Gyrus) Left	1.67444	830	-3.33223	1283	-2.50408	98	3.24363	827	-3.20782	1164	-2.60927	395
Cingulum (Cingulate Gyrus) Right	1.45551	1198	-3.2641	1544	-2.48373	130	3.66666	901	-3.47014	1379	-2.58096	607
Cingulum (Hippocampus) Left	2.7561	392	-3.00575	440	-	-	3.01151	661	-3.15832	554	-2.92657	48
Cingulum (Hippocampus) Right	3.66251	629	-2.85754	339	-	-	3.51395	637	-3.37125	445	-2.28163	9
Corticospinal Tract Left	-	-	-2.68242	238	-2.55957	230	2.24417	18	-2.67032	213	-2.49329	47
Corticospinal Tract Right	2.15949	4	-2.5322	202	-3.06774	441	2.49478	39	-2.54032	170	-2.68271	290
External Capsule Left	4.96551	3982	-2.89883	2927	-2.42796	228	4.80938	4112	-2.88797	2899	-2.50875	142
External Capsule Right	5.31557	4508	-2.84154	2403	-2.74169	74	5.24418	4609	-3.12232	2777	-2.44029	87
Fornix	3.32531	534	-2.57345	76	-	-	3.3493	568	-2.36062	2	-	-
Fornix (Stria Terminalis) Left	2.55488	187	-3.17894	449	-3.17425	471	2.83168	372	-3.09302	514	-3.03337	352
Fornix (Stria Terminalis) Right	2.54289	314	-3.11386	639	-3.09361	285	3.00705	483	-3.11597	717	-2.95099	183
Genu of Corpus Callosum	3.07472	2554	-3.11163	5402	-3.65759	2675	3.68326	3160	-3.0941	4177	-3.40993	2158
Inferior Cerebellar Peduncle Left	2.87831	597	-3.19273	373	-	-	3.7356	670	-3.03682	308	-	-
Inferior Cerebellar Peduncle Right	2.82202	448	-3.49623	486	-	-	3.82425	618	-3.51297	457	-	-
Medial Lemniscus Left	2.36283	35	-2.96292	424	-2.58254	26	2.73101	181	-2.85163	341	-2.12333	1
Medial Lemniscus Right	2.66956	66	-3.1332	468	-2.34502	11	3.18831	198	-2.94357	412	-2.40184	26
Middle Cerebellar Peduncle	3.37276	5259	-2.78029	3603	-2.87299	1013	3.93335	7809	-2.82492	2281	-2.78282	341
Pontine Crossing Tract	2.42306	155	-2.76216	235	-2.45303	138	2.83059	562	-2.62829	167	-2.59415	47
Posterior Limb of Internal Capsule Left	3.15549	1022	-3.28181	2709	-2.18622	6	3.37685	1775	-3.15102	2354	-	-
Posterior Limb of Internal Capsule Right	3.1489	1138	-3.26509	2923	-	-	3.27949	1821	-3.28953	2806	-2.4094	111
Posterior Corona Radiata Left	3.83749	2512	-2.83612	1454	-2.29141	58	3.90923	2823	-2.81598	1301	-2.44426	586
Posterior Corona Radiata Right	3.75498	2507	-2.99689	1797	-2.33281	62	4.15389	2797	-2.99351	1445	-2.40013	456
Posterior Thalamic Radiation Left	1.28771	737	-2.83665	1075	-	-	2.72503	1389	-2.73911	988	-2.73737	437
Posterior Thalamic Radiation Right	0.0417078	587	-2.89574	1771	-	-	2.53995	519	-2.71941	1192	-	-
Retrolenticular Part of Internal Capsule Left	2.56136	185	-2.97702	1800	-2.19036	4	2.81181	782	-2.97866	1603	-2.43298	35
Retrolenticular Part of Internal Capsule Right	2.89315	1154	-2.92485	1668	-2.00811	1	3.42271	1683	-3.11783	1558	-2.75135	195
Sagittal Stratum Left	2.67082	710	-2.93984	987	-2.58875	10	2.70798	1223	-2.7423	756	-2.58854	61
Sagittal Stratum Right	3.1452	612	-3.13742	1193	-	-	2.9771	717	-3.13236	810	-2.22612	5
Splenium of Corpus Callosum	-4.08816	8697	-3.35522	9509	-2.38366	414	2.94808	734	-2.93863	7444	-2.71555	1464
Superior Cerebellar Peduncle Left	2.48811	40	-3.05616	544	-2.77291	146	2.67907	117	-3.08858	523	-2.72583	85
Superior Cerebellar Peduncle Right	2.7062	71	-2.95315	369	-2.91914	287	3.13431	177	-2.89593	430	-2.73888	173
Superior Corona Radiata Left	4.30699	5160	-3.25459	4867	-2.41125	3	4.24473	5560	-3.28736	5126	-2.52336	502
Superior Corona Radiata Right	4.05888	4691	-3.14647	4355	-2.24575	116	3.94726	4748	-3.29918	4903	-2.53396	1201
Superior Fronto-occipital Fasciculus Left	5.51257	504	-3.27272	327	-	-	5.66162	504	-3.33294	380	-	-
Superior Fronto-occipital Fasciculus Right	5.79639	506	-3.1937	377	-	-	6.05077	506	-3.25661	357	-	-
Superior Longitudinal Fasciculus Left	3.79845	4731	-3.05095	2746	-	-	3.83925	4879	-2.80062	2285	-2.50148	247
Superior Longitudinal Fasciculus Right	4.16923	4440	-2.60186	1823	-	-	3.90416	4899	-2.618	1253	-2.51464	1824
Tapetum Left	3.55768	141	-2.49194	69	-2.76667	74	3.41007	223	-2.65093	119	-2.88292	91
TapetumRight	3.12546	106	-2.58601	14	-2.68316	132	3.39052	99	-2.30643	10	-2.85113	72
Uncinate Fasciculus Left	4.12404	317	-3.00451	265	-	-	4.39028	349	-2.97616	189	-	-
Uncinate Fasciculus Right	3.59145	265	-3.09523	276	-	-	4.40194	315	-2.84597	155	-	-
Thalamus	3.31457	12782	-3.07932	14067	-2.44884	255	3.41614	16117	-2.99439	11867	-2.53056	465

Table 2.3: Anatomical regions and white matter tracts with significant differences between cohorts. The t-statistic and cluster volumes are listed for fiber density (FD), fractional anisotropy (FA), and mean diffusivity (MD).

2.4 Discussion

The present study utilized a multimodal neuroimaging approach to elucidate differing structural and functional cerebral alterations between symptomatic DCM and ASCC patients. The findings demonstrate differing disease-dependent cerebral reorganization in response to chronic cord compression in which symptomatic DCM patients exhibited expansion of vision-related cortical regions, increased visual-motor and visual-cerebellar functional connectivity, and altered microstructural integrity within the thalamus and white matter pathways associated with motor function, while ASCC patients demonstrated cortical atrophy of sensorimotor cortical regions, reduced visual-motor and increased visual-temporal functional connectivity, and altered microstructural integrity along association pathways including the corpus callosum and superior longitudinal fasciculus compared to age-matched healthy controls.

Although symptomatic DCM and ASCC patients may exhibit similar changes within the spinal cord, including degree of stenosis or compression, they present distinctly differing degrees of functional impairment leading to a clinical-radiological mismatch. By understanding the differences between these two patient populations, we may better understand neuroprotective and compensatory mechanisms that prevent symptom development and disease progression. Typically studies regarding cervical stenosis or degenerative myelopathy either combined the symptomatic and asymptomatic cohorts or exclude the ASCC patients. Although not directly compared, symptomatic DCM and ASCC patients experience similar micro- and macro-structural changes within the cervical spinal cord [91,92]. However, studies have demonstrated that symptomatic DCM patients tend to have higher incidence of spinal cord T2 signal hyperintensity compared to asymptomatic patients [24,93] and presence of spinal cord hyperintensity in ASCC patients has been associated with a higher risk of developing symptoms [10]. Previous research in DCM has primarily focused on alterations within the cervical spinal cord, yet symptomatic DCM and ASCC patients may experience similar neuronal and axonal damage within the spinal cord. Therefore, it is crucial to investigate structural and functional upstream reorganization within the brain. To the best of our knowledge, the present study is the first to evaluate the supraspinal alterations that occur between symptomatic and asymptomatic spinal cord compression patients exclusively.

In combined symptomatic and asymptomatic SCC cohorts, previous studies have demonstrated cortical thinning of somatosensory, motor, and cerebellar cortices [59,60,62,67]. However, the present study identified differences in cortical morphometry, specifically gray matter volume (GMV), between symptomatic DCM and ASCC cohorts when compared to HCs. Symptomatic DCM patients demonstrated increased GMV throughout the lateral occipital cortices compared to HCs, while the ASCC patients exhibited cortical atrophy in the pre- and post-central gyri. Furthermore, when comparing symptomatic and asymptomatic cohorts, symptomatic DCM patients displayed larger GMV in cortical regions responsible for visual and visuospatial processing compared to ASCC patients. Our findings suggest symptomatic DCM patients may be recruiting vision-related cortical regions in response to symptom experience and motor deficits, while ASCC patients display motor cortical atrophy typically associated with DCM.

In addition to macrostructural differences, incorporation of brain DTI was critical in elucidating significant microstructural differences between symptomatic DCM and ASCC patients. By measuring the motion of water molecules within brain tissue, DTI of the brain can provide information about white matter microstructure and indirectly measure axonal integrity and structural architecture [94]. Of the few studies investigating diffusion characteristics of ASCC patients, one study directly compared DTI measures of the cervical spinal cord at the maximum compression level between symptomatic DCM and ASCC patients. The study reported lower fractional anisotropy (FA) values and higher apparent diffusion coefficient (ADC) values implying greater axonal damage in symptomatic DCM patients [50]. Although cerebral diffusion-based comparisons between symptomatic DCM and ASCC have not previously been published, studies have demonstrated white matter reorganization in pathways associated with somatosensory, motor, and pain perception and modulation, as well as alterations in microstructural connectivity between the brainstem and cortical regions in a combine symptomatic and asymptomatic SCC patient cohort compared to HCs [66,68].

In the present study, both symptomatic and asymptomatic patients exhibited extensive alterations in white matter tracts throughout the brain compared to HCs. Notably, DCM patients experienced alterations along corticospinal tracts that are composed of descending projections originating in the motor cortex traveling along the corona radiata and internal capsule thru the cerebral peduncle and brainstem to the cervical spinal cord [95]. Here, symptomatic DCM patients exhibited more extensive decreases in FA along the corona radiata and cerebral peduncle, while ASCC patients displayed broader decreases in MD along the corona radiata and internal capsule, and larger increases in FD along the corticospinal, internal capsule, and cerebral peduncle compared to HCs, suggesting greater axonal demyelination and damage along the corticospinal tract in symptomatic patients. In addition, symptomatic patients experienced more expansive decreases in FA along the thalamic radiation, tracts important for relaying sensorimotor and vision related information [96], while ASCC patients displayed larger increases in FD and decreases in MD along the thalamic radiation compared to HCs. Moreover, symptomatic DCM patients displayed larger decreases in FA and MD along the superior and middle cerebellar peduncles responsible for connecting the cerebellum to the thalamus and brainstem [97], while ASCC patients demonstrated more extensive increases in FD along the cerebellar peduncles compared to

HCs. In addition, commissural fibers including the body and splenium of the corpus callosum demonstrated reduced FD in symptomatic patients, but higher FD in asymptomatic patients compared to HCs. The symptomatic patients also demonstrated more extensive decreases in FA in the corpus callosum. Such alterations in cerebral white matter diffusion characteristics may result from chronic injury to the cervical spinal cord and may indicate upstream reorganization of key sensorimotor and association pathways in DCM patients. Furthermore, findings suggest more extensive degeneration in motor and cerebellar projecting tracts in symptomatic DCM patients, while ASCC patients maintain integrity and density in association pathways which may help facilitate effective functional recruitment and compensation.

Differing cerebral reorganization patterns between symptomatic and asymptomatic patients were further elucidated by variances in resting state functional connectivity. In a combine symptomatic and asymptomatic SCC cohort, previous studies have demonstrated increased FC within sensorimotor regions and decreased FC between the cingulate cortex and cerebellum, putamen, and thalamus in association with symptom severity [73,74]. Here, whole-brain FC analyses revealed increased FC between primary visual regions and cerebellar, thalamic, and brainstem regions, as well as decreased FC between primary visual regions and sensorimotor, frontal, and temporal regions in both symptomatic and asymptomatic cohorts compared to HCs. Interestingly, symptomatic DCM patients demonstrated more expansive involvement of visual cortices, including both primary and secondary visual regions, exclusively exhibiting increased FC between secondary visual regions and the thalamus, putamen, caudate, brainstem, and cerebellum. Secondary visual regions or the prestriate cortex are responsible for higher-level visual perception including object motion, orientation, and depth [98]. Furthermore, our findings are consistent with previous literature in which altered connectivity of visual cortices was significantly associated with symptom severity and postoperative outcomes in symptomatic DCM patients [99] suggesting that expansion of visual recruitment may provide visuo-spatial information crucial for motor planning and compensation.

In addition to enhanced visual recruitment, DCM patients experienced altered connectivity within motor related regions, including primary sensorimotor and cerebellar cortices. In the present study, both symptomatic and asymptomatic patients experienced decreased FC between sensorimotor and visual regions and increased FC between sensorimotor and thalamic regions compared to HCs, albeit symptomatic DCM patients exhibited more extensive functional reorganization of the pre- and post-central gyri. Moreover, cerebellar pathways, critical for balance, motor coordination, and motor learning [97], displayed differing FC patterns between cohorts. Specifically, symptomatic DCM patients demonstrated increased FC within the cerebellum and between the cerebellum and visual regions, including primary and secondary, the thalamus, and the brainstem, but decreased FC between the cerebellum and the superior and middle frontal gyri. In contrast, ASCC patients merely displayed increased FC between the cerebellum and primary visual regions and the thalamus compared to HCs. Similarly, symptomatic DCM patients displayed increased FC between the brainstem and primary and secondary visual regions, cerebellar, temporal, and limbic regions, while ASCC patients only displayed increased FC between the brainstem and primary visual and temporal cortices. Additionally, only symptomatic DCM patients exhibited decreased FC between the brainstem and superior and middle frontal gyri and anterior cingulate cortex. Notably, increased FC between the brainstem and visual centers has previously been described in a combine DCM cohort [66]. Such findings suggest expansion of visuo-cerebellar and cerebellar-brainstem connectivity may be driven by motor and neurological deficits to provide motor-related compensation, while maintenance of fronto-cerebellar and frontobrainstem connectivity may work to inhibit symptom presentation following chronic spinal cord compression.

The present findings support the hypothesis that symptomatic DCM and ASCC patients are experiencing upstream axonal damage to differing degrees and recruiting distinctive neural pathways in response to chronic spinal cord compression. Symptomatic DCM patients are experiencing degeneration of motor and cerebellar white matter pathways, but functional recruitment and cortical expansion of visual regions, while ASCC patients are experiencing less extensive white matter degeneration of sensorimotor pathways and expansion of association pathways and functional recruitment of temporal regions. As demonstrated in a recent study [77], such differences between symptomatic and asymptomatic patients may in part reflect disease progression, however we suspect neuroprotective and genetic components to play a role in driving symptom presentation. Preclinical studies have demonstrated that the drug Riluzole, a sodium channel/glutamate blocker designed to modulate excitatory neurotransmission [100], was effective in protecting spinal cord tissue and reducing neurological symptoms in rat models of DCM [30,31]. Although such findings were not recapitulated in human clinical trials [32], it does demonstrate endogenous neuroprotective and repair mechanisms that may be influencing glutamate excitotoxicity and thus disease progression and symptom presentation. Additionally, differences in neuroinflammatory responses at the site of compression and upstream post-ischemic inflammation may influence the release of apoptotic factors and the degree of neurodegeneration [15]. Chronic spinal cord compression induces activation of microglia and recruitment of macrophages, which can provide neuroprotective benefits or release pro-inflammatory cytokines which contribute to axonal demyelination and neuronal apoptosis [10]. Studies have demonstrated that hypoxia leads to fractalkine (CX3CL1) mediated microglial activation [101]. However, in a fractalkine receptor (CX3CR1) deficient DCM mouse model not only were microglia and macrophage activation and pro-inflammatory cytokine and chemokines reduced, but increased gray and white matter integrity and neuronal and oligodendrocyte preservation was observed [15,102]. Such differences in pathobiological mechanisms may be driving neuroprotective features in patient with asymptomatic SCC.

In addition, evidence supports a heritable predisposition [17] for developing DCM, as well as genetic influences on clinical phenotype and treatment response [16]. Studies have identified candidate genes including polymorphisms of the *BDNF* and *HIF1A* genes, to be associated with worsening neurological deficit [103,104], while a polymorphism in the *OPG* gene was associated with better symptom scores [105]. Future studies may benefit from incorporating genetic testing of DCM relevant genes when investigating differences between symptomatic and asymptomatic SCC patients and the relationship between genetic factors and supraspinal alterations. Moreover, effective compensatory reorganization, particularly recruitment of visuospatial and motor planning related regions, likely contributes to maintaining neurological function.

Although the present study was novel in examination and comparison of supraspinal alterations in symptomatic DCM and ASCC, several limitations exist. Firstly, the study was limited in sample size, specifically direct comparisons between symptomatic and asymptomatic cohorts would benefit from a larger patient population providing sufficient statistical power to detect group differences following correction for multiple comparisons. Although analyses corrected for subject age and BMI, future studies would benefit from inclusion of subject total intracranial volume (TICV) as a covariate to normalize for variations in head size. Additionally, the healthy control cohort would benefit from cervical spinal cord imaging to definitively rule out age-related cervical stenosis. Future studies would also benefit from inclusion of longitudinal data regarding patient progression from asymptomatic to symptomatic SCC. Such data may be utilized to further identify cerebral signatures responsible for effective motor and neurological compensation.

In conclusion, symptomatic and asymptomatic SCC patients experience unique supraspinal structural and functional alterations contributing to disease management and progression in response to compression-induced spinal cord injury. Thus, development of non-invasive imaging biomarkers and identification of such cerebral signatures may benefit patient monitoring and effective treatment planning.

CHAPTER 3

Investigating Macrostructural Measurements of the Cervical Spinal and associated Supraspinal Alterations in DCM

3.1 Introduction

Degenerative cervical myelopathy (DCM) is characterized by pathophysiological alterations within the cervical spine including disc degeneration, facet joint degeneration, hypertrophy and ossification of ligaments, and development of osteophytes or bone spurs [8]. Such age-related osseocartilaginous alterations result in narrowing of the spinal canal and contribute to the development of chronic spinal cord compression. Furthermore, mechanical pathophysiological factors of DCM lead to ischemia via damage of the spinal cord microvascular and the blood spinal cord barrier (BSCB), neuroinflammation, atrophy of whiter matter tracts, and apoptosis of neurons and oligodendrocytes [3]. In response to chronic cord compression, patients often experience symptoms ranging from neck pain to numbness in the hands to loss of fine motor skills [8].

As illustrated in **Figure 3.1**, patients vary in degree, location, and extent of cervical stenosis presenting a challenge to accurately measure cord compression and characterize the affected spinal segments. Furthermore, spinal cord compression can occur in central, lateral, or diffuse patterns diversely affecting the cord and projecting nerves [106]. Historically, spinal compression in DCM patients was measured using the Torg-Palov Ratio (TPR) on lateral x-ray images of the cervical spine [107]. On lateral cervical radiographs from C3 to C7, the TPR is defined as the ratio of the anterior to posterior canal diameter to the vertebral body diameter at each mid-vertebral body level [108]. Now that the diagnosis and standard of care for DCM patients includes magnetic resonance imaging (MRI) of the cervical spine, the TPR has been adapted to be quantified using sagittal MR images [109]. Although patients with DCM exhibit smaller TPRs compared to healthy controls (HCs) [107], the TPR fails to capture compression at the spinal segments where disc bulging occurs, and the spinal cord may be most compressed. Furthermore, it was demonstrated that the TPR poorly correlated with spinal cord and canal areas [110].

Additional methods of measuring spinal cord compression in DCM have been introduced including cross-section area of the cord or canal, compression ratio of the cord or canal (ratio of the anterior-posterior to transverse diameter of the cord/canal), and maximum spinal cord or canal compromise (ratio of anterior-posterior diameter of the cord or canal to the average anterior-posterior diameter of first normal level above and below compressed level/levels) [111,112]. Currently, there is no standardized methodology for measuring degree of spinal cord or canal compression in DCM in clinical practice.

A recently published study reported that the cervical spinal cord compression area ratio, as defined by the area of the herniated disc to the area of the spinal canal, was significantly correlated with symptom severity as measured by the modified Japanese Orthopedic Association (mJOA), neck disability index (NDI), and visual analog scale (VAS) scores [113]. Macrostructural spinal cord compression has also been related to surgical outcomes. One study observed significant relationships between preoperative transverse spinal cord area at the maximum site of compression and the preoperative and postoperative JOA scores, as well as between the postoperative transverse area and the recovery rate [39]. Overall, few studies have investigated the relationship between macrostructural measurements of spinal cord and canal compression on patient symptom severity, disease progression, and surgical outcome.

Chronic narrowing of the spinal canal not only induces structural and functional alterations within the spinal cord, but also leads to upstream changes within the brain [1]. Studies have shown that, when compared to HCs, DCM patients exhibit significant reductions in cortical volume and thickness in somatosensory, motor, and cerebellar cortices [59,60,62]. Furthermore, atrophy of sensorimotor and pain-related cortical regions was associated with patient symptom severity [59]. Studies using functional MRI (fMRI) revealed increased functional connectivity within sensorimotor areas and decreased functional connectivity between the cerebellum, putamen, and thalamus to the cingulate cortex and frontal lobe regions was associated with increased severity of patient neck disability [74] and neurological impairment [73]. Although these previous studies have identified unique supraspinal features associated with DCM, it remains unknown whether macroscopic properties of compression result in conventional anatomical and functional alterations within the brain.

The present study investigates the relationship between macrostructural measurements of compression within the cervical spine and alterations in supraspinal morphometry and connectivity in patients with DCM. A range of MRI-based cord and canal measurements were collected including area, anterior to posterior diameter, transverse diameter, and midvertebral body and canal diameters accompanied by structural T1-weighted and resting-state functional MR (rs-fMRI) imaging of the brain and patient symptom severity via mJOA score. I hypothesized that greater spinal compression at the maximum site of compression, averaged over all cervical spinal segments, and in the most affected spinal segments will be associated with lower mJOA scores, smaller GMV in sensorimotor cortices, and greater functional connectivity between cerebellar and visual cortices. Additionally, I suspect spinal cord area and anterior-posterior diameter measurements to provide more accurate representation of spinal cord compression and greater association with upstream cerebral reorganization than the traditionally implemented Torg-Pavlov ratio. Findings from the present study will contribute to our understanding of mechanical compression of the spinal cord and supraspinal compensation and plasticity in patients with DCM.

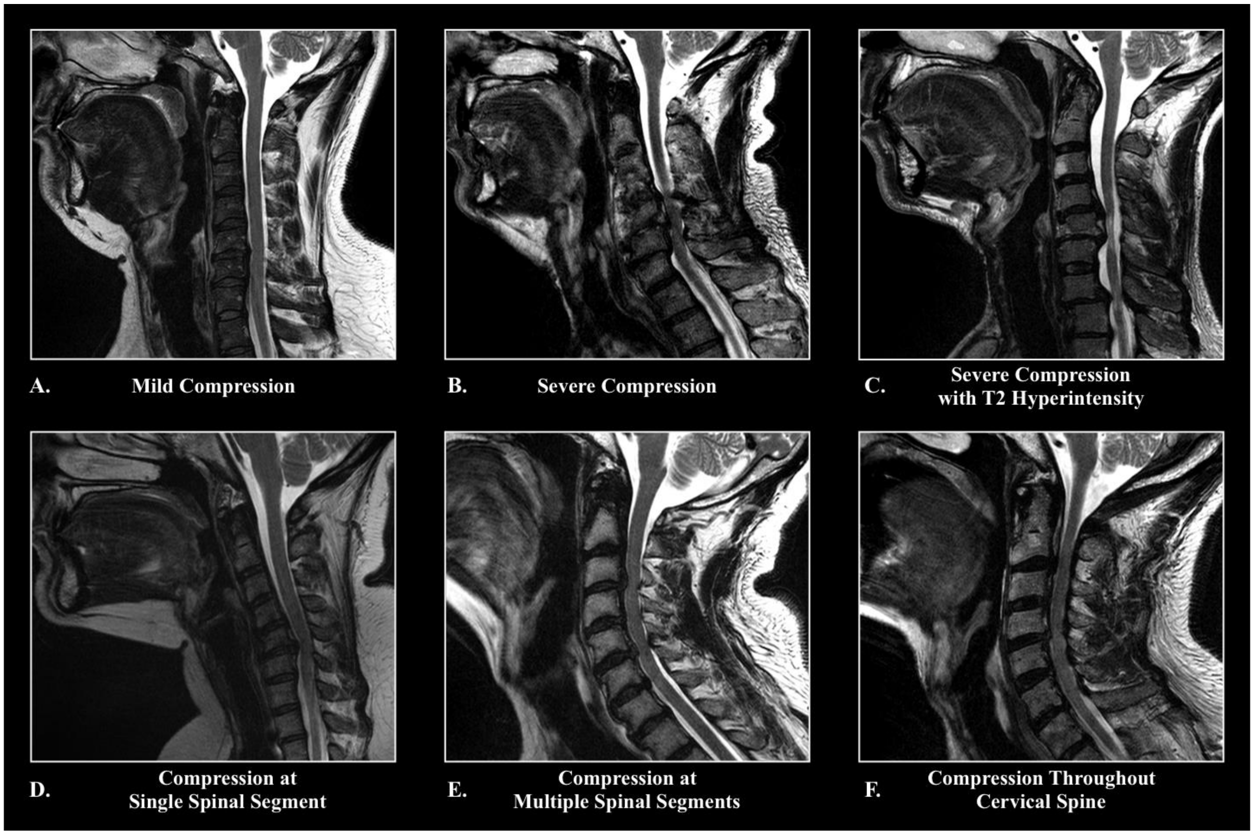

Figure 3.1: Spinal cord compression examples from patient population.

Degree, location, and extent of cervical spinal cord compression can vary greatly between patients from **(A)** mild to **(B)** severe compression, **(C)** presence of T2 hyperintensity, compression at **(D)** one or **(E)** multiple levels, and/or **(F)** compression throughout the cervical spine.

3.2 Material and Methods

3.2.1 Patient Population

A total of 100 patients were prospectively enrolled from 2015 to 2022 in a cross-sectional study including brain and spinal cord imaging as well as a neurological examination. Patients were recruited from the UCLA outpatient neurosurgery clinic and exhibited radiographic evidence of stenosis with evidence of spinal cord deformation, spinal canal narrowing, mass effect, and no visible cerebrospinal fluid signal around the spinal cord at the site of maximal compression on MRI. Patients included in this study had not undergone surgical intervention for cervical spinal cord compression at the time of brain imaging. All patients signed Institutional Review Board-approved consent forms, and all analyses were performed in compliance with the Health Insurance Portability and Accountability Act (HIPAA). The patient cohort consisted of 64 males and 36 females ranging in age from 31 to 81 years with a mean age of 58.3 years (standard deviation, 11.3 years). The modified Japanese Orthopedic Association (mJOA) score was used as a measure of neurological function. The mJOA scoring scale ranges from 0 to 18, where lower scores represent a worse neurological impairment, and an mJOA score of 18 represents no impairment of neurological function. Within the patient cohort, mJOA scores ranged from 10 to 18 with a mean score of 15.6 (standard deviation, 2.4). Of the 100 patients who completed the mJOA assessment, 9 patients were categorized with severe myelopathy (mJOA $\leq$ 11), 19 patients with moderate myelopathy (12 $\leq$ mJOA $\leq$ 14), and 45 patients with mild myelopathy (15 $\leq$ mJOA $\leq$ 17) at the time of the brain scan. 27 patients reported no neurological deficit (mJOA =18). All patients underwent brain and spinal cord imaging at UCLA. Patient demographic data was summarized in **Table 3.1**.

	Number of Subject (Male/Female)	**Age** (Median ± SD) [min, max]	**mJOA** (Median ± SD) [min, max]
DCM Patients	**100** (64/36)	(58.3 ± 11.3) [31, 81]	(15.6 ± 2.4) [10, 18]

Table 3.1: Cohort demographics.

Age is provided in mean years ± the standard deviation and minimum and maximum years. The modified Japanese Orthopedic Association (mJOA) score is provided in mean score ± the standard deviation with the minimum and maximum scores.

3.2.2 MR Imaging Acquisition

Cervical Spine Imaging

Standard T2-weighted structural cervical spine MRIs were acquired on a 3T MR scanner (Siemens Prisma; Siemens Healthcare, Erlangen, Germany) using a turbo spin echo (TSE) sequence, with a repetition time (TR) of 6700 to 9430 ms, a echo time (TE) of 84 ms, a flip angle of 160^o, slice thickness of 4 mm, field of view (FOV) of 180 x 180 mm, and acquisition matrix size of 274 x 384 in the axial orientation. In the sagittal orientation, a TSE sequence, with a TR of 4000 ms, a TE of 84 to 105 ms, a flip angle of 140^o, slice thickness of 3 mm, FOV of 220 x 220 mm, and acquisition matrix size of 288 x 384 was used.

Brain Imaging

High-resolution 1 mm 3-dimensional (3D) T1-weighted structural brain MRIs were acquired on a 3T MR scanner (Siemens Prisma; Siemens Healthcare, Erlangen, Germany) using a 3D magnetization-prepared rapid gradient-echo (MPRAGE) sequence in either the coronal, sagittal, or axial orientation, with a repetition time (TR) of 2300 to 2500 ms, a minimum echo time (TE) between 2 to 3 ms, an inversion time (TI) of 900 to 945 ms, a flip angle of 9^o to 20^o, slice thickness of 1 mm with no interslice gap, and field of view (FOV) of 240 x 320 mm and matrix size of 240 x 320.

To assess functional connectivity, resting state functional MRIs were acquired on a 3T MR scanner (Siemens Prisma; Siemens Healthcare, Erlangen, Germany) with a TR of 1500 to 2200 ms, TE of 28 to 30 ms, flip angle of 77^o, FOV of 220 to 245 mm with an acquisition matrix of 64 x 64 for an in-plane resolution of 3.4 to 3.8 mm, interleaved acquisition, slice thickness of 4 mm with no interslice gap, parallel imaging via CAIPIRNHA with a factor of 2, and multi-band acceleration with a factor of 2.

3.2.3 Spine Measurements

To assess macrostructural alterations of the spinal cord and canal, T2-weighted axial and sagittal images of the cervical spine and the Horos image viewer software (Horosproject.org) were used to quantify spinal cord and canal 1) area, 2) anterior-posterior diameter, and 3) transverse diameter at C2 and each spinal segment between C2 and T1. To account for variations in patient size, the above measurements were normalized to corresponding measurements at C2 (non-compressed site) for each patient. Using these spinal cord and canal measurements, degree of compression was quantified at each spinal segment between C2 and T1 with the following: 1) canal compression ratio (CR) (the ratio between the anterior-posterior diameter and the transverse diameter of the spinal canal), 2) cord compression ratio (CR) (the ratio between the anterior-posterior diameter and the transverse diameter of the spinal cord), and 3) spinal cord to spinal canal area ratio. Furthermore, the maximum site of compression for each patient was determined from sagittal and axial T2-weighted images as the spinal segment (C2-3 to C7-T1) with the greatest compression. In addition, a MRI version of the Torg-Pavlov ratio (ratio of anterior-posterior diameter of spinal canal to thickness of corresponding vertebral body) was calculated at each vertebral body from C2 to T1. The macrostructural spine measurements were used for subsequent comparisons with degree of neurological deficit (via mJOA), brain morphometry, and functional connectivity. Statistical analyses between spinal measurements and mJOA score were performed and plotted using the Prism software (Version 7.0c GraphPad Software, San Diego, California). Segmentation and quantification of each of the above measurements are demonstrated in **Figure 3.2**.

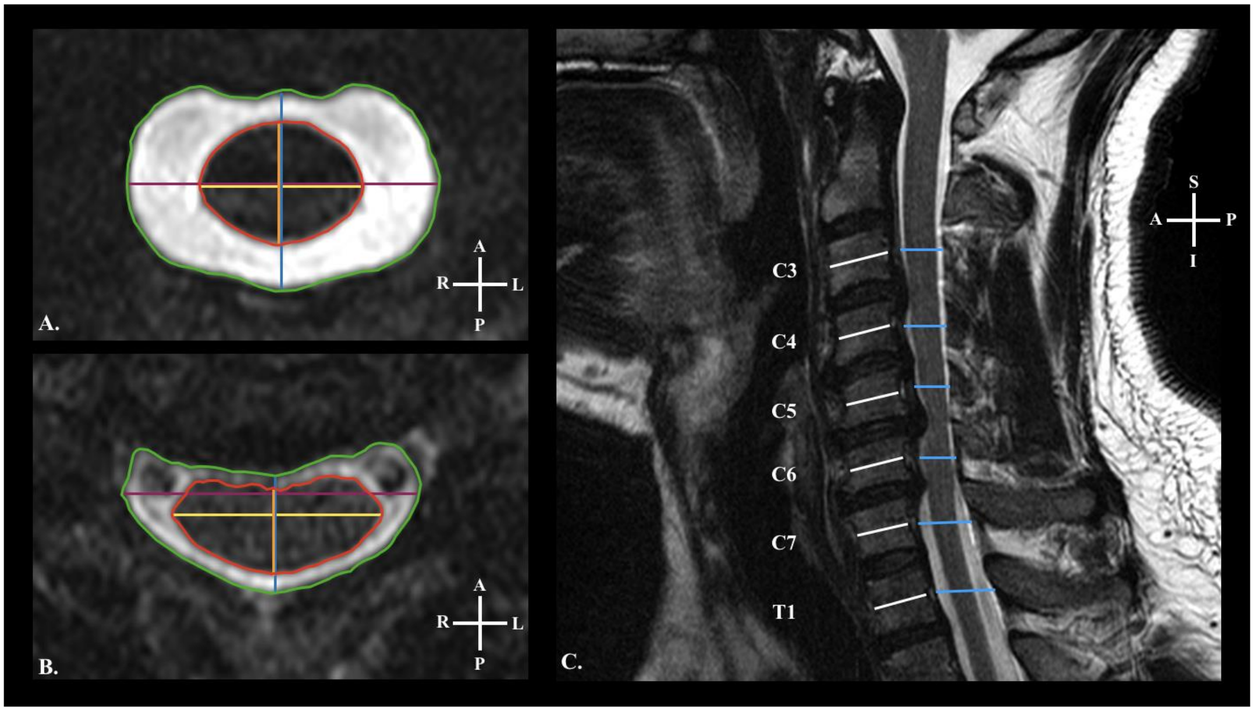

Figure 3.2: Measurement of the cervical spinal canal and cord.

Representative axial and sagittal T2-weighted MR images of the cervical spine of a patient with DCM. **(A-B)** Axial images of the spinal at **(A)** C2 and **(B)** C4-5 in which the cord area (red), cord anterior posterior diameter (orange), cord transverse diameter (yellow), canal area (green), canal anterior posterior diameter (blue), and canal transverse diameter (purple) are outlined in corresponding colors. **(C)** Sagittal image of the cervical spine in which the diameter of the midvertebral body (white) and the canal (blue) are outlined and used to calculate the adapted Torg-Pavlov ratio.

3.2.4 Image Processing and Statistical Analysis

Cortical segmentation and computation of gray matter volume (GMV) was performed using FreeSurfer (**https://surfer.nmr.mgh.harvard.edu/fswiki**) on T1-weighted brain images [114]. Processed brain surfaces were smoothed with a full-width half-maximum of 10 mm, then registered to a standard space defined by the Desikan-Killiany-Tourville (DKT) atlas [82]. Whole-brain cortical volume analysis was completed using FreeSurfer. A general linear model (GLM) was used to determine vertex-level significant correlations in spinal cord measurements outlined above and GMV while controlling for subject age. For each spinal cord measurement, the vertex-level correlations with cortical morphometry were assessed in 1) the segment with the maximum degree of compression, 2) across the average of values at all spinal segments, and 3) each spinal segment from C2-3 to C7-T1. The vertex-wise level of significance was set at $p < 0.05$, with multiple comparisons correction performed by using Monte Carlo permutations with a significance level of $p < 0.05$.

Functional brain MR images were processed using the CONN toolbox (https://www.nitrc.org/projects/conn) [85], which utilizes functions from the Statistic Parametric Mapping (SPM) toolbox (http://www.fil.ion.ucl.ac.uk/spm/). Functional and structural images were processed using the standard built-in preprocessing pipeline provided in the CONN toolbox. The default pipeline performs the following steps: 1) realignment of functional images including motion correction based on 12 degrees of freedom and unwarping, 2) slice-timing correction to correct for difference in acquisition time between slices, 3) registration of patient functional images to structural images from the first scanning timepoint, 4) registration of structural images to the Montreal Neurological Institute (MNI) defined standardized space, 5) removal of signal intensity spikes and functional volumes with excessive motion (threshold set at 2 mm translation and 2° rotation in any direction) using the Artifacts Detection Tool (ART) from SPM, 6) segmentation and normalization of functional images based on tissue type (gray matter, white matter, and cerebrospinal fluid) in MNI space, 6) segmentation and normalization of structural images based on tissue type (gray matter, white matter, and cerebrospinal fluid) in MNI space, and 7) spatial smoothing of functional data using 8 mm, full width at half maximum (FWHM) Gaussian kernel. Additionally, signals from the white matter, CSF, and motion parameters were regressed from the functional data, and signal filtering was performed using a band-pass filter of 0.008–0.09 Hz to reduce noise caused by scanner drift and physiological effects (i.e., pulsation and respiration).

Functional connectivity (FC) of the brain was assessed using ROI-to-voxel (also termed seed-to-voxel) analyses. Significant correlations between spinal measurements and GMV were extracted to create binary masks and imported into the CONN toolbox as regions of interest (ROIs). GLMs were used to evaluate significant correlations in each spinal cord measurement and functional connectivity between the whole-brain and corresponding significant GMV mask while accounting for the influence of age. For each spinal cord measurement, seed-to-voxel functional connectivity were assessed in 1) the segment with the maximum degree of compression, 2) across the average of values at all spinal segments, and 3) each spinal segment. For ROI-to-ROI analyses the connection-level significance was set at $p < 0.05$ and cluster-level significance was set at a false discovery rate (FDR) corrected $p < 0.05$. For seed-to-voxel analyses the voxel-level significance was set at $p < 0.01$ and cluster-level significance was set at a false discovery rate (FDR) corrected $p < 0.05$.

3.3 Results

3.3.1 Patient Characteristics

As summarized in **Table 3.1**, the patient cohort consisted of 64 males and 36 females ranging in age from 31 to 81 years with a mean age of 58.3 ± 11.34 years. Patient mJOA scores ranged from 10 to 18 with a mean score of 15.6 ± 2.4. Of the 100 patients included in the study, the site of maximum compression was observed at C2-3 in 1 patient, C3-4 in 16 patients, C4-5 in 26 patients, C5-6 in 38 patients, C6-7 in 16 patients, and C7-T1 in 3 patients (**Fig. 3.3**). C5-6 was the most common site of maximum spinal cord compression.

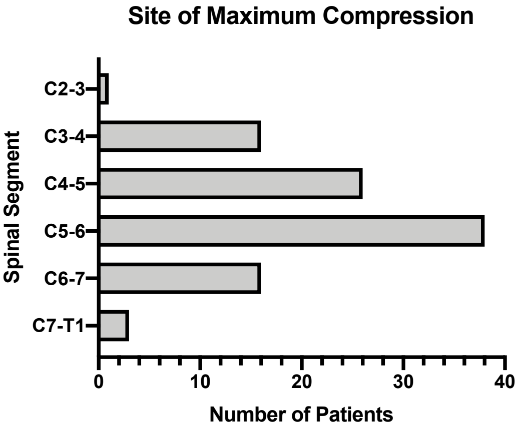

Figure 3.3: Site of maximum spinal cord compression within the patient cohort.

3.3.2 Correlation between Spinal Compression and mJOA Score

To determine whether spinal canal and cord measurements were predictors of neurological status, the relationship between spinal measurements and mJOA scores were investigated. The following spinal measurements were tested at the site of maximum compression and each spinal segment from C2-3 to C7-T: normalized canal area, normalized cord area, normalized canal anterior-posterior length, normalized cord anterior-posterior length, canal compression ratio, cord compression ratio, and cord canal area ratio. Normalized measurements were normalized to C2 to control for differences in patient body size and height. The Torg-Pavlov ratio was tested at the site of maximum compression and each vertebral body from C3 to T1. Two-tailed Pearson correlation coefficients for each measurement is listed in **Table 3.2**. Significant positive correlations were observed between canal compression ratio at C7-T1 and mJOA ($R^2=0.0682$, $p=0.0094$) **(Fig. 3.4)**.

Spinal Measurement	**Statistical Value**	**Maximum Site of Compression**	**C2-3**	**C3-4**	**C4-5**	**C5-6**	**C6-7**	**C7-T1**
Normalized Canal Area	R squared	0.0024	0.0020	0.0016	0.0169	0.0270	0.0270	0.0108
	P value	0.6249	0.6567	0.6897	0.1970	0.1025	0.1041	0.3032
Normalized Cord Area	R squared	0.0136	0.0001	0.0066	0.0018	0.0022	0.0009	0.0081
	P value	0.2487	0.9318	0.4227	0.6782	0.6453	0.7662	0.3740
Normalized Canal Anterior-Posterior Length	R squared	0.0131	0.0047	0.0038	0.0288	0.0242	0.0085	0.0050
	P value	0.2591	0.4991	0.5421	0.0929	0.1242	0.3634	0.4848
Normalized Cord Anterior-Posterior Length	R squared	0.0022	0.0003	0.0001	0.0142	0.0084	0.0005	6.90E-06
	P value	0.6456	0.8712	0.9220	0.2407	0.3650	0.8244	0.9793
Canal Compression Ratio	R squared	0.0011	0.0057	0.0107	0.0001	0.0039	0.0115	0.0682
	P value	0.7466	0.4571	0.3086	0.9429	0.5393	0.2902	**0.0094****
Cord Compression Ratio	R squared	0.0003	0.0128	0.0147	0.0004	0.0012	0.0226	0.0259
	P value	0.8553	0.2648	0.2350	0.8452	0.7349	0.1379	0.1133
Cord-Canal Area Ratio	R squared	1.81E-06	0.0118	0.0111	0.0001	0.0031	0.0022	0.0028
	P value	0.9894	0.2814	0.2964	0.9054	0.5851	0.6477	0.6041
Torg-Pavlov Ratio	R squared	0.0068	0.0277	0.0010	0.0070	0.0020	0.0138	0.0338
	P value	0.4160	0.0979	0.7589	0.4062	0.6602	0.2462	0.0715

Table 3.2: Correlation between spinal measurements and mJOA score.

The two-tailed Pearson correlation p-value is reported for each measurement at the maximum site of compression and each spinal segment from C2-3 to C7-T1. Note that the Torg-Pavlov ratio is reported for each vertebral body level from C3 to T1. The bolded p-values denote statistically significant correlation between the spinal measurement and mJOA score. mJOA, modified Japanese Orthopedic Association.

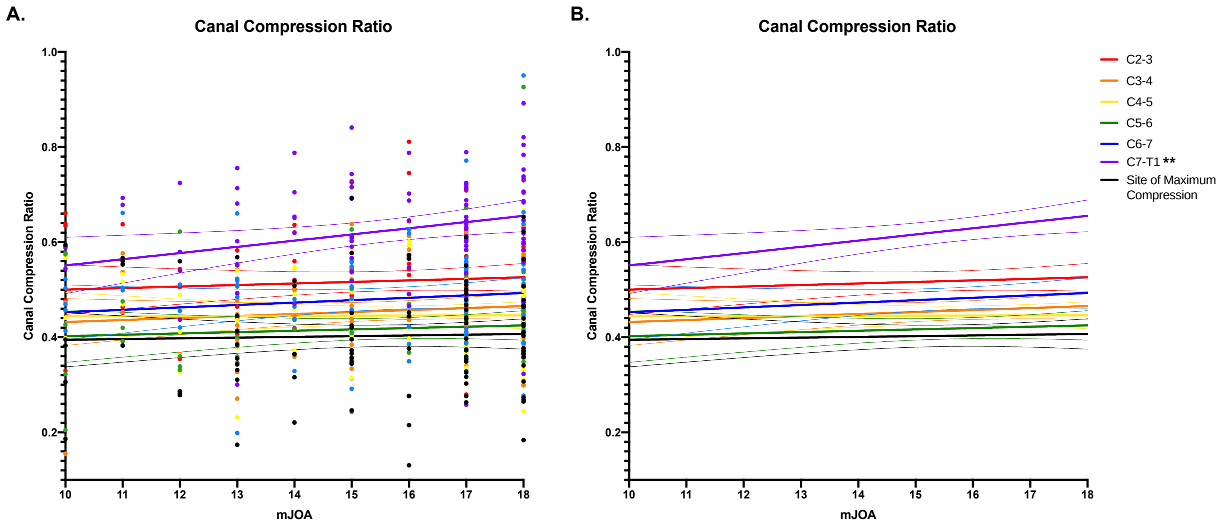

Figure 3.4: Correlation between spinal canal compression and neurological impairment.

Linear regression results comparing mJOA with canal compression ratio **(A)** with and **(B)** without individual patient data points. The linear regression (line) and standard error (shaded region) are plotted for the correlation between mJOA and canal compression ratio at the maximum site of compression (black), C2-3 (red), C3-4 (orange), C4-5 (yellow), C5-6 (green), C6-7 (blue), and C7-T1 (purple). Point color corresponds to canal measurements at maximum site of compression and each spinal segment. ** denotes $p < 0.01$.

3.3.3 Relationship between Spinal Compression and Cerebral Morphometry and Functional Connectivity

Spinal Compression at the Maximum Site of Compression

Results from whole-brain cortical volume analysis revealed significant correlations between gray matter volume (GMV) and spinal measurements at the maximum site of compression including the cord area, cord anterior-posterior length, and canal anterior-posterior length (**Fig. 3.5**). Patients exhibited significant correlations between spinal cord area at the site of maximum compression and GMV (i.e., greater cord compression, larger GMV) in the bilateral postcentral gyrus, bilateral superior frontal gyrus, bilateral middle frontal gyrus, bilateral supramarginal gyrus, and right pars opercularis (**Fig. 3.5 A**). Additionally, cord anterior-posterior length at the maximum site of compression was significantly associated with GMV. Specifically, patients displayed a positive correlation (i.e., greater anterior-posterior cord compression, larger GMV) between cord anterior-posterior compression and GMV in the left superior frontal gyrus and a negative correlation (i.e., greater anterior-posterior cord compression, smaller GMV) in the left fusiform gyrus (**Fig. 3.5 B**). No significant associations were observed between the functional connectivity of the cord area GMV seed nor the cord anterior-posterior length GMV seed and the corresponding spinal measurements.

Patients demonstrated significant negative correlations between canal compression, as measured by the anterior-posterior length, at the maximum site of compression and GMV in the left fusiform and right inferior temporal gyri (**Fig. 3.5 C**). Furthermore, significant negative correlations between normalized canal anterior-posterior length and functional connection (i.e., decreased FC with greater compression) were observed between the seed regions (left fusiform and right inferior temporal gyri) extracted from the GMV masks and various frontal, motor, temporal, and cerebellar regions including voxels in the frontal poles, superior frontal gyri, precentral gyri, and middle and inferior temporal gyri (**Fig. 3.5 C**). No significant correlations were observed between the Torg-Pavlov ratio (TPR) at the maximum site of compression and cerebral GMV.

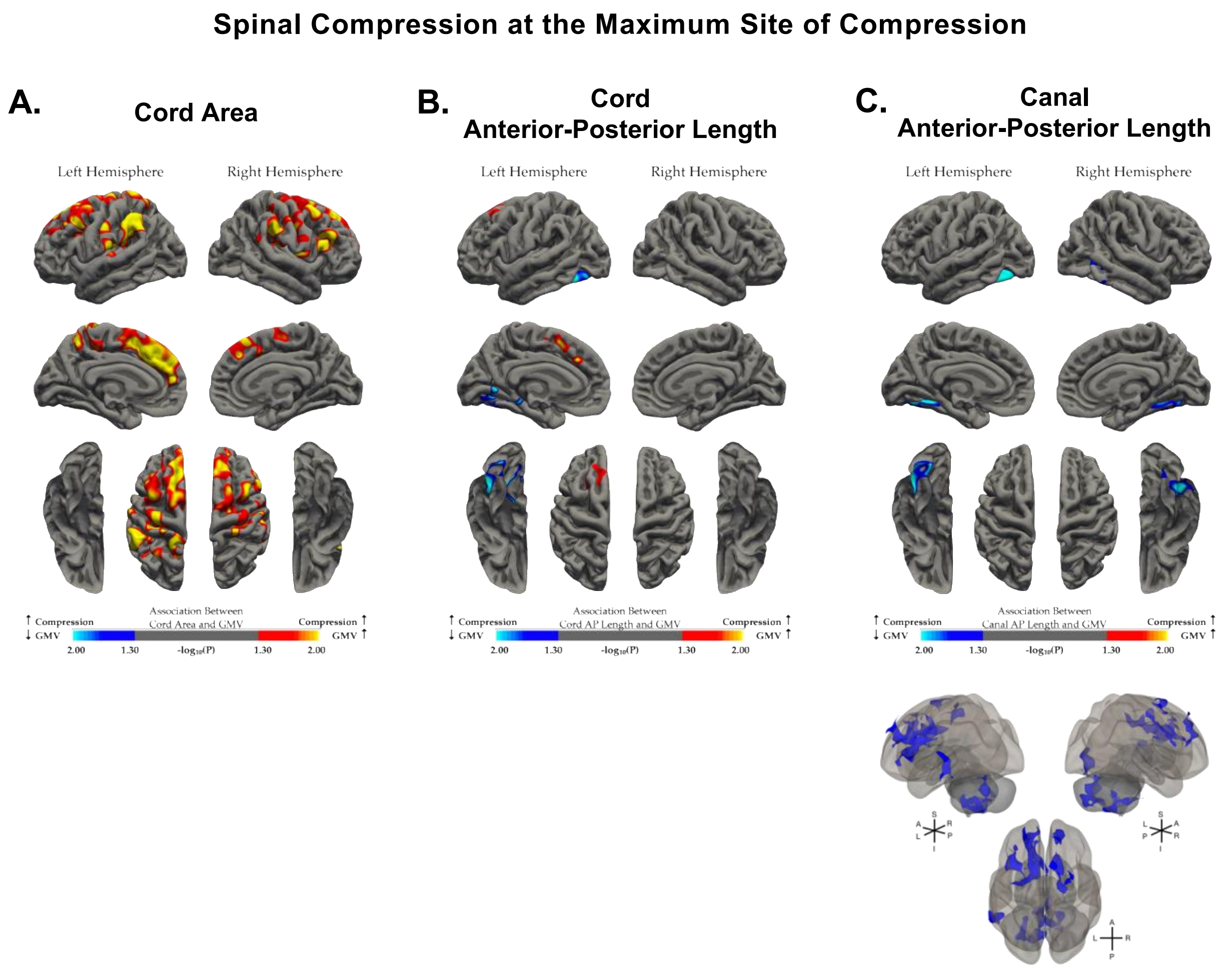

Figure 3.5: Relationship between GMV and spinal compression at the maximum site of compression. Whole-brain correlation analysis between gray matter volume (GMV) and spinal measurements at the maximum site of cervical spinal compression including (**A**) normalized cord area, (**B**) normalized cord anterior-posterior length, and (**C**) normalized canal anterior-posterior length, while controlling for patient age (**top row**). (**A-C, top row**) Red-yellow color denotes a positive correlation between spinal cord compression and GMV (i.e., greater compression, larger GMV), while blue-light blue color denotes a negative correlation between spinal cord compression and GMV (i.e., greater compression, smaller GMV). (**C, bottom row**) Seed-to-voxel functional connectivity (FC) analysis using corresponding significant GMV clusters as seeds, where the red color denotes significant regions with increased connectivity with greater compression and the blue color denotes significant regions with decreased connectivity with greater compression. Significant clusters were determined by thresholding based on statistical significance of $p <$

0.05 for GMV analyses and voxel-level significance of $p < 0.01$ and cluster-level false discovery rate (FDR) corrected $p < 0.05$ for FC analyses.

Average Spinal Compression across the Cervical Spine

When examining the relationship between average spinal compression from cervical spinal segments C2-3 to C7-T1 and GMV, patients demonstrated significant associations between normalized cord area and GMV, as well as between normalized cord anterior-posterior length and GMV (**Fig. 3.6**). Patients demonstrated significant positive correlations (i.e., greater compression, larger GMV) between the average normalized cord area and GMV in the right precentral gyrus (**Fig. 3.6 A**). Additionally, patients displayed significant positive correlations between functional connection and average cord area (i.e., increased functional connectivity with greater compression) between the extracted GMV seed region (right precentral gyrus) and voxels in various occipital and cerebellar regions including the bilateral lateral occipital cortex, bilateral occipital poles, bilateral occipital fusiform gyrus, cerebellar crus 1, and cerebellar hemisphere regions 6,7b, and 8 (**Fig. 3.6 A**). In addition, significant negative correlations between functional connection and average cord area were observed between the seed region (right precentral gyrus) and voxels in the left precentral gyrus, left postcentral gyrus, right supplementary motor area (SMA) (**Fig. 3.6 A**).

When examining the relationship between average normalized cord anterior-posterior length and GMV, patients demonstrated significant negative correlations (i.e., greater compression, smaller GMV) in the right precuneus (**Fig. 3.6 B**). No significant associations were observed between the functional connectivity of the average normalized cord anterior-posterior length GMV seed and the average normalized cord anterior-posterior length. Additionally, no significant correlations were observed between the average normalized canal anterior-posterior length from C2-3 to C7-T1 and GMV nor between the average TPR between C3 and T1 and GMV.

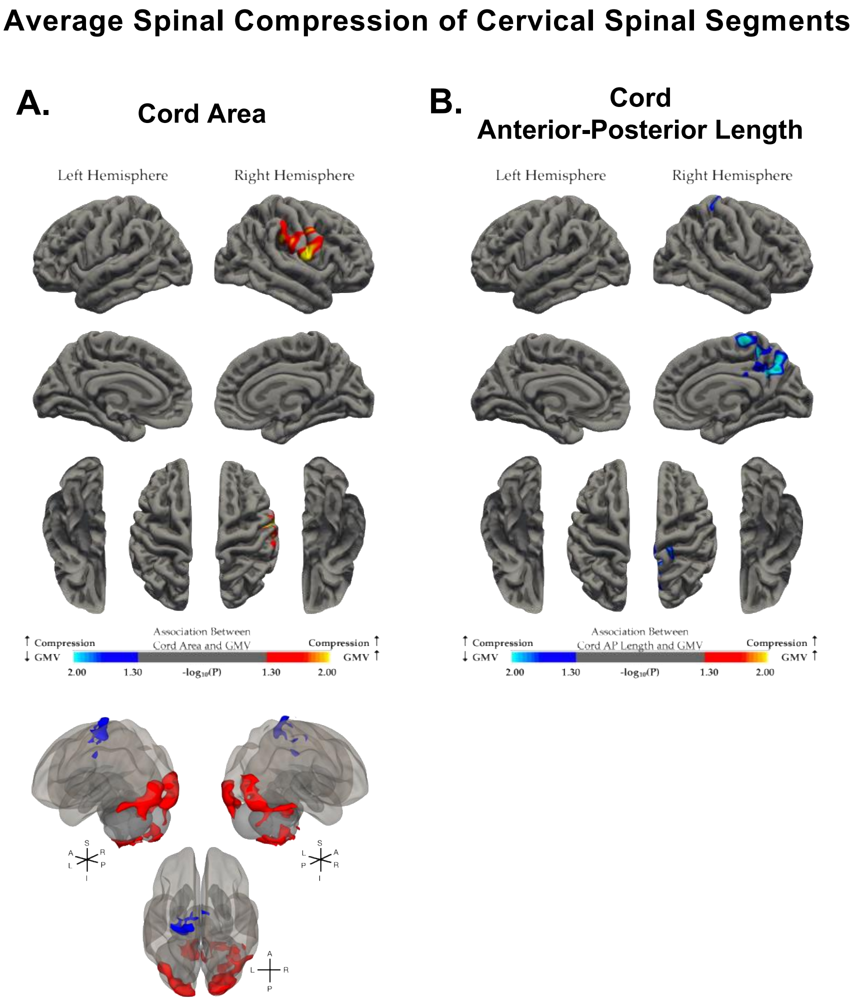

Figure 3.6: Relationship between GMV and average spinal compression of cervical spinal segments. Whole-brain correlation analysis between gray matter volume (GMV) and average spinal measurements from C2-3 to C7-T1 including (**A**) normalized cord area and (**B**) normalized cord anterior-posterior length, while controlling for patient age (**top row**). (**A-B, top row**) Red-yellow color denotes a positive correlation between spinal cord compression and GMV (i.e., greater compression, larger GMV), while blue-light blue color denotes a negative correlation between spinal cord compression and GMV (i.e., greater compression, smaller GMV). (**A, bottom row**) Seed-to-voxel functional connectivity (FC) analysis using corresponding significant GMV clusters as seeds, where the red color denotes significant regions with increased

connectivity with greater compression and the blue color denotes significant regions with decreased connectivity with greater compression. Significant clusters were determined by thresholding based on statistical significance of $p < 0.05$ for GMV analyses and voxel-level significance of $p < 0.01$ and cluster-level false discovery rate (FDR) corrected $p < 0.05$ for FC analyses.

Spinal Compression at C2-3

Significant positive correlations (i.e., greater compression, larger GMV) were observed between normalized spinal cord area and anterior-posterior length at spinal segment C2-3 and GMV (**Fig. 3.7**). Specifically, patients demonstrated that greater cord compression, as measured by cord area at C2-3, was associated with larger GMV in the left supramarginal, right postcentral, and right fusiform gyri (**Fig. 3.7 A**). No significant associations were observed between the functional connectivity of the cord area GMV seed and the cord area at C2-3.

When evaluating the association between cord anterior-posterior length and GMV, patients displayed a positive association in the left inferior parietal, left superior temporal, and right postcentral gyri (**Fig. 3.7 B**). Furthermore, significant negative correlations between cord compression at C2-3, as measured by normalized cord anterior-posterior length, and functional connection (i.e., decreased FC with greater compression) were observed between the seed regions (left supramarginal, right postcentral, and right fusiform gyri) extracted from the GMV masks and voxels in the left superior and middle frontal gyri (**Fig. 3.7 B**). No significant correlations were observed between the normalized canal anterior-posterior length at spinal segment C2-3 and GMV.

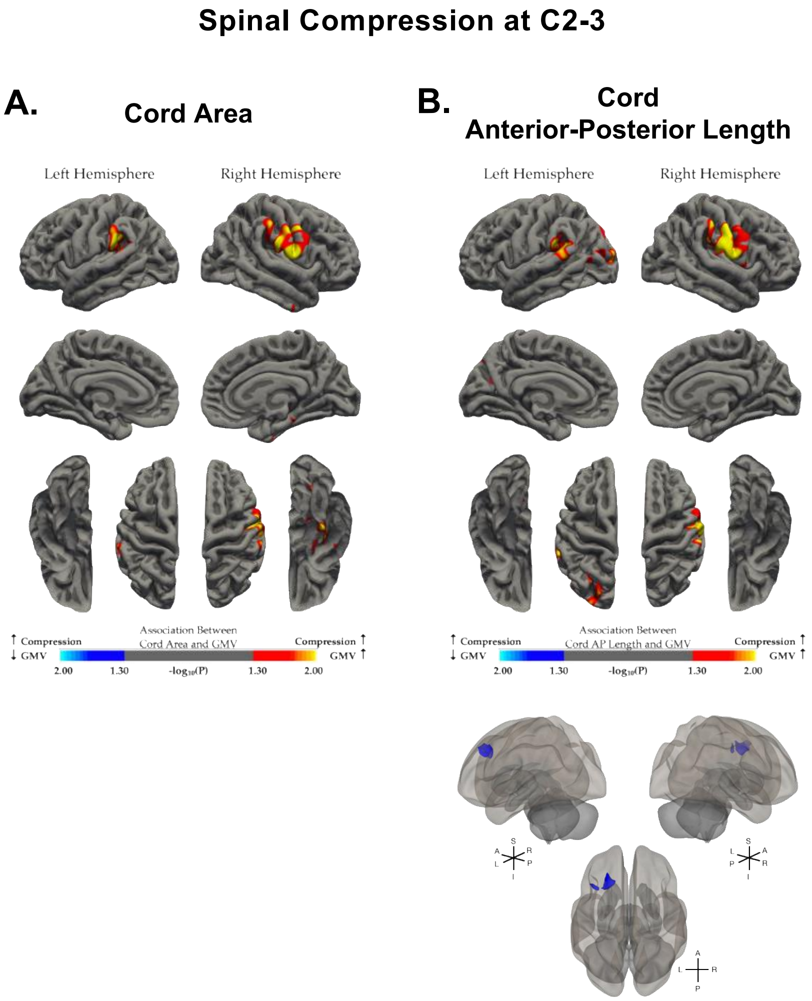

Figure 3.7: Relationship between GMV and spinal compression at C2-3.

Whole-brain correlation analysis between gray matter volume (GMV) and spinal measurements (**A**) normalized cord area and (**B**) normalized cord anterior-posterior length at C2-3, while controlling for patient age (**top row**). (**A-B, top row**) Red-yellow color denotes a positive correlation between spinal compression and GMV (i.e., greater compression, larger GMV), while blue-light blue color denotes a negative correlation between spinal cord compression and GMV (i.e., greater compression, smaller GMV). (**B, bottom row**) Seed-to-voxel functional connectivity (FC) analysis using corresponding significant GMV clusters as seeds, where the red color denotes significant regions with increased connectivity with greater compression and the blue color denotes significant regions with decreased connectivity with greater compression. Significant clusters were determined by thresholding based on statistical significance of $p <$

0.05 for GMV analyses and voxel-level significance of $p < 0.01$ and cluster-level false discovery rate (FDR) corrected $p < 0.05$ for FC analyses.

Spinal Compression at C3-4

When examining the relationship between spinal compression at C3-4 and GMV, patients demonstrated significant associations between normalized canal anterior-posterior length at C3-4 and GMV, as well as between the TPR at C3 and GMV (**Fig. 3.8**). Patients demonstrated negative correlations (i.e., greater compression, smaller GMV) between normalized canal anterior-posterior length and GMV in the left superior frontal gyrus (**Fig. 3.8 A**). In contrast, patients displayed significant positive correlations (i.e., greater compression, larger GMV) between the TPR at C3 and GMV in the left supramarginal and right inferior temporal gyri (**Fig. 3.8 B**). Patients also demonstrated significant negative correlations between functional connection and canal compression at C3-4 between the extracted GMV seed region (left superior frontal gyrus) and various occipital regions including voxels in the bilateral lateral occipital cortex, the bilateral occipital poles, the left intracalcarine cortex (ICC), and the left occipital fusiform gyrus (**Fig. 3.8 A**). No significant associations were observed between the functional connectivity of the TPR GMV seed and the TPR at C3. No significant correlations were observed between GMV and the normalized cord area nor the normalized canal anterior-posterior length at C3-4.

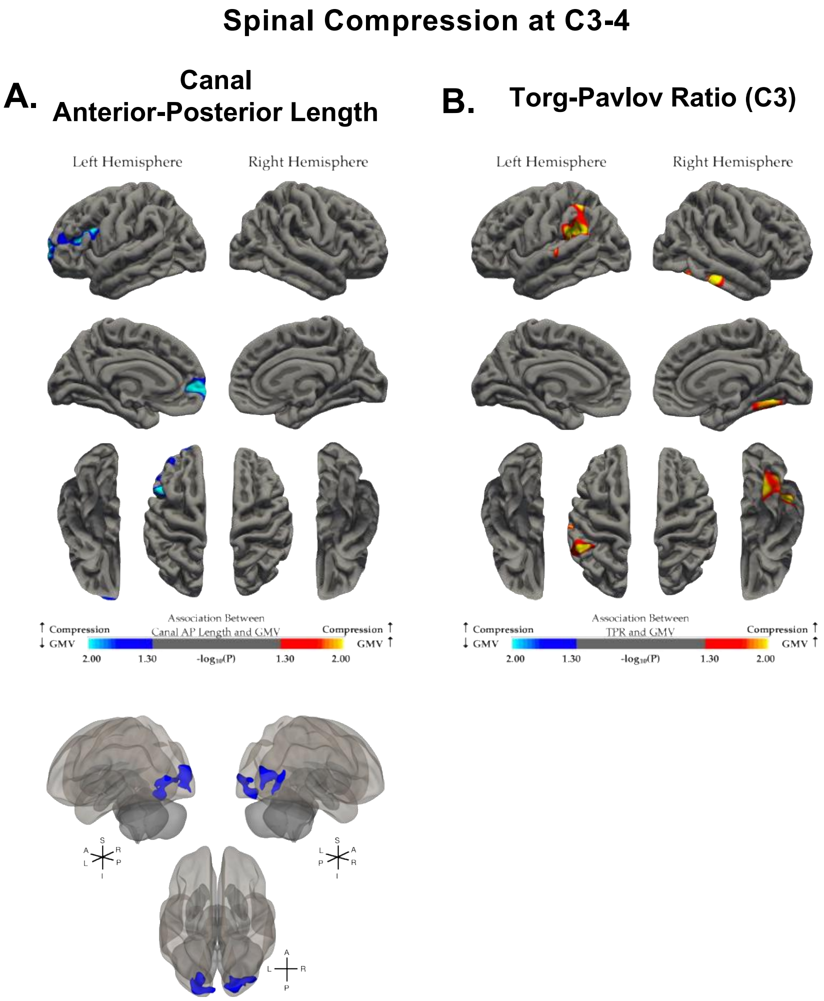

Figure 3.8: Relationship between GMV and spinal compression at C3-4.

Whole-brain correlation analysis between gray matter volume (GMV) and spinal measurements (**A**) normalized canal anterior-posterior length at C3-4 and (**B**) Torg-Pavlov Ratio (TPR) at C3, while controlling for patient age (**top row**). (**A-B, top row**) Red-yellow color denotes a positive correlation between spinal compression and GMV (i.e., greater compression, larger GMV), while blue-light blue color denotes a negative correlation between spinal compression and GMV (i.e., greater compression, smaller GMV). (**A, bottom row**) Seed-to-voxel functional connectivity (FC) analysis using corresponding significant GMV clusters as seeds, where the red color denotes significant regions with increased connectivity with greater compression and the blue color denotes significant regions with decreased connectivity with greater compression. Significant clusters were determined by thresholding based on statistical significance of $p < 0.05$ for GMV analyses and voxel-level significance of $p < 0.01$ and cluster-level false discovery rate (FDR) corrected $p < 0.05$ for FC analyses.

Spinal Compression at C4-5

Results from whole-brain cortical volume analysis revealed significant associations between spinal measurements at C4-5 and GMV (**Fig. 3.9**). Patients exhibited significant positive correlations between spinal cord area at C4-5 and GMV (i.e., greater cord compression, larger GMV) in the left precentral gyrus and left caudal middle frontal gyrus (**Fig. 3.9 A**). Moreover, patients demonstrated significant negative correlations between normalized cord area and functional connection (i.e., decreased FC with greater compression) between the seed regions (left precentral gyrus and caudal middle frontal gyri) extracted from the GMV masks and voxels in the bilateral precentral gyri, right postcentral gyrus, and the precuneus (**Fig. 3.9 A**).

Patients also displayed significant correlations between normalized cord anterior-posterior length and GMV, specifically exhibiting positive correlation in the right supramarginal gyrus and negative correlation in the left lingual gyrus (**Fig. 3.9 B**). When examining the relationship between normalized canal anterior-posterior length and GMV, patient exhibited a significant negative correlation in the left lateral occipital cortex (**Fig. 3.9 C**). Lastly, patient demonstrated a significant positive correlation between the TPR at C4 and GMV in the left supramarginal gyrus (**Fig. 3.9 D**). No significant associations were observed between the functional connectivity of the cord anterior-posterior length GMV seed, the canal anterior-posterior length GMV seed, nor the TPR GMV seed and the corresponding spinal measurements.

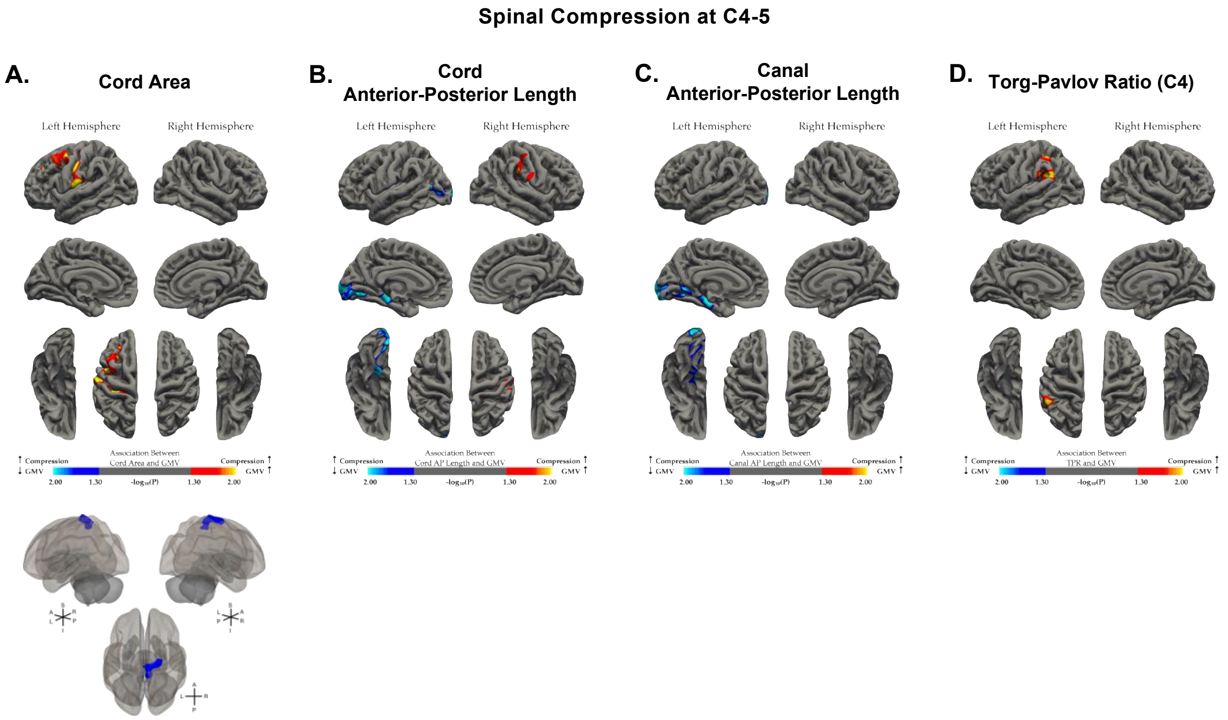

Figure 3.9: Relationship between GMV and spinal compression at C4-5.

Whole-brain correlation analysis between gray matter volume (GMV) and spinal measurements at C4-5 including (**A**) normalized cord area, (**B**) normalized cord anterior-posterior length, (**C**) normalized canal anterior-posterior length, and (**D**) Torg-Pavlov Ratio (TPR) at C4, while controlling for patient age (**top row**). (**A-D, top row**) Red-yellow color denotes a positive correlation between spinal compression and GMV (i.e., greater compression, larger GMV), while blue-light blue color denotes a negative correlation between spinal compression and GMV (i.e., greater compression, smaller GMV). (**A, bottom row**) Seed-to-voxel functional connectivity (FC) analysis using corresponding significant GMV clusters as seeds, where the red color denotes significant regions with increased connectivity with greater compression and the blue color denotes significant regions with decreased connectivity with greater compression. Significant clusters were determined by thresholding based on statistical significance of $p < 0.05$ for GMV analyses and voxel-level significance of $p < 0.01$ and cluster-level false discovery rate (FDR) corrected $p < 0.05$ for FC analyses.

Spinal Compression at C5-6

Significant negative correlations (i.e., greater compression, smaller GMV) were observed between normalized spinal cord and canal anterior-posterior lengths at C5-6 and GMV (**Fig. 3.10**). Specifically, patients demonstrated significant negative association between the normalized cord anterior-posterior length and GMV in the bilateral orbitofrontal gyri, left lateral occipital cortex, and left inferior temporal gyrus (**Fig. 3.10 A**). Furthermore, significant negative correlations between cord compression at C5-6, as measured by normalized cord anterior-posterior length, and functional connection (i.e., decreased FC with greater compression) were observed between the seed regions (bilateral orbitofrontal gyri, left lateral occipital cortex, and left inferior temporal gyrus) extracted from the GMV masks and voxels in the bilateral occipital poles, bilateral cuneal cortices, right parietal operculum cortex, right planum temporale, and right central opercular cortex (**Fig. 3.10 A**).

When evaluating the relationship between canal anterior-posterior length and GMV, patients displayed a negative association in the left superior temporal gyrus and left lateral occipital cortex (**Fig. 3.10 B**). Patients also demonstrated significant negative correlations between canal compression at C5-6, as measured by normalized canal anterior-posterior length, and functional connection (i.e., decreased FC with greater compression) between the seed regions (left superior temporal gyrus and lateral occipital cortex) extracted from the GMV masks and voxels in right superior frontal gyrus, right frontal pole, right supramarginal gyrus, and right parietal operculum cortex (**Fig. 3.10 B**). No significant correlations were observed between the normalized cord area at C2-3 and GMV nor between the TPR at C5 and the GMV.

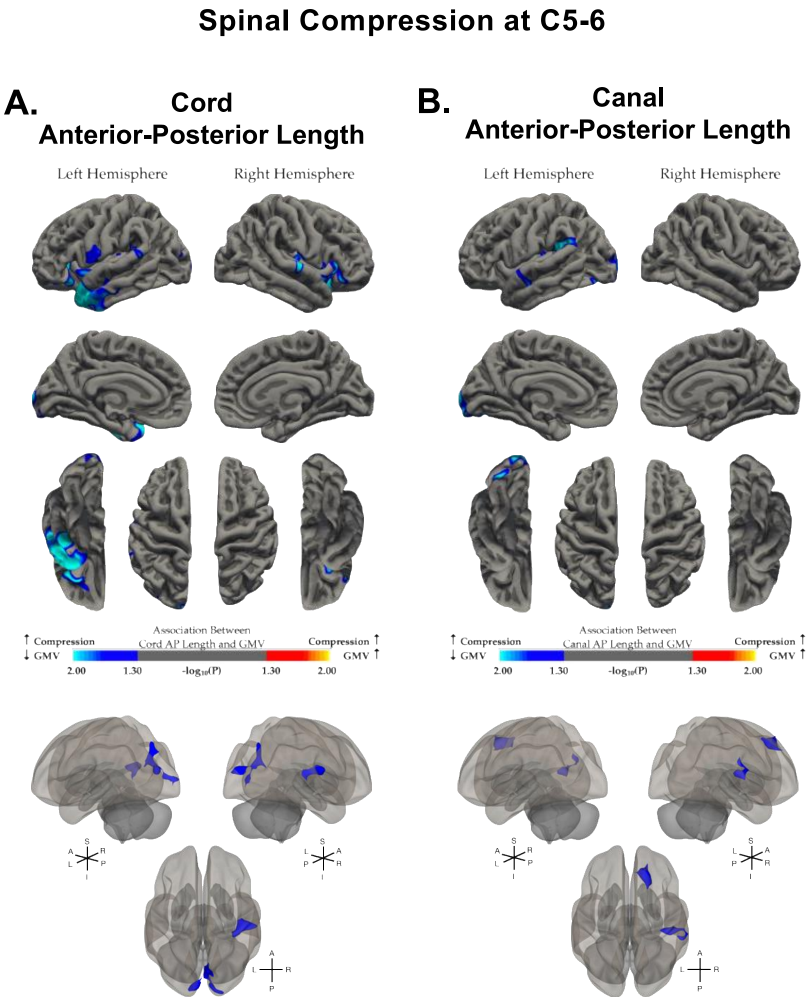

Figure 3.10. Relationship between GMV and spinal compression at C5-6.

Whole-brain correlation analysis between gray matter volume (GMV) and spinal measurements at C5-6 including (**A**) normalized cord anterior-posterior length and (**B**) normalized canal anterior-posterior length, while controlling for patient age (**top row**). (**A-B, top row**) Red-yellow color denotes a positive correlation between spinal compression and GMV (i.e., greater compression, larger GMV), while blue-light blue color denotes a negative correlation between spinal compression and GMV (i.e., greater compression, smaller GMV). (**A-B, bottom row**) Seed-to-voxel functional connectivity (FC) analysis using corresponding significant GMV clusters as seeds, where the red color denotes significant regions with increased connectivity with greater compression and the blue color denotes significant regions with decreased connectivity with greater compression. Significant clusters were determined by thresholding based on statistical significance of $p < 0.05$ for GMV analyses and voxel-level significance of $p < 0.01$ and cluster-level false discovery rate (FDR) corrected $p < 0.05$ for FC analyses.

Spinal Compression at C6-7

Patients demonstrated significant negative associations (i.e., greater compression, smaller GMV) between spinal measurements at spinal segment C6-7 and GMV (**Fig. 2.11**). When examining the relationship between normalized cord anterior-posterior length at C6-7 and GMV, patients displayed significant negative correlations in several cortical regions including the left lateral occipital cortex, left temporal pole, left pars triangularis, right postcentral gyrus, right precuneus, right parahippocampus, and right rostral middle frontal gyrus (**Fig. 2.11 A**). Additionally, patients exhibited significant negative correlations between the normalized canal anterior-posterior length at C6-7 and GMV in the bilateral fusiform gyrus, left insular cortex, left inferior temporal gyrus, left lingual gyrus, right postcentral gyrus, and right inferior parietal cortex (**Fig. 2.11 B**). No significant correlations were observed between normalized spinal cord area at C6-7 and GMV nor between the TPR at C6 and GMV. When performing seed-to-voxel functional connectivity analyses using significant GMV masks (**Fig. 2.11**), no significant correlations were observed between functional connectivity and corresponding spinal measurements at C7-T1.

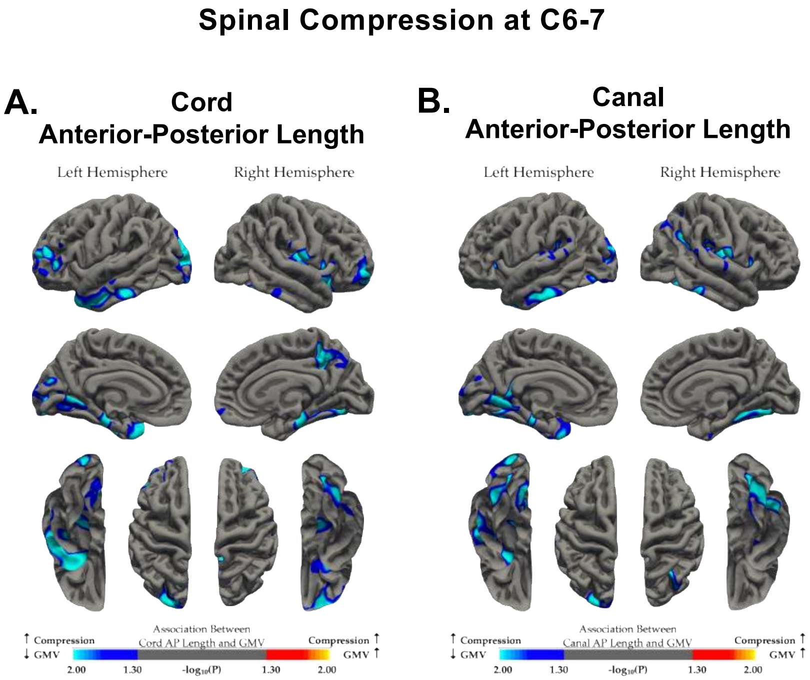

Figure 3.11: Relationship between GMV and spinal compression at C6-7.

Whole-brain correlation analysis between gray matter volume (GMV) and spinal measurements at C5-6 including (**A**) normalized cord anterior-posterior length and (**B**) normalized canal anterior-posterior length, while controlling for patient age. (**A-B**) Red-yellow color denotes a positive correlation between spinal compression and GMV (i.e., greater compression, larger GMV), while blue-light blue color denotes a negative correlation between spinal compression and GMV (i.e., greater compression, smaller GMV). Significant clusters were determined by thresholding based on statistical significance of $p < 0.05$.

Spinal Compression at C7-T1

Significant correlations were observed between spinal measurements at spinal segment C7-T1 and GMV (**Fig. 2.12**). Specifically, patients exhibited significant negative correlations (i.e., greater compression, smaller GMV) between the normalized spinal cord area at C7-T1 and GMV in the left posterior cingulate cortex, left fusiform gyrus, right precuneus, and right caudal middle frontal gyrus (**Fig. 2.12 A**). Patients demonstrated significant negative correlations between the normalized cord anterior-posterior length at C7-T1 and GMV in various cortical regions including the bilateral precuneus, bilateral parahippocampus, left precentral gyrus, left lateral occipital gyrus, left inferior temporal gyrus, and right pars opercularis (**Fig. 2.12 B**). When examining the relationship between normalized canal anterior-posterior length at C7-T1 and GMV, patients demonstrated significant negative correlation in the left lateral occipital cortex and the right fusiform gyrus (**Fig. 2.12 C**). No significant correlations were observed between the TPR at C7 and GMV. When performing seed-to-voxel functional connectivity analyses using significant GMV masks (**Fig. 2.12**), no significant correlations were observed between functional connectivity and corresponding spinal measurements at C7-T1.

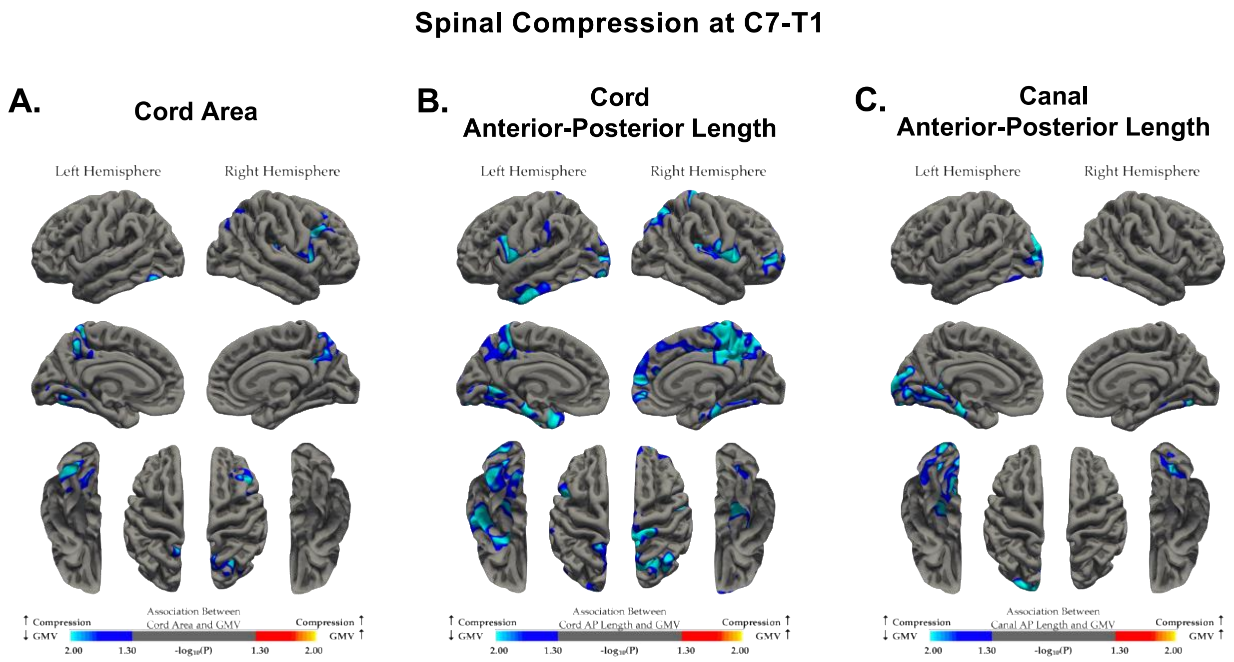

Figure 3.12: Relationship between GMV and spinal compression at C7-T1.

Whole-brain correlation analysis between gray matter volume (GMV) and spinal measurements at C5-6 including (**A**) normalized cord area, (**B**) normalized cord anterior-posterior length, and (**C**) normalized canal anterior-posterior length, while controlling for patient age. (**A-C**) Red-yellow color denotes a positive correlation between spinal compression and GMV (i.e., greater compression, larger GMV), while blue-light blue color denotes a negative correlation between spinal compression and GMV (i.e., greater compression, smaller GMV). Significant clusters were determined by thresholding based on statistical significance of $p < 0.05$.

3.4 Discussion

The present study identifies unique supraspinal alterations associated with degree of cervical spinal cord and canal compression in patients with DCM. With greater cord atrophy and spinal compression, patients demonstrated cortical plasticity in motor related regions and increased functional connectivity between motor, visual, and cerebellar brain regions, along with cortical atrophy of occipital regions and decreased functional connectivity within vision related regions. Study findings further elucidate cerebral compensatory mechanisms and demonstrate such cortical reorganization is dependent on severity of spinal cord compression in patients with DCM.

Consistent with the present literature, our patient cohort experienced maximum spinal cord compression most frequently at spinal segment C5-6 [115]. Historically, spinal measurements in DCM patients have been taken either at the spinal segment with the most compression or at the cervical midvertebral body levels using the Torg-Pavlov Ratio (TPR) [107]. Although these methods are relatively simple to implements, majority of patients experience compression at multiple spinal levels [12] and measurements at the maximum site of compression may fail to capture atrophy and compression throughout the cervical spine. Furthermore, patients in the present study did not exhibit significant correlations between spinal cord and canal measurements at the maximum site of compression and mJOA score. Except for canal compression ratio at C7-T1, patients exhibited no significant correlation between spinal cord and canal measurements and mJOA at each cervical spinal segment demonstrating that degree of spinal compression is not associated with symptom severity. Previous studies have reported similar findings in which anterior-posterior spinal canal diameter [116], TPR [116], and cord volume [76] at the site maximum compression, and maximum canal compromise, maximum cord compromise, and cord compression ratio at each cervical spinal segment [111] did not correlate with patient mJOA scores.

At a superficial level we may expect degree of cord and canal compression to be related to symptom severity, but the presentation of asymptomatic DCM patients, a current enigma in the field, may provide some insight. Asymptomatic DCM patients demonstrate radiographic evidence of mild to severe compression of the spinal cord, however these patients present with no clinical symptoms and therefore have an mJOA score of 18. It remains unclear why this subgroup of patients does not experience neurological deficits, although we suspect it may be related to neuroprotective and effective supraspinal compensatory mechanisms. Such findings illustrate the critical need for imaging biomarkers equip to characterize macro- and micro-structural cerebral alterations and therefore inform progression and prognosis in patients with DCM.

As DCM patients experience chronic mechanical compression on the spinal cord, secondary cellular damage including ischemia, glutamatergic toxicity, neuroinflammation, and apoptosis occurs and results in atrophy of the spinal cord [14,117,118]. Previous studies have demonstrated both gray and white matter atrophy of the cervical spinal cord in patients with DCM [45,118-120], as well as reductions in spinal cord area in patients compared to HCs [121]. The present study implemented normalized cord area measurements at each spinal segment to provide a metric of spinal cord atrophy at the maximum site of compression, averaged across all cervical segments, and at each spinal segment.

At the maximum site of compression, we observed that with increased spinal cord atrophy or smaller cord area, GMV increased in various bilateral motor-related cortical regions. Additionally, a decrease in average cord area across cervical spinal segments was significantly associated with increased cortical volume in the primary motor cortex. Furthermore, we observed increased functional connectivity between the right precentral gyrus and various occipital and cerebellar regions, as well as decreased connectivity with other motor-related regions. Although previous studies have reported thinning of sensorimotor cortices in DCM patients in relation to symptom severity [59,60], previous reports and findings in the present study demonstrate that degree of compression is not significantly correlated with symptom severity [111,116]. Additionally, researchers have reported that during motor tasks, patients with DCM recruit greater activation of motor related brain regions compared to HCs [75]. While DCM patients may experience an overall atrophy of motor-related cortices with disease progression, patients may also experience neuroplasticity or expansion of these regions in which disease response and successful compensatory mechanisms involve reduced interconnectivity of motor regions, expansion of cortical motor representations [122], and functional recruitment of visual and cerebellar regions. Further evidence of this proposed neuroplastic signature was observed when investigating individual spinal segments. For example, at spinal segment C4-5, increased cord atrophy was correlated with increased GMV in motor related regions and decreased functional connectivity between the significant mask in the left motor cortex and bilateral sensorimotor regions.

In addition to cord atrophy, the study demonstrated that degree of cord and canal compression via anterior-posterior diameter measurements, were significantly associated with supraspinal alterations. A task-based fMRI study previously revealed that greater spinal cord compression in DCM patients, as measured by cord volume in the compressed region, was significantly associated with increased functional activation of the contralateral primary motor cortex, cerebellum, and thalamus during a finger tapping task [76]. This study showed that expansion of cerebral activation during a motor task was related to degree of cord compression. The present study expands on previous findings and demonstrates that DCM patients experience cortical atrophy in occipital and temporal brain regions, as well as reduced functional connectivity within vision related regions with greater spinal cord compression.

Specifically, greater cord and canal compression at the maximum site of compression was associated with cortical atrophy of the fusiform and inferior temporal gyri, while average compression throughout the cervical spine cord was associated with decreased cortical volume in the precuneus. At more dorsal cervical spinal segments, greater compression was associated with larger GMV in parietal, temporal, and sensorimotor regions, and decreased functional connectivity between these and motor related regions. At spinal segments most commonly affected by stenosis, patients demonstrated that increased cord and canal compression were related to smaller GMV in occipital and temporal regions and decreased functional connectivity between vision related regions. At lower cervical segments, patients also displayed smaller GMV in occipital and temporal regions with greater cord and canal compression.

Such patterns of reorganization may be driven by compression induced atrophy of spinal pathways and tracts, particularly those impacted by anterior and posterior compression. Based on the white matter organization of the cervical spine [123], anterior compression most directly disrupts descending motor pathways including the ventral corticospinal, vestibulospinal, and reticulospinal tracts, and ascending pathways including the spinothalamic tract [124], while posterior compression most directly impacts the dorsal columns responsible for conveying sensory information to the postcentral gyrus [125]. We suspect axonal injury to such tracts results in upstream cerebral alterations necessary for effective compensation of compression induced motor-deficits. Our findings illustrate that with greater spinal cord compression, the sensorimotor cortex is expanding in inferior parietal regions and with reduced functional interconnectivity is recruiting connectivity with occipital and cerebellar regions. Patients with greater spinal compression, as measured by anterior-posterior spinal cord and canal diameter, may experience injury induced cortical recruitment of alterative, undamaged motor and visual pathways.

Historically, the Torg-Pavlov ratio (TPR) was used to assess degree of spinal compression on lateral x-ray images of the cervical spine [108], but now that MRI is the “gold standard” for diagnosis and monitoring of patients with DCM new techniques for measuring spinal compression have been proposed. Nonetheless, TPR was included in the present analyses in order to compare the proposed methods of measuring spinal compression. We found no significant correlations between GMV and TPR at the vertebral body level above the maximum site of compression nor average TPR across cervical vertebral bodies C3 to C7. However, at vertebral body level C3 and C4, patients demonstrated larger GMV in the left supramarginal gyrus with increased compression. Although TPR has been significantly correlated with diffusion-based measurements of the spine [57], to the best of our knowledge this is the first study to examine the relationship between cortical morphometry and TPR. We suspect TPR is not an effective measure of spinal compression because it lacks the ability to capture compression at the spinal segments caused be disc bulging and ligament hypertrophy. Findings from the present study demonstrate that spinal cord area and anterior-posterior spinal cord and canal diameter at cervical spinal segments have a strong relationship with upstream cerebral alterations compared to traditional TPR measurements.

Although the present study is one of the first to compare cerebral alterations with spinal cord and canal compression in DCM, the study can benefit from a larger sample size and more extensive quantification of spinal cord and canal compression. Measurement of spinal cord and canal volume throughout the entire cervical spine may provide a more precise measure of compression in DCM patients but presents challenges for normalization and comparison between patients. Additionally, such techniques may be challenging to implement in the clinical setting, while the methods used in the present study can easily be quantified with existing radiographic tools in the clinic. Although analyses corrected for subject age, future studies would benefit from inclusion of subject total intracranial volume (TICV), body mass index (BMI), and sex as additional covariates. Furthermore, inclusion of a healthy control population may be useful when normalizing and comparing spinal measurements and disease-related degree of compression.

In conclusion, findings from the present study demonstrate that with greater spinal cord compression, DCM patients experience cortical atrophy of occipital and temporal brain regions, expansion of sensorimotor regions in the inferior partial cortex, and increased functional connectivity between motor, occipital, and cerebellar regions. Furthermore, our findings illustrate that the proposed macrostructural spinal cord and canal measurements are more sensitive and significantly associated with disease-related structural and functional cerebral alterations than traditional Torg-Pavlov ratio measurements. Compression-induced supraspinal neuroplasticity and reorganization demonstrated in the present study may act in response to disease pathogenesis and with further investigation may provide imaging biomarkers capable of meticulously tracking disease progression in DCM.

CHAPTER 4

Characterizing Microstructural Spinal Cord Alterations and associated Cerebral Reorganization in Patients with Degenerative Cervical Myelopathy using fMRI, DTI, and MR Spectroscopy

4.1 Introduction

While magnetic resonance imaging (MRI) remains the "gold standard" in DCM diagnosis and management, advanced imaging techniques provide invaluable information of pathophysiological and biochemical perturbations within the brain and spinal cord. Previous studies have demonstrated patients with DCM experience cellular, metabolic, and microstructural alterations within the cervical spinal cord, providing evidence of greater axonal/neuronal loss and membrane turnover in DCM patients compared to healthy controls [45,57,70,119]. With diffusion tensor imaging (DTI) of the cervical spinal cord, previous studies have demonstrated reduced fractional anisotropy (FA) and increased mean diffusivity (MD) of the compressed cord in DCM patients compared to HCs, indicating microstructural damage to the cord [44-46]. Furthermore, reduced FA of the compressed cord were significantly correlated with symptom severity as measured by mJOA [45,120,126], pain assessment survey [46], and the Nurick score [47]. Such diffusion-based measurements were more effective in characterizing cord degenerative and demyelination than T2-weighted imaging [43], and more informative of post-operative prognostic [48].

In addition to diffusion-weighted imaging, metabolic imaging of the spinal cord using magnetic resonance spectroscopy (MRS) has revealed biochemical and cellular alterations in patients with DCM. The MRS technique provides a measure of molecular concentrations of metabolites including *N*-acetyl aspartate (NAA), myo-inositol (Myo-I), choline (Cho), and creatine (Cr) [54]. NAA is a metabolite only found within neurons and their axons and is accepted as an indicator of neuronal and axonal viability and density [56,127]. In contrast, Myo-I is a glial cell marker used to reflect the gliosis or the reactivity and proliferation of glial cells [128]. Whereas choline (Cho) containing compounds denote membrane synthesis and degradation, while creatine (Cr) concentrations indicate tissue energy metabolism [54,56]. Studies have demonstrated that patients with DCM experience lower cervical spinal cord NAA/Cr ratio compared to HCs, reflective of axonal and neuronal loss [56]. In addition, metabolite concentration of the spinal cord at C2 was shown to change with DCM disease progression [57,58]. In early stages of DCM, patients demonstrated slightly elevated Myo-I, glutamine-glutamate complex, and NAA concentrations, revealing early stages of neuroinflammation and axonal demyelination [57,58]. While patients in later disease stages displayed higher Cho/Cr ratio and a Cho peak indicating more extensive demyelination and gliosis [57,58]. Additionally, Cho/NAA concentration has been shown to be significantly correlated with symptom severity, as measured by mJOA score, and in combination with DTI-based measurements of spinal cord fiber density and MD was able to accurately predict mJOA score [57,58].

Moreover, evidence revealed that DCM patients experience upstream macro- and micro-structural cerebral alterations in response to chronic spinal cord compression. Studies report that when compared to healthy controls, DCM patients experience atrophy within primary motor, somatosensory, and cerebellar cortices [59,60,62,129], as well as reduced white matter fiber density along the corticospinal tract, lower fractional anisotropy in the middle cerebellar peduncles, and increased quantitative anisotropy in fiber pathways associated with sensorimotor functions [66-68]. Furthermore, DCM patients demonstrate functional reorganization in sensorimotor, pain, and vision related brain regions suggested to be essential for motor symptom related compensation [62,66,73,74]. The severity of symptom presentation and neurological impairment have been correlated with structural and functional cerebral alterations. Although DCM is regarded as the most common spinal cord injury in adults [79], our understanding of chronic cervical cord compression's impact on the entire central nervous system and its compensatory responses remains limited.

In the present study, we utilized a multimodal imaging approach consisting of MRS and DTI of the cervical spinal cord in combination with structural, functional, and diffusion-weighted imaging of the brain to elucidate the relationship between compression-induced spinal cord alterations and upstream cerebral reorganization associated with DCM. Inclusion of proton MRS provides sophisticated examination of spinal cord biochemical function at the cellular level by noninvasively measuring metabolite concentrations including N-acetyl aspartate (NAA), myo-inositol (Myo), choline (Cho) and creatine (Cr) [54]. In addition to metabolic information, spinal cord microstructure and white matter integrity can be assessed using DTI. Alongside spinal cord imaging, brain imaging using T1-weighted imaging, resting-state functional MRI (rs-fMRI), and DTI is critical in characterization of cortical morphometry, intrinsic functional connectivity, and cerebral white matter tract integrity and density, respectively. The findings may demonstrate microstructural and cellular alterations within the cervical spine are reflected in cerebral reorganization potentially indicating compensatory mechanisms in response to chronic cord compression. I hypothesize lower FA and higher MD of cervical spinal cord are correlated with smaller GMV of the sensorimotor cortices, decreased FC between brainstem-cerebellar connections, and reduced FA and MD along the corticospinal tracts and corona radiata. Whereas metabolic measurements of the cervical spinal cord in DCM, specifically higher Cho/NA, Myo-I/NAA, and Cr/NAA concentrations, will be significantly correlated with smaller GMV of sensorimotor cortices, increased FC between frontal-cerebellar, brainstem-occipital, and brainstem-cerebellar connections, decreased FC between sensorimotor-occipital connections, and increase FA and MD along the corpus callosum and thalamic radiations. Our findings may further elucidate disease pathophysiology and provide valuable imaging biomarkers to better define disease progression and benefit patient management and treatment of DCM.

4.2 Materials and Methods

4.2.1 Patient Population

A total of 88 patients with degenerative cervical myelopathy were included in this prospective, multimodal study. Between 2015 and 2022, patients who displayed spinal cord compression with evidence of spinal cord deformation and mass effect on standard MR imaging were recruited from the UCLA outpatient neurosurgery clinic and enrolled in the study. Exclusion criteria included: 1) previous cervical spinal cord surgery, 2) visible cerebrospinal fluid signal around the spinal cord at the site of maximal compression on MRI, and 3) spinal cord compression at the C-2 level or cervicomedullary junction. All patients signed Institutional Review Board-approved consent forms, and all analyses were performed in compliance with the Health Insurance Portability and Accountability Act (HIPAA). All patients underwent clinical evaluation of symptoms and neurological function via the modified Japanese Orthopedic Association (mJOA) score [80]. The mJOA scoring scale ranges from 0 to 18, where lower scores represent a worse neurological impairment, and an mJOA score of 18 represents no impairment of neurological function. Of the 88 patients, 7 patients were categorized with severe myelopathy (mJOA $\leq$ 11), 10 patients with moderate myelopathy (12 $\leq$ mJOA $\leq$ 14), and 45 patients with mild myelopathy (15 $\leq$ mJOA $\leq$ 17) at the time of the imaging. 26 patients reported no neurological deficit (mJOA =18).

All patients underwent brain and spinal cord imaging at UCLA. Due to the impact of imaging artifacts on spinal cord measurements, particularly on MRS measures, various patient cohorts were included for each analysis. The relationship between cortical morphometry (GMV) and spinal cord FA were analyzed in all 88 patients, while a sub-cohort of 59 patients were included for brain GMV and spinal cord MD analyses. Furthermore, a sub-cohort of 54 patients were included for brain GMV and spinal cord NAA-Cho analyses, while 50 patients were selected for GMV – NAA-

Myo analyses, and 48 patients for GMV – NAA-Cr analyses. For brain functional connectivity (FC), 80 patients were included for brain FC and spinal cord FA/MD analyses, while 46 patients were selected for FC – NAA-Cho analyses, 42 patients for FC – NAA-Myo analyses, and 40 patients for FC – NAA-Cr analyses. For microstructural brain connectivity and integrity analyses, 40 patients were included for brain FA/MD/SC and spinal cord FA/MD analyses, while 23 patients were selected for brain FA/MD/SC and spinal cord NAA-Cho/NAA-Myo/NAA-Cr analyses. Cohort size and demographics are presented in **Table 4.1**.

Brain Measurment	**Spine Measurement**	**Number of Subject** (Male/Female)	**Age** (Median ± SD) [min, max]	**mJOA** (Median ± SD) [min, max]
Cortical Morphometry (GMV)	FA	88 (55/33)	(59.1 ± 12.7) [35, 82]	(15.9 ± 2.3) [9, 18]
	MD	59 (35/24)	(59.5 ± 12.2) [37, 82]	(16.2 ± 2.0) [9, 18]
	NAA-Cho	54 (32/22)	(60.0 ± 12.1) [35, 82]	(16.0 ± 2.5) [9, 18]
	NAA-Myo	50 (28/22)	(59.8 ± 12.1) [35, 82]	(16.0 ± 2.5) [9, 18]
	NAA-Cr	48 (28/20)	(60.2 ± 12.0) [35, 82]	(15.9 ± 2.7) [9, 18]
Functional Connectivity (FC)	FA	80 (50/30)	(59.9 ± 11.9) [36, 82]	(15.9 ± 2.4) [9, 18]
	MD	80 (50/30)	(59.9 ± 11.9) [36, 82]	(15.9 ± 2.4) [9, 18]
	NAA-Cho	46 (27/19)	(60.7 ± 11.0) [39, 82]	(16.0 ± 2.5) [9, 18]
	NAA-Myo	42 (23/19)	(60.5 ± 11.0) [39, 82]	(15.9 ± 2.6) [9, 18]
	NAA-Cr	40 (23/17)	(61.0 ± 10.7) [42, 82]	(15.9 ± 2.6) [9, 18]
White Matter Integrity (FA,MD,SC)	FA	40 (22/18)	(60.4 ± 12.8) [35, 82]	(15.9 ± 2.3) [9, 18]
	MD	40 (22/18)	(60.4 ± 12.8) [35, 82]	(15.9 ± 2.3) [9, 18]
	NAA-Cho	23 (12/11)	(60.2 ± 12.1) [37, 82]	(16.2 ± 2.5) [9, 18]
	NAA-Myo	23 (12/11)	(60.2 ± 12.1) [37, 82]	(16.2 ± 2.5) [9, 18]
	NAA-Cr	23 (12/11)	(60.2 ± 12.1) [37, 82]	(16.2 ± 2.5) [9, 18]

Table 4.1: Patient demographics.

Age is provided in mean years ± the standard deviation and minimum and maximum years. The modified Japanese Orthopedic Association (mJOA) score is provided in mean score ± the standard deviation with the minimum and maximum scores.

4.2.2 MR Imaging Acquisition

Imaging of the Brain

All imaging, including T1-weighted anatomic images and rs-fMRI of brain, DTI of brain and spinal cord, and MRS of the spinal cord, were acquired using a Siemens Prisma 3T MRI scanner (Siemens Healthcare, Erlangen, Germany).

High-resolution, 1 mm isotropic 3-dimensional (3D) T1-weighted structural MRIs on the brain were acquired using an isotropic 3D magnetization-prepared rapid gradient-echo (MPRAGE) sequence in either the coronal, sagittal, or axial orientation, with a repetition time (TR) of 2300 to 2500 ms, a minimum echo time (TE) of 2 to 3 ms, an inversion time (TI) of 900 to 945 ms, a flip angle of 9^o to 15^o, slice thickness of 1 mm with no interslice gap, and field of view (FOV) of 240 x 320 mm and matrix size of 240 x 320.

To assess functional connectivity of the brain, resting state functional MRIs were acquired with a TR of 1500 to 2200 ms, TE of 28 to 30 ms, flip angle of 77^o, FOV of 220 to 245 mm with an acquisition matrix of 64 x 64 for an in-plane resolution of 3.4 to 3.8 mm, interleaved acquisition, slice thickness of 4 mm with no interslice gap, parallel imaging via CAIPIRNHA with a factor of 2, and multi-band acceleration with a factor of 2.

Diffusion tensor imaging (DTI) of the brain was collected using echo planar imaging with a TR of 9500 to 11400 ms, TE of 82 to 88 ms, flip angle of 90^o, FOV of 256 by 256 mm with an acquisition matrix of 128 by 128 for a 2mm isotropic voxel size. DTI was collected in 64 directions using b=1000 s/mm^2 along with a single b=0 s/mm^2 image.

Imaging of the Spinal Cord

DTI of the spinal cord was collected axially through the level of most significant canal narrowing and cord compression using a custom 2-dimensional (2D), spatially selective radiofrequency excitation pulse (2D-RF) and a reduced FOV EPI readout with ramp sampling known as Zoomed-EPI. Imaging parameters included a TE of 73 to 100 ms, TR of 3000-10000 ms, FOV of 53 mm by 140 mm with an acquisition matrix of 48 by 128, slice thickness of 4 to 5 mm with no gap, number of averages of 4 to 10, and 12 to 20 diffusion sensitizing directions with b values of 500 s/mm^2 and 0 s/mm^2.

MR spectroscopy (MRS) of the spinal cord was acquired using a point resolved spectroscopy sequence with water suppression with a TE of 2000ms/30ms, 256 averages, and a voxel size of 7×7×35mm^3. Water enhanced T1 saturation was applied prior to image localization, followed by application of three frequency selective pulses and a spoiler gradient to suppress the water MR signal. A non-water suppressed MR spectrum was acquired with four averages to correct for eddy current. Additionally, a pulse oximeter was used during image acquisition for posthoc artifact reduction caused by spinal cord movement and cerebrospinal fluid pulsation.

4.2.3 MR Image Processing

Following image acquisition, computation of cortical volume was performed on T1-weighted images using FreeSurfer software package (https://surfer.nmr.mgh.harvard.edu/fswiki) [81]. Processed brain surfaces were smoothed with a full-width half-maximum (FWHM) of 10 mm, then registered to standard space as defined by Desikan-Killiany-Tourville (DKT) atlas [82].

Rs-fMRI brain images were processed using the standard built-in preprocessing pipeline within the CONN toolbox (https://www.nitrc.org/projects/conn) [85] including: 1) realignment of functional images with motion correction and unwarping with on 12 degrees of freedom, 2) slice-timing correction, 3) outlier detection, 4) registration of functional to structural brain images, 5) registration of structural images to the Montreal Neurological Institute (MNI) defined standardized space, 6) segmentation and normalization of functional and structural images based on tissue type (gray matter, white matter, and cerebrospinal fluid) in MNI space, 7) spatial smoothing of functional data using 8 mm full width at half maximum (FWHM) Gaussian kernel, and 8) signal filtering using a band-pass filter of 0.008–0.10 Hz to reduce noise caused by scanner drift and physiological effects (i.e., pulsation and respiration).

The following steps were used to preprocess DTI of the brain: 1) image denoising using the MRtrix3 software package (Brain Research Institute, Melbourne, Australia, http://www.brain.org.au/software/mrtrix) [90], 2) eddy current and motion correction using the FMRIB's Diffusion Toolbox (FDT) (www.fmrib.ox.ac.uk/fsl), 3) registration to the first no-diffusion weighted (b=0 s/mm^2), and 4) skull extraction using the Brain Extraction Tool (BET) tool from FSL. Following preprocessing, fractional anisotropy (FA) and mean diffusivity (MD) values at the voxel level were calculated for DTI using masks consisting of the disjunction between the white matter and deep gray matter masks of interest (namely the basal ganglia and thalamus, defined by the Harvard-Oxford subcortical atlas) as described previously [130]. FA and MD maps were then registered to the Johns Hopkins University DTI atlas (ICBM-DTI-81 1mm FA atlas) using the FLIRT and FNIRT commands in FSL. The MRtrix3 software was used to perform fixel-based analysis via probabilistic tractography by seeding 10 million voxels randomly throughout the brain and counting the number of fiber tracts passing through each voxel. Resulting fiber track density (TD) images of each subject were registered to the Johns Hopkins University DTI atlas (ICBM-DTI-81 1mm FA atlas) using FLIRT and FNIRT commands in FSL.

DTI of the spinal cord was preprocessed using the MRtrix3 software package (Brain Research Institute, Melbourne, Australia, http://www.brain.org.au/software/mrtrix) [90] for image denoising and the FMRIB's Diffusion Toolbox (FDT) (www.fmrib.ox.ac.uk/fsl) for eddy-current and motion correction. MD and FA were calculated from the spinal cord DTI for each subject.

Processing of MR spectroscopy was completed by placing the MRS voxel was at the posterior C2 vertebral level surrounded by 6 saturation bands for outer volume suppression. Manual shimming was performed to determine shim currents. Resulting MR spectra peaks were used to quantify N-acetylaspartate (NAA), choline (Cho), creatine (Cr), and myo-inositol (Myo) metabolite concentrations. MRS was not performed at the site of maximum compression due to magnetic susceptibility issues causing local magnetic field inhomogeneities, reduced spinal cord volume resulting in need for varying voxel size, and increased motion artifacts.

4.2.4 Statistical Analysis

A general linear model (GLM) was created using the FreeSurfer 6.0 build-in tool, QDEC (the Query, Design, Estimate, Contrast, https://surfer.nmr.mgh.harvard.edu/fswiki/Qdec) to determine significant vertex-level correlations between brain gray matter volume and spinal cord parameters including FA, MD, NAA-Cho ratio, NAA-Myo ratio, and NAA-Cr ratio. Age, which has a predominantly linear relation to cortical thickness and volume [131], was included as a covariate in the analyses. The vertex-wise level of significance was set at $p < 0.05$ with the false discovery rate (FDR) < 0.05.

Correlations between brain diffusion measures (FA, MD and TD) and spinal cord parameters (FA, MD, NAA-Cho ratio, NAA-Myo ratio, and NAA-Cr ratio) were analyzed using the voxel-wise GLM implemented with the AFNI *3dttest++* command. To control FDR, significant clusters from *3dttest++* were filtered through the spatial autocorrelation function implemented in *3dFWHMx*, and appropriate cluster-based thresholds based on permutation testing were determined using *3dClustSim* using a level of significance, $p<0.05$, and FDR<0.05. Age was included as covariate.

Whole brain functional (FC) and structural (SC) connectivity of the brain was assessed using a ROI-to-ROI (also known as seed-to-seed) approach. Within both the supratentorial and the infratentorial brain, regions of interest (ROIs) were selected from the Harvard-Oxford Automated Anatomical Labeling (AAL) atlases [86]. GLMs were implemented to evaluate the association between functional and structural brain connectivity and spinal cord parameters (FA, MD, NAA-Cho ratio, NAA-Myo ratio, and NAA-Cr ratio) while accounting for the effect of subject age. The level of significance was set at $p < 0.05$ for the individual connections with a FDR < 0.05.

4.3 Results

4.3.1 Patient Characteristics

As summarized in **Table 4.1**, the patient cohort consisted of 55 males and 33 females ranging in age from 35 to 82 years with a mean age of 59.1 ± 12.7 years. Patient mJOA scores ranged from 9 to 18 with a mean score of 15.9 ± 2.3. Following quality check of patient brain and spine imaging, 88 patients were included for brain GMV and spinal cord FA analyses, 59 patients for brain GMV and spinal cord MD analyses, 80 patients for brain FC and spinal cord FA/MA analyses, and 40 patients for brain FA/MD/SC and spinal cord FA/MD analyses. Due to the sensitivity of MRS to imaging artifacts, additional sub-cohorts were included for spinal cord MRS analyses. Data quality and accuracy was prioritized over cohort size. All sub-cohort demographics are listed in **Table 4.1**.

4.3.2 Relationship between Spinal Cord Microstructure and Cerebral Structure and Function

Correlation Between Microstructural Spinal Cord Integrity and Cerebral Morphometry

Results from spinal cord integrity and whole-brain gray matter volume (GMV) analyses revealed significant associations between cervical spinal cord fractional anisotropy (FA) and cerebral GMV (**Fig. 4.1 A**). After accounting for subject age, patients demonstrated significantly smaller cerebral GMV in the bilateral precentral gyri, left superior frontal gyrus, left inferior parietal lobule, left middle temporal gyrus, right superior temporal gyrus, right precuneus, and right occipital gyrus with higher spinal cord FA values (**Fig. 4.1 A**). In addition, DCM patients displayed larger GMV in the left orbitofrontal cortex with higher spinal cord mean diffusivity

(MD), but significantly smaller GMV in the bilateral precentral gyri with lower spinal cord MD (**Fig. 4.1 B**).

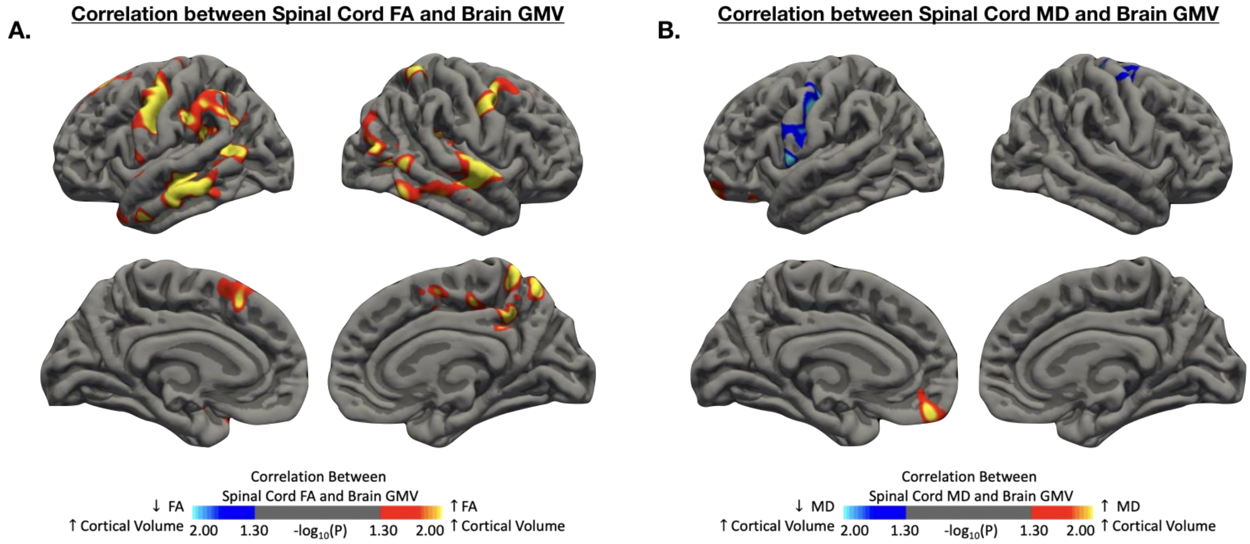

Figure 4.1: Relationship between spinal cord FA and MD and cortical morphometry.

Whole-brain correlation analysis between cervical spinal cord (**A**) fractional anisotropy (FA), (**B**) mean diffusivity (MD), and cerebral gray matter volume (GMV) in patients with DCM while regressing out the effect of age. Red-yellow color denotes a significant positive correlation in which higher spinal cord (**A**) FA or (**B**) MD is associated with larger cerebral GMV, while blue-light blue color denotes a significant negative correlation in which lower spinal cord (**A**) FA or (**B**) MD is associated with larger cerebral GMV. Significant clusters were determined by thresholding based on statistical significance of $p < 0.05$.

Correlation Between Microstructural Spinal Cord Integrity and Cerebral Connectivity

When investigating the relationship between spinal cord microstructural integrity and cerebral functional connectivity (FC), DCM patients displayed significant positive associations between spinal cord FA and cerebral FC (i.e., higher FA with stronger FC) between the brainstem and various cerebral regions including frontal, parietal, cerebellar, and subcortical regions, as well as between cerebellar and temporal regions (**Fig. 4.2 A**). DCM patients also exhibited fewer, but more widespread negative correlations between spinal cord FA and cerebral FC (i.e., lower FA with stronger FC) including within the cerebellum and between frontal and parietal, occipital, and cerebellar regions (**Fig. 4.2 A**).

Correlation analyses between spinal cord MD and cerebral FC revealed similar association patterns throughout the brain. Specifically, patients demonstrated increased FC between frontal, occipital, and brainstem regions with increased spinal cord diffusivity (higher MD) (**Fig. 4.2 B**). Whereas increased FC between the cerebellum to the brainstem, frontal, temporal, and parietal regions was associated with lower MD (**Fig. 4.2 B**). Additionally, significant negative associations were observed between the bilateral putamen and various brainstem nuclei.

In addition to the functional connectivity, significant associations between spinal cord integrity and cerebral structural connectivity (SC) were observed. Generally, patients exhibited higher spinal cord FA with cerebral SC between occipital regions and contralateral frontal, contralateral temporal, and ipsilateral cerebellar ROIs, while lower spinal cord FA was associated with greater SC between frontal and temporal regions of the left hemisphere (**Fig. 4.2 C**). When examining the associations between spinal cord MD and cerebral SC, patient displayed significant positive correlations (i.e., higher spinal cord MD with greater SC) between frontal and temporal regions primarily in the left hemisphere (**Fig. 4.2 D**). Patients also demonstrated significant negative correlations (i.e., lower spinal cord MD with greater SC) throughout the brain, specifically between left temporal regions and bilateral occipital, contralateral frontal, and brainstem regions (**Fig. 4.2 D**).

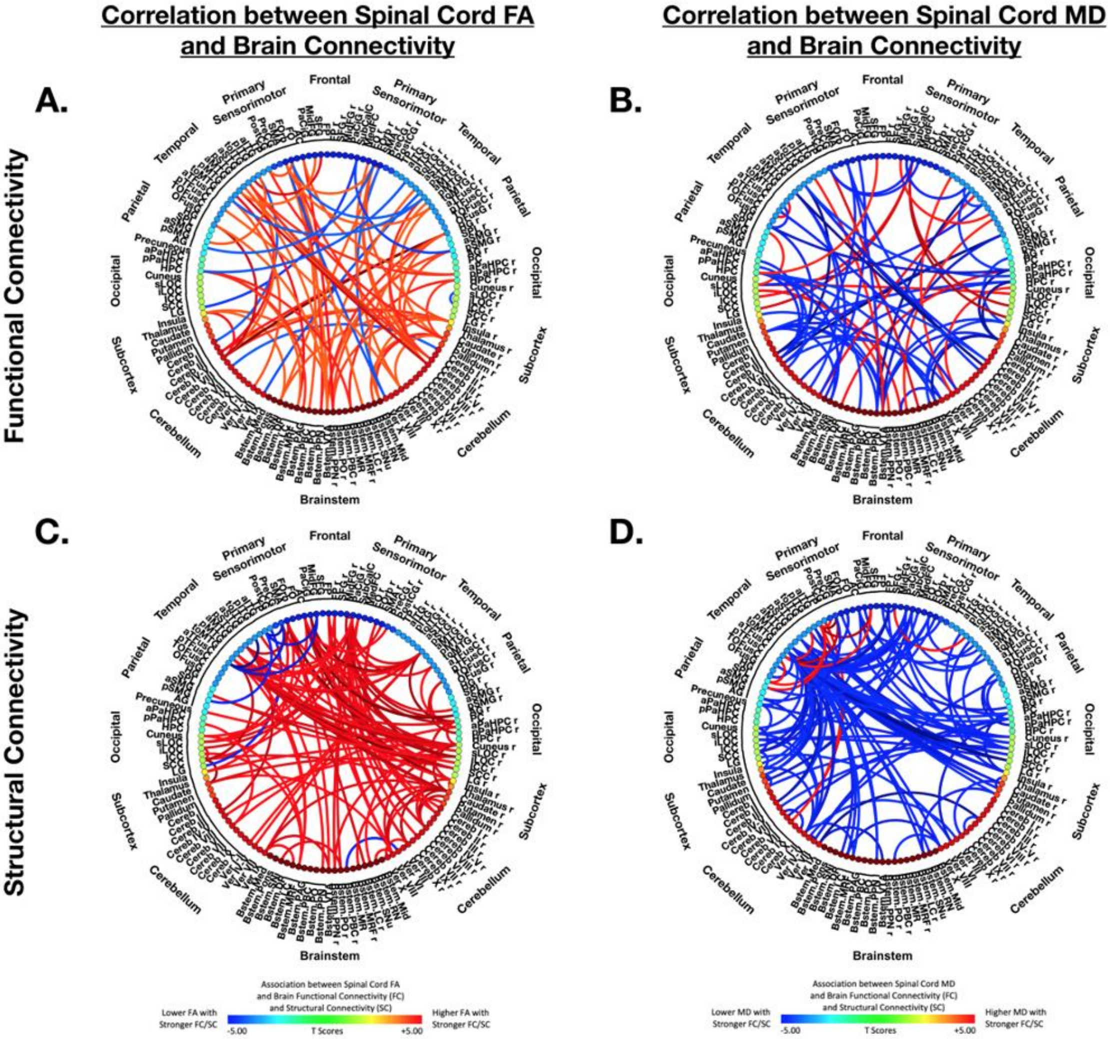

Figure 4.2: Relationship between spinal cord FA and MD and brain connectivity.

Connectome diagrams illustrating whole-brain ROI-to-ROI correlation analysis between cervical spinal cord microstructural integrity and cerebral connectivity in patients with DCM while regressing out the effect of age. (**A**) Association between spinal cord fractional anisotropy (FA) and cerebral functional connectivity (FC). (**B**) Association between spinal cord mean diffusivity (MD) and cerebral FC. (**C**) Association between spinal cord FA and cerebral structural connectivity (SC). (**D**) Association between spinal cord MD and cerebral SC. Colors on the connectome denote the value of the T-statistic in which red-orange color denotes a significant positive association, while blue-light blue denotes a significant negative association. ROIs are labeled with l = left hemisphere and r = right hemisphere. Significant connection-level threshold was set at p-value < 0.01 and ROI-level threshold was set at FDR-corrected p-value < 0.05.

Correlation Between Spinal Cord and Cerebral Microstructural Integrity

When investigating the relationship between spinal cord and brain microstructural integrity, DCM patient demonstrated significant upstream alterations associated with chronic spinal cord compression and damage. Specifically, lower FA of the spinal cord was associated with higher FA in voxels located at the right anterior-posterior portion of the superior longitudinal fasciculus within the parietal lobe and within the right posterior corona radiata (**Fig. 4.3 A**). Whereas lower FA of the spinal cord was associated with higher MD in voxels located along the external capsule including the inferior fronto-occipital and uncinate fasciculi, as well as at the anterior corona radiata of the right hemisphere (**Fig. 4.3 C**).

In contrast, patients displayed significant positive associations between MD of the spinal cord and FA and MD of the brain. Higher MD of the cervical spinal cord was associated with higher FA of the brain in voxels located at the left superior corona radiata (**Fig. 4.3 B**). Additionally, higher MD of the spinal cord was associated with higher MD within voxels located at the anterior corona radiata, as well as along the uncinate fasciculus of the right hemisphere (**Fig. 4.3 C**). Significant anatomical locations, cluster sizes, and T-statistics are listed in **Table 4.2**.

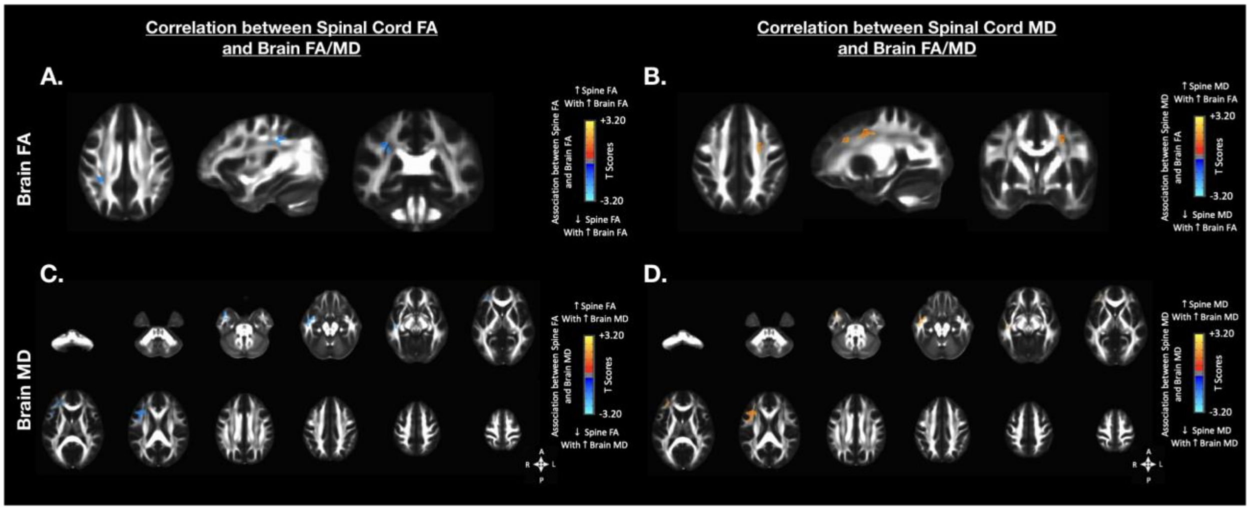

Figure 4.3: Relationship between spinal cord and brain microstructural integrity.

Anatomical localization of significant correlations between spinal cord and brain FA and MD. The following significant associations are illustrated; (**A**) spinal cord and brain fractional anisotropy (FA), (**B**) spinal cord mean diffusivity (MD) and brain FA, (**C**) spinal cord FA and brain MD, and (**D**) spinal cord and brain MD. Colors denote the value of the T-statistic in which red-orange denotes a significant positive association, while blue-light blue denotes a significant negative association. Significant clusters were determined by thresholding based on statistical significance of p-value < 0.05 and cluster size. Cluster volume and strength of T-statistic are listed in **Table 4.2**.

Anatomical Region	Spinal Cord FA				Spinal Cord MD			
	Brain FA		Brain MD		Brain FA		Brain MD	
	T-statistic	Cluster Volume (µL)	T-statistic	Cluster Volume (µL)	T-statistic	Cluster Volume (µL)	T-statistic	Cluster Volume (µL)
Anterior Corona Radiata Right	-	-	-2.37019	299	-	-	2.42194	129
External Capsule Right	-	-	-2.44415	37	-	-	-	-
Posterior Corona Radiata Right	-2.23608	37	-	-	-	-	-	-
Sagittal Striatum Right	-	-	-2.16919	30	-	-	-	-
Superior Corona Radiata Left	-	-			2.33605	69	-	-
Superior Longitudinal Fasciculus Right	-2.33438	279	-	-	-	-	-	-
Uncinate Fasciculus Right	-	-	-2.69919	213	-	-	2.82683	158

Table 4.2: Anatomical regions and white matter tracts with significant correlations between spinal cord and brain FA and MD.

T-statistic and cluster volume in microliters are listed for significant clusters.

4.3.3 Relationship between Spinal Cord Metabolic Signatures and Cerebral Structure and Function

Correlation Between Metabolic Spinal Cord Integrity and Cerebral Morphometry

When examining the relationship between metabolic signatures of the spinal cord and cerebral morphometry, no significant associations were observed between Cho/NAA ratio and GMV nor between Cr/NAA ratio and GMV, but significant negative correlations were observed between Myo/NAA ratio and GMV. DCM patients demonstrated significantly larger GMV in the bilateral precentral gyri, right superior frontal gyrus, left superior and middle temporal gyri, and right lingual gyrus with lower Myo/NAA ratios (**Fig 4.4**).

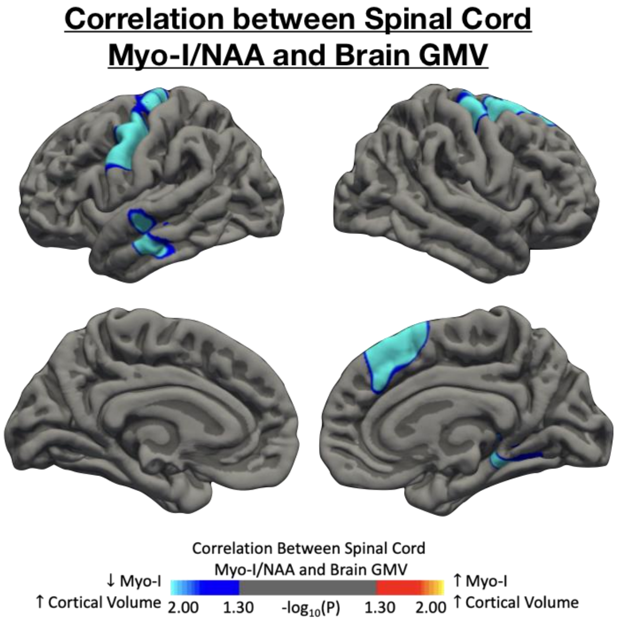

Figure 4.4: Relationship between cervical spinal cord Myo-I/NAA and cerebral morphometry.

Whole-brain correlation analysis between cervical spinal cord Myo-I/NAA concentration and cerebral gray matter volume (GMV) in patients with DCM while regressing out the effect of age. Red-yellow color denotes a significant positive correlation in which higher spinal cord Myo-I/NAA is associated with larger cerebral GMV, while blue-light blue color denotes a significant negative correlation in which lower Myo-I/NAA is associated with larger cerebral GMV. Significant clusters were determined by thresholding based on statistical significance of $p < 0.05$.

Correlation Between Metabolic Spinal Cord Integrity and Cerebral Connectivity

Connectometry analysis identified significant positive and negative associations between metabolic spinal cord concentrations, including Cho/NAA, Myo-I/NAA, and Cr/NAA ratios, and whole-brain ROI-to-ROI functional connectivity. Accounting for differences in age, DCM patients exhibited positive correlations between Cho-NAA ratio and FC (i.e., higher Cho/NAA with stronger FC) between frontal and temporal, cerebellar, and brainstem regions, as well as between hippocampal and cerebellar regions (**Fig. 4.5 A**). DCM patients also displayed significant negative correlations between spinal cord Cho-NAA ratio and FC (i.e., lower Cho/NAA with stronger FC) between sensorimotor brain regions and hippocampal and cerebellar regions (**Fig. 4.5A**). Additionally, DCM patients demonstrated negative correlations between cerebellar and temporal, occipital, and brainstem ROIs.

When examining the association between spinal cord Myo-I/NAA ratio and brain FC, stronger FC between the brainstem and frontal, occipital, and basal ganglia regions, as well between the cerebellum and frontal, temporal, and parietal ROIs were associated with higher Myo-I/NAA spinal cord concentrations (**Fig. 4.5 B**). In contrast, patients demonstrated lower Myo-I/NAA concentrations with stronger FC between sensorimotor regions, (including the pre- and post-central gyri and SMA) and occipital and temporal regions (**Fig. 4.5 B**). DCM patients also exhibited negative correlations between Myo-I/NAA ratio and FC between brainstem regions and temporal, insular, and cerebellar ROIs.

In addition, positive correlations between Cr/NAA spinal cord concentrations and whole-brain FC (i.e., higher Cr/NAA with stronger FC) were observed between the cerebellum and frontal and occipital regions, as well as between the brainstem and temporal, parietal, and occipital regions (**Fig. 4.5 C**). Whereas DCM patients exhibited significant negative correlations (i.e., lower Cr/NAA with stronger FC) between the cerebellum and frontal, temporal, and occipital regions (**Fig. 4.5 C**).

Furthermore, significant correlations were observed between Cho/NAA spinal cord concentrations and SC. Specifically, DCM patients displayed significant positive correlations (i.e., higher spinal cord Cho/NAA with stronger SC) between right temporal regions and bilateral frontal and brainstem regions, as well as significant negative correlations (i.e., lower spinal cord Cho/NAA with stronger SC) throughout the brain, specifically between the brainstem and frontal, parietal, and occipital regions (**Fig. 4.5 D**). Patients also demonstrated significant positive correlations between Myo-I/NAA spinal cord concentrations and cerebral SC. Patients primary exhibited higher spinal cord Myo/NAA with stronger SC between right temporal regions and bilateral frontal, cerebellar, and brainstem regions (**Fig. 4.5 E**). Moreover, patients demonstrated significant positive associations between Cr/NAA ratio and brain SC, specifically higher Cr/NAA ratio with stronger SC between sensorimotor and brainstem ROIs, as well as between occipital and cerebellar regions (**Fig. 4.5 F**).

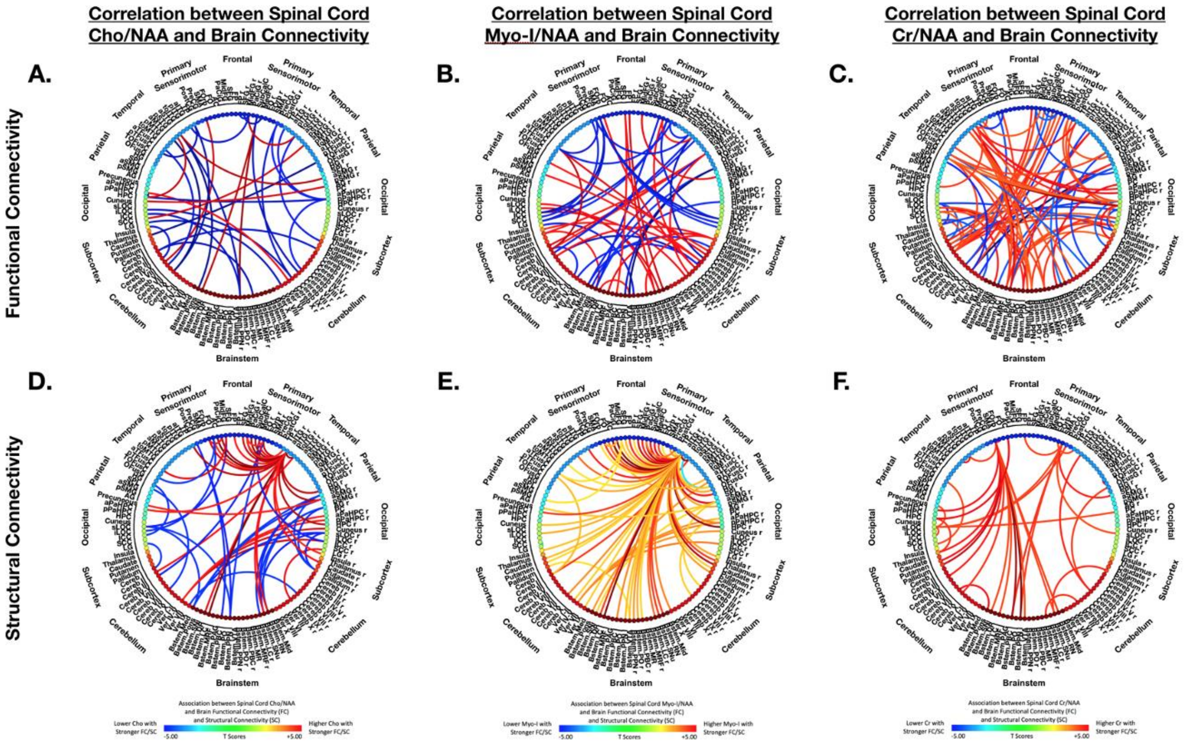

Figure 4.5: Relationship between metabolic spinal cord integrity and cerebral connectivity.

Connectome diagrams illustrating whole-brain ROI-to-ROI correlation analysis between cervical spinal cord metabolic concentrations and cerebral connectivity in patients with DCM while regressing out the effect of age. Association between spinal cord (**A**) Cho/NAA concentration, (**B**) Myo-I/NAA concentration, (**C**) Cr/NAA concentration and cerebral functional connectivity (FC). Association between spinal cord (**D**) Cho/NAA concentration, (**E**) Myo-I/NAA concentration, (**F**) Cr/NAA concentration and cerebral structural connectivity (SC). Colors on the connectome denote the value of the T-statistic in which red-orange denotes a significant positive association, while blue-light blue denotes a significant negative association. ROIs are labeled with l = left hemisphere and r = right hemisphere. Significant connection-level threshold was set at p-value < 0.01 and ROI-level threshold was set at FDR-corrected p-value < 0.05.

Correlation Between Metabolic Spinal Cord Integrity and Cerebral Microstructure

We further examined the correlation between spinal cord metabolic ratios (Cho/NAA, Myo/NAA, Cr/NAA) and brain microstructural measurements (FA, and MD) while controlling for subject age. Although no significant correlation was observed between spinal cord Cho/NAA and cerebral FA, DCM patients demonstrated higher Cho/NAA ratios with higher MD in voxels located at the left posterior corona radiata, the left superior longitudinal fasciculus, and the splenium of the corpus callosum (**Fig. 4.6 C**).

When investigating the relationship between spinal cord Myo/NAA and cerebral microstructure, patients exhibited significantly higher Myo/NAA with higher brain FA along the splenium and body of the corpus callosum, the posterior limb and retrolenticular portion of the internal capsule, the left superior and posterior corona radiata, as well as at the thalamus and bilateral posterior thalamic radiations (**Fig. 4.6 A**). Furthermore, voxels located within the thalamus and along the fornix, corpus callosum, bilateral corona radiata, and left striatum showed significantly increased Myo/NAA with higher brain MD (**Fig. 4.6 B**). No significant correlations were observed between spinal cord Cr/NAA and cerebral FA nor between spinal cord Cr/NAA and cerebral MD. Significant anatomical locations, cluster sizes, and T-statistics are listed in **Table 3.3**.

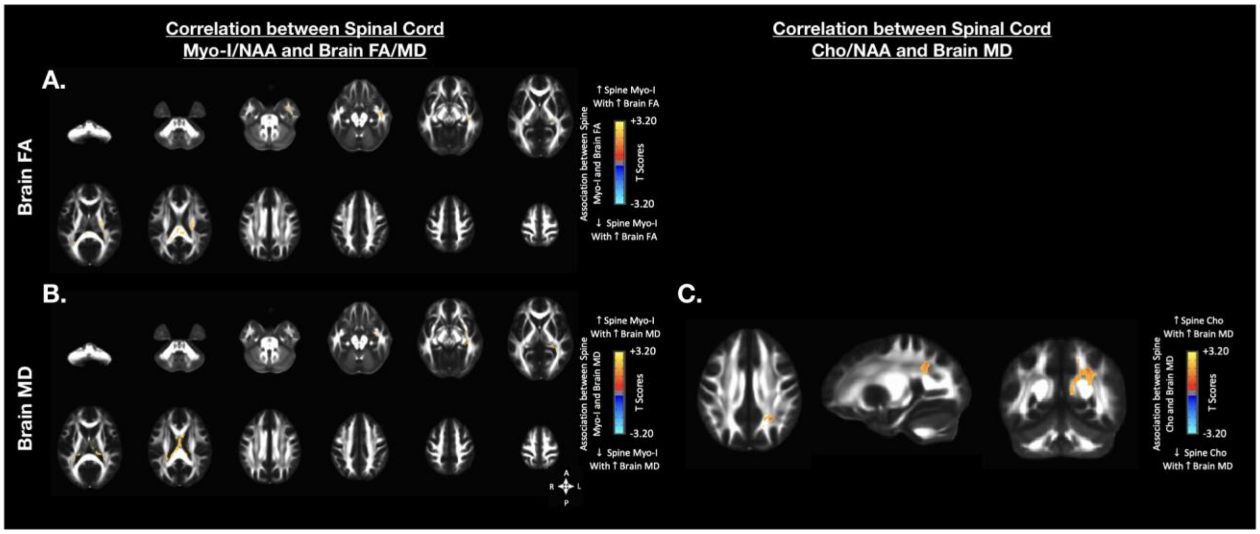

Figure 4.6: Relationship between spinal cord metabolic concentrations and brain microstructural integrity.

Anatomical localization of significant correlations between spinal cord metabolic concentration and brain microstructural integrity. The following significant associations are illustrated; (**A**) spinal cord Myo-I/NAA concentration and brain fractional anisotropy (FA), (**B**) spinal cord Myo-I/NAA concentration and brain mean diffusivity (MD), and (**C**) spinal cord Cho/NAA concentration and brain MD. Colors denote the value of the T-statistic in which red-orange denotes a significant positive association, while blue-light blue denotes a significant negative association. Significant clusters were determined by thresholding based on statistical significance of p-value < 0.05 and cluster size. Cluster volume and strength of T-statistic are listed in **Table 4.3**.

Anatomical Region	Spinal Cord Cho/NAA		Spinal Cord Myo-I/NAA			
	Brain MD		Brain FA		Brain MD	
	T-statistic	Cluster Volume (μL)	T-statistic	Cluster Volume (μL)	T-statistic	Cluster Volume (μL)
Body of Corpus Callosum	-	-	2.54154	45	2.78386	822
External Capsule Left	-	-	2.76586	39	2.67207	102
Fornix	-	-	-	-	3.04232	185
Fornix (Stria Terminalis) Left	-	-	-	-	2.74265	74
Posterior Limb of Internal Capsule Left	-	-	2.68872	392	-	-
Posterior Corona Radiata Left	2.55615	205	2.67891	154	2.3878	77
Posterior Corona Radiata Right	-	-	-	-	2.75482	146
Posterior Thalamic Radiation Left	-	-	2.63486	42	-	-
Posterior Thalamic Radiation Right	-	-	2.5619	34	2.60774	96
Retrolenticular Part of Internal Capsule	-	-	2.52976	366	2.92074	65
Sagittal Striatum Left	-	-	2.94557	217	2.72934	119
Splenium of Corpus Callosum	2.82434	47	2.44628	763	2.77311	213
Superior Corona Radiata Left	-	-	2.90449	394	-	-
Superior Longitudinal Fasciculus Left	2.60326	91	-	-	-	-
Tapetum Left	-	-	-	-	2.8129	113
TapetumRight	-	-	2.4367	49	2.70969	63
Thalamus	-	-	2.72223	281	2.73571	1353

Table 4.3: Anatomical regions and white matter tracts with significant correlations between spinal cord metabolic concentrations and brain FA and MD.

T-statistic and cluster volume in microliters are listed for significant clusters.

4.4 Discussion

By implementing multimodal, advanced spine and brain MR imaging, the present study demonstrated that chronic compression induced alterations within the cervical spinal cord are significantly associated with cerebral morphometry, functional and structural connectivity, and white matter integrity in patients with DCM. Additionally, by imaging metabolite concentrations of cervical spinal cord, the present study elucidated the relationship between cellular and biochemical alterations of the spinal cord and upstream structural, functional, and diffusion-based alterations within the brain.

DTI is a non-invasive imaging technique ideal for visualizing white matter tracts in the brain and spinal cord [50] and has previously been utilized to study cord microstructural alterations in patient with DCM [92]. By measuring free water diffusion in the extracellular space, we can quantify the degree of anisotropic water movement or fractional anisotropy (FA) and the average or mean diffusivity (MD) and can therefore indicate microstructural white matter properties including axonal integrity, demyelination, and degradation due to chronic cord compression [94]. Here, we found that lower spinal cord FA in the compressed cord, likely due to increased extracellular water concentration and decreased axon density, was significantly associated with atrophy of motor and language related brain regions and decreased structural and functional connectivity throughout the brain including between temporal and occipital regions. Furthermore, lower spinal cord FA was associated with increased FA within the anterior-posterior portion of the superior longitudinal fasciculus (SLF), a major white matter tract connecting frontal and parietal cortices, and increased MD in the anterior corona radiata and uncinate fasciculus. The anterior-posterior portion of the SLF is involved in visuospatial processing [132], while the integrity of the corticospinal tract along the corona radiata is vital for motor function [133,134]. We suspect that as chronic compression induces atrophy of the spinal cord and sensorimotor related cortices, the brain recruits occipital and temporal brain regions and related white matter tracts to compensate for presentation of motor symptoms.

Furthermore, with greater axonal damage indicated by higher spinal cord MD, DCM patients exhibited cortical atrophy of the precentral gyri and neuroplasticity of the left orbitofrontal cortex, altered structural and functional connectivity between cortical, subcortical, and cerebellar regions, higher FA in the left superior corona radiata, and higher MD within the right anterior corona radiata and uncinate fasciculus. Our findings indicate that as the degenerative microstructural alterations within the cervical spinal cord occur, cerebral reorganization occurs at various levels. Specifically, patients demonstrate that with greater degenerative effects on the cord (i.e., higher MD values), functional connectivity between frontal, occipital, and brainstem regions increased, while functional connectivity between the cerebellum to the brainstem, frontal, temporal, and parietal regions decreased. We suspect that as motor-related gray matter regions, white matter tracts, and function of the brain and spinal cord deterioration; visual, executive motor-planning, and proprioceptive related regions are strengthen in DCM.

With the inclusion of proton MR spectroscopy, we were able to measure metabolite concentrations and non-invasively detect compression-induced cellular alterations with the cervical spinal cord associated with DCM. Metabolite ratios of Cho/NAA, Myo-I/NAA, and Cr/NAA indicate neuronal membrane synthesis, gliosis, and cellular metabolism in proportion to neuronal density [56]. Here, patients demonstrated higher Cho/NAA ratios, implying increased membrane turnover in response to axonal degeneration, in relation to higher functional and structural connectivity between frontal, temporal, and brainstem regions, but lower FC between sensorimotor, hippocampal, and cerebellar regions and lower SC between the brainstem and frontal, parietal, and occipital regions. Furthermore, higher Cho/NAA was observed in correlation with higher MD of the left superior longitudinal fasciculus and posterior corona radiata. Results suggest that as spinal cord damage, axonal loss, and membrane turnover increase, integrity and connectivity between typical motor-related pathways decrease while alternative functional pathways are strengthened in DCM patients.

Additionally, higher Myo-I metabolite concentration indicates reactive gliosis and suggests greater spinal cord inflammation and axonal demyelination. As the Myo-I/NAA increased, DCM patients exhibited atrophy of the precentral, superior frontal, superior and middle temporal, and lingual gyri, as well as weaker FC between sensorimotor regions and occipital/temporal regions and between brainstem regions and temporal, insular, and cerebellar ROIs. In contrast, FC was strengthened between the brainstem and frontal, occipital, and basal ganglia regions and higher SC was observed between temporal regions and frontal, cerebellar, and brainstem regions. Patients also exhibited increased Myo-I/NAA with higher FA and MD of the corona radiata, thalamic radiation, corpus callosum, and thalamus. With greater spine-disease related neuro-inflammatory responses, patients exhibit selective neurodegeneration and reorganization of motor, cerebellar, and thalamic tracts and related cortical regions.

Moreover, high Cr to NAA ratios suggest increased cellular metabolic activity and neuronal turnover. Patients with DCM demonstrated that with higher Cr/NAA, structural and functional connectivity increased between the cerebellum and occipital regions, as well as between the brainstem and temporal and occipital regions, but decreased between the cerebellum and frontal, temporal, and occipital regions. Together, biochemical features of the spinal cord denoting neuronal damage, inflammation, and turnover are associated with atrophy of sensorimotor and cerebellar connectivity and cortical volume accompanied by increased structural and functional recruitment of brainstem, occipital, and temporal brain regions.

The present study was limited by cohort size predominantly due to the high incidence of artifacts and noise present with the MR spectroscopy technique. Not only does the anatomy and small diameter of the spinal cord propose a challenge, the low abundance of metabolites of interest results in low signal to noise [54,127]. Additionally, patients who have undergone cervical spine surgery (i.e., laminoplasty) exhibit extensive imaging artifacts due to implanted hardware. To avoid artifact contamination and inaccurate metabolite measurements, only patients and scans with the best MR signal quality were included in the present study. With a larger patient population, future studies will be able to stratify cohorts and analyses based on patient symptom severity via mJOA score, further elucidating how spinal and supraspinal alterations are related to disease progression.

Our findings demonstrate compression induced cervical spinal cord neurodegeneration and biochemical alterations are significantly associated with upstream alterations in cerebral cortical volume, functional connectivity, microstructural connectivity, and white matter integrity. Non-invasive characterization of spinal cord dysfunction and degeneration, in combination with cerebral atrophy and reorganization may benefit prognosis and management in patients with DCM particularly in asymptomatic patients or those whose symptoms are stable.

CHAPTER 5

Sex-Dependent Cortical Volume Changes in Patients with Degenerative Cervical Myelopathy *

*** Note:** The present chapter have been adapted from a published article of the same title in the *Journal of Clinical Medicine* with T.C. Oughourlian as the first author.

5.1 Introduction

Chronic degeneration of the spinal canal in degenerative cervical myelopathy (DCM) not only induces structural and functional alterations within the spinal cord, but also leads to changes within the brain as well [1]. Studies have shown that, when compared to healthy subjects, DCM patients exhibit significant reductions in cortical volume in somatosensory, motor, and cerebellar cortices [59,60,62]. Furthermore, patients demonstrate increased anatomical and functional connectivity within sensorimotor and pain related brain regions associated with patient symptom severity [73,74], possibly due to compensatory mechanisms resulting from spinal cord neuronal atrophy [59,60,66,73,74,135]. Although these previous studies have identified unique anatomic features associated with DCM, the potential of sex as a biological variable in this disease remains largely unexplored.

Numerous studies suggest sex hormones influence neuroprotective and inflammatory responses to neurotrauma. Following brain injury, damaged neurons release glutamate resulting in excess intracellular calcium, thus triggering several pathological events including loss of dendritic spines, axonal myelin damage, mitochondrial dysfunction, and neuronal cell death, further leading to glial cell activation and neuroinflammation [136]. Sex hormone receptors are expressed in neurons, glia, and immune cells; and directly influence cellular responses to central nervous system (CNS) injury [137]. Preclinical studies have demonstrated neuroprotective effects of testosterone, estrogen, and progesterone [136-142]. In traumatic brain injury (TBI), investigators reported significant sex-specific differences in overall brain damage, sex hormone receptor gene expression, and proinflammatory responses to hormone treatment [143-145]. A clinical study found serum sex hormone levels were altered after TBI; furthermore higher levels of testosterone were correlated with a higher probability of recovery [146]. Differences in sex hormones may influence a patient's response to neurotrauma within the spinal cord [147], consequently affecting compensatory changes within the brain.

The investigation of sex as a biological variable has become a priority of the National Institute of Health and other federal funding sources due to its potential impact on disease pathogenesis and treatment. In the present study, we sought to investigate the role of sex differences on brain structure in degenerative cervical myelopathy and determine how those structural differences are related to measures of neurological function as measured using the modified Japanese Orthopedic Association (mJOA) score. We tested the hypotheses that 1) sex-dependent differences in GMV exist between patients and healthy controls in sensorimotor and pain related brain regions, and 2) there is a sex-dependent association between GMV and mJOA within sensorimotor cortices in patients with DCM.

5.2 Materials and Methods

5.2.1 Patient Population

A total of 85 patients were prospectively enrolled from 2016 to 2021 in a cross-sectional study including brain and spinal cord imaging as well as a neurological examination. Patients were recruited from an outpatient neurosurgery clinic and exhibited spinal cord compression with evidence of spinal cord deformation, mass effect, and no visible cerebrospinal fluid signal around the spinal cord at the site of maximal compression on MRI. All patients signed Institutional Review Board-approved consent forms, and all analyses were performed in compliance with the Health Insurance Portability and Accountability Act (HIPAA). The patient cohort consisted of 52 males and 33 females ranging in age from 31 to 81 years with a mean age of 58.5 years for males and 58 years for females. All patients underwent brain and spinal cord imaging at UCLA. The modified Japanese Orthopedic Association (mJOA) score was used as a measure of neurological function [80]. The mJOA scoring scale ranges from 0 to 18, where lower scores represent a worse neurological impairment and an mJOA score of 18 represents no impairment of neurological function. Patient demographic data was summarized in **Table 5.1**.

Subject Population	**Number of Subject (Male/Female)**	**Age (Male/Female) [min,max] *p-value***	**mJOA (Male/Female) [min,max] *p-value***
DCM Patients	85 (52/33)	(58.5 ± 11.6 / 58.0 ± 10.7) [31,81] *p = 0.8068*	(15.0 ± 2.7 / 15.6 ± 2.4) [9,18] *p = 0.3885*
Healthy Controls	90 (53/37)	(58.7 ± 6.4 / 59.8 ± 6.3) [45,70] *p = 0.4076*	18 *

Table 5.1: Cohort demographics.

Age is provided in mean years ± the standard deviation, minimum and maximum years, and p-value of Wilcoxon-Mann-Whitney test between age of males and females. The modified Japanese Orthopedic Association (mJOA) score is provided in mean score ± the standard deviation, minimum and maximum scores, and p-value of Wilcoxon-Mann-Whitney test between scores of males and females. *= HCs were categorized with a mJOA score of 18 due to their healthy neurological status.

5.2.2 Healthy Control Population

A total of 90 age-matched healthy control (HC) volunteers were included from the Parkinson's Progression Markers Initiative (PPMI) data repository (www.ppmiinfo.org/data) [148]. (For up-to-date information on this database, visit www.ppmiinfo.org. PPMI – a public-private partnership – is funded by the Michael J. Fox Foundation for Parkinson's Research and funding partners, including [list the full names of all of the PPMI funding partners found at www.ppmiinfo.org/fundingpartners].) Study investigators completed the PPMI Data Use and Biospecimen Use Agreements. The HC cohort used consisted of 53 males and 37 females ranging in age from 45 to 70 years with a mean age of 59.1 years. Male or female HCs between the ages of 45 and 70 with T1-weighted brain images were included. Exclusion criteria implemented by the PPMI investigators consisted of 1) significant neurological or psychiatric disorder at the time of study participation, 2) first degree relative with idiopathic Parkinson's Disease, 3) a Montreal Cognitive Assessment (MoCA) score of 26 or less, 4) women who are pregnant, planning to become pregnant, or lactating at time of study, 5) use of medication that may interfere with dopamine transporter SPECT imaging, and 6) use of investigational drug or device within 60 days prior to study participation [148]. Due to the above exclusion criteria, the healthy control subjects included in this study were categorized as neurologically asymptotic and assigned a mJOA score of 18. HC demographic data was also summarized in **Table 5.1**.

5.2.3 MR Imaging Acquisition

For the patient cohort, high-resolution 1 mm 3-dimensional (3D) T1-weighted structural MRIs were acquired on a 3T MR scanner (Siemens Prisma or Trio; Siemens Healthcare, Erlangen, Germany) using a 3D magnetization-prepared rapid gradient-echo (MPRAGE) sequence in either the coronal, sagittal, or axial orientation, with a repetition time (TR) of 2300 to 2500 ms, a minimum echo time (TE), an inversion time (TI) of 900 to 945 ms, a flip angle of 9^o to 15^o, FOV = 240 x 320 mm and matrix size of 240 x 320, slice thickness = 1 mm. For the HC cohort, high-resolution 3-dimensional (3D) T1-weighted structural MRIs were acquired on a 3T MR scanner using a 3D T1-weighted sequence (e.g. MPRAGE or SPGR) with a slice thickness = 1.5 mm or less with no interslice gap. All other parameters including repetition (TR) and echo (TE) time were specific to site scanner manufacturer recommendations for a T1- weighted, 3D sequence.

5.2.4 Image Processing and Analysis

Cortical segmentation and computation of GMV were performed using FreeSurfer (https://surfer.nmr.mgh.harvard.edu/fswiki) on the T1-weighted described above images [81]. Processed brain surfaces were smoothed with a full-width half-maximum of 10 mm, then registered to a standard space defined by the Desikan-Killiany-Tourville (DKT) atlas [149]. Whole-brain cortical volume analysis was completed using FreeSurfer. A general linear model (GLM) was used to determine vertex-level significant differences in GMV between the following groups: 1) male HCs and female HCs, 2) male patients and male HCs, 3) female patients and female HCs, and 4) male patients and female patients. To control for the influence of age on GMV, age was included as a covariate in morphometric analyses [131,150]. When comparing GMV between male patients and female patients, both age and mJOA score were included as covariates. To evaluate the association between sex, cortical volume, and neurological deficit, a GLM was used to determine vertex-level significant correlations between GMV and mJOA score in A) male patients and HCs, and B) female patients and HCs. Following the overlapping of significant clusters observed in the male group and significant clusters observed in the female group, we identified common cortical regions showing significant correlations between GMV and mJOA in both male and female groups. Additionally, average GMVs for each individual subject were extracted from the mutually significant clusters and corrected for subject age. In the male patient group and the female patient group, linear regression analyses were performed between age corrected average GMV and mJOA score within sensorimotor and pain related brain regions. In addition, linear regression analyses were used to identify differences in GMV and mJOA slope and intercept between male and female patients. Healthy controls were excluded in regression analyses. Regression analyses were performed using MATLAB (Release 2018a, MathWorks, Natick, MA) and GraphPad Prism software (Version 7.0c GraphPad Software, San Diego, California). The vertex-wise level of significance was set at $p < .05$, with multiple comparisons correction performed by using Monte Carlo permutations with a significance level of $p < .05$.

5.3 Results

5.3.1 Subject Characteristics

As summarized in **Table 5.1**, the patient cohort consisted of 52 males with a mean age of 58.5 ± 11.6 years and 33 females with a mean age of 58.0 ± 10.7 years. There was no significant difference in age between male patients and female patients (Wilcoxon-Mann-Whitney test, $p = 0.8068$). The mJOA scores within the cohort ranged from 9 to 18 with a mean score of 15.0 ± 2.7 for male patients and 15.6 ± 2.4 for female patients. Of the 85 total study patients, 19 had asymptomatic spinal cord compression (mJOA =18), 38 presented with mild myelopathy ($15 \leq \text{mJOA} \leq 17$), 19 exhibited moderate myelopathy ($12 \leq \text{mJOA} \leq 14$), and 9 patients were categorized with severe myelopathy ($\text{mJOA} \leq 11$).

No significant difference in mJOA score was observed between male and female patients (Wilcoxon-Mann-Whitney test, $p = 0.3885$). The HC cohort consisted of 53 males with a mean age of 58.7 ± 6.4 years and 37 females with a mean age of 59.8 ± 6.3 years. There was no significant difference in age between male and female HCs (Wilcoxon-Mann-Whitney test, $p = 0.4076$). Additionally, no significant difference in age was found between the patient cohort and the HC cohort (Mann-Whitney test, $p = 0.9206$). Due to lack of neurological impairment, all HC participants had an mJOA score of 18.

5.3.2 Sex-dependent Cortical Volumetric Differences

Results from the whole-brain cortical volume analysis revealed no significant difference in GMV between males and females within the HC cohort, but significant differences in gray matter volume (GMV) between male and female within patients with DCM. We observed that male DCM patients compared to female patients (**Fig. 5.1 A**) exhibited significantly larger GMV in the caudal middle frontal, superior temporal, transverse temporal, and lingual gyrus of the left hemisphere, as well as in the precentral gyrus, insula, and lingual gyrus of the right hemisphere. Additionally, when controlling for mJOA, male DCM patients demonstrated significantly larger GMV than female patients in the bilateral lateral occipital gyri, left superior temporal gyrus, right insula, right middle temporal gyrus, and right lingual gyrus (**Fig. 5.1 B**).

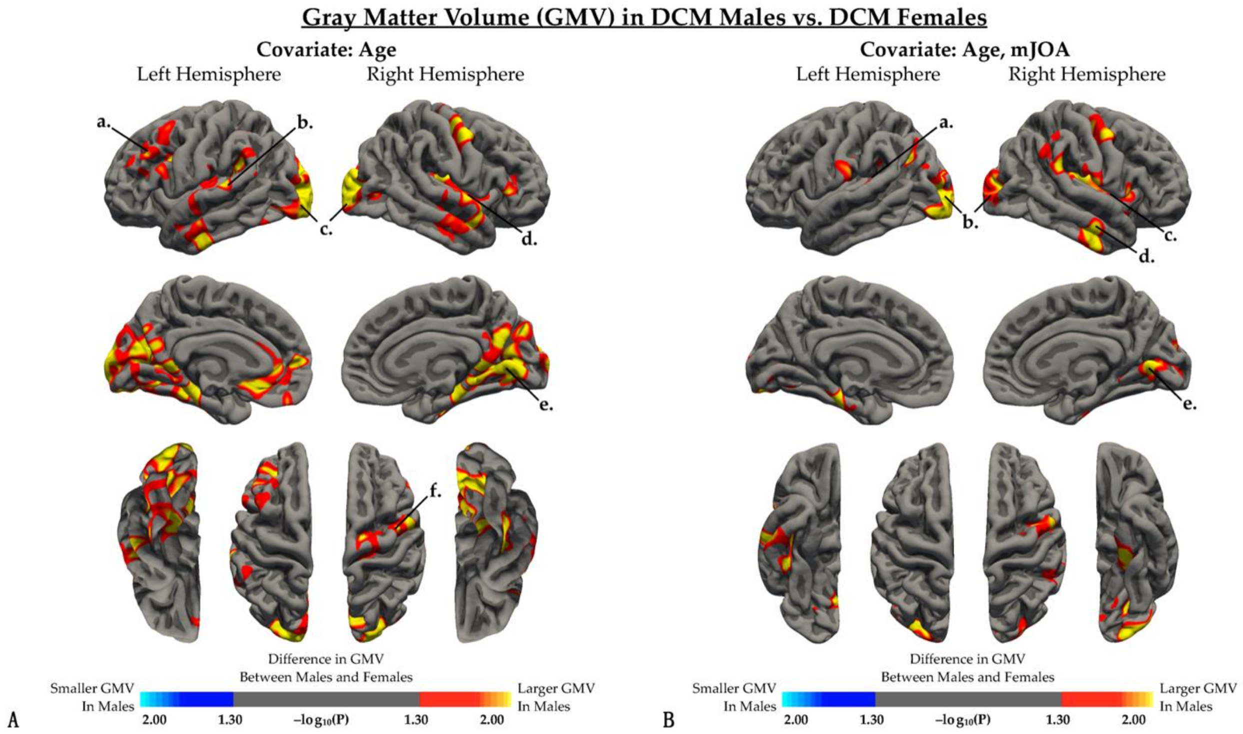

Figure 5.1: Cortical morphometry analysis between DCM males and DCM females.

Whole brain analysis comparing gray matter volume (GMV) between DCM males and DCM females after regressing out the effects of **(A)** age and **(B)** both age and mJOA score. **(A,B)** Red-yellow color denotes larger GMV in males, while blue-light blue color denotes smaller GMV in males compared to females. **(A)** When controlling for age, regions with significant differences in GMV were identified in the *a*, left rostral middle frontal gyrus; *b*, left superior temporal gyrus; *c*, bilateral lateral occipital cortex; *d*, right insular cortex; *e*, right lingual gyrus; and *f*, right precentral gyrus. **(B)** When controlling for both age and mJOA, regions with significant differences in GMV were identified in the *a*, left superior temporal gyrus; *b*, bilateral lateral occipital cortex; *c*, right insular cortex; *d*, right middle temporal gyrus; and *e*, right lingual gyrus. Significant clusters were determined by thresholding based on statistical significance (p<0.05).

Male DCM patients displayed significantly *larger* gray matter volume (GMV) in the left parahippocampal gyrus, left paropercularis, right lateral occipital cortex, and right lingual gyrus compared with male HCs (**Fig. 5.2 A**). On the contrary, female DCM patients exhibited significantly smaller GMV compared with female HCs, specifically in the left pericalcarine cortex and right lingual gyrus (**Fig. 5.2 B**).

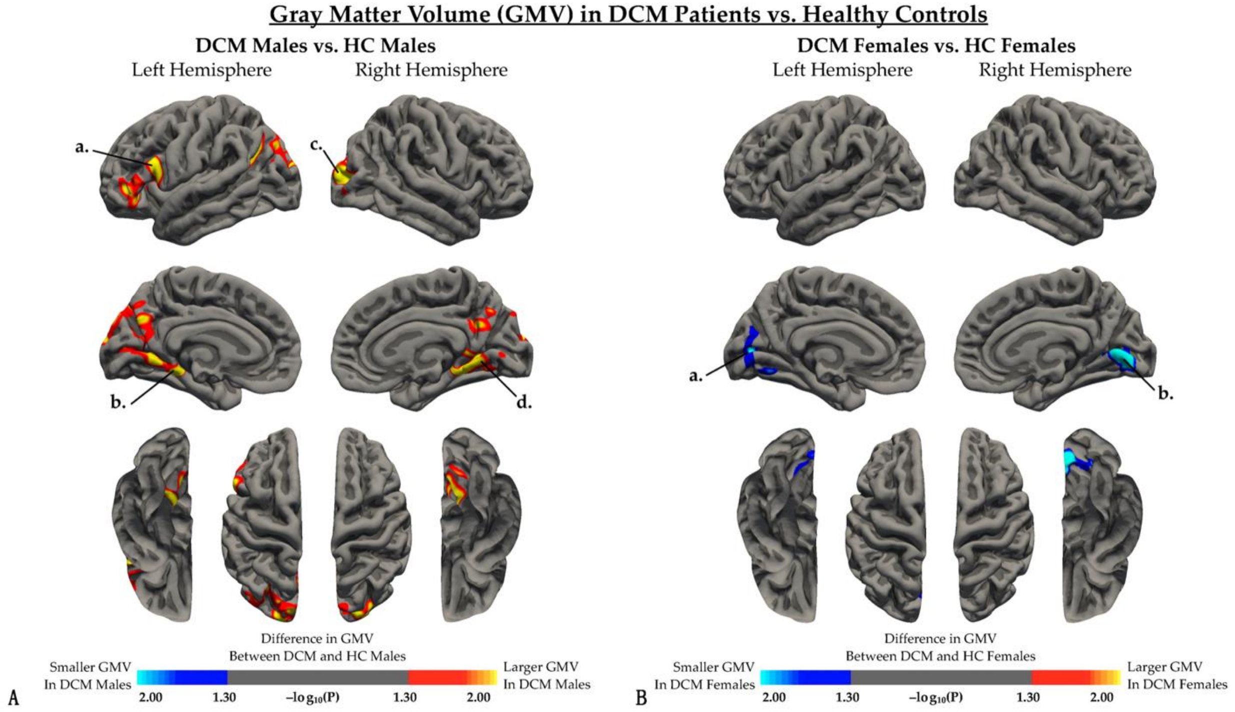

Figure 5.2: Cortical morphometry analysis between DCM patients and healthy controls.

Whole brain analysis comparing gray matter volume (GMV) between DCM patients and healthy controls when regressing out the effect of age in **(A)** males and **(B)** females. **(A)** Red-yellow color denotes larger GMV in DCM males, while blue-light blue color denotes smaller GMV in DCM males compared to HC males. When controlling for age, regions with significant differences in GVM were identified in the *a*, left parsopercularis; *b*, left parahippocampal gyrus; *c*, right lateral occipital cortex; and *d*, left lingual gyrus. **(B)** Red-yellow color denotes larger GMV in DCM females, while blue-light blue color denotes smaller GMV in DCM males compared to HC females. When controlling for both age and mJOA, regions with significant differences in GMV were identified in the *a*, left pericalcarine cortex; and *b*, right lingual gyrus. Significant clusters were determined by thresholding based on statistical significance ($p<0.05$).

5.3.3 Interaction between Cortical Volume and mJOA Scores

When examining the effect of sex on the association between GMV and mJOA score (**Fig. 5.3**), both male (**Fig. 5.3 A**) and females (**Fig. 5.3 B**) demonstrated a significant positive correlation between GMV and mJOA score across multiple cortical regions. Female subjects demonstrated associations between GMV and mJOA in similar regions to male subjects, but regions in female subjects appeared to extend across a broader area of the brain perhaps suggesting more widespread cortical changes in females. Mutually significant regions with a positive correlation between GMV and mJOA common for both males and females are illustrated in **Fig. 5.4 A** and outlined in **Table 5.2**. While both males and females demonstrated significant correlations between age corrected GMV and mJOA within similar regions, the degree of change (i.e. slope of the regression line) and overall GMV (i.e. intercept of regression line) were different between males and females within the left superior frontal ($p = 0.0013$), right superior frontal ($p = 0.0301$), left paracentral ($p < 0.0001$), right rostral middle frontal ($p < 0.0001$), left precentral ($p < 0.0001$), and right precentral ($p < 0.0001$) gyri, as well as the anterior, isthmus, and posterior cingulate cortex, the insula, and the precuneus (**Table 5.2**). Within DCM patients only (excluding HCs), a significant positive correlation between GMV and mJOA was observed in females, bilaterally within the precentral gyrus and in the left rostral anterior cingulate cortex (**Fig. 5.5**).

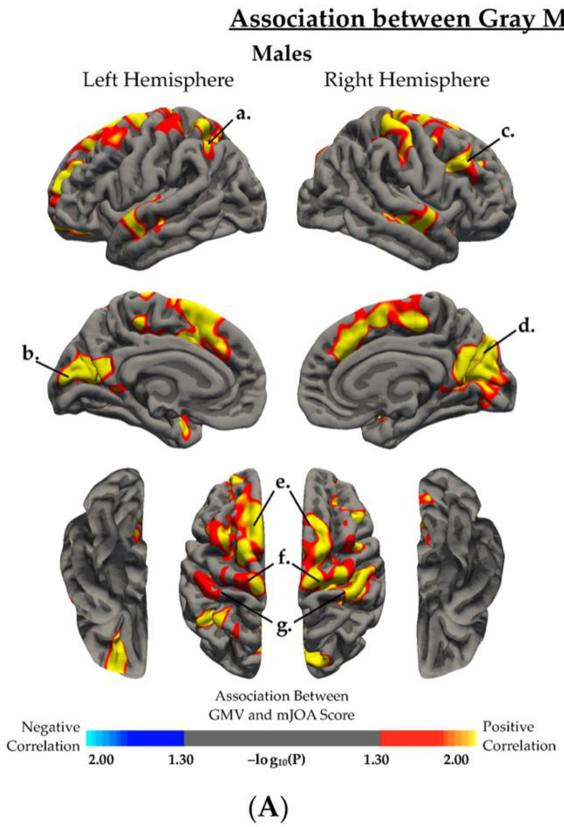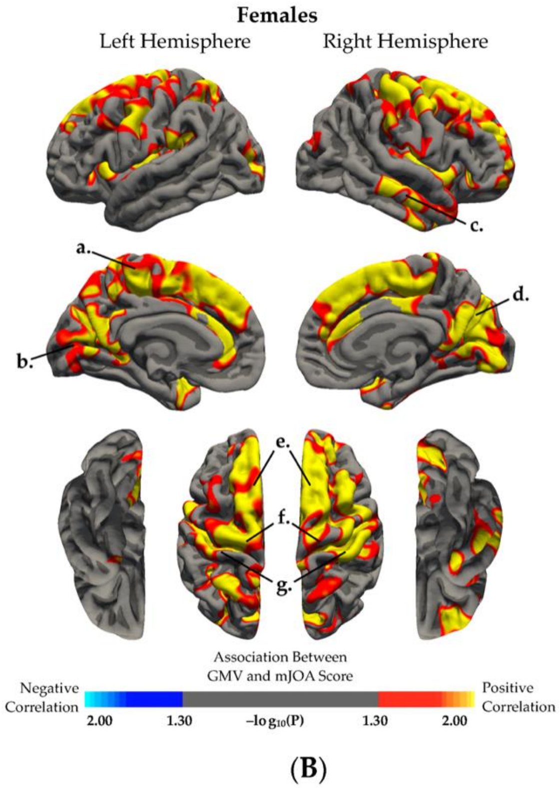

Figure 5.3: Sex-specific association between gray matter volume (GMV) and mJOA score in DCM patients and healthy controls.

Association between gray matter volume (GMV) and mJOA score in **(A)** DCM and HC males, and **(B)** DCM and HC females, regressing out the effect of age. (A,B) Red-yellow color indicated a positive association between GMV and mJOA score, while blue-light blue color indicated negative association between GMV and mJOA score. **(A)** In males, regions with significant association between GMV and mJOA were identified in several regions including the *a*, left inferior parietal cortex; *b*, left pericalcarine cortex; *c*, right rostral middle frontal gyrus; *d*, right cuneus; *e*, bilateral superior frontal gyrus; *f*, bilateral precentral gyrus; and *g*, bilateral postcentral gyrus. **(B)** In females, regions with significant association between GMV and mJOA were identified in several regions including the *a*, left paracentral gyrus; *b*, left pericalcarine and lingual gyrus; *c*, right middle temporal gyrus; *d*, right cuneus and pericalcarine cortex; *e*, bilateral superior frontal gyrus; *f*, bilateral precentral gyrus; and *g*, bilateral postcentral gyrus. Significant clusters were determined by thresholding based on statistical significance ($p<0.05$).

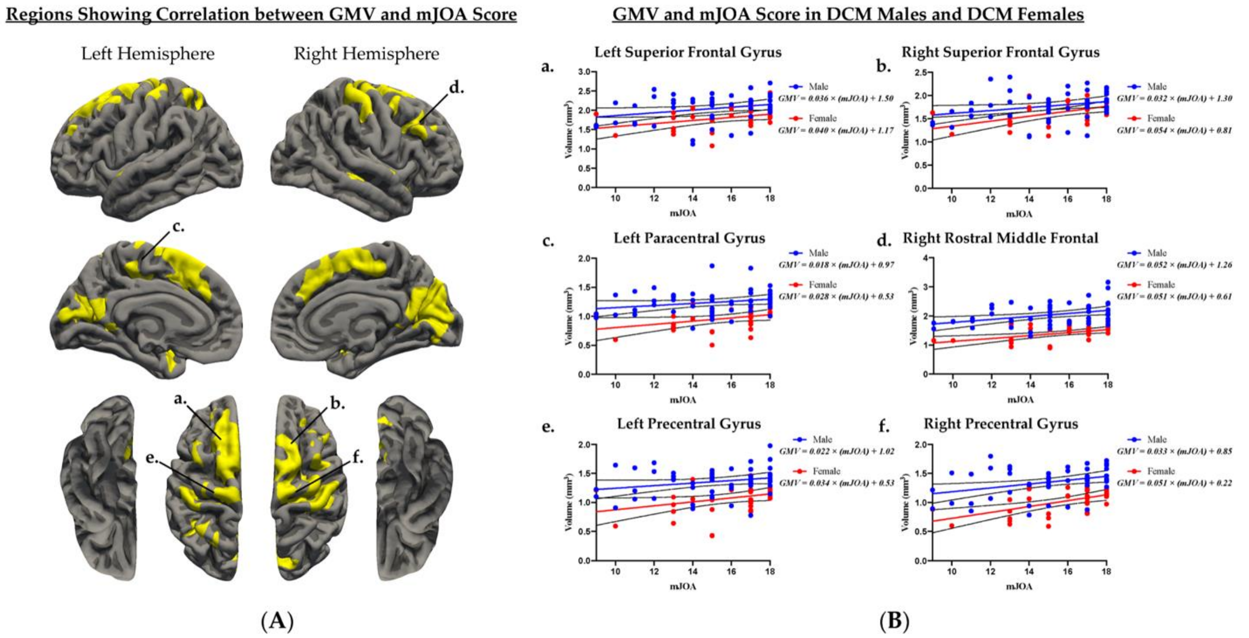

Figure 5.4: Cortical regions with significant positive association between gray matter volume (GMV) and mJOA score in both males and females.

(A) Cortical regions with significant positive association between gray matter volume (GMV) and mJOA score in both males and females. **(A)** Age corrected average GMV was extracted from mutually significant cortical regions and **(B)** are plotted against patient mJOA score in DCM males and DCM females. ROI regions include the *a*, left superior frontal gyrus; *b*, right superior frontal gyrus; *c*, left paracentral gyrus; *d*, right rostral middle frontal gyrus; *e*, left precentral gyrus; and *f*, right precentral gyrus. **(B)** Age corrected average GMV and mJOA plots include simple linear regression for male patients (blue line) and female patients (red line). The light blue region denotes the 95% confidence interval for male patients and the pink region denotes the 95% confidence interval for female patients.

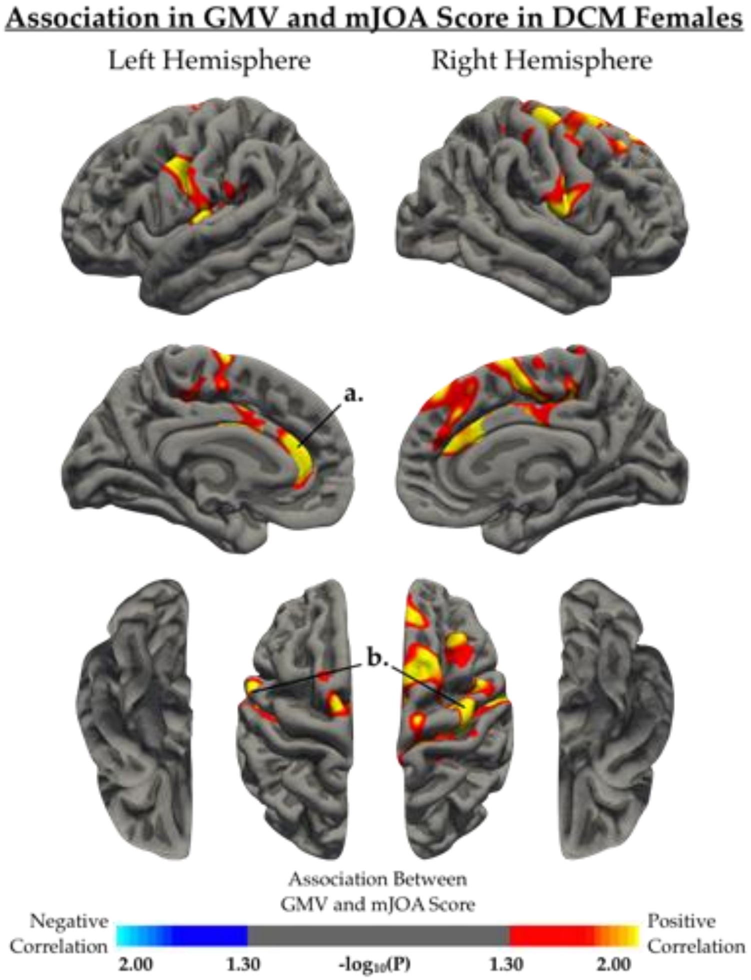

Figure 5.5: Correlation between GMV and mJOA score in only DCM females after accounting for age.

Red-yellow color indicated a positive association between GMV and mJOA score, while blue-light blue color indicated negative association between GMV and mJOA score. Regions with significant association between GMV and mJOA were identified in several regions including the *a*, left rostral anterior cingulate cortex; and *b*, bilateral precentral gyrus. Significant clusters were determined by thresholding based on statistical significance ($p<0.05$).

Region	Size of ROI (mm^2)	Comparison of Male & Female Fits p-Value	Male Simple Linear Regression p-Value	Female Simple Linear Regression p-Value	Male R^2	Female R^2
LH Paracentral	322.69	**<0.0001**	0.0954	0.0543	0.05462	0.1143
RH Paracentral	518.81	0.8711	**0.0379**	**0.0218**	0.08336	0.1583
LH Postcentral	674.12	0.9319	0.1626	0.1628	0.03862	0.06187
RH Postcentral	1414.2	0.1601	0.0571	**0.0237**	0.0705	0.1544
LH Precentral	439.37	**<0.0001**	0.0762	**0.0473**	0.06152	0.121
RH Precentral	1205.41	**<0.0001**	**0.0102**	**0.001**	0.1248	0.2986
LH Superior Frontal	2874.67	**0.0013**	**0.0469**	0.0515	0.0767	0.1169
RH Superior Frontal	1894.1	**0.0301**	**0.0452**	**0.004**	0.0778	0.2382
LH Rostral Middle Frontal	150.27	0.9753	0.1075	0.1016	0.05099	0.0841
RH Rostral Middle Frontal	473.04	**<0.0001**	**0.0063**	**0.0027**	0.1398	0.2561
LH Superior Parietal	698.91	0.0556	**0.0255**	**0.0273**	0.09588	0.1476

RH Superior Parietal	308.98	**<0.0001**	0.0623	**0.041**	0.06777	0.1279
LH Supramarginal	144.22	**<0.0001**	**0.0029**	**0.0413**	0.1638	0.1275
RH Supramarginal	341.88	**0.0005**	0.0656	0.0845	0.06618	0.09296
LH caudal ACC	22.44	**<0.0001**	0.2588	0.107	0.02543	0.08163
RH caudal ACC	2.18	**<0.0001**	0.492	**0.0159**	0.00949	0.1736
RH rostral ACC	43.86	**<0.0001**	0.1569	**0.009**	0.03968	0.2003
LH isthmus Cingulate	227.99	**<0.0001**	0.2472	**0.0242**	0.02669	0.1535
RH isthmus Cingulate	107.14	**<0.0001**	0.3069	0.0996	0.02087	0.08505
LH posterior Cingulate	61.68	**<0.0001**	0.5837	**0.0184**	0.006048	0.1666
LH Insula	55.35	**<0.0001**	0.7624	0.0534	0.001845	0.1151
RH Insula	40.95	**<0.0001**	0.443	0.2181	0.01182	0.04851
LH Precuneus	855.31	**<0.0001**	**0.0398**	0.0525	0.0818	0.116
RH Precuneus	1421.53	**<0.0001**	0.0686	0.0732	0.06477	0.09986

Table 5.2: Regression analyses quantifying the association between average gray matter volume (GMV) and mJOA score for regions found significant in both sexes.

LH denotes left hemisphere and RH denotes right hemisphere. The table includes the following: mutually significant anatomical region, surface area of cortical region of interest (ROI), p-value evaluating whether male and female linear fits are significantly different in slope and y-intercept, p-value evaluating whether a linear relationship occurs between average GMV and mJOA score in males, p-value evaluating whether a linear relationship occurs between average GMV and mJOA score in females, goodness of fit for males, and goodness of fit for females.

5.4 Discussion

The present study demonstrates significant sex-related differences in cortical volume in patients with degenerative cervical myelopathy. Prior to this investigation, the role of sex on brain structure in DCM remained largely understudied. Our findings may foster further investigation and understanding of the influence of sex and sex hormones on supraspinal plasticity following spinal cord injury.

The current study found no statistically significant differences in GMV between HC males and females. Literature investigating sex-related differences in cortical morphometry of the healthy brain remains controversial, with some studies reporting significant sex-related differences in GMV and other citing no significant difference [151-154]. To address these inconsistencies, Sanchis-Segura *et al.* examined how the number, size, and direction of sex differences in regional GMV vary depending on how total intercranial volume (TIV) is statistically controlled; and concluded that when TIV effects are properly accounted for, sex differences in GMV are relatively small in healthy adults [155].

When investigating volumetric differences within patients, we found male patients exhibited larger GMV in various regions compared to female patients, including motor, language, and pain related cortices. Previous studies have revealed DCM patients exhibit functional and morphological alterations within primary motor and sensorimotor cortices when compared to age-matched HCs [67,135,156]. We suspect patients experience alterations in such brain regions due to hormonal, neuroinflammatory, and neuronal compensatory differences between sexes [147]. Preclinical studies of spinal cord injury (SCI), stroke, and traumatic brain injury (TBI) have shown sex steroids, particularly 17-estradiol, estrogen, progesterone, and testosterone, can provide neuroprotective, pro-myelination, and anti-inflammatory effects resulting in improved tissue sparing and motor function [136-142].

In humans with acute traumatic SCI, administration of progesterone and vitamin D was associated with better functional recovery and outcome [141]. Interestingly, preclinical studies have shown testosterone treatment also provides neuroprotective benefits following SCI, but in the clinical setting about 43-57% of male patients experience low levels of testosterone following SCI, and low levels of testosterone were associated with severity of injury [138,146,157,158]. Sex-dependent volumetric differences observed within DCM patients and between patients and HCs may be driven by variations in hormone levels. In the male group, DCM patients exhibited larger GMV in regions involved in memory, vision, and language. Female patients exhibited fewer alterations than male patients when compared to healthy counterparts, a possible indication of the neuroprotective effects of normal or elevated progesterone and estrogen levels.

Furthermore, significant positive associations between GMV and mJOA score were found in both male and female groups primarily across somatosensory and motor related cortical regions. Such findings are consistent with previous reports in which cortical alterations and cerebral reorganization were correlated with neurological function, proposing a compensatory relationship between cortical alterations and symptom progression in patients with cervical spondylosis [59,66,156]. A positive association between GMV and mJOA appears to confirm that patients with worsening neurological symptoms exhibit decreasing GMV across sensorimotor related cortices. females exhibited an association between GMV and mJOA across a broader range of brain regions compared with male patients, including regions believed to be involved in pain processing [159]. Independent of mJOA, female patients consistently showed lower GMV than males within various regions involved in sensorimotor function. Our results reflect the possible influence of sex hormones on cerebral compensatory mechanisms and disease progression between males and females with DCM. Based on these novel preliminary studies, future investigations that evaluate supraspinal microstructural and functional alterations are warranted and will provide additional insight into the role of sex hormones in DCM neural plasticity.

Although our patient and healthy control cohorts were well matched in terms of age and numbers of male and female subjects, it is important to note the healthy control subjects were acquired retrospectively from an image repository. Therefore, collection of age- and gender-matched HCs with brain and spinal cord imaging and mJOA testing is warranted for validating our findings and future studies. Furthermore, the present analyses corrected for subject age, however future studies would benefit from inclusion of subject total intracranial volume (TICV) and body mass index (BMI) as additional covariates. Lastly, measurement and assessment of serum sex hormones in relation to sex and neurological function would greatly benefit our understanding of the mechanisms underlying sexual dimorphism in DCM.

To the best of our knowledge this is the first study to investigate sex differences in cortical volume in patients with DCM. Results suggest males with DCM exhibit significantly larger GMV compared to female DCM patients in various brain regions, and DCM patients exhibit significant sex-related differences in the association between GMV and neurological function, particularly in brain areas involved in sensorimotor function.

CHAPTER 6

Sex-Specific Alterations in Functional Connectivity and Network Topology in Patients with Degenerative Cervical Myelopathy **

**** Note:** The present chapter have been adapted from a manuscript of the same title that has been submitted to a journal for publication with T.C. Oughourlian as the first author.

6.1 Introduction

In patients with Degenerative Cervical Myelopathy (DCM), chronic spinal cord compression induces upstream structural and functional alterations within the brain and brainstem [59,60,66,67,73,74,160]. Several studies have revealed that patients with DCM experience significant reductions in cortical volume and thickness in somatosensory, motor, and pain related regions, including the somatosensory cortex, frontal gyrus, cingulate cortex, cerebellum, precuneus, and putamen when compared to healthy controls (HCs) [59,60,62]. Additionally, DCM patients exhibit altered functional connectivity (FC) in sensorimotor and pain regions, as well as in regions important to visual processing [62,66,73,74]. The degree to which morphometric and functional alterations occur has been correlated to the severity of patients' neurological deficit and pain. Thus, it is believed that the cerebral alterations observed in DCM patients are compensatory mechanisms for the preservation of neurological function. Although these previous studies have identified unique supraspinal features associated with DCM, the influence of sex on cerebral alterations and disease pathology remains largely unexplored.

Cervical myelopathy is more common in males than females with a reported incidence ratio as high as 2.7-to-1 [12]. When investigating the differences in cortical morphometry between males and females with DCM, recent results have suggested male DCM patients exhibit larger gray matter volume (GMV) in sensorimotor regions, as well as more anatomically precise associations between GMV and neurological deficit than female patients [161]. Research in traumatic spinal cord injury (SCI) offers ample support for sex-dependent differences in neurotraumatic response, which may be applied to understand DCM pathophysiology. Studies in both animal models and human patients show spinal cord gene expression to differ between males and females following traumatic SCI, with females exhibiting greater functional recovery following injury [162-164]. These findings support the hypothesis that DCM may result in sex-dependent alterations of brain structure.

In the present study, resting state functional magnetic resonance imaging (rs-fMRI) was used to investigate the influence of sex on FC in patients with DCM. Furthermore, graph-theory based brain network analyses of rs-fMRI signals was used to examine differences in topological network properties between DCM patients and HCs, as well as between male and female patients with DCM. By treating the brain as a complex network, where anatomical regions serve as nodes and functional or anatomical connections as edges or links, we theorized graph-based network approaches could provide meaningful metrics that describe the network topological organization and the efficiency of information processing [165], as similar studies have revealed abnormal connectivity in various neurological conditions, including Alzheimer’s disease [166], multiple sclerosis [167], and schizophrenia [168]. In the present study, we tested the following hypotheses:

1) sex-dependent differences in functional connectivity exist in patients with DCM, specifically between the cerebellum, sensorimotor regions, and visual networks, and 2) male patients exhibit more streamlined topological network properties, while female patients exhibit more diffuse properties. We theorized that the influence of sex on FC may provide insight into individual patients' response to chronic neurotrauma and sex-specific compensatory alterations driven by chronic spinal cord compression.

6.2 Materials and Methods

6.2.1 Patient Population

A total of 100 patients were prospectively enrolled from 2015 to 2022 in a cross-sectional study including brain and spinal cord imaging as well as a neurological examination. The cohort included 75 patients with DCM and 25 with asymptomatic spinal cord compression. Patients were recruited from the UCLA outpatient neurosurgery clinic and exhibited spinal cord compression with evidence of spinal cord deformation, mass effect, and no visible cerebrospinal fluid signal around the spinal cord at the site of maximal compression on MRI. Patients included in this study had not undergone surgical intervention for cervical spinal cord compression at the time of imaging. All patients signed Institutional Review Board-approved consent forms, and all analyses were performed in compliance with the Health Insurance Portability and Accountability Act (HIPAA). The patient cohort consisted of 58 males and 42 females ranging in age from 31 to 81 years with a mean age of 58.1 years for males and 57.3 years for females. In addition, the mean body mass index (BMI) for male patients was 26.2 and 26.1 for female patients. Previous studies have demonstrated relationships between BMI and altered functional brain connectivity [87-89], therefore BMI was included as a covariate in the present study. The modified Japanese Orthopedic Association (mJOA) score was used as a measure of neurological function [80]. The mJOA scale ranges from 0 to 18, with lower scores representing worse neurological impairment and an mJOA score of 18 reflecting no impairment. All patients underwent brain and spinal cord imaging at UCLA. Patient demographic data was summarized in **Table 6.1**.

Subject Population	**Number of Subject** (Male/Female)	**Age** (Male/Female) [min,max] *p-value*	**BMI** (Male/Female) [min,max] *p-value*	**mJOA** (Male/Female) [min,max] *p-value*
DCM Patients	**100** (58/42)	(58.1 ± 11.5 / 57.3 ± 11.0) [31,81] $p = 0.6423$	(26.2 ± 3.9 / 26.1 ± 5.0) [18.9,41.0] $p = 0.5509$	(15.3 ± 2.5 / 15.8 ± 2.2) [10,18] $p = 0.4291$
Healthy Controls	**59** (28/31)	(50.4 ± 5.0 / 49.6 ± 3.5) [45,73] $p = 0.5278$	(27.1 ± 4.3 / 26.3 ± 5.2) [19.2,40.7] $p = 0.3098$	18 *

Table 6.1: Cohort demographics.

Age is provided in mean years ± the standard deviation, minimum and maximum years, and p-value of Wilcoxon-Mann-Whitney test between age of males and females. The body mass index (BMI) is provided in mean BMI ± the standard deviation with the minimum and maximum BMI. The modified Japanese Orthopedic Association (mJOA) score is provided in mean score ± the standard deviation with the minimum and maximum scores. The p-value of Wilcoxon-Mann-Whitney test between scores of males and females is reported for age, BMI, and mJOA score. *= HCs were categorized with a mJOA score of 18 due to their healthy neurological status.

6.2.2 Healthy Control Population

A total of 59 neurologically intact age-matched healthy control (HC) volunteers were included from the UCLA Center for Neurobiology of Stress and Resilience (CNSR). The HC cohort consisted of 28 males and 31 females ranging in age from 45 to 73 years with a mean age of 50.4 years for males and 49.6 years for females. The mean BMI for male HCs was 27.1 and 26.3 for female HCs. Exclusion criteria implemented by the CNSR investigators consisted of 1) significant neurological or psychiatric disorder, 2) chronic gastrointestinal disorder, 3) chronic pain disorder, 4) active autoimmune or infectious disorder, 5) history of cancer, and 6) women who are pregnant or planning to become pregnant at time of study. Healthy participant demographic data was summarized in **Table 6.1**.

6.2.3 Magnetic Resonance Imaging Acquisition

High-resolution, 1 mm isotropic, 3-dimensional T1-weighted structural MRI scans were acquired on a 3T MR scanner (Siemens Prisma; Siemens Healthcare, Erlangen, Germany) using a magnetization-prepared rapid gradient-echo (MPRAGE) sequence in either the coronal, sagittal, or axial orientation, with a repetition time (TR) of 2300-2500 ms, a minimum echo time (TE) between 2-3 ms, an inversion time (TI) of 900-945 ms, a flip angle of 9^o-20^o, slice thickness of 1 mm with no interslice gap, a field of view (FOV) of 240 x 320 mm and matrix size of 240 x 320.

Additionally, resting state functional MRI scans were acquired with a TR of 1500-2200 ms, TE of 28-30 ms, flip angle of 77^o, FOV of 220 to 245 mm with an acquisition matrix of 64 x 64 for an in-plane resolution of 3.4 to 3.8 mm, interleaved acquisition, slice thickness of 4 mm with no interslice gap, parallel imaging via CAIPIRNHA with a factor of 2, and multi-band acceleration with a factor of 2.

6.2.4 Image Processing and Analysis

Functional MR images were processed using the CONN toolbox (https://www.nitrc.org/projects/conn) [85], which utilizes functions from the Statistic Parametric Mapping (SPM) toolbox (http://www.fil.ion.ucl.ac.uk/spm/). Functional and structural images were processed using the standard built-in preprocessing pipeline provided in the CONN toolbox. The default pipeline performs the following steps: 1) realignment of functional images including motion correction based on 12 degrees of freedom and unwarping, 2) slice-timing correction to correct for difference in acquisition time between slices, 3) registration of functional images to structural images, 4) registration of structural images to the Montreal Neurological Institute (MNI) defined standardized space, 5) removal of signal intensity spikes and functional volumes with excessive motion (threshold set at 2 mm translation and 2° rotation in any direction) using the Artifacts Detection Tool (ART) from SPM, 6) segmentation and normalization of functional images based on tissue type (gray matter, white matter, and cerebrospinal fluid) in MNI space, 6) segmentation and normalization of structural images based on tissue type (gray matter, white matter, and cerebrospinal fluid) in MNI space, and 7) spatial smoothing of functional data using 8 mm, full width at half maximum (FWHM) Gaussian kernel. Additionally, signals from the white matter, CSF, and motion parameters were regressed from the functional data, and signal filtering was performed using a band-pass filter of 0.008–0.10 Hz to reduce noise caused by scanner drift and physiological effects (i.e., pulsation and respiration).

Functional connectivity (FC) of the brain was assessed using 1) whole brain ROI-to-ROI (also termed seed-to-seed) and 2) seeds of interest ROI-to-ROI analyses. Regions of interest (ROIs) were selected from the Harvard-Oxford Automated Anatomical Labeling (AAL) atlases [86]. Whole-brain ROI-to-ROI analyses used 132 cerebral ROIs, while seeds of interest were selected based on previously published studies which observed altered FC between DCM patients and HCs [62,66,99,169,170]. For the seeds of interest ROI-to-ROI analyses, the following ROIs were selected: the superior frontal gyrus (sFG), the middle frontal gyrus (mFG), the frontal medial cortex, the precentral gyrus, the postcentral gyrus, the supplementary motor area (SMA), the superior parietal lobule (SPL), the insular cortex, the precuneus, the thalamus, the putamen, intracalcarine cortex (ICC), the anterior and posterior cingulate gyri, the brainstem, the cerebellar crus (1 and 2), the cerebellar hemispheres (3, 4/5, 6, 7b, 8, 9, and 10), the cerebellar vermis (1/2,3,4/5,6,7,8,9, and 10), the lateral prefrontal cortex, the posterior parietal cortex, and the lateral, medial, and occipital visual networks (**Table 6.2**). General linear models (GLMs) were used to evaluate group differences in functional connectivity while accounting for the effects of subject age and BMI. Statistical analyses were performed using the CONN toolbox [85], MATLAB (Release 2018a, MathWorks, Natick, MA), and GraphPad Prism software (Version 7.0c GraphPad Software, San Diego, California). For the connection threshold, significance was set at $p < 0.01$ and at the ROI level, significance was set at a false discovery rate (FDR) corrected $p < 0.05$.

Regions of Interest

Frontal	
L Superior Frontal Gyrus	R Superior Frontal Gyrus
L Middle Frontal Gyrus	R Middle Frontal Gyrus
Frontal Medial Cortex	
Sensorimotor	
L Precentral Gyrus	R Precentral Gyrus
L Postcentral Gyrs	R Postcentral Gyrs
L Supplemental Motor Area	R Supplemental Motor Area
Parietal	
L Superior Parietal Lobule	R Superior Parietal Lobule
L Insula	R Insula
Precuneus	
Thalamus/Basal Ganglia	
L Thalamus	R Thalamus
L Putamen	R Putamen
Occipital Cortex	
L Intracalcarine Cortex	R Intracalcarine Cortex
Cingulate Cortex	
Anterior Cingulate Gyrus	Posterior Cingulate Gyrus
Subcortical	
Brainstem	

Cerebellum	
L Cerebellum Crus1	R Cerebellum Crus1
L Cerebellum Crus2	R Cerebellum Crus2
L Cerebellum 3	R Cerebellum 3
L Cerebellum 4/5	R Cerebellum 4/5
L Cerebellum 6	R Cerebellum 6
L Cerebellum 7b	R Cerebellum 7b
L Cerebellum 8	R Cerebellum 8
L Cerebellum 9	R Cerebellum 9
L Cerebellum 10	R Cerebellum 10
Vermis 1/2	
Vermis 3	
Vermis 4/5	
Vermis 6	
Vermis 7	
Vermis 8	
Vermis 9	
Vermis 10	
FrontoParietal Network	
L Lateral Prefrontal Cortex	R Lateral Prefrontal Cortex
L Posterior Parietal Cortex	R Posterior Parietal Cortex
Visual Network	
L Lateral Visual Network	R Lateral Visual Network
Medial Visual Network	
Occipital Visual Network	

Table 6.2: Regions of Interest.

These Harvard-Oxford Automated Anatomical Labeling (AAL) atlas defined regions and networks were selected as regions of interest for ROI-to-ROI and ROI-to-voxel analyses.

6.2.5 Graph Theory-based Network Connectivity Analyses

A graph theory-based approach was used to model the brain as a complex network and investigate its topological organization. This network is represented as a graph consisting of anatomical nodes and their pairwise connections or edges [171]. Here, nodes were defined as 132 anatomical ROIs derived from the Harvard-Oxford Automated Anatomical Labeling (AAL) atlases [86]. The nodes used in this analysis were consistent with the regions used in the whole-brain functional connectivity analyses. In the present study, edges were extracted from rs-fMRI data and defined as functional connectivity correlations between ROIs. The connectivity matrix (connectivity values between nodes) of each subject was calculated using the CONN toolbox [85]. In this network, the edges were weighted and undirected. Measures of global (network-wise) connectivity properties were calculated and analyzed using Matlab and the Graph Theory GLM (GTG) toolbox (www.nitrc.org/projects/metalab_gtg). In the present study, the clustering coefficient, characteristic path length, and small-world index were calculated for each subject. Graph theory-based measures are illustrated in **Figure 6.5**. Because connectivity values vary between subjects due to noise and intrasubject variation, multiple thresholds were applied to subject's connectivity matrices [171]. Thresholds ranged from 0.2 to 0.6 with a step of 0.05 (i.e., 0.2 refers to 20 percent of the strongest connections are maintained). Clustering coefficient, characteristic path length, and small-world index were calculated for the above threshold range and plotted using GraphPad Prism (Version 7.0c GraphPad Software, San Diego, California). The area under the curve (AUC) was calculated for each cohort and compared between groups using the Mann-Whitney unpaired t-test on GraphPad Prism. Level of significance was set at $p < 0.05$.

Node Degree

Node degree (k) is a local (nodal) connectivity measurement defined as the number of edges or connections maintained by each node (i) and is calculated as

$$k_i = \sum_{j \neq i} a_{ij}$$

in which a_{ij} is the *i*th row and the *j*th column of the connectivity matrix [165]. The more connections a node has (higher node degree), the more important that node (i.e., anatomical brain region) may be in the brain network [172]. In addition, node degree represents how connected a node is with the rest of the nodes in a brain network [165].

Clustering Coefficient

For each node (i), the clustering coefficient (C) measures the proportion of neighboring nodes that are interconnected (i.e., the number of triangles in the network) [173]. The clustering coefficient is a local (nodal) measurement, while the average clustering coefficient acts as a global (network) measurement [173]. The local clustering coefficient is calculated by dividing the number of connected edges between node i's adjacent nodes $t_i = \frac{1}{2}\sum_{i \leftrightarrow j \leftrightarrow h} a_{ij}a_{ih}a_{jh}$ by the number of all possible edges [172].

$$C(i) = \frac{2t_i}{k_i(k_i - 1)}$$

The clustering coefficient is a measure of functional segregation and local connectedness [173]. The higher the clustering coefficient, the more densely interconnected the brain regions are [172]. By averaging the clustering coefficient of all the nodes in a network, we can measure the interconnectedness of the whole network.

$$C = \frac{1}{N}\sum_i C(i) = \frac{1}{N}\sum_i \frac{2t_i}{k_i(k_i - 1)}$$

The Characteristic Path Length

The characteristic path length (L) refers to the average distance or minimum number of edges between nodes in the network [165]. The shortest path length (l) between each node pair is measured as

$$l_{ij} = \sum_{a_{st} \in l_{i\leftrightarrow j}} a_{st}$$

where $l_{i\leftrightarrow j}$ is the shortest path between node i and node j. The characteristic path length (L) is the average of the shortest path length for all nodes within a network and is denoted as

$$L = \frac{1}{N}\sum_i l_i$$

Path length is a measure of functional integration and is used to characterize the internal structure of the brain network. Shorter path lengths can transmit information more rapidly and efficiently [172]. Therefore, the smaller the characteristic path length, the higher the routing efficiency of the network [165].

Small World Brain Connectivity

A small-world network is defined as having high local clustering (i.e., high clustering coefficient) and a low minimum path length between pairs of nodes (i.e., low characteristic path length) [165]. The human brain exhibits small-world network properties, with its highly connected and modular structure being ideal for efficient information processing [165]. To determine if a network is considered a small-world network, the global clustering coefficient (C) and characteristic path length (L) are compared with those of a random network [172]. Using the Graph Theory GLM toolbox, a null model (random network) was generated using subject data over 1,000 repetitions.

$$\gamma = \frac{C}{C_{rand}} \qquad \lambda = \frac{L}{L_{rand}}$$

The following two conditions must be true: $\gamma \gg 1$ and $\lambda \approx 1$ [172]. The small-world index (σ) of a network is quantified as

$$\sigma = \frac{\gamma}{\lambda}$$

6.3 Results

6.3.1 Subject Characteristics

As summarized in **Table 6.1**, the patient cohort consisted of 58 males with a mean age of 58.1 ± 11.5 years and 42 females with a mean age of 57.3 ± 11.0 years. The age of patients ranged from 31 to 81 years. No significant difference in age between male patients and female patients was observed (Wilcoxon-Mann-Whitney test, $p = 0.6423$). Within the patient cohort, body mass index (BMI) ranged from 18.9 to 41.0 with a mean BMI of 26.2 ± 3.9 in male patients and 26.1 ± 5.0 in female patients. There was no significant difference in BMI between male and female patients (Wilcoxon-Mann-Whitney test, $p = 0.5509$). Patient mJOA scores ranged from 10 to 18 with a mean score of 15.3 ± 2.5 for male patients and 15.8 ± 2.2 for female patients. Of the 100 patients who completed the mJOA assessment, 8 patients were categorized with severe myelopathy (mJOA $\leq$ 11), 21 patients with moderate myelopathy (12 $\leq$ mJOA $\leq$ 14), and 46 patients with mild myelopathy (15 $\leq$ mJOA $\leq$ 17) at the time of the brain scan. 25 patients reported no neurological deficit (mJOA =18). No significant difference in mJOA score was observed between male and female patients (Wilcoxon-Mann-Whitney test, $p = 0.4291$).

The HC cohort consisted of 28 males with a mean age of 50.4 ± 5.0 years and 31 females with a mean age of 49.6 ± 3.5 years. All HC subjects had an mJOA score of 18. There was no significant difference in age between male and female HCs (Wilcoxon-Mann-Whitney test, $p = 0.5278$). Within the HC cohort, BMI ranged from 19.2 to 40.7 with a mean BMI of 27.1 ± 4.3 in males and 26.3 ± 5.2 in females. No significant difference in BMI was observed between male and female HCs (Wilcoxon-Mann-Whitney test, $p = 0.3098$).

6.3.2 Disease-Dependent Differences in ROI-to-ROI Functional Connectivity

To evaluate functional changes associated with DCM, whole-brain ROI-to-ROI functional connectivity analysis was performed between the DCM patient and HC cohorts while accounting for the effects of subject age and BMI on FC. When compared to HCs, DCM patients displayed widespread significant differences in FC (**Fig. 6.1 A**). Specifically, DCM patients exhibited higher FC between primary/secondary visual ROI's and cerebellar, thalamic, basal ganglia, and brainstem ROIs compared to HCs (**Fig. 6.1 A**). Higher FC in DCM patients was also observed between thalamus and motor, limbic, and temporal ROIs, as well as between cerebellar regions. DCM patients showed lower FC compared to HCs primarily between motor regions and visual and temporal regions (**Fig. 6.1 A**).

Based on previous studies identifying functional alterations in DCM patients and results from whole-brain FC analysis [62,66,99,169,170], 59 ROIs were selected for further ROI-to-ROI analyses and are listed in **Table 6.2**. When accounting for subject age and BMI, FC analysis among selected seeds of interest revealed higher FC in DCM patients compared to HCs between visual and cerebellar regions including cerebellar hemispheres and vermis, as well as between the visual networks and the brainstem, bilateral thalamus, and bilateral intracalcarine cortices (ICC) (**Fig. 6.1 B**). Higher FC in DCM patients was also observed between the postcentral gyri and thalamus and putamen. In contrast, DCM patients exhibited lower FC between visual networks and motor-related brain regions including the precentral gyri, postcentral gyri, and the supplemental motor area (SMA) (**Fig. 6.1 B**). Additionally, lower FC in DCM patients was observed between visual regions and frontal regions including the superior and middle frontal gyri (**Fig. 6.1 B**).

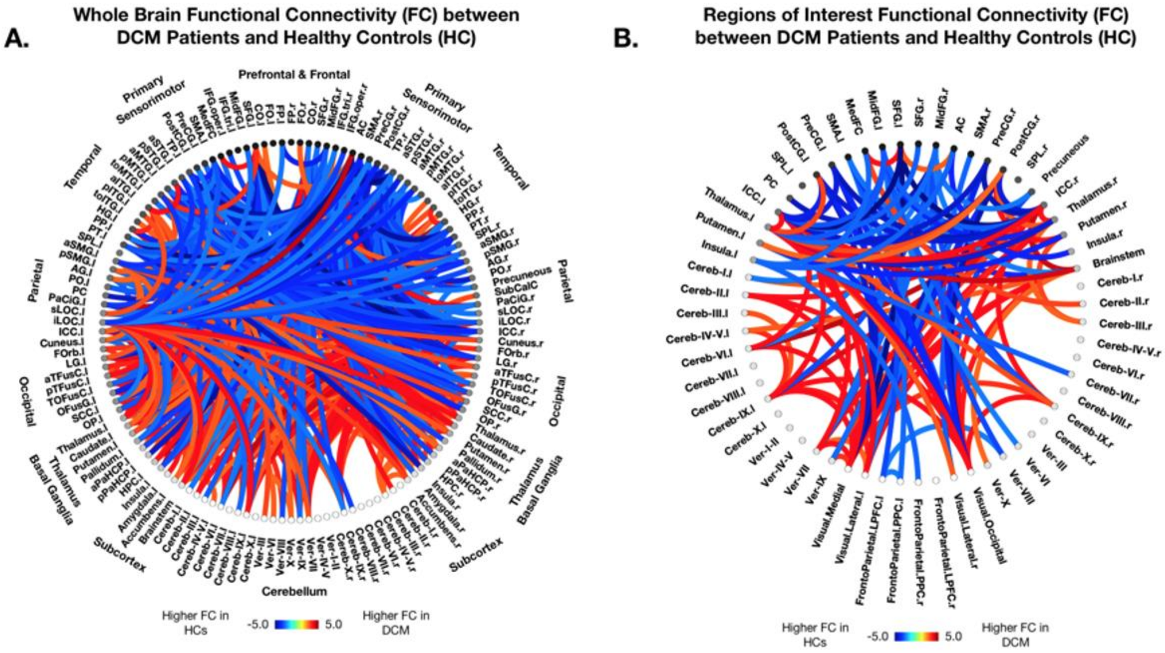

Figure 6.1: Whole-brain functional connectivity (FC) analysis in DCM vs HCs.

ROI-to-ROI functional connectivity (FC) analysis between patients with Degenerative Cervical Myelopathy (DCM) and Healthy Controls (HCs) after regressing out the effects of age and body mass index (BMI). **(A)** Whole brain FC analysis using 132 Harvard-Oxford Automated Anatomical Labeling (AAL) atlas defined ROIs. **(B)** Regions of interest FC analysis using 59 AAL atlas defined ROIs previously shown to or hypothesized to be involved in cerebral alterations driven by DCM. Seeds of interest are listed in Table 2. (A-B) Colors denote value of T-statistic in which red-orange color denotes higher FC in DCM patients compared to HCs, while blue-light blue denotes higher FC in HCs compared to DCM patients. ROIs are labeled with l = left hemisphere and r = right hemisphere. Significant connections between ROIs were determined by thresholding based on an FDR-corrected p-value < 0.05.

6.3.3 Sex-Specific Differences in ROI-to-ROI Functional Connectivity

Results from the whole-brain and select seeds of interest ROI-to-ROI analyses revealed no significant differences in FC between males and females within the HC cohort when accounting for age and BMI. In contrast, significant sex-specific differences between DCM patients and HCs were observed for both whole-brain and seeds of interest FC analyses. Whole-brain analysis between male DCM patients and male HCs revealed higher FC in DCM males between the left ICC and bilateral thalamus, bilateral caudate, brainstem, and various cerebellar regions (**Fig. 6.2 A**). DCM males also displayed higher FC between the anterior cingulate cortex (AC) and bilateral parietal regions, including the superior lateral occipital cortex (sLOC) and paracingulate gyrus (PaCiG) (**Fig. 6.2 A**). Compared with healthy males, DCM males exhibited lower FC between sensorimotor and temporal/parietal regions, specifically the left ICC and left bilateral planum polare (PP) (**Fig. 6.2 A**).

In females, FC analysis revealed higher FC between the cerebellum, parietal, and occipital regions in DCM females compared to HC females (**Fig. 6.2 B**). Specifically, higher FC was observed between the cerebellar vermis region VII and various parietal/occipital regions including bilateral ICC, bilateral cuneus, bilateral lingual gyri (LG), and bilateral fusiform cortices (FusC/FusG). Higher FC in female patients was also observed between the thalamus and the right postcentral gyrus, while lower FC was observed across sensorimotor, temporal, and occipital regions (**Fig. 6.2 B**). Bilateral primary sensorimotor regions, including the SMA and the precentral and postcentral gyri, displayed lower FC with the LOC, ICC, cuneus, and fusiform cortices in DCM females as compared to HC females (**Fig. 6.2 B**). Generally, male patients demonstrated fewer but more specific alterations in FC, while female patients exhibited more widespread and diffuse alterations when compared to healthy counterparts.

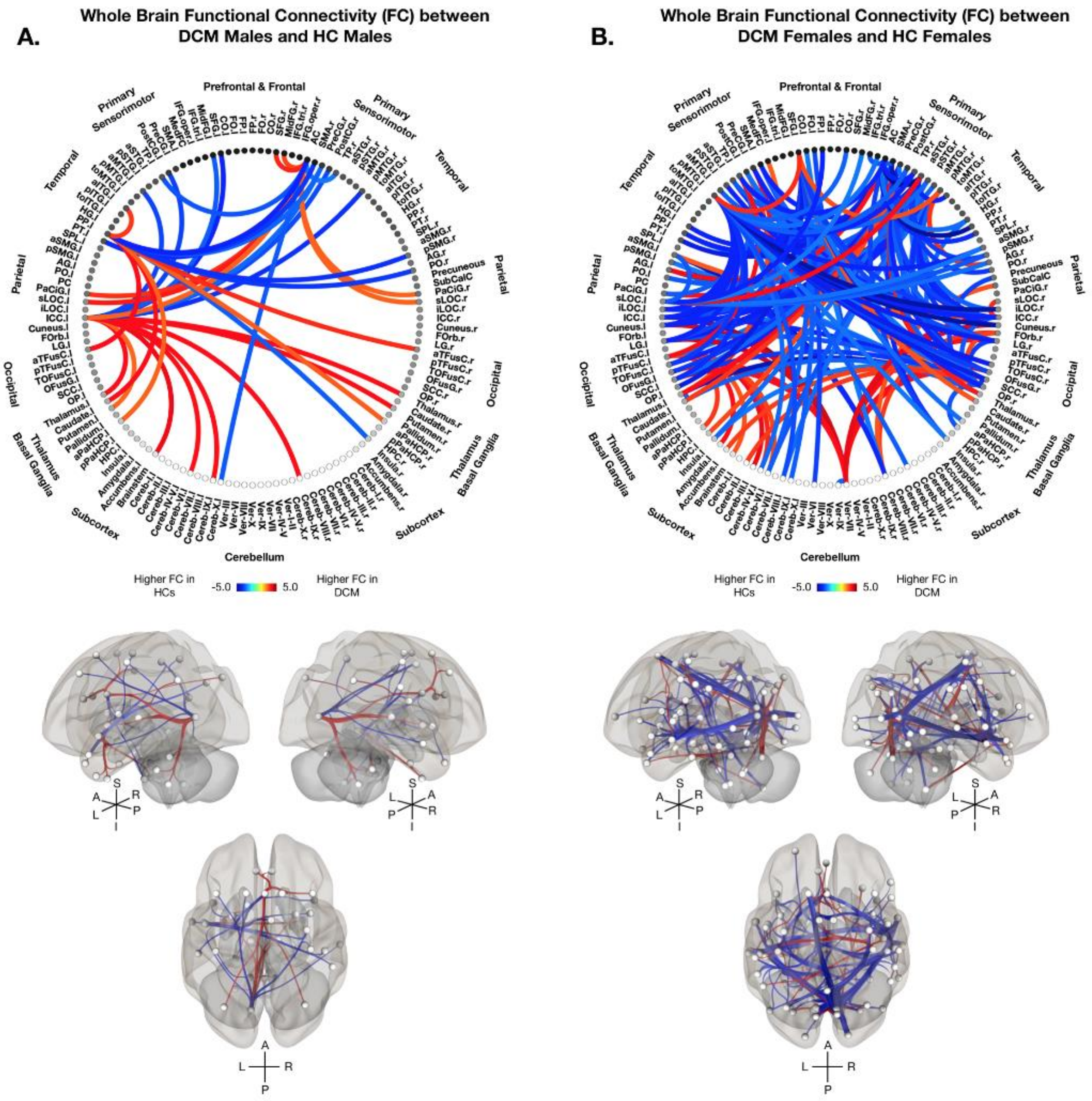

Figure 6.2: Sex-specific whole-brain functional connectivity (FC) analysis in DCM vs HCs.

Sex-specific whole brain functional connectivity (FC) analysis using 132 Harvard-Oxford Automated Anatomical Labeling (AAL) atlas defined ROIs between **(A)** DCM males and HC males, and **(B)** DCM females and HC females after regressing out the effects of age and body mass index (BMI). **(A-B, top)** Colors on the functional connectome diagrams denotes the value of T-statistic in which red-orange color denotes higher FC in DCM patients compared to HCs, while blue-light blue denotes higher FC in HCs compared to DCM patients. ROIs are labeled with l = left hemisphere and r = right hemisphere. **(A-B,**

bottom) Left, right, and superiors views of a 3D brain rendering illustrating significant ROIs as spheres and significant differences in FC between the ROIs as lines with red denoting higher FC in DCM patients compared to HCs and blue denoting higher FC in HCs compared to DCM patients. Lighter spheres represent more superficial ROIs relative to the viewer, while darker sphere represent ROIs deeper within the brain. Significant connections between ROIs were determined by thresholding based on an FDR-corrected p-value < 0.05.

In addition to whole-brain connectivity analyses, seeds of interest ROI-to-ROI analyses were performed to provide a more refined investigation of sex-specific FC differences in DCM. When comparing DCM males and HC males, higher FC in male patients was observed primarily between cerebellar hemispheres, thalamic and visual regions (**Fig. 6.3 A**). DCM males displayed higher FC between bilateral ICC and cerebellar regions, the thalamus, the putamen, and the brainstem (**Fig. 6.3 A**). DCM males displayed lower FC between the intracalarine cortices and the pre- and post- central gyri, as well as between visual regions and frontal regions (**Fig. 6.3 A**). In contrast, DCM females displayed higher FC between the thalamus and bilateral sensorimotor regions, as well as between the cerebellar vermis and bilateral ICC when compared to HC females (**Fig. 6.3 B**). Additionally, DCM females demonstrated lower FC between the ICC and sensorimotor regions including the pre- and post- central gyri and SMA, as well as between visual, motor, and frontal regions (**Fig. 6.3 B**).

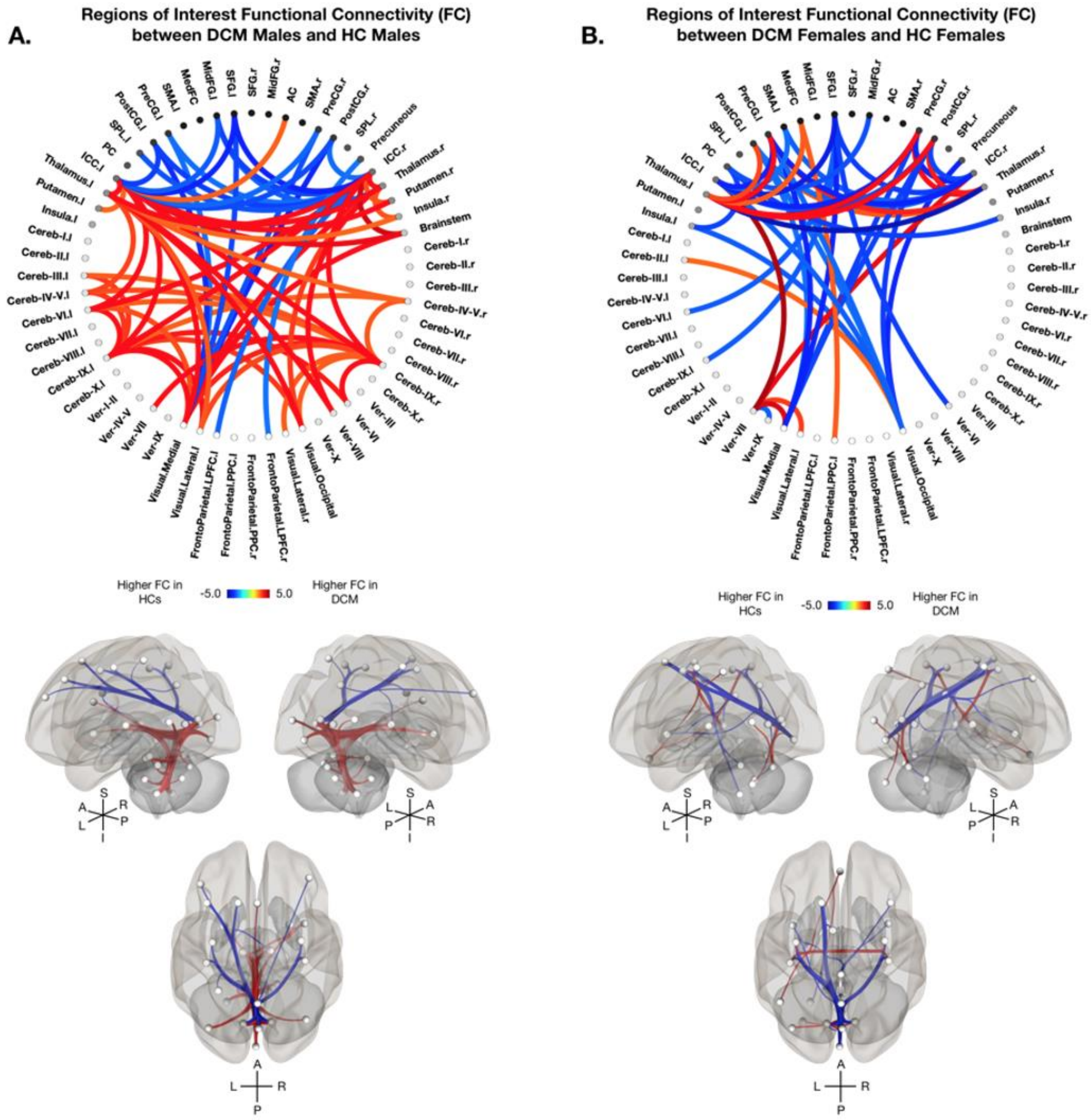

Figure 6.3: Sex-specific regions of interest functional connectivity (FC) analysis in DCM vs HCs.

Sex-specific regions of interest functional connectivity (FC) analysis using 59 AAL atlas defined ROIs between **(A)** DCM males and HC males, and **(B)** DCM females and HC females after regressing out the effects of age and body mass index (BMI). **(A-B, top)** Colors on the functional connectome diagrams denotes the value of T-statistic in which red-orange color denotes higher FC in DCM patients compared to HCs, while blue-light blue denotes higher FC in HCs compared to DCM patients. ROIs are labeled with l

= left hemisphere and r = right hemisphere. **(A-B, bottom)** Left, right, and superiors views of a 3D brain rendering illustrating significant ROIs as spheres and significant differences in FC between the ROIs as lines with red denoting higher FC in DCM patients compared to HCs and blue denoting higher FC in HCs compared to DCM patients. Lighter spheres represent more superficial ROIs relative to the viewer, while darker sphere represent ROIs deeper within the brain. Significant connections between ROIs were determined by thresholding based on an FDR-corrected p-value < 0.05.

Whole-brain FC analyses revealed DCM males experience higher FC primarily within the cerebellum, between cerebellar and parietal/occipital regions compared to DCM females (**Fig. 6.4 A**). DCM males also displayed higher FC between the posterior cingulate cortex and frontal, parietal, temporal, and cerebellar regions (**Fig. 6.4 A**). DCM females demonstrated higher FC between sensorimotor regions and the thalamus and cerebellum compared to DCM males (**Fig. 6.4 A**). Furthermore, seeds of interest analyses demonstrated significant sex-dependent differences in FC in DCM, in which higher FC was observed within the cerebellum and between cerebellar regions and the thalamus and brainstem in DCM males compared to DCM females (**Fig. 6.4 B**). DCM males also observed higher FC compared to DCM females between the posterior cingulate cortex and the ICC, the cerebellum, and visual regions **(Fig. 6.4 B**). Whereas DCM females exhibited higher FC between fronto-parietal regions and the posterior cingulate cortex, cerebellum, and visual regions (**Fig. 6.4 B**). Additionally, DCM females displayed higher FC between cerebellar and sensorimotor and frontal regions compared to DCM males (**Fig. 6.4 B**).

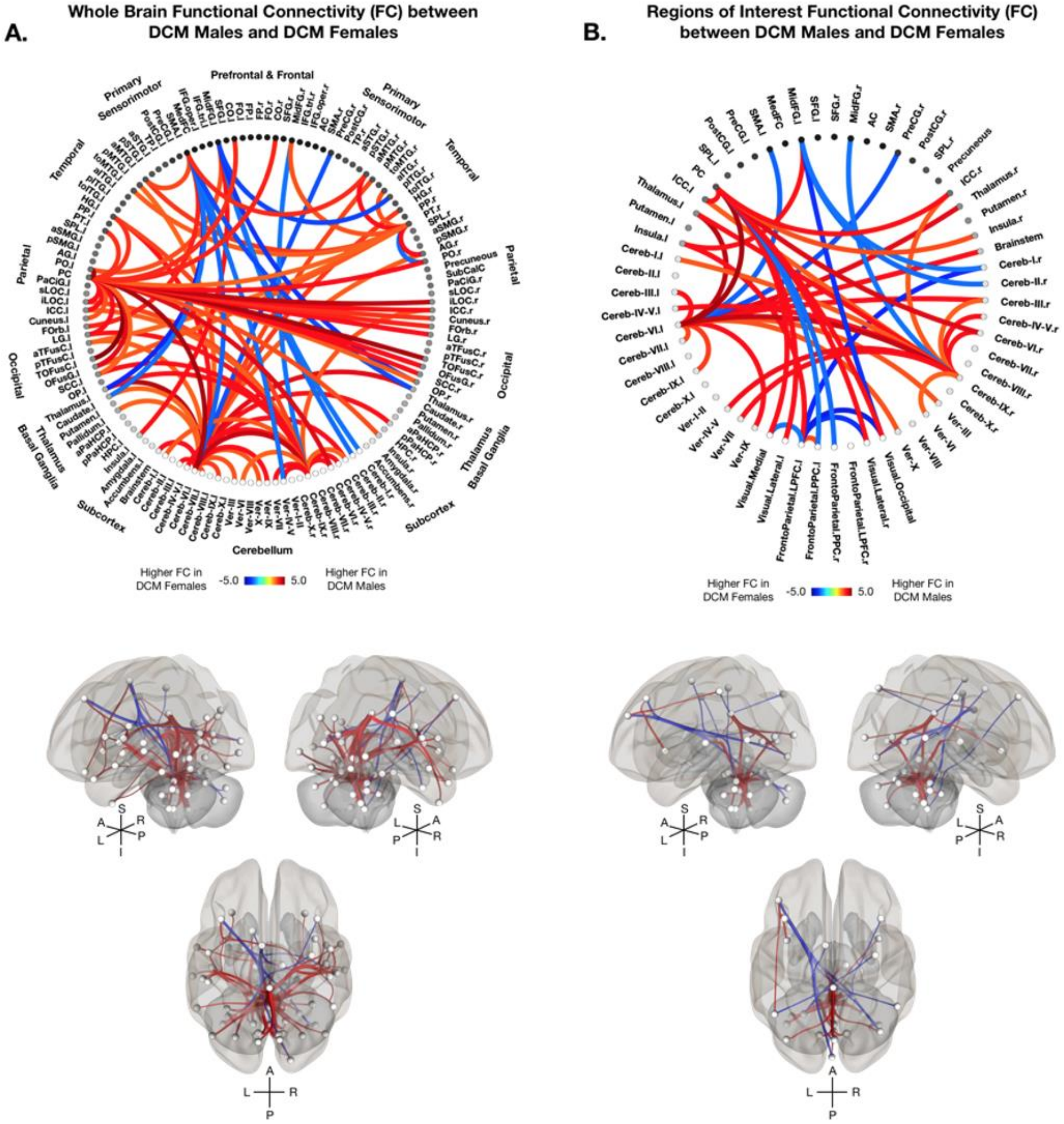

Figure 6.4: Functional connectivity (FC) analysis in DCM males vs females.

(A) Sex-specific whole brain functional connectivity (FC) analysis using 132 Harvard-Oxford Automated Anatomical Labeling (AAL) atlas defined ROIs between DCM males and DCM females after regressing out the effects of age and body mass index (BMI). **(B)** Regions of interest functional connectivity (FC) analysis using 59 AAL atlas defined ROIs between male and female DCM patients after regressing out the effects of age and body mass index (BMI). **(A-B, top)** Colors on the functional connectome diagrams denotes the value of T-statistic in which red-orange color denotes higher FC in DCM males compared to DCM females, while blue-light blue denotes higher FC in DCM females compared to DCM males. ROIs are labeled with l = left hemisphere and r = right hemisphere. **(A-B, bottom)** Left, right, and superiors views of a 3D brain rendering illustrating significant ROIs as spheres and significant differences in FC between the ROIs as lines with red denoting higher FC in DCM males compared to DCM females and blue denoting higher FC in DCM females compared to DCM males. Lighter spheres represent more superficial ROIs relative to the viewer, while darker sphere represent ROIs deeper within the brain. Significant connections between ROIs were determined by thresholding based on an FDR-corrected p-value < 0.05.

6.3.4 Network Characterization

Graph-theory based network analyses of rs-fMRI signals were employed to investigate sex-specific differences in global network topology. The clustering coefficient, path length, and small-world index were calculated for each subject based on their respective functional connectivity matrix. As illustrated in **Figure 6.5**, the clustering coefficient reflects general network connectivity (i.e., higher clustering coefficient, more connected network) and the path length represents efficiency of information transfer through the network (i.e., low path length, more efficient network). No statistically significant difference in area under the curve (AUC) for subjects' clustering coefficient, characteristic path length, and small-world index were observed between the HC males and HC females, nor between DCM males and DCM females (**Fig. 6.6**). However, DCM males exhibited significantly higher clustering coefficient AUC (**Fig. 6.6 A**, $P = 0.0363$), lower characteristic path length AUC (**Fig. 6.6 B**, $P = 0.0080$), and lower small-world index AUC (**Fig. 6.6 C**, $P = 0.0317$) than HC males. No significant difference was observed in AUC between DCM females and HC females.

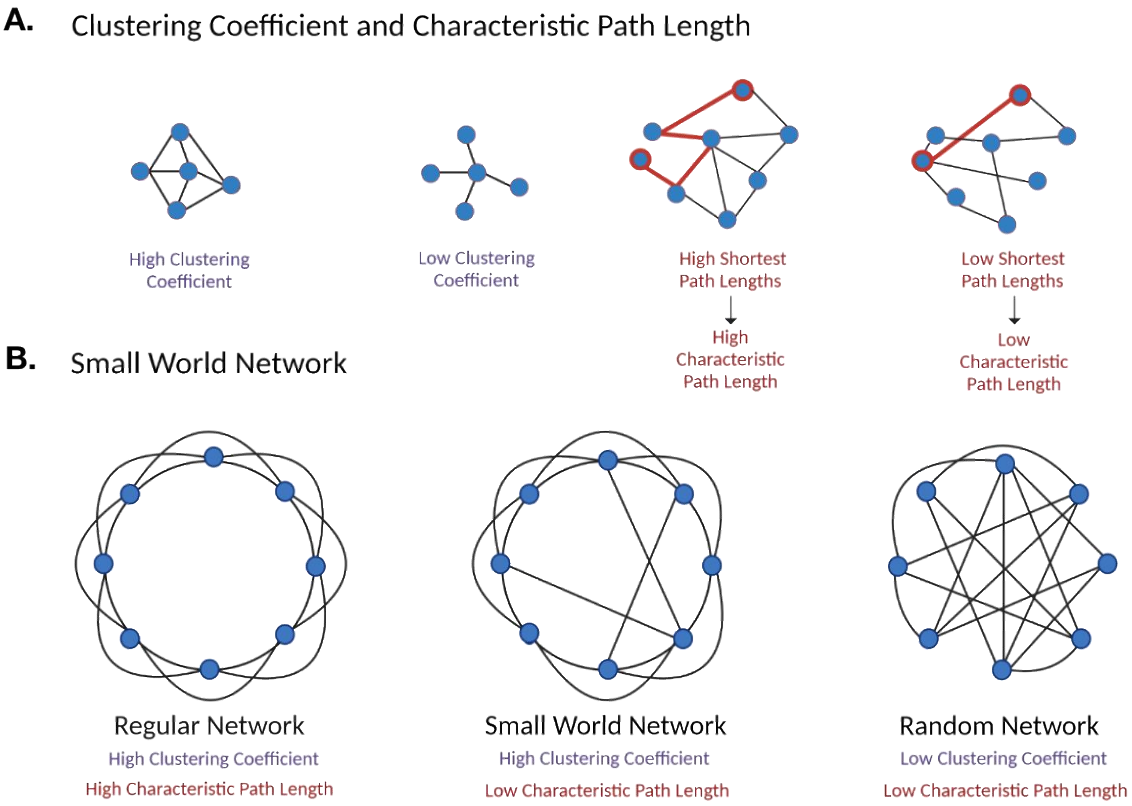

Figure 6.5: Illustration of network measurements and characterizations.

(A) The clustering coefficient value measures the degree to which nodes in a network are clustered through their connectivity, or how well-connected a group of nodes are to one another **(left)**. The characteristic path length is a measure of the average shortest path length between all pairs of nodes in a network **(right)**. **(B)** A regular network possesses an ordered pattern of connectivity, resulting in a high clustering coefficient and high characteristic path length **(left)**. A random network possesses an unordered, random pattern of connectivity, resulting in a low clustering coefficient and low characteristic path length **(right)**. A small world network possesses an intermediate degree of regularity and randomness in its connectivity, resulting in a high clustering coefficient and low characteristic path length **(middle)**.

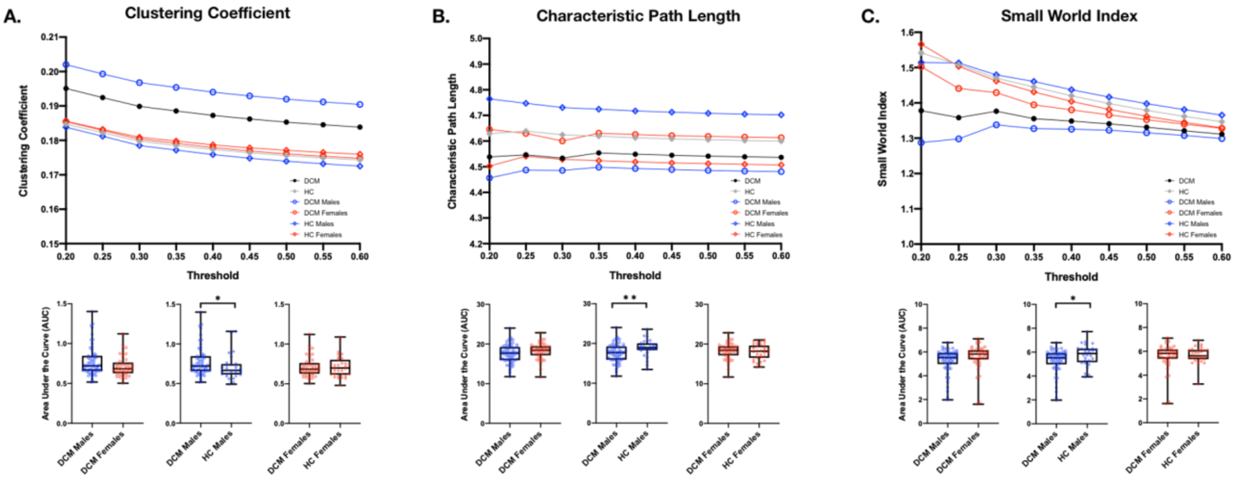

Figure 6.6: Graph theory-based network properties in DCM and HCs.

Graph theory-based network measurements, including **(A)** global clustering coefficient, **(B)** characteristic path length, and **(C)** small-world index are plotted for each network threshold ranging from 0.2 to 0.6 for the DCM cohort (black circle), HC cohort (gray diamond), DCM males (blue circle), DCM females (red circle), HC males (blue diamond), and HC females (red diamond) (top row). The area under the curve (AUC) for each subject's **(A)** global clustering coefficient, **(B)** characteristic path length, and **(C)** small-world index are plotted and compared between the following cohorts, 1) DCM males and DCM females, 2) DCM males and HC males, and 3) DCM females and HC females (bottom row). "*" and "**" refer to statistically significant difference in network measurement between cohorts of ($P < 0.05$) and ($P < 0.01$).

6.4 Discussion

Using resting-state fMRI and graph-theory based network characterization, the present study demonstrated significant sex-specific alterations in FC in patients with DCM compared with age-matched HCs. Female DCM patients exhibited more widespread, yet subtle changes in FC, whereas male DCM patients exhibited more defined alterations within few and specific pathways. Additionally, the current study investigated FC network-based properties between patients with DCM and HCs in addition to sex-dependent differences finding that male DCM patients showed greater overall informational network connectivity compared to healthy males indicating sex-specific differences in functional connectivity, global integration, and global segregation of whole-brain networks in DCM.

Findings from whole-brain and seed-based ROI-to-ROI FC analyses between DCM patients and HCs were consistent with the present literature, including patients exhibiting higher FC between and within visual and cerebellar regions [99,174], higher FC between the thalamus and cerebellum [169], lower FC between frontal and visual regions [175], lower FC between sensorimotor and thalamic [176], and lower FC between subcortical and frontal regions [73] compared to HCs. However, few studies have implemented graph-theory based investigation of network differences in DCM patients have found DCM patients exhibit less optimal small-world properties (i.e., high clustering coefficient and low characteristic path length) compared to HCs [63,177].

By modeling the brain as a complex network, graph-theory based topological analyses characterize global network structure, efficiency, and functional integration and segregation [172]. This method has been employed in previous studies to investigate the influence of sex on healthy brain connectivity, as well as the influence of various brain disorders [178-181]. In the present study, the global clustering coefficient, characteristic path length, and small-world index were quantified from functional connectivity matrices to characterize network interconnectivity, efficiency of information transfer, and overall network organization, respectively. Interestingly, DCM males and HC males exhibited significant differences in clustering coefficient, characteristic path length, and small-world index implying that potential disease-specific changes may be concealed when not accounting for the influence of sex.

Additionally, no significant difference in small-world index nor clustering coefficient were observed between healthy males and females. However, previous studies with large healthy cohorts of young adults have reported higher network connectivity (i.e., clustering coefficient) in healthy females compared to males, a trend also observed in the present study but likely due to differences in cohort age and size was not statistically significant [179,182,183]. Healthy females also demonstrated overall shorter path lengths, thus exhibiting more efficient networks than healthy males. Interestingly, DCM males and females demonstrated the opposite trends in functional integration and segregation. While male HCs tend to exhibit lower connectivity (i.e., low clustering coefficient and high characteristic path length) compared with female HCs, male DCM patients demonstrate greater intra-network connectivity and efficiency (i.e., high clustering coefficient and low characteristic path length) compared to female DCM patients, suggesting that in DCM, female brain networks are comprised of numerous weak links compared to male patients, however further analyses with a large patient cohort are necessary. When compared to healthy counterparts, DCM males exhibited greater network efficiency and connectivity indicating sex-specific topological reorganization in DCM.

ROI-to-ROI functional connectivity analyses complemented topological network findings and suggest that male DCM patients exhibited more targeted and segregated FC network alterations, while female DCM patients experience more subtle and diffuse FC alterations in response to chronic spinal cord compression. Overall, both male and female DCM patients exhibited higher FC between intracalcarine cortices (ICC) and cerebellar brain regions, lower FC between the ICC and sensorimotor and frontal regions, and lower FC between the left SFG and bilateral ICC compared to healthy participants. In contrast, only DCM males displayed higher FC between the ICC and brainstem. The intracalcarine cortex (ICC) is part of the primary visual cortex and has been shown to be active during visuospatial sequence learning [184], a function that may be important for correction of motor related symptoms caused by chronic spinal cord compression in DCM.

While male patients demonstrated higher FC between the thalamus and ICC, female patients demonstrated higher FC between the thalamus and sensorimotor cortices compared to HCs. The thalamus is an integrative brain hub that relays sensory and motor information across cortical networks [185], and previous studies have shown altered thalamocortical and cerebellar connectivity in DCM [73]. However, the present study expands on this previous work and suggests thalamocortical recruitment may be sex-specific, in which thalamus-ICC connections may be strengthened in males, while thalamus-sensorimotor connections are strengthened in females.

The current study also suggests sex-dependent differences in cerebellar involvement, in which males employ the cerebellar hemispheres, while females employ the cerebellar vermis, in functional connections to cortical visual regions. These regions are functionally distinct, with the cerebellar vermis (spinocerebellum) coordinating motor movements, and the cerebellar hemispheres (cerebrocerebellum) being involved in motor planning and timing [186]. When compared to HCs, DCM patients exhibit increased connectivity between the cerebellum and visual cortices, and that more effective connectivity between these areas was positively correlated with better visual recovery following surgical decompression [187]. We theorize visual-cerebellar plasticity and information integration in DCM may be sex-dependent and may influence visual feedback and motor compensation.

Furthermore, when comparing DCM males and females, male patients exhibited higher connectivity between the posterior cingulate cortex (PCC) and various visual regions including the ICC, while female patients exhibited higher FC between the PCC and frontoparietal regions. The PCC receives inputs from visual and somatosensory regions and has been shown to be involved in spatial processing, learning, and memory [188,189]. With recruitment of the PCC, males with DCM may rely more on visual compensation, while females with DCM may implement cortical motor planning and execution.

We suspect sex-specific structural and functional supraspinal differences in DCM, as well as the higher incidence of cervical myelopathy in males, may be driven in part by hormonal, neuroprotective, and compensatory differences following chronic spinal cord compression. Preclinical studies of spinal cord injury (SCI) have demonstrated that androgens (testosterone) and ovarian hormones (estradiol, estrogen, and progesterone) influence neuronal loss and myelination, prevent structural atrophy, attenuate neuroinflammation, and increase motor functional recovery [137-140,142,147]. Sex steroid concentration has also been shown to affect functional recovery following SCI in humans [141,157,158]. Furthermore, previous studies have demonstrated that sex steroid administration, including testosterone, estradiol, and progesterone, can induce alterations in functional connectivity of the brain [190-194]. Based on such findings, it has been theorized that androgens increase FC between subcortical regions, but decrease cortical-subcortical FC, while ovarian hormones increase cortical-cortical and cortical-subcortical FC [195]. Moreover, males and females may be utilizing different compensatory mechanisms in response to disease progression and motor-related symptoms, with females strengthening thalamo-sensorimotor connections, while males strengthen thalamo-visual and thalamo-cerebellar connections.

Although the present study was one of the first to investigate sex as a biological variable in DCM, it is important to note study limitations. The study would benefit from a larger patient population and inclusion an interaction contrast. Specifically, testing for the interaction of sex or the difference of differences (DCM [females – males] – HC [females – males]) can be utilized to determine whether sex differences in FC differed based on diagnosis. The present patient population did not have the statistical power to test for such interactions, however with larger patient samples future studies may include such investigations. measurement and assessment of serum sex hormones in relation to sex and neurological function would greatly benefit our understanding of the mechanisms underlying sexual dimorphism in DCM. Furthermore, the measurement and assessment of serum sex hormones in relation to neurological function, cerebral reorganization, and functional recovery following surgical intervention would greatly benefit our understanding of the mechanisms underlying sexual dimorphism in DCM.

The present study reveals significant sex-specific supraspinal functional reorganization in patients with DCM. Overall, male patients demonstrated more densely connected and efficient brain networks that exhibited stronger bilateral intracalcarine-thalamic, ICC-brainstem, and ICC-cerebrocerebellar connectivity, while females displayed brain networks that exhibited stronger thalamic-sensorimotor and ICC-spinocerebellar connectivity, but weaker visual-motor connectivity. Our findings provide unique insights into sex-specific cerebral responses to chronic spinal cord injury and may spark novel treatment strategies in DCM.

CHAPTER 7

Sex-Dependent Differences in Cerebral Structure and Function between Patients with Asymptomatic Spinal Cord Compression and Symptomatic Degenerative Cervical Myelopathy

7.1 Introduction

As discussed in Chapter 2, the factors separating asymptomatic spinal cord compression (ASCC) patients from those who develop chronic symptoms, as seen in DCM, remains an enigma within the field. The study discussed in Chapter 2 elucidated the differing structural and functional supraspinal alterations between the ASCC and DCM patient cohorts. In summary, DCM patients exhibited expansion of vision-related cortical regions, alongside increased visual-motor and visual-cerebellar functional connectivity, while ASCC patients demonstrated reduced visual-motor connectivity but increased visual-temporal connectivity and maintained microstructural integrity of white matter association pathways. Furthermore, the study presented in Chapter 3 found no significant relationship between spinal cord and canal compression measurements and degree of symptom severity or lack of symptom presentation. It is evident that although DCM and ASCC patients may experience similar changes within the spinal cord, including degree of stenosis or compression, they present distinctly differing degrees of functional impairment further supporting my hypothesis that these patient populations employ differing neuroprotective and compensatory mechanisms.

In addition, Chapters 5 and 6 demonstrated significant sex-specific differences in cerebral morphometry, functional connectivity, and network characteristics. In the combined symptomatic and asymptomatic cohorts, male patients exhibited expansion of motor, language, and vision related brain regions, as well as higher functional connectivity within the cerebellum and between vision-related and cingulate cortices compared to female patients. Whereas female patients exhibited greater recruitment of frontal regions, specifically displaying higher functional connectivity between frontal and cingulate, cerebellum, and visual regions. As discussed previously, DCM is more prevalent in males compared to females and as hypothesized in Chapters 5 and 6 may be driven by differing sex hormones and neuroprotective hormonal influences. Given these findings, I hypothesize DCM and ASCC patients will exhibit differing sex-specific alterations in cerebral structure and function and may further reveal disease- and sex-specific reorganization and compensatory mechanisms driving disease progression and symptom presentation in DCM.

The present exploratory study aimed to investigate sex-specific differences in cerebral morphometry, functional connectivity (FC), and white matter microstructure between symptomatic DCM and ASCC patients. Using a multimodal imaging approach, as described in Chapter 2, cerebral gray matter volume (GMV), whole-brain functional connectivity, white matter fiber density (FD), fractional anisotropy (FA), and mean diffusivity (MD) were measured and compared between the following cohorts: symptomatic DCM males and females, ASCC males and females, DCM males and HC males, ASCC males and HC males, DCM females and HC females, and ASCC females and HC females. Based on our previous findings, I hypothesize that symptomatic DCM patients will exhibit greater vision-related recruitment with DCM males experiencing functional and microstructural recruitment of visuo-cerebellar connectivity, while DCM female will employ greater visuo-motor and visuo-spatial recruitment. I hypothesize the ASCC patients will display greater frontal and temporal cerebral involvement, in which ASCC males will exhibit strengthening of fronto-cerebellar functional and structural pathways, while ASCC females will experience strengthening of fronto-visual pathways. To the best of our knowledge this is the first study to investigate sex-specific differences in symptomatic DCM and ASCC patients exclusively.

7.2 Materials and Methods

7.2.1 Patient Population

A total of 102 patients were prospectively enrolled from 2015 to 2022 in a cross-sectional study including brain and spinal cord imaging as well as a neurological examination. Patients were recruited from the UCLA outpatient neurosurgery clinic and exhibited spinal cord compression with evidence of spinal cord deformation, mass effect, and no visible cerebrospinal fluid signal around the spinal cord at the site of maximal compression on MRI. Patients included in this study had not undergone surgical intervention for cervical spinal cord compression at the time of brain imaging. All patients signed Institutional Review Board-approved consent forms, and all analyses were performed in compliance with the Health Insurance Portability and Accountability Act (HIPAA). The modified Japanese Orthopedic Association (mJOA) score was used as a measure of neurological function [80]. The mJOA scoring scale ranges from 0 to 18, where lower scores represent a worse neurological impairment and an mJOA score of 18 represents no impairment of neurological function. Patients with an mJOA score of 18 were categorized as ASCC, while patients with an mJOA between 17 and 0 were categorized as symptomatic DCM. The patient cohort consisted of 67 symptomatic and 35 asymptomatic patients. The symptomatic cohort consisted of 46 males and 21 females with ranging in age from 37 to 81 years with a mean age of 57.7 years with a standard deviation of 10.2 years. The ASCC cohort consisted of 19 males and 16 females with ranging in age from 31 to 80 years with a mean age of 58.6 years with a standard deviation of 13.3 years. All patients underwent brain and spinal cord imaging at UCLA. All 102 patients underwent anatomical and resting-state fMRI imaging of the brain, while 48 symptomatic DCM patients and 23 ASCC patients also underwent diffusion-weighted brain imaging. Patient demographic data was summarized in **Table 7.1**.

	Number of Subject (Male/Female)	**Age** (Median ± SD) [min, max]	**mJOA** (Median ± SD) [min, max]
Symptomatic DCM Patients (T1, fMRI)	**67** (46/21)	(57.7 ± 10.2) [37, 81] p = 0.8536	(14.6 ± 2.3) [10, 17] p = 0.5137
DCM DTI Sub-cohort	**48** (31/17)	(57.9 ± 9.8) [37, 87] p = 0.8267	(14.3 ± 2.3) [10, 17] p = 0.3708
ASCC Patients (T1, fMRI)	**35** (19/16)	(58.6 ± 13.3) [31, 80] p = 0.3451	18
ASCC DTI Sub-cohort	**23** (11/12)	(57.7 ± 12.4) [31, 75] p = 0.4215	18

Table 7.1: Patient demographics.

Age is provided in mean years ± the standard deviation, minimum and maximum years, and the p-value of Wilcoxon-Mann-Whitney test between age of males and females. The modified Japanese Orthopedic Association (mJOA) score is provided in mean score ± the standard deviation, minimum and maximum scores, and the p-value of Wilcoxon-Mann-Whitney test between scores of males and females.

7.2.2 Healthy Control Population

For cortical morphometry and functional connectivity analyses 59 age-matched healthy control (HC) volunteers were included from the UCLA Center for Neurobiology of Stress and Resilience (CNSR). The HC cohort consisted of 28 males and 31 females ranging in age from 45 to 73 years with a mean age of 49.9 years with a standard deviation of 4.2 years. Exclusion criteria implemented by the CNSR investigators consisted of 1) significant neurological or psychiatric disorder, 2) chronic gastrointestinal disorder, 3) chronic pain disorder, 4) active autoimmune or infectious disorder, 5) history of cancer, and 6) women who are pregnant or planning to become pregnant at time of study. Due to the above exclusion criteria, the healthy control subjects included in this study were categorized as neurologically asymptotic and assigned a mJOA score of 18. All healthy controls underwent anatomical and resting-state functional brain imaging at UCLA. Of the 59 HCs, 17 subjects underwent diffusion-weighted brain imaging at UCLA. Healthy participant demographic data was summarized in **Table 7.2**.

	Number of Subject (Male/Female)	**Age** (Median ± SD) [min, max]
Healthy Controls (T1, fMRI)	**59** (28/31)	(49.9 ± 4.2) [45, 73] *p* = 0.5278
DTI Sub-cohort	**17** (13/4)	(53.3 ± 8.2) [44, 73] *p* = 0.3618

Table 7.2: Healthy control demographics.

Age is provided in mean years ± the standard deviation, minimum and maximum years, and the p-value of Wilcoxon-Mann-Whitney test between age of males and females. Healthy controls were categorized with an mJOA score of 18 due to their healthy neurological status.

7.2.3 MR Imaging Acquisition, Processing, and Statistical Analysis

Note: The MR imaging acquisition and processing for this study was the same as described in Chapter 2.

Structural Magnetic Resonance Imaging

High-resolution 1 mm isotropic 3-dimensional (3D) T1-weighted structural MRIs of the brain were acquired on a 3T MR scanner (Siemens Prisma or Trio; Siemens Healthcare, Erlangen, Germany) using a 3D magnetization-prepared rapid gradient-echo (MPRAGE) sequence in either the coronal, sagittal, or axial orientation, with a repetition time (TR) of 2300 to 2500 ms, a minimum echo time (TE) between 2 to 3 ms, an inversion time (TI) of 900 to 945 ms, a flip angle of 9^o to 20^o, slice thickness of 1 mm with no interslice gap, and field of view (FOV) of 240 x 320 mm and matrix size of 240 x 320 (in the patient cohort) or FOV of 220 x 220 mm and matrix size of 256 x 256 (in the healthy cohort).

Cortical parcellation and computation of gray matter volume of the brain were conducted using the FreeSurfer software package (https://surfer.nmr.mgh.harvard.edu/fswiki) on the T1-weighted images described above [81]. Brain surfaces were preprocessed, smoothed with a full-width half-maximum of 10 mm, and registered to the standard space as defined by Desikan-Killiany-Tourville

(DKT) atlas [82]. Whole-brain cortical volume analysis was completed using FreeSurfer. A general linear model (GLM) was used to determine vertex-level significant differences in GMV between the following groups: 1) symptomatic DCM males and symptomatic DCM females, 2) ASCC DCM males and ASCC DCM females, 3) symptomatic DCM males and HC males, 4) ASCC DCM males and HC males, 5) symptomatic DCM females and HC females, and 6) ASCC DCM females and HC females. To control for the influence of age on GMV, age was included as covariates in morphometric analyses. The vertex-wise level of significance was set at $p < 0.05$, with multiple comparisons correction performed using Monte Carlo permutations with a significance level of $p < 0.05$.

Resting-state Functional Magnetic Resonance Imaging (rs-fMRI)

To assess functional connectivity, resting state functional MRIs were acquired on a 3T MR scanner (Siemens Prisma; Siemens Healthcare, Erlangen, Germany) with a TR of 1500 to 2200 ms, TE of 28 to 30 ms, flip angle of 77^o, FOV of 220 to 245 mm with an acquisition matrix of 64 x 64 for an in-plane resolution of 3.4 to 3.8 mm, interleaved acquisition, slice thickness of 4 mm with no interslice gap, parallel imaging via CAIPIRNHA with a factor of 2, and multi-band acceleration with a factor of 2.

Functional MR images were processed using the CONN toolbox (https://www.nitrc.org/projects/conn) [85], which utilizes functions from the Statistic Parametric Mapping (SPM) toolbox (http://www.fil.ion.ucl.ac.uk/spm/). Functional and structural images were processed using the standard built-in preprocessing pipeline provided in the CONN toolbox. The default pipeline performs the following steps: 1) realignment of functional images including motion correction based on 12 degrees of freedom and unwarping, 2) slice-timing correction to correct for difference in acquisition time between slices, 3) registration of functional images to structural images, 4) registration of structural images to the Montreal Neurological Institute (MNI) defined standardized space, 5) removal of signal intensity spikes and functional volumes with excessive motion (threshold set at 2 mm translation and 2° rotation in any direction) using the Artifacts Detection Tool (ART) from SPM, 6) segmentation and normalization of functional images based on tissue type (gray matter, white matter, and cerebrospinal fluid) in MNI space, and 7) spatial smoothing of functional data using 8 mm, full width at half maximum (FWHM) Gaussian kernel. Additionally, signals from the white matter, CSF, and motion parameters were regressed from the functional data and signal filtering was performed using a band-pass filter of 0.008–0.10 Hz to reduce noise caused by scanner drift and physiological effects (i.e., pulsation and respiration).

Functional connectivity (FC) of the brain was assessed using whole brain ROI-to-ROI (also termed seed-to-seed) analyses. Regions of interest (ROIs) were selected from the Harvard-Oxford Automated Anatomical Labeling (AAL) atlases [86]. Whole-brain ROI-to-ROI analyses used 132 cerebral ROIs. GLMs were used to evaluate significant group differences in functional connectivity between the following cohorts: 1) symptomatic DCM males and symptomatic DCM females, 2) ASCC DCM males and ASCC DCM females, 3) symptomatic DCM males and HC males, 4) ASCC DCM males and HC males, 5) symptomatic DCM females and HC females, and 6) ASCC DCM females and HC females. To control for the influence of age on FC, age was included as covariates in FC analyses. The connection-level significance was set at $p < 0.01$ uncorrected. Statistical analyses were performed using the CONN toolbox [85], MATLAB (Release 2018a, MathWorks, Natick, MA) and GraphPad Prism software (Version 7.0c GraphPad Software, San Diego, California).

Diffusion Tensor Imaging (DTI)

Diffusion-weighted images of the brain were collected using standard spin-echo echo planar imaging on a Siemens Prisma 3T MR scanner (Siemens Prisma; Siemens Healthcare, Erlangen, Germany) with a TR of 9500 to 11400 ms, TE of 82 to 88 ms, flip angle of 90^o, FOV of 256 by 256 mm with an acquisition matrix of 128 by 128 for voxel size of 2 mm x 2 mm x 2 mm. Diffusion weighting was distributed along 65 directions using b values of 0 s/mm^2 and 1000 s/mm^2. Subject space data was resampled to 1 mm isotropic resolution for analyses in standard MNI space.

The following steps were used to preprocess diffusion weighted images: 1) image denoising using the MRtrix3 software package (Brain Research Institute, Melbourne, Australia, http://www.brain.org.au/software/mrtrix) [90], 2) eddy current and motion correction using the FMRIB's Diffusion Toolbox (FDT) (www.fmrib.ox.ac.uk/fsl), 3) b zero image registration (registration to subject's first non-diffusion weighed images), and 4) skull extraction using the Brain Extraction Tool (BET) from FSL. The MRtrix3 software was then used to perform fixel-based analysis via probabilistic tractography by seeding 10 million random voxels throughout the brain and counting the number of fiber tracts passing through each voxel resulting in fiber density (FD) maps for each subject. Fractional anisotropy (FA) and mean diffusivity (MD) values were calculated from the diffusion tensor and registered to the Johns Hopkins University DTI atlas (ICBM-DTI-81 1mm FA atlas) using the linear (FLIRT) and nonlinear (FNIRT) commands in FSL. The AFNI (Analysis of Functional NeuroImages) software and *3dttest++* and *3dClustSim* commands were used to implement a GLM to evaluate voxel-wise differences in FD, FA, and MD between cohorts while accounting subject age. Cluster significance was set at $p < 0.05$ (two-sided) with a false discovery rate (FDR) < 0.05.

7.3 Results

7.3.1 Subject Characteristics

As summarized in **Table 7.1**, the symptomatic DCM patient cohort consisted of 67 patients, 46 males and 21 females, with a mean age of 57.7 ± 10.2 years and mean mJOA score of 14.6 ± 2.3. Of the 67 symptomatic patients, 9 patients were categorized with severe myelopathy (mJOA ≤ 11), 19 patients exhibited moderate myelopathy ($12 \leq$ mJOA ≤ 14), and 39 patients presented with mild myelopathy ($15 \leq$ mJOA ≤ 17) at the time of the brain scan. A sub-cohort of patients was included for diffusion-based analyses. The sub-cohort of symptomatic DCM with diffusion-weighted imaging consisted of 48 patients, 31 males and 17 females, with a mean age of 57.9 ± 9.8 years and mean mJOA score of 14.3 ± 2.3. No significant difference in age or mJOA score was observed between the entire cohort of symptomatic male and female patients (Wilcoxon-Mann-Whitney test, age: $p = 0.8536$, mJOA: $p = 0.5137$) nor between the DTI sub-cohort of symptomatic male and female patients (Wilcoxon-Mann-Whitney test, age: $p = 0.8267$, mJOA: $p = 0.3708$).

The ASCC cohort consisted of 35 patients, 19 males and 16 females, with a mean age of 58.6 ± 13.3 years. The sub-cohort of ASCC patients with diffusion-weighted imaging consisted of 23 patients, 11 males and 12 females, with a mean age of 57.7 ± 12.4 years. No significant difference in age was observed between the entire cohort of ASCC male and female patients (Wilcoxon-Mann-Whitney test, age: $p = 0.3451$) nor between the DTI sub-cohort of ASCC male and female patients (Wilcoxon-Mann-Whitney test, age: $p = 0.4215$).

The HC cohort consisted of 59 subjects, 28 males and 31 females with a mean age of 49.9 ± 4.2 years. The sub-cohort of HCs with diffusion-weighted imaging consisted of 17 subjects, 13 males and 4 females, with a mean age of 53.3 ± 8.2 years. No significant difference in age was observed between the entire cohort of HC males and females (Wilcoxon-Mann-Whitney test, age:

$p = 0.3451$) nor between the DTI sub-cohort of HC males and females (Wilcoxon-Mann-Whitney test, age: $p = 0.4215$).

7.3.2 Sex-specific Differences in Cortical Morphometry

Results from whole-brain cortical volume analysis revealed significant sex-specific differences in gray matter volume (GMV) among DCM and ASCC patient cohorts. Specifically, symptomatic DCM males exhibited larger GMV in the left lateral occipital cortex compared to symptomatic DCM females (**Fig. 7.1 A**). When comparing cortical volume between ASCC males and females, ASCC males exhibited significantly larger GMV in the right precentral gyrus, bilateral postcentral gyri, and right superior frontal gyrus (**Fig. 7.1 B**). In addition, ASCC males demonstrated larger GMV in the bilateral lingual gyrus, the bilateral inferior parietal lobule, left insula, and right superior temporal gyrus compared to ASCC females (**Fig. 7.1 B**).

When comparing GMV between males, significant differences were observed between symptomatic DCM males and HC males, as well as between ASCC males and HC males. Symptomatic DCM males demonstrated significantly smaller GMV in the right superior frontal gyrus compared to healthy males (**Fig. 7.1 C**). Whereas ASCC males exhibited significantly smaller GMV in the bilateral middle temporal gyrus and right rostral middle frontal gyrus compared to healthy males (**Fig. 7.1 D**). When comparing ASCC females with healthy females, ASCC females demonstrated significantly smaller GMV in the left superior frontal gyrus, left inferior parietal lobule, left precentral gyrus, right postcentral gyrus, and right superior temporal gyrus frontal (**Fig. 7.1 E**). No significant differences in GMV were observed between DCM females and healthy female cohorts.

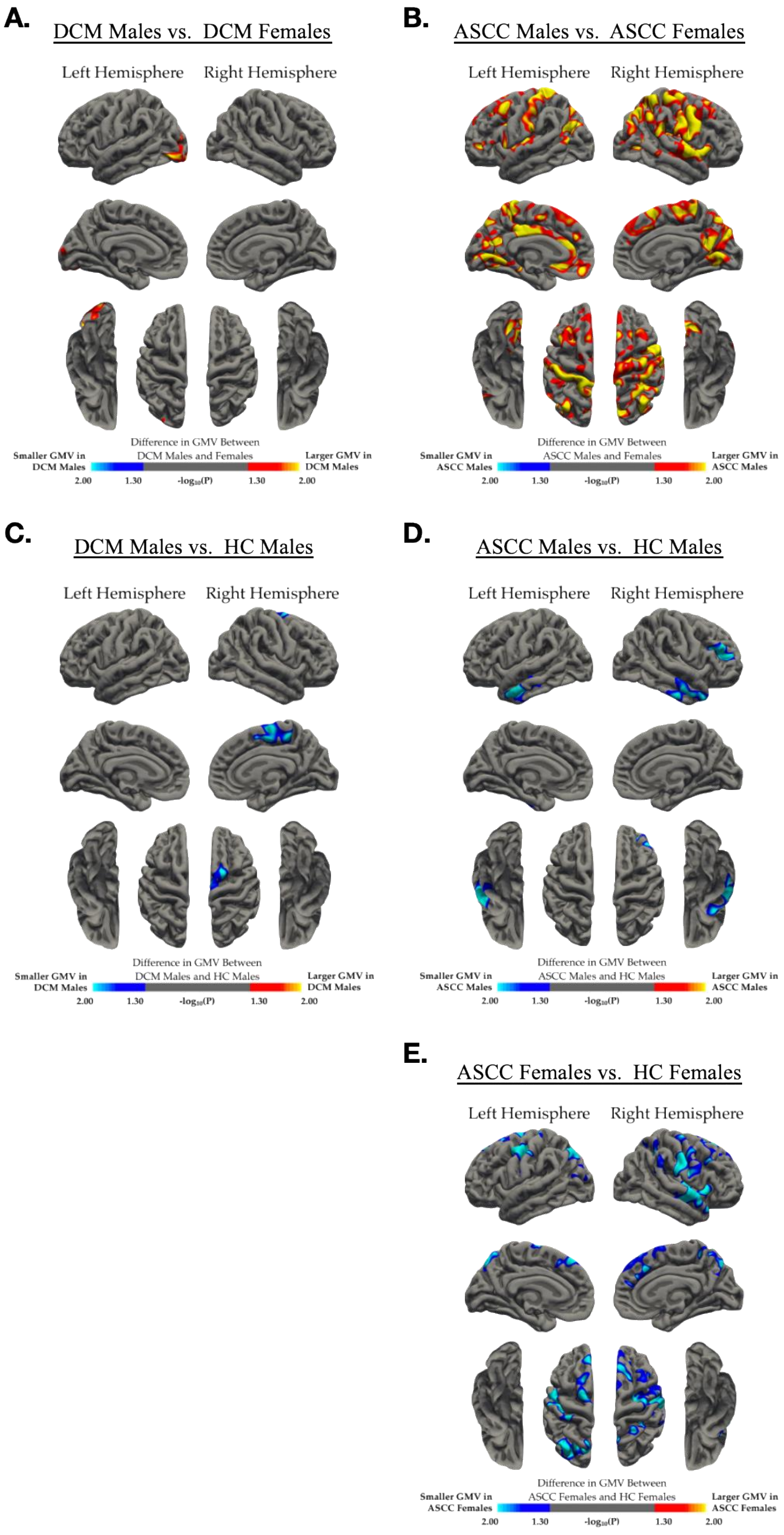
A.
DCM Males vs. DCM Females
Left Hemisphere
Right Hemisphere
Difference in GMV Between DCM Males and Females
Smaller GMV in DCM Males
Larger GMV in DCM Males
2.00
1.30
-log10(P)
1.30
2.00
B.
ASCC Males vs. ASCC Females
Left Hemisphere
Right Hemisphere
Difference in GMV Between ASCC Males and Females
Smaller GMV in ASCC Males
Larger GMV in ASCC Males
2.00
1.30
-log10(P)
1.30
2.00
C.
DCM Males vs. HC Males
Left Hemisphere
Right Hemisphere
Difference in GMV Between DCM Males and HC Males
Smaller GMV in DCM Males
Larger GMV in DCM Males
2.00
1.30
-log10(P)
1.30
2.00
D.
ASCC Males vs. HC Males
Left Hemisphere
Right Hemisphere
Difference in GMV Between ASCC Males and HC Males
Smaller GMV in ASCC Males
Larger GMV in ASCC Males
2.00
1.30
-log10(P)
1.30
2.00
E.
ASCC Females vs. HC Females
Left Hemisphere
Right Hemisphere
Difference in GMV Between ASCC Females and HC Females
Smaller GMV in ASCC Females
Larger GMV in ASCC Females
2.00
1.30
-log10(P)
1.30
2.00

Figure 7.1: Sex-specific cortical morphometry analysis between symptomatic DCM, ASCC, and HCs.

Whole-brain correlation analysis comparing gray matter volume (GMV) between males and females while regressing out the effects of age. Whole-brain GMV comparisons between (**A**) DCM males and DCM females, (**B**) ASCC males and ASCC females, (**C**) DCM males and HC males, (**D**) ASCC males and HC males, and (**E**) ASCC females and HC females. (**A,C**) Red-yellow color denotes larger GMV in DCM males, while blue-light blue color denotes smaller GMV in DCM males. (**B,D**) Red-yellow color denotes larger GMV in ASCC males, while blue-light blue color denotes smaller GMV in ASCC males. (**E**) Red-yellow color denotes larger GMV in ASCC females, while blue-light blue color denotes smaller GMV in ASCC females compared to HC females. Significant clusters were determined by thresholding based on statistical significance of $p < 0.05$.

7.3.3 Sex-specific Differences in Cerebral Functional Connectivity

To evaluate functional alterations sex differences in functional connectivity, whole-brain ROI-to-ROI functional connectivity analyses were performed between DCM males and females, as well as between ASCC males and females while accounting for the effect of subject age on FC.

Symptomatic DCM males demonstrated significantly higher FC between frontal and motor regions compared to symptomatic DCM females (**Fig. 7.2A**). In addition, DCM males displayed higher FC between the motor regions, including the left pre- and post-central gyri, and occipital regions. When compared to DCM females, DCM males exhibited decreased FC between the cerebellum and frontal, motor, and occipital regions (**Fig. 7.2A**). Furthermore, DCM males demonstrated reduced FC between the thalamus, frontal, and occipital regions.

When compared to ASCC females, ASCC males displayed widespread significant differences in FC (**Fig. 7.2B**). Largely, ASCC males demonstrated higher FC between cerebellar regions and sensorimotor, temporal, parietal, and occipital cortices compared to female counterparts (**Fig.**

7.2B). Cerebellar regions including the cerebellar area 4-5 and 6 exhibited stronger FC with superior and middle temporal gyri in ASCC males compared to females. Additionally, ASCC males displayed higher FC between the thalamus and temporal and cerebellar regions (**Fig. 7.2B**). However, ASCC males did demonstrate decreased FC between primary motor regions and the putamen, as well as between supplementary motor regions and the cerebellum compared to ASCC females (**Fig. 7.2B**).

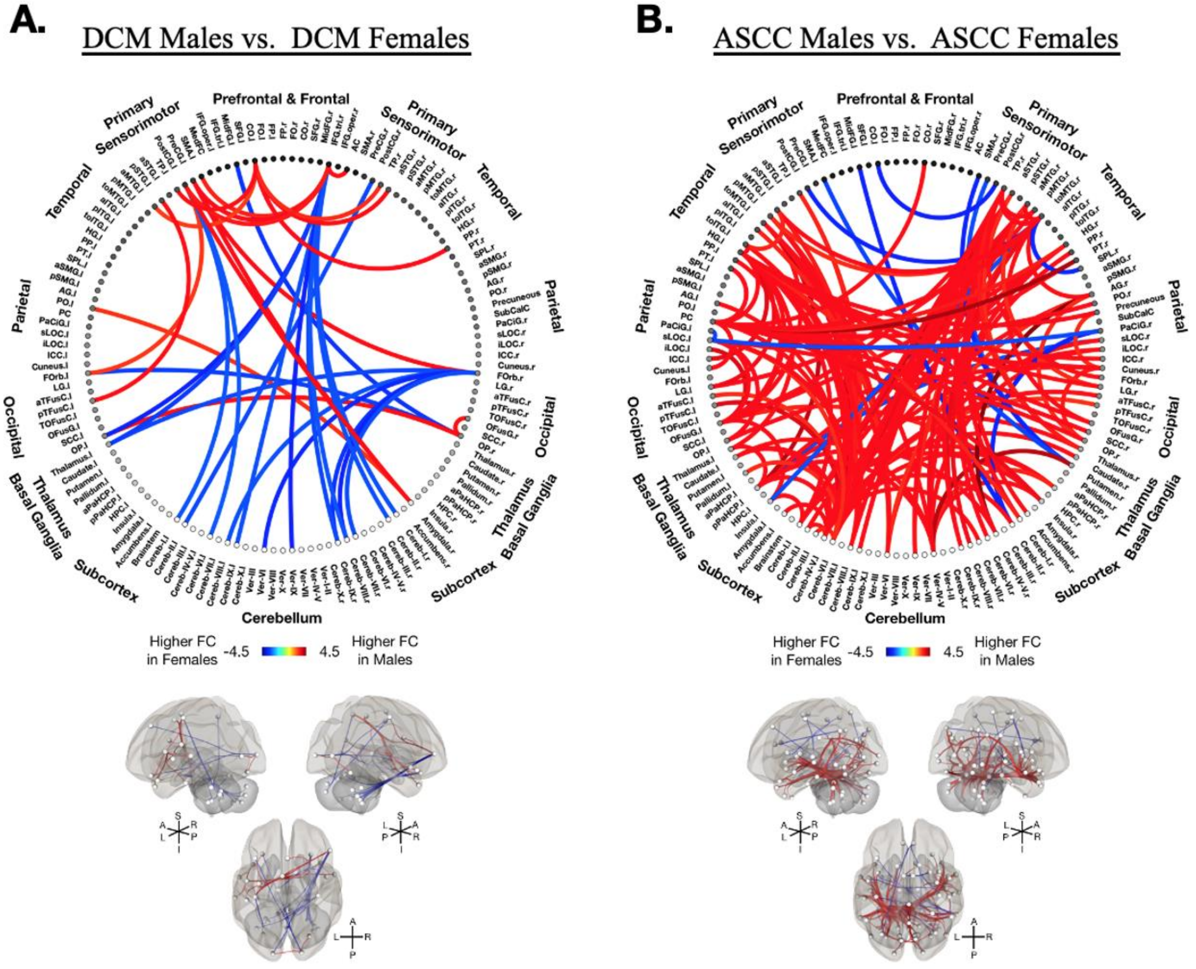

Figure 7.2: Disease-specific functional connectivity (FC) analysis between males and females.

Whole-brain functional connectivity (FC) analysis between males and females while regressing out the effects of age. **(A,B)** ROI-to-ROI functional connectome diagrams using 132 Harvard-Oxford Automated

Anatomical Labeling (AAL) atlas defined ROIs. **(Top)** Colors on the connectome denote the value of the T-statistic in which red-orange color denotes higher FC in **(A)** DCM or **(B)** ASCC males compared to **(A)** DCM or **(B)** ASCC females, while blue-light blue denotes higher FC in females compared to males. ROIs are labeled with l = left hemisphere and r = right hemisphere. **(Bottom)** Left, right, and superiors views of a 3D brain rendering illustrating significant ROIs as spheres and significant differences in FC between the ROIs as lines with red denoting higher FC in **(A)** DCM or **(B)** ASCC compared to **(A)** DCM or **(B)** ASCC females and blue denoting higher FC in females compared to males. Lighter spheres represent more superficial ROIs relative to the viewer, while darker sphere represent ROIs deeper within the brain. Significant connection-level threshold was set at p-value < 0.01 uncorrected.

In the male cohort, DCM males demonstrated widespread alterations in whole-brain functional connectivity compared to HC males. Generally, DCM males exhibited higher FC within the cerebellum and between cerebellar and occipital regions (**Fig. 7.3A**). Higher FC was also observed between the brainstem and vision-related regions including the bilateral intracalarine cortex (ICC) and lateral occipital cortex (LOC) in DCM males compared to healthy males (**Fig. 7.3A**). DCM males also displayed lower FC between vision related regions, including the ICC and LOC, and primary sensorimotor and frontal regions compared to HC males (**Fig. 7.3A**).

Similarly, ASCC males exhibited altered FC throughout the brain compared to HCs albeit more widespread. Particularly, ASCC males demonstrated higher FC within the cerebellum and between the cerebellum and motor, temporal, and occipital regions compared to healthy males (**Fig. 7.3B**). In addition, ASCC males displayed higher FC between thalamic regions and motor, parietal, and occipital regions compared to healthy males (**Fig. 7.3B**). In contrast, ASCC males demonstrated lower FC than healthy males between motor regions, as well as between motor and temporal cortices (**Fig. 7.3B**). ASCC males also displayed lower FC between frontal and occipital regions compared to HC males (**Fig. 7.3B**).

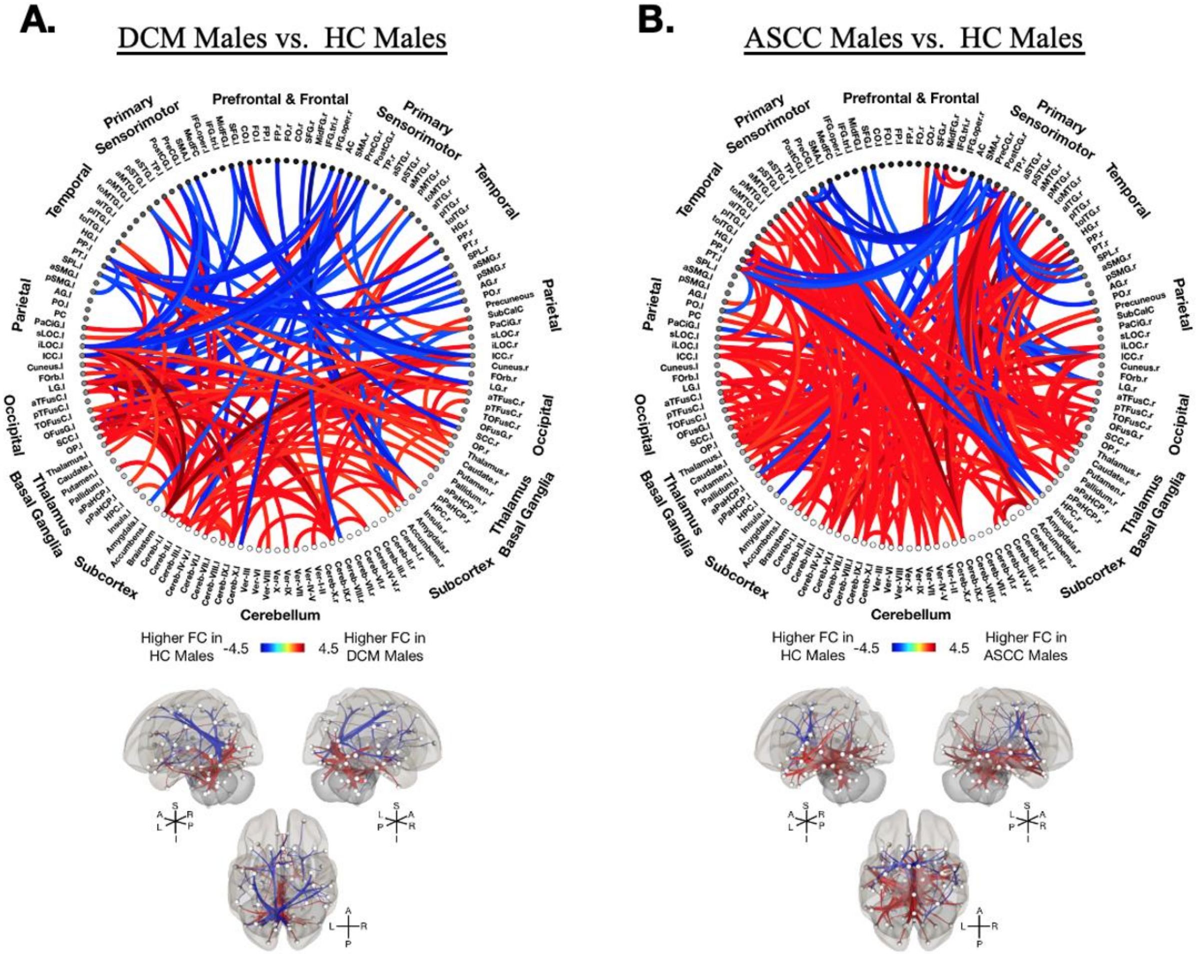

A. DCM Males vs. HC Males

B. ASCC Males vs. HC Males

Figure 7.3: Disease-specific functional connectivity (FC) analysis between male patients and HC males.

Whole-brain functional connectivity (FC) analysis between male cohorts while regressing out the effects of age. **(A,B)** ROI-to-ROI functional connectome diagrams using 132 Harvard-Oxford Automated Anatomical Labeling (AAL) atlas defined ROIs. **(Top)** Colors on the connectome denote the value of the T-statistic in which red-orange color denotes higher FC in **(A)** DCM or **(B)** ASCC males compared to HC males, while blue-light blue denotes higher FC in HCs compared to patients. ROIs are labeled with l = left hemisphere and r = right hemisphere. **(Bottom)** Left, right, and superiors views of a 3D brain rendering illustrating significant ROIs as spheres and significant differences in FC between the ROIs as lines with red denoting higher FC in **(A)** DCM or **(B)** ASCC compared to HC males and blue denoting higher FC in HCs compared to patients. Lighter spheres represent more superficial ROIs relative to the viewer, while darker sphere represent ROIs deeper within the brain. Significant connection-level threshold was set at p-value < 0.01 uncorrected.

Whole-brain FC analyses also revealed significant cerebral connectivity alterations in female patients compared to healthy females. Like the DCM males, DCM females displayed higher FC between cerebellar and occipital regions compared to healthy counterparts (**Fig. 7.4A**). However, DCM females displayed higher FC between the thalamus and sensorimotor and temporal regions when compared to healthy females (**Fig. 7.3A**). In addition, DCM females exhibited higher FC between vision-related regions including the LOC and sensorimotor and occipital regions (**Fig. 7.3A**). When compared to HC females, DCM females demonstrated lower FC throughout the brain, particularly between vision-related occipital regions and frontal, motor, thalamic, and cerebellar regions (**Fig. 7.3A**). DCM females also revealed lower FC between sensorimotor regions and temporal, parietal, and motor regions when compared to healthy females (**Fig. 7.3A**).

In the ASCC female cohort, patients exhibited increased FC between the ICC and frontal, sensorimotor, and temporal regions compared to healthy females (**Fig. 7.3B**). Additionally, ASCC females displayed increased FC compared to HC females within sensorimotor regions, as well as between sensorimotor and temporal, occipital, and cerebellar cortices (**Fig. 7.3B**). In contrast, lower FC in ASCC females compared to healthy counterparts was observed between the cerebellar vermis and vision-related regions, as well as between sensorimotor regions and the caudate (**Fig. 7.3B**).

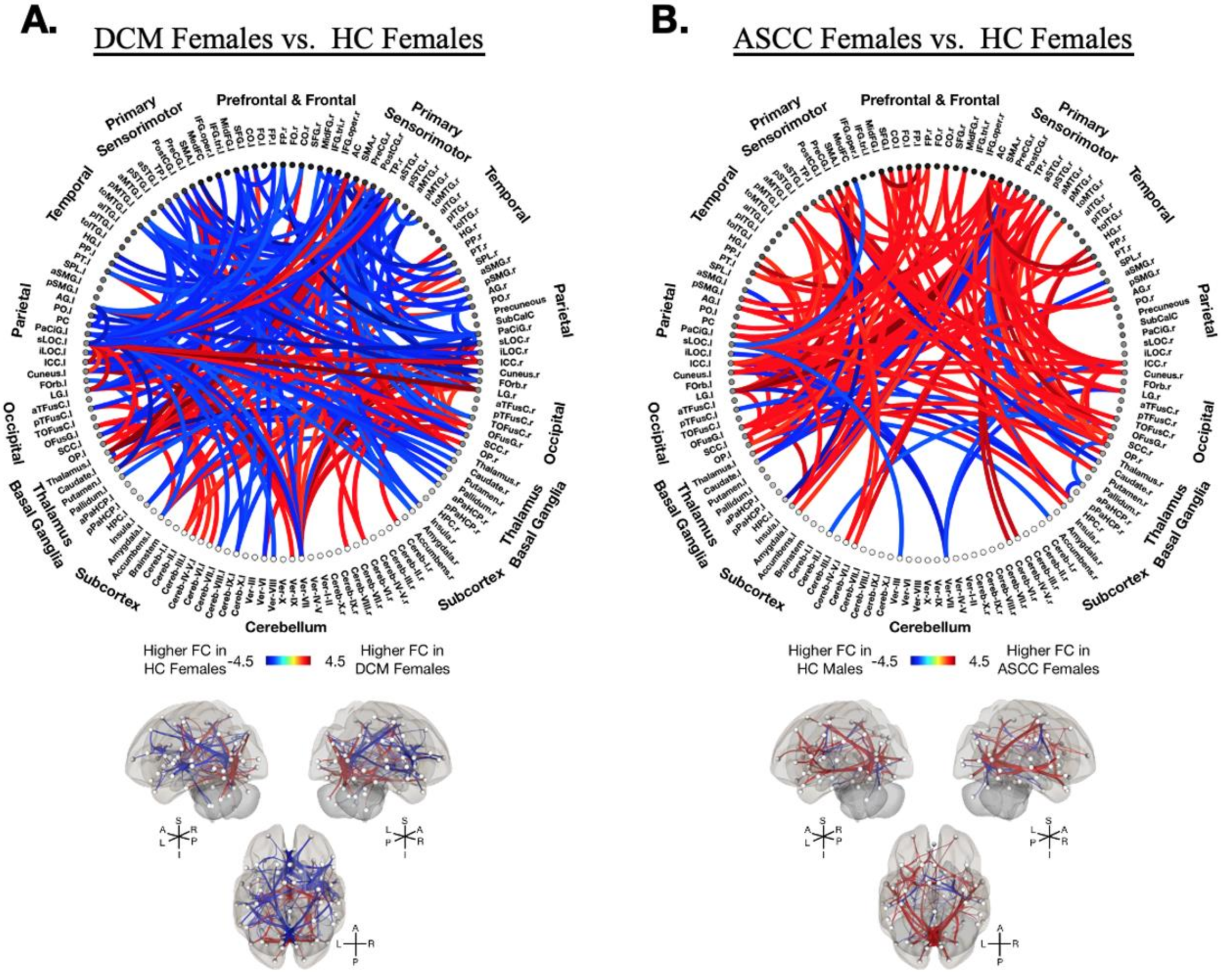

Figure 7.4: Disease-specific functional connectivity (FC) analysis between female patients and HC females.

Whole brain functional connectivity (FC) analysis between female cohorts while regressing out the effects of age. **(A,B)** ROI-to-ROI functional connectome diagrams using 132 Harvard-Oxford Automated Anatomical Labeling (AAL) atlas defined ROIs. **(Top)** Colors on the connectome denote the value of the T-statistic in which red-orange color denotes higher FC in **(A)** DCM or **(B)** ASCC females compared to HC females, while blue-light blue denotes higher FC in HCs compared to patients. ROIs are labeled with l = left hemisphere and r = right hemisphere. **(Bottom)** Left, right, and superiors views of a 3D brain rendering illustrating significant ROIs as spheres and significant differences in FC between the ROIs as lines with red denoting higher FC in **(A)** DCM or **(B)** ASCC compared to HC females and blue denoting higher FC in HCs compared to patients. Lighter spheres represent more superficial ROIs relative to the viewer, while darker sphere represent ROIs deeper within the brain. Significant connection-level threshold was set at p-value < 0.01 uncorrected.

7.3.4 Sex-specific Differences in Cerebral Microstructure

DCM patients exhibited sex-specific differences in fiber density (FD), fractional anisotropy (FA), and mean diffusivity (MD) along various white matter pathways. Specifically, DCM males displayed lower FD in voxels located along the internal and external capsules, cingulate, corpus callosum (body, genu, and splenium), corona radiata (anterior, posterior, and superior regions), and the superior longitudinal fasciculi (**Fig. 7.5 A**) compared with DCM females. DCM males also demonstrated lower FD compared to DCM females in voxels located at the thalamus and along the thalamic radiation (**Fig. 7.5 A**). However, DCM males demonstrated higher FA in voxels located at the body of the corpus callosum and right cingulate gyrus compared to DCM females (**Fig. 7.5 B**). When comparing differences in voxel-wise MD, DCM males exhibited significantly lower MD in the corticospinal tracts, cerebral peduncles, middle cerebellar peduncles, and pontine crossing tract compared to health counterparts (**Fig. 7.5 C**).

When comparing males and females in the ASCC cohort, ASCC males exhibited lower FD throughout white matter tracts of the brain largely in voxels located along the internal and external capsules, cingulate, corpus callosum (body, genu, and splenium), corona radiata (anterior, posterior, and superior regions), cerebral peduncles and the superior longitudinal fasciculi (**Fig. 7.6 A**). Additionally, ASCC males displayed lower FD in voxels located in the thalamus and along the thalamic radiations compared to ASCC females (**Fig. 7.6 A**). ASCC males also experienced higher FA compared to ASCC females in voxels located along the the superior longitudinal fasciculi and corona radiata (anterior, posterior, and superior regions) (**Fig. 7.6 B**). No significant differences in voxel-wise MD were observed between ASCC males and ASCC females. Significant anatomical locations, cluster sizes, and T-statistics are listed in **Table 7.3**.

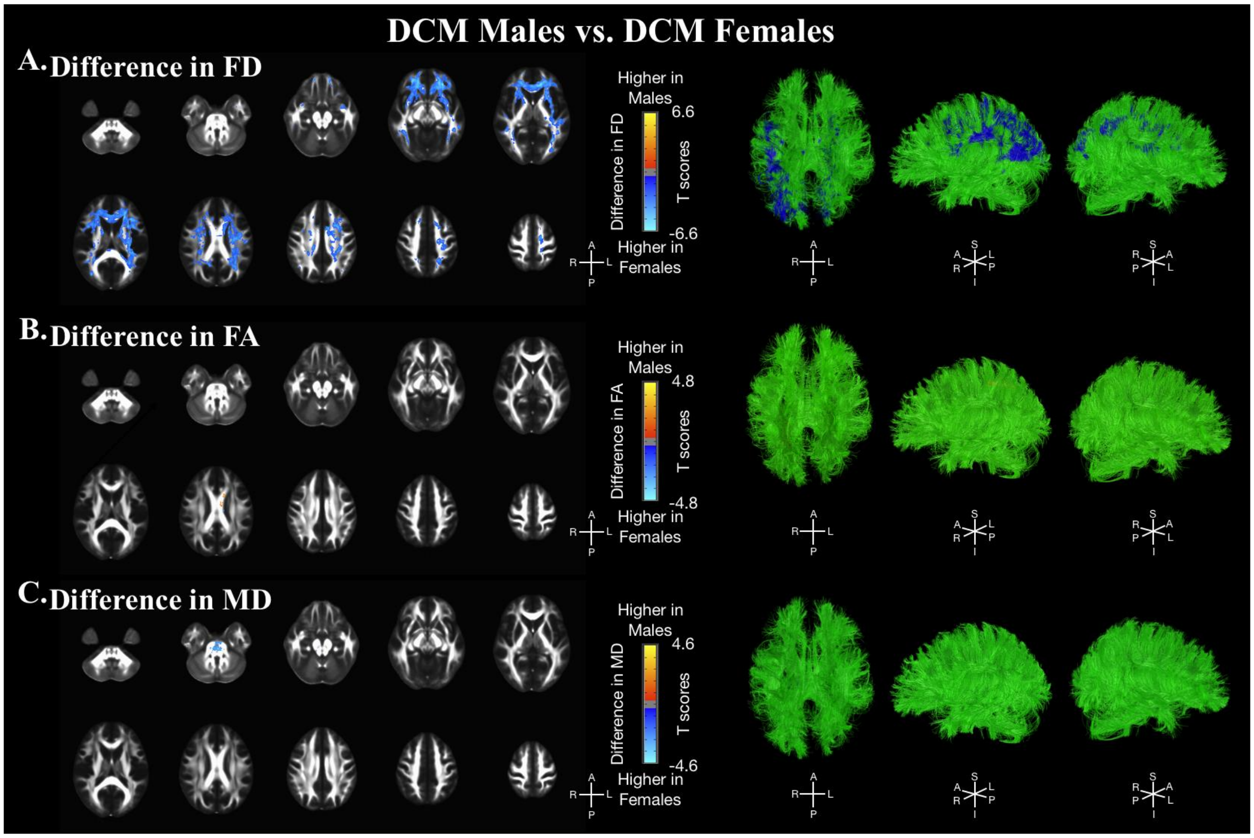

Figure 7.5: Voxel-wise diffusion tenor imaging (DTI) analysis between DCM males and females.

Anatomical localization of clusters with significantly different **(A)** fiber density (FD), **(B)** fractional anisotropy (FA), and **(C)** mean diffusivity (MD) between DCM males and DCM females, while controlling for subject age. **(Left)** Colors on axial brain white matter tract template denote the value of the corresponding T-statistic in which red-orange color denotes higher values in DCM males compared to females, while blue-light blue denotes higher values in DCM females compared to males. **(Right)** 3-dimenstional representation of fiber tracts and corresponding significant clusters. Significant clusters were determined by thresholding based on level of statistical significance of $p < 0.05$ and cluster-based corrections using permutation test.

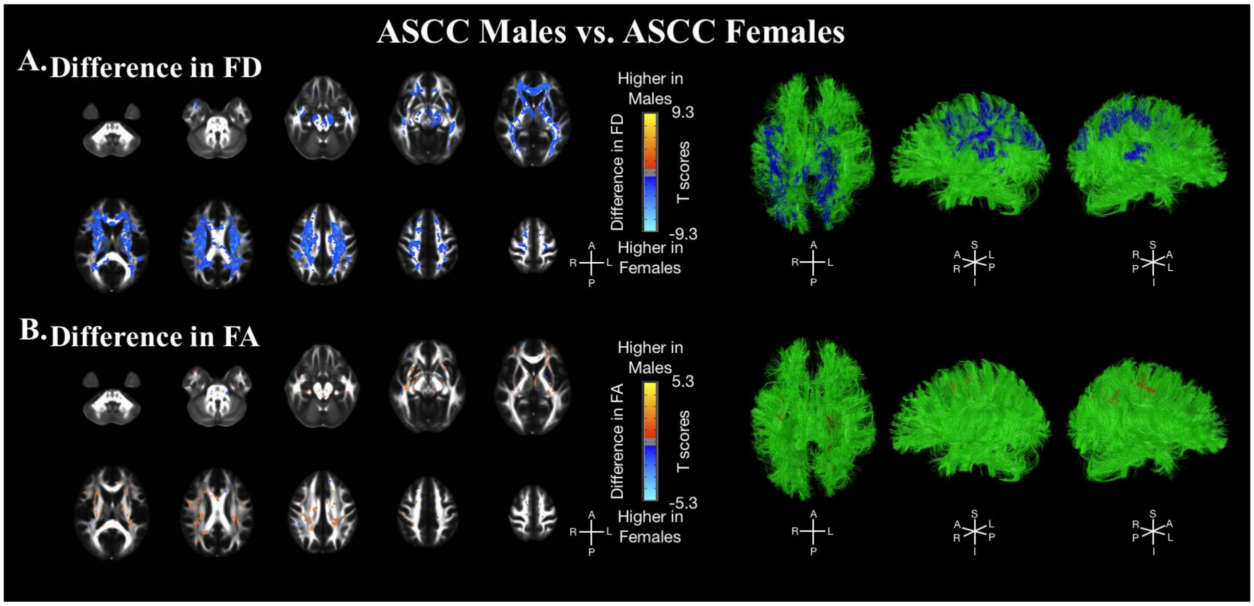

Figure 7.6: Voxel-wise diffusion tenor imaging (DTI) analysis between ASCC males and females.

Anatomical localization of clusters with significantly different **(A)** fiber density (FD), **(B)** fractional anisotropy (FA), and **(C)** mean diffusivity (MD) between ASCC males and ASCC females, while controlling for subject age. **(Left)** Colors on axial brain white matter tract template denote the value of the corresponding T-statistic in which red-orange color denotes higher values in ASCC males compared to females, while blue-light blue denotes higher values in ASCC females compared to males. **(Right)** 3-dimenstional representation of fiber tracts and corresponding significant clusters. Significant clusters were determined by thresholding based on level of statistical significance of $p < 0.05$ and cluster-based corrections using permutation test.

Anatomical Region	DCM Males vs. DCM Females							ASCC Males vs. ASCC Females			
	FD		FA		MD			FD		FA	
	T-statistic	Cluster Volume (µL)	T-statistic	Cluster Volume (µL)	T-statistic	Cluster Volume (µL)		T-statistic	Cluster Volume (µL)	T-statistic	Cluster Volume (µL)
Anterior Limb of Internal Capsule Left	-2.6049	1389	-	-	-	-		-2.8693	2018	2.5650	37
Anterior Limb of Internal Capsule Right	-2.5748	1221	-	-	-	-		-2.6164	1145	-	-
Anterior Corona Radiata Left	-3.0367	5013	-	-	-	-		-2.9583	4548	2.7825	225
Anterior Corona Radiata Right	-3.2190	6114	-	-	-	-		-2.8010	3380	-	-
Body of Corpus Callosum	-2.4731	2805	2.50345	484	-	-		-2.5931	4266	-	-
Cerebral Peduncle Left	-	-	-	-	-2.3307	12		-2.4109	833	-	-
Cerebral Peduncle Right	-	-	-	-	-2.7538	14		-2.5859	1521	-	-
Cingulum (Cingulate Gyrus) Left	-2.7262	519	-	-	-	-		-2.6988	655	-	-
Cingulum (Cingulate Gyrus) Right	-2.3974	133	2.46999	151	-	-		-2.5873	396	-	-
Cingulum (Hippocampus) Left	-	-	-	-	-	-		-	-	-	-
Cingulum (Hippocampus) Right	-	-	-	-	-	-		-	-	-	-
Corticospinal Tract Left	-	-	-	-	-2.5530	107		-2.3917	200	-	-
Corticospinal Tract Right	-	-	-	-	-2.5812	183		-2.5336	233	-	-
External Capsule Left	-2.6165	1842	-	-	-	-		-2.9685	1483	2.7423	191
External Capsule Right	-2.8015	4193	-	-	-	-		-2.6689	1757	-	-
Fornix	-	-	-	-	-	-		-2.3699	60	-	-
Fornix (Stria Terminalis) Left	-	-	-	-	-	-		-2.3952	512	-	-
Fornix (Stria Terminalis) Right	-2.2187	6	-	-	-	-		-2.2437	190	-	-
Genu of Corpus Callosum	-2.8467	5656	-	-	-	-		-2.9483	5113	-	-
Inferior Cerebellar Peduncle Left	-	-	-	-	-	-		-	-	-	-
Inferior Cerebellar Peduncle Right	-	-	-	-	-	-		-	-	-	-
Medial Lemniscus Left	-	-	-	-	-	-		-	-	-	-
Medial Lemniscus Right	-	-	-	-	-2.7057	18		-	-	-	-
Middle Cerebellar Peduncle	-	-	-	-	-2.6254	777		-2.2596	22	-	-
Pontine Crossing Tract	-	-	-	-	-2.5948	458		-2.3179	41	-	-
Posterior Limb of Internal Capsule Left	-2.2727	143	-	-	-	-		-2.6906	1833	-	-
Posterior Limb of Internal Capsule Right	-2.5782	971	-	-	-	-		-2.7969	2436	-	-
Posterior Corona Radiata Left	-2.4518	1267	-	-	-	-		-2.7819	2452	2.6524	279
Posterior Corona Radiata Right	-2.7287	2097	-	-	-	-		-3.0075	3073	2.5653	316
Posterior Thalamic Radiation Left	-2.4770	1149	-	-	-	-		-2.4557	1877	2.5417	2
Posterior Thalamic Radiation Right	-2.7558	2141	-	-	-	-		-2.8187	2128	-	-
Retrolenticular Part of Internal Capsule Left	-2.1464	74	-	-	-	-		-2.6637	1001	2.8034	24
Retrolenticular Part of Internal Capsule Right	-2.5311	890	-	-	-	-		-2.9024	1672	-	-
Sagittal Stratum Left	-2.5488	351	-	-	-	-		-2.4472	764	-	-
Sagittal Stratum Right	-2.4662	414	-	-	-	-		-2.8191	891	-	-
Splenium of Corpus Callosum	-2.3387	678	-	-	-	-		-2.4585	1819	2.5579	19
Superior Cerebellar Peduncle Left	-	-	-	-	-	-		-2.1906	15	-	-
Superior Cerebellar Peduncle Right	-	-	-	-	-	-		-2.2708	44	-	-
Superior Corona Radiata Left	-2.4159	2131	-	-	-	-		-3.1486	5878	2.8473	167
Superior Corona Radiata Right	-2.6302	4280	-	-	-	-		-3.0641	6026	2.9840	49
Superior Fronto-occipital Fasciculus Left	-2.4128	266	-	-	-	-		-3.3679	469	-	-
Superior Fronto-occipital Fasciculus Right	-3.0071	366	-	-	-	-		-2.5820	196	-	-
Superior Longitudinal Fasciculus Left	-2.4977	1523	-	-	-	-		-3.0340	3634	2.7541	513
Superior Longitudinal Fasciculus Right	-2.7769	3807	-	-	-	-		-3.2967	4438	2.7276	693
Tapetum Left	-2.9825	303	-	-	-	-		-2.3806	158	2.6143	9
TapetumRight	-2.6992	215	-	-	-	-		-2.9607	74	-	-
Uncinate Fasciculus Left	-2.5646	164	-	-	-	-		-2.7793	57	-	-
Uncinate Fasciculus Right	-2.7936	317	-	-	-	-		-2.3185	15	-	-
Thalamus	-2.3839	1275	-	-	-	-		-2.5098	8159	-	-

Table 7.3: Anatomical regions and white matter tracts with significant differences between males and females.

The t-statistic and cluster volumes are listed for fiber density (FD), fractional anisotropy (FA), and mean diffusivity (MD).

When compared to healthy males, both DCM males and ASCC males exhibited higher FD, but lower FA and MD in voxels located in white matter regions throughout the brain. Specifically, DCM males demonstrated higher FD in voxels located largely in the corona radiata (anterior, posterior, and superior regions), cerebellar peduncle, internal and external capsules, the superior longitudinal fasciculi, corpus callosum (body, genu, and splenium), and cingulum (**Fig. 7.7 A**). In addition, a large cluster of voxels with significantly higher FD in DCM males was observed in the thalamus (**Fig. 7.7 A**). In contrast, DCM males demonstrated lower FA compared to healthy males throughout the brain, primarily in the thalamus, corpus callosum (body, genu, and splenium), corona radiata (anterior, posterior, and superior regions), internal and external capsules, the superior longitudinal fasciculi, and cerebellar peduncles (**Fig. 7.7 B**). DCM males also displayed significantly lower MD compared to healthy males in voxels located along the body and genu of the corpus callosum, anterior corona radiata, fornix, corticospinal tracts, middle cerebellar peduncle, and thalamus (**Fig. 7.7 C**).

Similarly, ASCC males displayed significantly higher FD in voxels located throughout the brain compared to health counterparts. The most prominent significant differences were observed along the internal capsule, posterior corona radiata, cingulum, medial lemniscus, superior fronto-occipital fasciculus, cerebellar peduncles, cerebral peduncle, and thalamic radiations (**Fig. 7.8 A**). Additionally, ASCC males demonstrated lower FA in voxels located in the medial lemniscus, internal capsule, fornix, superior fronto-occipital fasciculus, cingulum, cerebral peduncle, thalamus, and corona radiata compared to healthy males (**Fig. 7.8 B**). Similarly, albeit across fewer white matter structures, ASCC males displayed lower MD compared to healthy males in voxels located primarily along the medial lemniscus, cerebellar peduncle, cerebral peduncle, internal capsule, fornix, superior fronto-occipital fasciculus, thalamic radiations, and cingulum (**Fig. 7.8 C**). Significant anatomical locations, cluster sizes, and T-statistics are listed in **Table 7.4**.

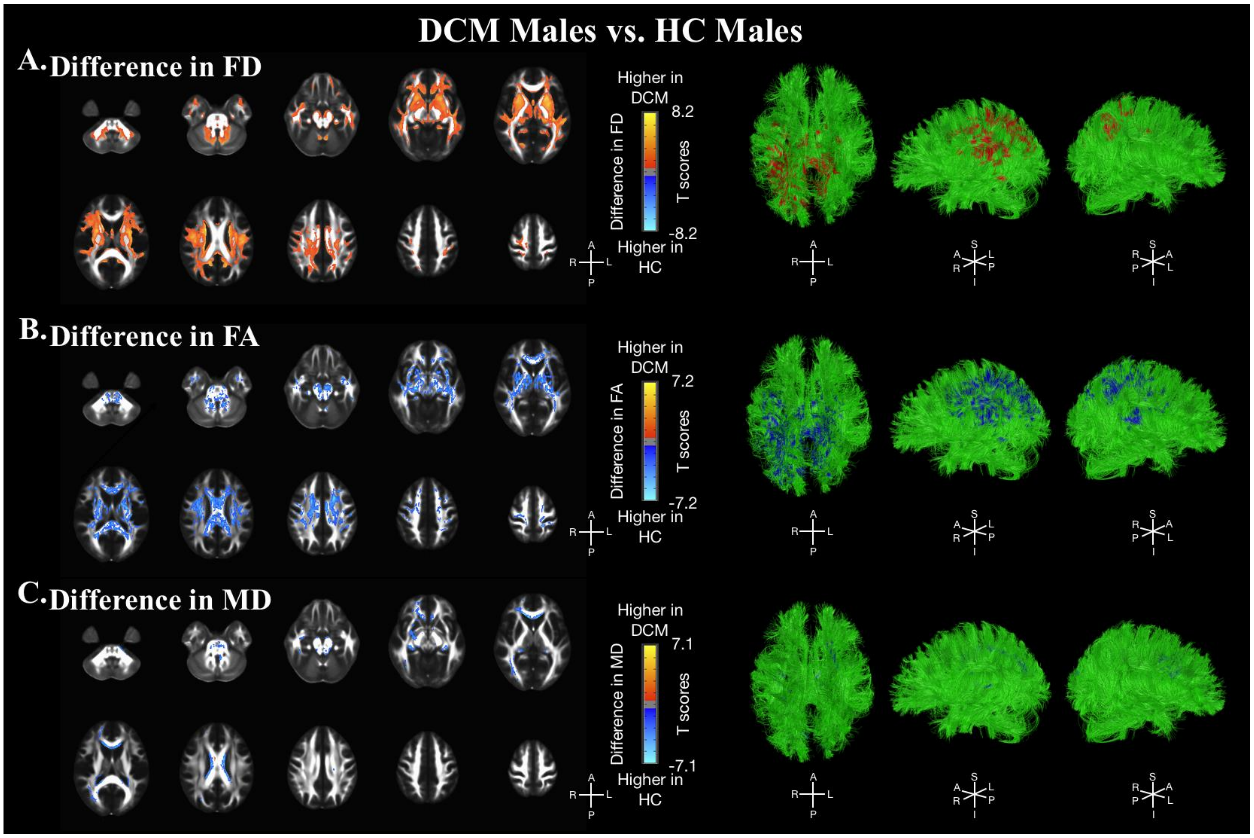

DCM Males vs. HC Males

A. Difference in FD

B. Difference in FA

C. Difference in MD

Figure 7.7: Voxel-wise diffusion tenor imaging (DTI) analysis between DCM males and HC males.

Anatomical localization of clusters with significantly different **(A)** fiber density (FD), **(B)** fractional anisotropy (FA), and **(C)** mean diffusivity (MD) between DCM males and HC males, while controlling for subject age. **(Left)** Colors on axial brain white matter tract template denote the value of the corresponding T-statistic in which red-orange color denotes higher values in DCM males compared to HC males, while blue-light blue denotes higher values in HC males compared to DCM males. **(Right)** 3-dimensional representation of fiber tracts and corresponding significant clusters. Significant clusters were determined by thresholding based on level of statistical significance of $p < 0.05$ and cluster-based corrections using permutation test.

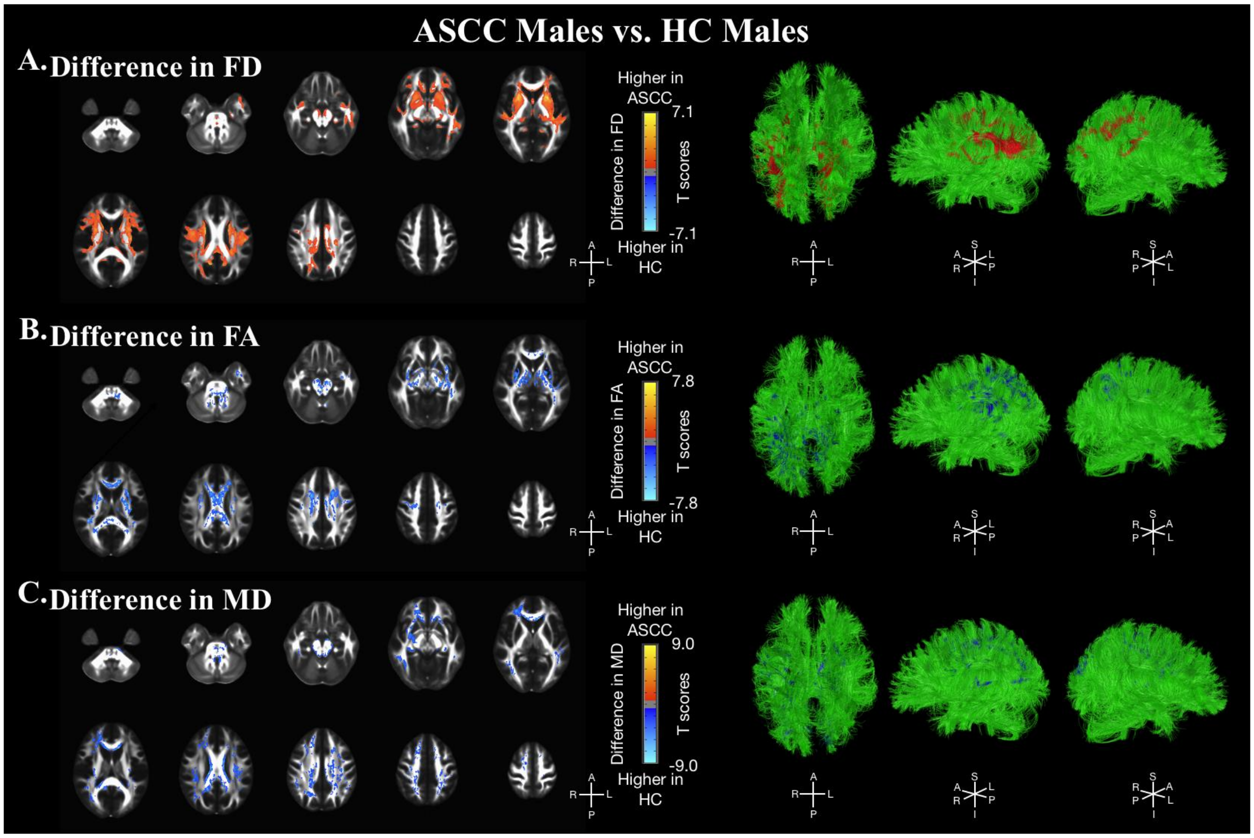

Figure 7.8: Voxel-wise diffusion tenor imaging (DTI) analysis between ASCC males and HC males.

Anatomical localization of clusters with significantly different **(A)** fiber density (FD), **(B)** fractional anisotropy (FA), and **(C)** mean diffusivity (MD) between ASCC males and HC males, while controlling for subject age. **(Left)** Colors on axial brain white matter tract template denote the value of the corresponding T-statistic in which red-orange color denotes higher values in ASCC males compared to HC males, while blue-light blue denotes higher values in HC males compared to ASCC males. **(Right)** 3-dimenstional representation of fiber tracts and corresponding significant clusters. Significant clusters were determined by thresholding based on level of statistical significance of $p < 0.05$ and cluster-based corrections using permutation test.

Anatomical Region	DCM Males vs. HC Males						ASCC Males vs. HC Males					
	FD		FA		MD		FD		FA		MD	
	T-statistic	Cluster Volume (μL)	T-statistic	Cluster Volume (μL)	T-statistic	Cluster Volume (μL)	T-statistic	Cluster Volume (μL)	T-statistic	Cluster Volume (μL)	T-statistic	Cluster Volume (μL)
Anterior Limb of Internal Capsule Left	3.4541	1870	-2.9930	1156	-	-	3.4434	1273	-2.8501	677	-2.2355	1
Anterior Limb of Internal Capsule Right	3.5544	1863	-2.9841	1021	-	-	3.5403	1304	-2.7351	593	-	-
Anterior Corona Radiata Left	3.5235	3642	-2.5262	1194	-2.6540	1118	3.1352	2719	-2.6677	403	-2.8935	2811
Anterior Corona Radiata Right	3.2701	3627	-2.7838	2425	-2.5703	64	3.6057	2983	-2.7526	998	-2.7408	507
Body of Corpus Callosum	3.1417	1211	-3.0240	7779	-2.3310	2292	3.3988	661	-2.8577	5564	-2.8744	3036
Cerebral Peduncle Left	2.4062	132	-3.1425	1041	-2.4986	117	2.3701	124	-2.7447	455	-2.7563	129
Cerebral Peduncle Right	2.4970	217	-3.0047	1132	-2.5194	151	2.6154	172	-2.9762	693	-2.5763	116
Cingulum (Cingulate Gyrus) Left	2.8505	435	-2.9875	918	-2.0957	1	2.9271	332	-2.8094	604	-2.9534	255
Cingulum (Cingulate Gyrus) Right	3.4817	679	-3.0693	1130	-2.5383	70	3.2283	636	-2.8529	669	-2.7012	501
Cingulum (Hippocampus) Left	2.5813	267	-2.8151	223	-	-	2.3476	64	-	-	-3.0156	52
Cingulum (Hippocampus) Right	3.6152	625	-2.4704	8	-	-	3.0371	307	-	-	-2.4206	9
Corticospinal Tract Left	-	-	-2.5233	214	-2.5353	202	-	-	-2.7768	7	-2.4571	137
Corticospinal Tract Right	2.1886	1	-2.6137	172	-2.8812	475	-	-	-2.3967	11	-2.5922	301
External Capsule Left	4.1457	3233	-2.7563	2146	-2.5225	245	4.0047	2542	-2.6687	1018	-2.7022	515
External Capsule Right	4.4350	4166	-2.7212	1540	-	-	4.4049	3574	-2.7305	1186	-2.6542	248
Fornix	3.4087	519	-2.5814	42	-	-	2.8370	233	-	-	-2.1020	1
Fornix (Stria Terminalis) Left	2.3337	91	-2.8632	262	-3.1213	545	2.2521	6	-2.7446	153	-3.0477	280
Fornix (Stria Terminalis) Right	2.4074	224	-2.8449	420	-3.1702	286	2.3158	28	-2.7324	302	-2.8128	150
Genu of Corpus Callosum	2.9884	1484	-2.8052	4082	-3.5918	2634	3.2435	1670	-2.8245	2187	-3.6060	2687
Inferior Cerebellar Peduncle Left	2.6822	587	-3.0585	355	-	-	-	-	-2.8657	144	-	-
Inferior Cerebellar Peduncle Right	2.5649	373	-3.2046	421	-2.3183	6	-	-	-3.0098	278	-	-
Medial Lemniscus Left	2.2103	21	-2.7128	297	-2.5088	10	2.3609	18	-2.6908	274	-2.3729	58
Medial Lemniscus Right	2.5057	56	-2.9486	375	-2.2318	7	2.7427	35	-2.7731	305	-2.6229	173
Middle Cerebellar Peduncle	3.0534	4632	-2.7664	2115	-2.6171	421	2.3912	29	-2.6459	568	-2.8008	383
Pontine Crossing Tract	2.3491	109	-2.7215	212	-2.4197	212	2.4883	211	-2.5293	24	-2.4064	155
Posterior Limb of Internal Capsule Left	3.0003	846	-3.0947	2483	-	-	2.7626	581	-2.8240	1242	-2.5029	112
Posterior Limb of Internal Capsule Right	2.7876	894	-3.0561	2484	-	-	2.7032	583	-3.0221	1924	-2.6615	21
Posterior Corona Radiata Left	3.6408	2309	-2.5832	773	-1.7728	122	3.1944	1601	-2.2861	60	-2.7002	911
Posterior Corona Radiata Right	3.4960	2162	-2.8609	1539	-2.4550	88	3.7673	1707	-2.5160	386	-2.4854	424
Posterior Thalamic Radiation Left	2.5118	241	-2.6848	708	-2.6988	398	2.6124	3	-2.6597	126	-2.7596	346
Posterior Thalamic Radiation Right	2.8676	158	-2.7310	1229	-2.0967	15	2.4839	67	-2.6693	288	-2.5109	21
Retrolenticular Part of Internal Capsule Left	2.6330	114	-2.8113	1440	-2.4253	31	2.6212	29	-2.6497	320	-2.4405	85
Retrolenticular Part of Internal Capsule Right	2.6917	864	-2.8482	1237	-1.7255	38	2.9670	670	-2.7994	639	-2.3650	64
Sagittal Stratum Left	2.5681	395	-2.9639	807	-2.5083	57	-	-	-2.5983	58	-2.7238	132
Sagittal Stratum Right	3.1479	551	-3.0313	997	-	-	3.1076	314	-2.8566	469	-2.4081	19
Splenium of Corpus Callosum	2.9525	334	-3.0575	7870	-2.5139	211	2.8542	358	-2.7094	3457	-2.8477	1552
Superior Cerebellar Peduncle Left	2.6352	33	-2.9209	407	-2.2812	19	-	-	-2.8484	307	-2.6353	153
Superior Cerebellar Peduncle Right	2.6624	66	-2.7461	231	-2.9539	286	-	-	-2.8052	246	-2.8837	235
Superior Corona Radiata Left	3.9236	4703	-2.9716	3787	-2.2563	5	3.5822	3427	-2.8280	2418	-2.5078	605
Superior Corona Radiata Right	3.6802	4241	-2.9551	3583	-2.4495	68	3.4417	2763	-2.9187	2448	-2.6114	1115
Superior Fronto-occipital Fasciculus Left	4.9108	496	-2.9697	232	-	-	4.1576	462	-2.9166	225	-	-
Superior Fronto-occipital Fasciculus Right	4.8101	498	-3.1756	260	-	-	4.0951	475	-2.9600	167	-	-
Superior Longitudinal Fasciculus Left	3.4853	3933	-2.9083	2212	-2.3147	46	3.1494	2410	-2.6372	255	-2.4494	910
Superior Longitudinal Fasciculus Right	3.9591	3332	-2.5331	1488	-	-	3.4800	2332	-2.6263	311	-2.7737	2275
Tapetum Left	3.4246	107	-2.6315	44	-2.9098	119	3.1083	74	-2.4792	7	-3.1306	109
TapetumRight	3.1456	68	-2.4190	35	-2.8139	153	3.3008	41	-2.3593	14	-2.8267	63
Uncinate Fasciculus Left	3.4394	285	-2.9191	153	-	-	2.9984	285	-2.2766	11	-2.1241	2
Uncinate Fasciculus Right	2.8452	161	-2.7981	166	-	-	2.9374	239	-2.5373	33	-	-
Thalamus	3.1059	11424	-2.9406	11199	-2.6015	327	2.7574	4743	-2.7752	5277	-2.4651	178

Table 7.4: Anatomical regions and white matter tracts with significant differences between male cohorts. The t-statistic and cluster volumes are listed for fiber density (FD), fractional anisotropy (FA), and mean diffusivity (MD).

When compared to healthy females, DCM and ASCC females demonstrated significant differences in FD, FA, and MD measurements across various cerebral white matter regions. Specifically, DCM females displayed higher FD compared to health females in voxels located along the corona radiata (anterior, posterior, and superior regions), internal and external capsules, superior longitudinal fasciculi, and thalamus (**Fig. 7.9 A**). DCM females exhibited lower FA in voxels located in white matter region throughout the brain; although largely along the splenium and body of the corpus callosum, superior and anterior corona radiata, and thalamus compared to healthy females (**Fig. 7.9 B**). DCM females also displayed significantly lower MD compared to HC females in voxels located along the cerebral peduncles, middle cerebellar peduncle, corticospinal tract, and pontine crossing fibers (**Fig. 7.9 C**).

ASCC females experienced higher FD and lower FA compared to healthy females in voxels throughout the brain. Higher FD was observed largely in voxels located along the superior longitudinal fasciculi, thalamus, corona radiata (anterior, posterior, and superior regions), and external and internal capsules in ASCC females compared to healthy counterparts (**Fig. 7.10 A**). In contrast, ASCC females demonstrated significantly lower FA compared to healthy females in voxels located at the thalamus, internal and external capsules, corpus callosum (body, genu, and splenium), fornix, and stratum (**Fig. 7.10 B**). No statistically significant differences in MD was observed between the ASCC female and HC female cohorts. Significant anatomical locations, cluster sizes, and T-statistics are listed in **Table 7.5**.

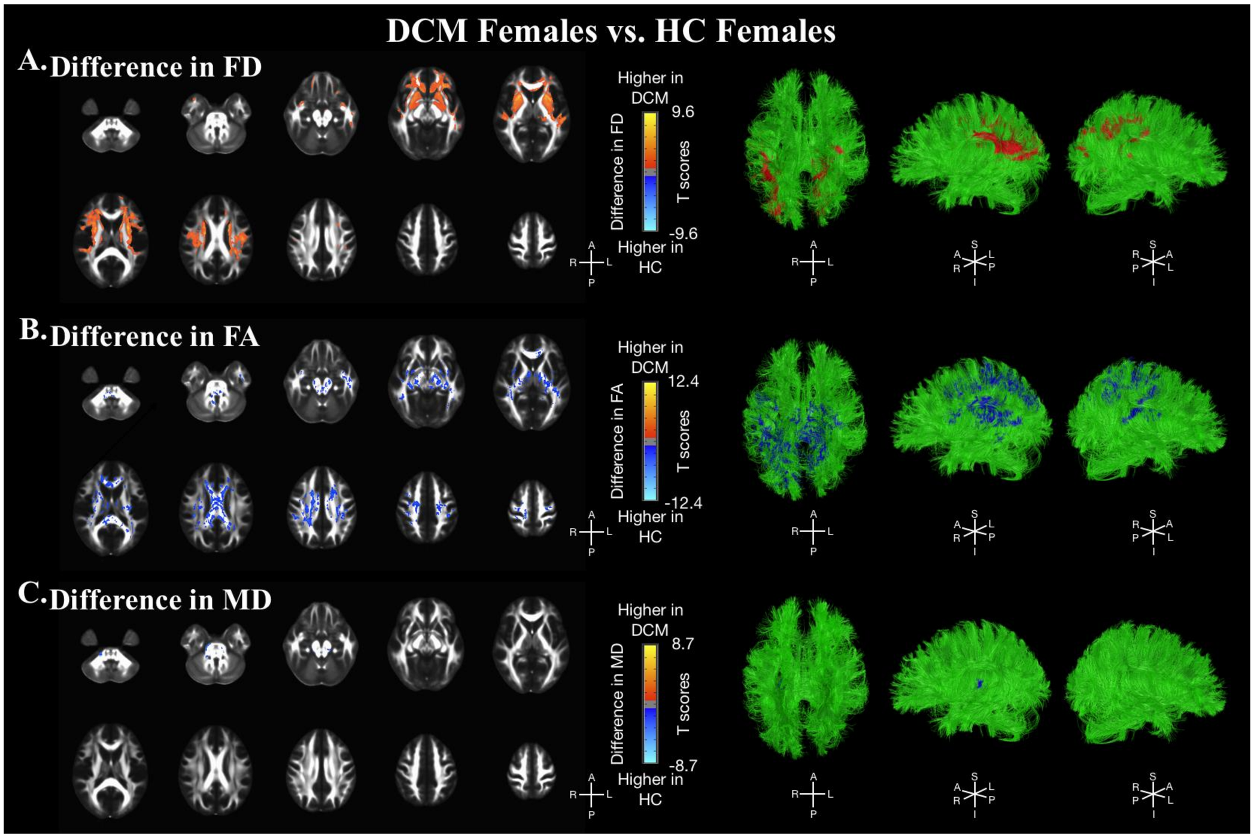

Figure 7.9: Voxel-wise diffusion tenor imaging (DTI) analysis between DCM females and HC females.

Anatomical localization of clusters with significantly different **(A)** fiber density (FD), **(B)** fractional anisotropy (FA), and **(C)** mean diffusivity (MD) between DCM females and HC females, while controlling for subject age. **(Left)** Colors on axial brain white matter tract template denote the value of the corresponding T-statistic in which red-orange color denotes higher values in DCM females compared to HC females, while blue-light blue denotes higher values in HC females compared to DCM females. **(Right)** 3-dimensional representation of fiber tracts and corresponding significant clusters. Significant clusters were determined by thresholding based on level of statistical significance of $p < 0.05$ and cluster-based corrections using permutation test.

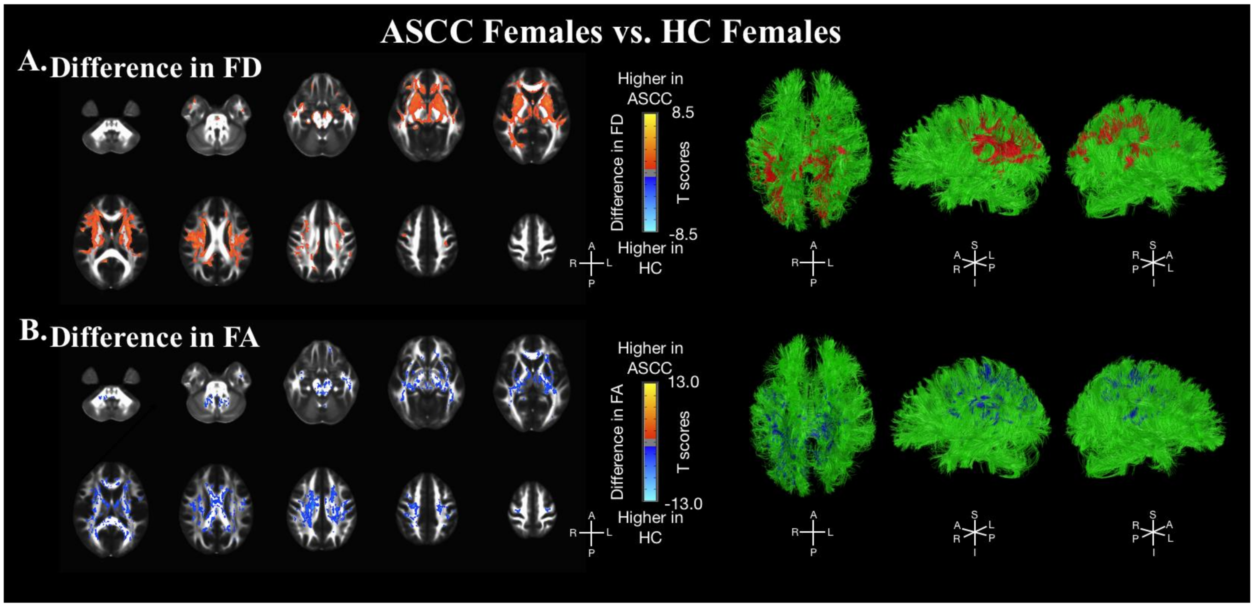

Figure 7.10: Voxel-wise diffusion tenor imaging (DTI) analysis between ASCC females and HC females. Anatomical localization of clusters with significantly different **(A)** fiber density (FD), **(B)** fractional anisotropy (FA), and **(C)** mean diffusivity (MD) between ASCC females and HC females, while controlling for subject age. **(Left)** Colors on axial brain white matter tract template denote the value of the corresponding T-statistic in which red-orange color denotes higher values in ASCC females compared to HC females, while blue-light blue denotes higher values in HC females compared to ASCC females. **(Right)** 3-dimenstional representation of fiber tracts and corresponding significant clusters. Significant clusters were determined by thresholding based on level of statistical significance of $p < 0.05$ and cluster-based corrections using permutation test.

Anatomical Region	DCM Females vs. HC Females						ASCC Females vs. HC Females			
	FD		FA		MD		FD		FA	
	T-statistic	Cluster Volume (µL)	T-statistic	Cluster Volume (µL)	T-statistic	Cluster Volume (µL)	T-statistic	Cluster Volume (µL)	T-statistic	Cluster Volume (µL)
Anterior Limb of Internal Capsule Left	3.0986	618	-2.7115	465	-	-	3.1684	1123	-2.8875	615
Anterior Limb of Internal Capsule Right	3.1231	898	-2.4433	24	-	-	3.1147	1611	-2.9756	461
Anterior Corona Radiata Left	3.1777	2728	-3.0498	1170	-	-	3.6439	3604	-2.8952	722
Anterior Corona Radiata Right	3.2692	3267	-2.7395	622	-	-	3.3335	3386	-2.8318	1211
Body of Corpus Callosum	2.4445	82	-3.0879	6493	-	-	3.0193	279	-3.1208	5675
Cerebral Peduncle Left	-	-	-3.0441	538	-2.6740	28	2.8937	132	-2.9129	412
Cerebral Peduncle Right	-	-	-2.9079	658	-2.7568	128	2.6746	243	-2.9705	519
Cingulum (Cingulate Gyrus) Left	-	-	-2.9442	774	-	-	3.2709	353	-3.1717	758
Cingulum (Cingulate Gyrus) Right	-	-	-2.8805	633	-	-	3.2059	1	-3.2051	811
Cingulum (Hippocampus) Left	-	-	-	-	-	-	2.8316	296	-2.8726	3
Cingulum (Hippocampus) Right	-	-	-	-	-	-	-	-	-	-
Corticospinal Tract Left	-	-	-2.9644	84	-2.7008	88	2.7551	1	-	-
Corticospinal Tract Right	-	-	-	-	-2.7154	137	2.5907	45	-	-
External Capsule Left	3.9206	3275	-2.8976	890	-	-	3.8760	3786	-2.9640	1245
External Capsule Right	4.0072	3202	-2.9188	749	-	-	3.7962	3211	-2.9852	1401
Fornix	-	-	-2.3339	14	-	-	2.6561	138	-2.4196	2
Fornix (Stria Terminalis) Left	-	-	-3.0949	412	-	-	3.0323	202	-3.2236	587
Fornix (Stria Terminalis) Right	2.3664	2	-2.9766	339	-	-	2.7184	230	-3.1419	504
Genu of Corpus Callosum	2.9842	1625	-2.7374	1616	-	-	3.1237	2196	-2.8766	1930
Inferior Cerebellar Peduncle Left	-	-	-2.9039	77	-	-	-	-	-3.0085	197
Inferior Cerebellar Peduncle Right	-	-	-	-	-	-	-	-	-3.2154	48
Medial Lemniscus Left	-	-	-2.6405	133	-	-	-	-	-2.8736	78
Medial Lemniscus Right	-	-	-2.5836	95	-	-	-	-	-2.6834	59
Middle Cerebellar Peduncle	-	-	-3.1135	50	-2.8393	502	2.4558	49	-3.1260	1006
Pontine Crossing Tract	-	-	-2.6778	13	-2.9053	140	2.6240	34	-	-
Posterior Limb of Internal Capsule Left	2.3821	94	-2.7416	708	-	-	3.4729	793	-3.2330	1126
Posterior Limb of Internal Capsule Right	2.6578	293	-2.7491	895	-	-	3.0064	875	-3.0132	1260
Posterior Corona Radiata Left	3.0988	546	-2.7544	810	-	-	3.4120	1491	-3.1880	1529
Posterior Corona Radiata Right	3.1242	877	-2.7125	402	-	-	3.3390	1398	-3.0444	985
Posterior Thalamic Radiation Left	-	-	-2.6378	258	-	-	2.8985	920	-2.7782	478
Posterior Thalamic Radiation Right	-	-	-2.8248	462	-	-	2.3873	6	-3.0213	580
Retrolenticular Part of Internal Capsule Left	-	-	-2.7790	424	-	-	2.9313	658	-3.1834	877
Retrolenticular Part of Internal Capsule Right	2.5292	138	-2.5826	472	-	-	3.1061	878	-3.1591	923
Sagittal Stratum Left	2.2423	2	-2.7153	112	-	-	2.5535	172	-2.7475	414
Sagittal Stratum Right	-	-	-2.6785	316	-	-	2.5387	69	-2.9280	397
Splenium of Corpus Callosum	-	-	-2.8379	2699	-	-	2.6488	72	-2.8783	2397
Superior Cerebellar Peduncle Left	-	-	-3.0071	231	-2.7038	17	2.6048	5	-3.0246	212
Superior Cerebellar Peduncle Right	-	-	-2.5896	111	-	-	2.3570	2	-2.9528	243
Superior Corona Radiata Left	3.1928	2347	-2.9801	2261	-	-	3.5566	3513	-3.3396	3193
Superior Corona Radiata Right	3.0993	1771	-2.7257	1166	-	-	3.2781	2106	-3.0639	2472
Superior Fronto-occipital Fasciculus Left	3.1969	344	-2.7273	173	-	-	3.9493	439	-3.2662	271
Superior Fronto-occipital Fasciculus Right	3.7021	424	-2.7218	51	-	-	4.0806	470	-2.9808	235
Superior Longitudinal Fasciculus Left	2.9152	2112	-2.8755	850	-	-	3.3842	3383	-2.9554	1450
Superior Longitudinal Fasciculus Right	3.2260	2464	-2.5600	307	-	-	3.2895	3310	-2.7655	635
Tapetum Left	-	-	-	-	-	-	3.3830	98	-3.0140	42
TapetumRight	2.4392	55	-2.4518	7	-	-	2.8743	52	-2.9061	10
Uncinate Fasciculus Left	2.7648	171	-2.8617	114	-	-	3.7091	285	-3.0661	138
Uncinate Fasciculus Right	3.0296	213	-3.1215	157	-	-	3.6352	285	-3.3213	100
Thalamus	2.7548	1685	-2.8327	4850	-2.5056	2	3.1467	10401	-3.1098	7280

Table 7.5: Anatomical regions and white matter tracts with significant differences between female cohorts.

The t-statistic and cluster volumes are listed for fiber density (FD), fractional anisotropy (FA), and mean diffusivity (MD).

7.4 Discussion

Previous studies have shown patients with DCM experience alterations in cerebral structure and function compared to healthy controls. Patients with DCM primarily exhibit cortical atrophy and altered functional connectivity in sensorimotor and cerebellar regions [59,60,62,71-73], as well as reductions in white matter fiber density and integrity along the corticospinal tracts and association pathways responsible for sensorimotor function and pain modulation [65-68]. However, due to smaller cohort sizes most previous investigations were conducted on a combined symptomatic DCM and asymptomatic spinal cord compression (ASCC) cohort or excluded the ASCC patients altogether. Although studies have demonstrated DCM and ASCC patients experience similar macro- and micro-structural changes within the cervical spinal cord [92,196], little research has been published on supraspinal alterations in ASCC patients alone or in comparison to symptomatic DCM patients. The study in Chapter 2 revealed symptomatic DCM and ASCC patients experience unique supraspinal structural and functional alterations and suggest such differences may contribute to symptom management and disease progression. In summary, DCM patients demonstrated cortical expansion of vision-related regions, increased visual-motor and visual-cerebellar functional connectivity (FC), and altered microstructural integrity in the thalamus and white matter pathways associated with motor function. In contrast, ASCC patients exhibited atrophy of sensorimotor cortices, increased visual-temporal FC, and altered microstructural integrity along association pathways.

Furthermore, epidemiological studies have found DCM to be almost three times more prevalent in males than females [8,12]. As discussed in Chapters 4 and 5, sex hormones play a role in neuroprotection and the patient’s response to neurotrauma, therefore it is important to consider sex as a biological variable especially in investigations of DCM and ASCC. Prior to the work presented in Chapters 4 and 5, the influence of sex in DCM remained largely unknown. The studies discussed in Chapters 4 and 5 were conducted on a combined DCM and ASCC cohort and revealed that male patients exhibited larger gray matter volume in motor, language, and pain related cortices compared to female patients. In addition, male patients demonstrated greater FC between visual and cerebellar, thalamic, and brainstem regions, while female patient displayed higher FC between frontal regions and occipital and cerebellar cortices. To further expand on such findings, the present study separated the patient cohort by sex and symptom presentation (DCM and ASCC) and using a multimodal imaging approach aimed to better understand the sex-specific differences in cerebral morphometry, FC, and white matter microstructure between symptomatic DCM and ASCC patients.

In the present study, both symptomatic DCM and ASCC cohorts demonstrated significant sex-specific differences in cerebral structure and function. Some alterations were similar to those observed in the entire DCM cohort discussed in previous chapters and some were unique to symptom presentation specific subgroups. As described previously, the combined cohort of DCM males exhibited larger GMV in frontal, parietal, temporal, and occipital cortices when compared to DCM females. Additionally, the combined cohort of DCM males experienced greater FC within the cerebellum and between visual-thalamic, visual-cerebellar, cerebellar-thalamic, and parietal-occipital regions, while females displayed higher FC between motor-cerebellar regions, as well as frontal-visual regions. However, when the cohort only included symptomatic patients, DCM males demonstrate larger GMV in the lateral occipital cortex compared to females and higher FC between frontal-motor and occipital-motor cortices compared to symptomatic females. In contrast, the symptomatic DCM females exhibited higher FC between frontal-cerebellar, motor-cerebellar, and frontal-thalamic regions. Furthermore, when compared to healthy males, symptomatic DCM males displayed cortical atrophy in the superior frontal gyrus and increased FC between visual-brainstem and occipital-cerebellar regions, as well as decreased FC between motor-occipital and motor-cerebellar regions. The symptomatic DCM female exhibited increased motor-thalamic and visual-cerebellar FC, but decreased parietal-cerebellar FC compared to HC females.

By evaluating the cerebral alterations that overlap and differ between the entire DCM, symptomatic, and asymptomatic cohorts, we may begin to elucidate which supraspinal reorganization patterns may be driven by chronic spinal cord compression, sex-differences, symptom presentation, and effective compensation. Previous studies have demonstrated that DCM patients experience cortical atrophy of sensorimotor and cerebellar regions [59,60], however symptomatic DCM males demonstrate cortical expansion of occipital regions accompanied by greater FC between vision-related regions and motor, cerebellar, and brainstem regions. Evidence shows that DCM is not only impacting the sensorimotor cortices, but that recruitment of cerebellar and occipital regions may be critical for males to compensate for motor deficits through higher visuospatial and motor planning [66,67,99]. On the other hand, the symptomatic females displayed recruitment of frontal brain regions and increase frontal-visual and frontal-cerebellar connectivity, suggesting DCM females utilize frontal regions for planning and timing of motor programs in response to symptom presentation [197].

When examining sex differences in the ASCC cohort, males displayed larger GMV in sensorimotor, frontal, language, and temporal brain regions alongside widespread alterations in FC. Specifically, ASCC males exhibited higher FC between parietal-occipital, temporal-cerebellar, and visual-cerebellar regions, while ASCC females displayed higher FC between sensorimotor-thalamic and parietal-cerebellar regions. When compared to sex-specific HCs, ASCC males and females demonstrated more widespread alterations in FC than symptomatic

DCM patients compared to healthy counterparts. Furthermore, such widespread changes involved different cortical regions and notably more sensorimotor and temporal involvement than symptomatic males and females. When compared to sex-specific HC cohorts, the ASCC males displayed higher FC between sensorimotor-cerebellar, temporal-cerebellar, occipital-thalamic, and cerebellar-thalamic regions, while ASCC females exhibited higher FC between sensorimotor-visual, frontal-visual, and motor-cerebellar. ASCC females displayed much fewer alterations in cerebellar connectivity than ASCC males. Such findings suggest that in response to chronic spinal cord compression, ASCC males strengthen primary motor and cerebellar pathways, as well as temporal-cerebellar connectivity, while ASCC females strengthen sensorimotor-visual and frontal-visual connectivity. This cerebral reorganization may be critical to manage disease-related progression and symptom presentation.

In addition to cerebral morphometry and functional connectivity, microstructural alterations were examined and included in this chapter as preliminary findings. In a combined symptomatic DCM and ASCC patient cohort, previous studies have demonstrated white matter reorganization in motor, somatosensory, and pain related pathways, as well as microstructural alterations in pathways between the brainstem and cerebral cortex [66,68]. Findings from Chapter 2 reveal that symptomatic DCM patients experience alterations along corticospinal and thalamic tracts associated with greater axonal demyelination and damage compared to the ASCC patients. In addition to decreased microstructural integrity and fiber density along pathways responsible for connecting motor, cerebellar, and brainstem cortices, symptomatic DCM patients exhibited reorganization of association pathways compared to ASCC patients.

The present study further separated the cohorts based on sex and found significant sex-specific microstructural alterations in DCM and ASCC patients. Specifically, symptomatic DCM males displayed lower FD throughout the corpus callosum, within the thalamus, and along the corona radiata, SLF, and internal and external capsules compared to DCM females. DCM also displayed higher FA along the corpus callosum, but lower MD in the cerebral and cerebellar peduncles. When compared to healthy males, DCM males exhibited higher FD largely within the thalamus and along the SLF, corona radiata, and middle cerebellar peduncles, as well as lower FA and MD predominantly in thalamus and thalamic radiation, corpus callosum, cerebral and cerebellar peduncles, and corticospinal tracts. When compared to healthy females, DCM females displayed higher FD and lower FA along the SLF, corona radiata, corpus callosum, internal and external capsules, and thalamus, as well as lower MD along the cerebral and cerebellar peduncles. Such findings suggest symptomatic DCM males experience expansion and microstructural integrity of cerebral and cerebellar peduncles critical for motor planning and proprioceptive sensory input, whereas DCM females present greater expansion of association pathways including the corpus callosum and external capsule and less extensive degeneration of corticospinal and SLF tracts.

In the ASCC cohort, ASCC males demonstrated lower FD along corticospinal tracts, fornix, thalamus, cingulum, and cerebral and cerebellar peduncles compared to ASCC females. ASCC males also exhibited lower FD and FA along the SLF, internal and external capsules, and corona radiata. When compared to HCs, ASCC males displayed higher FD, lower FA, and lower MD along the internal and external capsules, fornix, corona radiata, corpus callosum, and cingulum. whereas ASCC females displayed higher FD and lower FA along the SLF, internal and external capsules, corpus callosum, cingulum, fornix, and thalamus compared to HC females. Moreover, when compared to healthy counterparts ASCC males exhibited higher FD while ASCC females demonstrated lower FA along the cerebellar peduncles. Although ASCC patients presented less distinct sex-specific alterations in cerebral white matter diffusion characteristics that symptomatic

DCM patients, the findings suggest ASCC males experience more extensive corticospinal tract axonal degeneration whereas the ASCC females exhibit more extensive cerebellar peduncle axonal degeneration. Furthermore, in comparing findings from symptomatic DCM and ASCC males, the results reveal DCM males experience greater expansion of cerebellar peduncle and thalamic fibers, however greater axonal degeneration in the thalamus and along the thalamic radiations. In contrast, ASCC females displayed more extensive increases fiber density along the cingulum and fornix not observed in the symptomatic DCM females. Due to the small sample size, such preliminary results must be interpreted with caution and future studies will require greater statistical power in order to reveal more reliable and conclusive findings.

As discussed in previous chapters, such sex-specific alterations may be driven by differences in sex hormone concentrations, thus impacting neuroprotection and neural response to chronic injury. Narrowing of the spinal canal and chronic mechanical compression on the cervical spinal cord result in impaired spinal cord perfusion and ischemia triggering endothelial cell dysfunction, hypoxic cell death, and neuroinflammation [13,15]. In response, damaged neurons will release glutamate prompting glutamate excitotoxicity, axonal demyelination, and ultimately apoptosis [14]. Sex steroid receptors are expressed in neurons, glia, and immune cells and thus influence pathobiological responses to chronic injury [198]. Both preclinical and clinical studies of spinal cord injury (SCI) have revealed sex hormone concentration, including testosterone, estradiol, and progesterone, influence neuronal loss and demyelination, neuroinflammation, and motor functional recovery [136,141,142,198-202]. Such neuroprotective effects of sex hormones may influence upstream sex-specific cerebral differences in response to chronic spinal cord injury, as well as impact effective compensatory reorganization, symptom presentation, and disease progression. Future studies investigating sex differences in DCM and ASCC will benefit from sampling patients' blood sex steroids concentrations and examining the relationship between concentration of sex hormones and symptom severity and cerebral reorganization.

Although the current study was the first to investigate sex-specific supraspinal differences in DCM and ASCC patients exclusively, a larger patient cohort is necessary to conduct a more thorough investigation. With a larger sample size, the study could have the statistical power required to detect small, but important differences between DCM males and ASCC males, as well between DCM females and ASCC females directly. In addition, the current whole-brain functional connectivity analyses did not have the sufficient statistical power to detect group differences following correction for multiple comparisons and therefore would also benefit from a larger patient sample, as well as inclusion of total intracranial volume (TICV) as an additional covariate. However, the present study did provide critical preliminary results to support a larger study to further identify sex-specific cerebral signatures in DCM and ASCC patient populations.

In conclusion, the present study revealed significant sex-specific supraspinal differences in DCM and ASCC patients. The findings suggest DCM males strengthen visual, cerebellar, and brainstem related pathways for visuospatial planning and proprioceptive input, while DCM females utilize frontal and association pathways for motor planning. In contrast, ASCC patients displayed greater sensorimotor, temporal, and parietal involvement with ASCC males recruiting primary motor, cerebellar, and temporal pathways, whereas ASCC females expand visual, frontal, and sensorimotor pathways. The present study provides preliminary evidence to support sex and symptom specific cerebral reorganization in chronic cervical spinal cord compression patients and may inform future studies and more effective disease treatment.

CHAPTER 8

Conclusions and Future Directions

8.1 Conclusions

This dissertation utilized advanced neuroimaging techniques to investigate the spinal and supraspinal alterations occurring in patients with chronic spinal cord compression. The present chapter summarizes the findings and implications of the three dissertation aims.

8.1.1 Characterization and comparison of spinal cord compression induced alterations in brain structure and function in symptomatic and asymptomatic patients

Aim 1 of this dissertation set out to characterize alterations in cerebral morphometry, functional connectivity, and white matter microstructure in response to compression-induced spinal cord injury in DCM and ASCC patients. In Chapter 2, the findings demonstrated differing disease-dependent cerebral reorganization between symptomatic DCM and ASCC patients, suggesting differing supraspinal compensatory mechanisms. The symptomatic DCM patients experienced expansion of vision-related cortical regions, increased functional connectivity between visual-motor and visual-cerebellar regions, and white matter damage along the corticospinal tracts and thalamic radiations. In contrast, the ASCC patients exhibited cortical atrophy of sensorimotor cortices, increased functional connectivity between temporal-cerebellar and temporal-brainstem regions, and maintained white matter integrity and density along association pathways. The findings reveal symptomatic DCM patients experience degeneration of motor and cerebellar white matter pathways and recruit of primary and secondary visual cortices in response to symptom experience, suggesting prioritization of visuo-spatial information critical for motor planning and motor-related compensation. Whereas ASCC patients experience less extensive white matter degeneration of sensorimotor pathways and recruitment of frontal regions and association pathways which may facilitate effective functional recruitment and compensation. Because symptomatic DCM and ASCC patients are exhibiting distinct degrees of upstream axonal damage and unique recruitment of neural pathways, findings from Aim 1 may support the development of imaging biomarkers to better inform disease progression and treatment planning.

8.1.2 Correlation of macro- and micro-structural cervical spinal cord measurements with supraspinal alterations in patients with DCM

In Aim 2 of the dissertation, macrostructural, microstructural, and metabolic properties of the cervical spinal cord were quantified and used to determine the interrelationship between cord compression and upstream supraspinal structural and functional alterations in patients with DCM. In **Chapter 3**, T2-weighted cervical spine MRI was used to measure spine cord and canal area and diameter at each cervical spinal segment, alongside anatomical and functional MR imaging of the brain. The findings revealed that with more severe spinal compression and greater cord atrophy, patients exhibited cortical atrophy of occipital and temporal cortices, decreased functional connectivity within visual regions, and increased functional connectivity between motor, visual, and cerebellar brain regions. Spinal cord and canal measurements did not significantly correlate with symptom severity as measured using mJOA score. However, spinal cord area and anterior-posterior spinal cord and canal diameter at cervical spinal segments are more sensitive and significantly associated with upstream cerebral alterations than the traditionally used Torg-Pavlov ratio (TPR) measurements.

In **Chapter 4**, MR spectroscopy (MRS) was utilized to measure spinal cord metabolite concentrations and provide insight into cord cellular and biochemical function in patients with DCM. Furthermore, metabolic and DTI-based measurements within the cervical spinal cord were investigated in relation to cerebral structural and functional signatures. The metabolic based analyses revealed that increased axonal degeneration, neuroinflammation, and cell turnover within the cervical spinal cord was associated with atrophy of sensorimotor and cerebellar connectivity, degeneration of association and thalamic pathways, and increased structural and functional recruitment of frontal, temporal, occipital, and brainstem regions. In addition, the diffusion-based findings demonstrated that increased axonal damage to the cervical spinal cord, as measured by lower FA and higher MD values, was associated with atrophy of motor-related cortices and white matter tracts, decreased structural and functional connectivity between temporal and occipital regions, expansion of visual and orbitofrontal regions, and functional and structural strengthening of visual, executive motor-planning, and proprioceptive related pathways. Thus, the findings from Aim 2 illustrate cortical reorganization is related to the severity of cervical spinal cord compression and neuronal damage in patients with DCM.

8.1.3 Identification of sex-dependent alterations in brain structure and connectivity in DCM patients

Not only is DCM significantly more prevalent in males than females, but previous studies have shown sex differences influence neuroprotective mechanisms and the central nervous system's response to neural injury. Thus, **Aim 3** was designed to evaluate sex as a biological variable in DCM and determine sex-dependent supraspinal alterations in response to chronic cervical cord compression. In **Chapter 5**, the results revealed male patients with DCM experience cortical expansion of motor, language, and vision related brain regions compared to female patients. DCM males also exhibited significant correlations between cortical volume and mJOA scores, in which patients with worsening neurological symptoms demonstrated greater cortical atrophy across somatosensory and motor related cortices. DCM females exhibited a similar associated, albeit across a broader range of cortical regions including areas involved in pain processing. The study presented in **Chapter 6** investigated the role of sex on brain functional connectivity (FC) and found DCM males exhibit higher FC between visual-cerebellar and visual-brainstem regions, but lower FC between visual-frontal and visual-somatosensory cortices. Whereas DCM females demonstrated higher FC frontal-cerebellar and visual-frontal, but lower FC between visual-sensorimotor regions. In addition, global network topological analyses revealed DCM males exhibited significantly greater intra-network connectivity (i.e., higher global clustering coefficient) and efficiency (i.e., lower characterlike path length) compared to healthy males. The findings indicate DCM males may be recruiting visual, cerebellar, and brainstem connections in response to chronic spinal cord compression and motor deficits, while DCM females may be utilizing visual and frontal cortices. Overall, such findings may reflect hormonal influences on cerebral reorganization and differing compensatory mechanisms between males and females with DCM and may inform development of novel, neuroprotective drug therapies.

Lastly, **Chapter 7** was included in this dissertation as preliminary investigation of sex-dependent differences in cerebral structure, function, and white matter integrity in symptomatic DCM and ASCC patients. Due to patient sample size, the previous chapters included a combined symptomatic and asymptomatic DCM cohort. The findings from Chapter 7 revealed DCM males exhibit functional and microstructural recruitment of visual, cerebellar, and brainstem related pathways, whereas DCM females utilize frontal, visual, and association pathways. In contrast, the ASCC patients displayed greater frontal and temporal cerebral involvements with ASC males strengthening motor, cerebellar, and temporal pathways, while ASCC females displayed expansion of frontal, visual, and sensorimotor pathways.

8.2 Future Directions

Regarding the body of clinical research on cervical myelopathy and cervical spinal cord compression, the present dissertation provided novel insights into disease-dependent cerebral reorganization, the interrelationship between spinal and supraspinal alterations, and sex as a biological variable in cerebral structure and function. This dissertation lays the foundation for future research with the hopes of better understanding disease progression and improving treatment planning.

The clinical-radiological mismatch presented in ASCC patients remains an enigma in the field with relatively little published research on the neural differences between ASCC and DCM patients. Although DCM and ASCC patients exhibit similar degrees of cervical spinal cord compression, patients with DCM experience a range of motor and neurological symptoms. Future longitudinal studies that include neuroimaging data during the patient's progression from asymptomatic to symptomatic SCC may be utilized as a non-invasive imaging biomarker to predict disease progression and useful for patient monitoring and treatment planning. Additionally, such studies may be able to further identify cerebral signatures responsible for effective motor and neurological compensation. As previously mentioned, the preliminary findings investigating sex differences in ASCC and DCM cohorts exclusively will benefit from larger patient cohorts and have the statistical power to identify important disease- and sex-specific cerebral signatures.

To the best of our knowledge, the studies descripted in this dissertation were the first to incorporate sex as a biological variable when investigating DCM and revealed sex-dependent cerebral reorganization indicative of differing cerebral compensatory mechanisms. However, future studies are necessary to understand the relationship between sex-hormone concentration, cerebral reorganization, and functional recovery in DCM. Collection of patient blood samples and analysis of sex hormone serum concentrations, including testosterone, estrogen, and progesterone, will provide critical quantitative data. Not only can hormone concentration be examined in relation to neurological status and neuroimaging-based measurements of the brain and spine but can be measured in patients pre- and post-operatively and may be able to predict functional recovery.

Lastly, the dissertation revealed unique thalamic and cerebellar involvement in DCM. The thalamus has been referred to as the brain's "switchboard" and is responsible for relaying information throughout the brain. I suspect alterations within thalamic pathways and connectivity in DCM are a critical compensatory strategy to recruit supplementary pathways, including visual and association pathways, when sensorimotor cortices and corticospinal tracts experience cervical stenosis induced neuronal damage. Such reorganization of thalamic projections can be investigated using DTI and probabilistic tractography in DCM, ASCC, and HC cohorts. Furthermore, the dissertation also indicated unique cerebellar involvement and sex-specific alterations in DCM. The cerebellum is known to be critical for motor planning, coordination, and balance. However, in the context of DCM and ASCC, the role of the cerebellum remained relatively understudied. Future studies will benefit from a more comprehensive investigation of the cerebellum by utilizing cerebellar atlases and advanced imaging techniques, including probabilistic tractography and seed-to-voxel functional connectivity analyses, to uncover alterations between the cerebellum, cerebrum, and brainstem in DCM. With a better understanding of thalamic and cerebellar reorganization, we may develop imaging biomarkers to predict disease progression and prognosis in patients with DCM and ASCC.

References

1. Theodore N (2020) Degenerative Cervical Spondylosis. N Engl J Med 383(2):159-168. https://doi.org/10.1056/NEJMra2003558

2. Tracy JA, Bartleson JD (2010) Cervical spondylotic myelopathy. Neurologist 16(3):176-187. https://doi.org/10.1097/NRL.0b013e3181da3a29

3. Karadimas SK, Erwin WM, Ely CG, Dettori JR, Fehlings MG (2013) Pathophysiology and natural history of cervical spondylotic myelopathy. Spine (Phila Pa 1976) 38(22 Suppl 1):S21-36. https://doi.org/10.1097/BRS.0b013e3182a7f2c3

4. Binder AI (2007) Cervical spondylosis and neck pain. BMJ 334(7592):527-531. https://doi.org/10.1136/bmj.39127.608299.80

5. Badhiwala JH, Ahuja CS, Akbar MA, Witiw CD, Nassiri F, Furlan JC, Curt A, Wilson JR, Fehlings MG (2020) Degenerative cervical myelopathy - update and future directions. Nat Rev Neurol 16(2):108-124. https://doi.org/10.1038/s41582-019-0303-0

6. Fehlings MG, Wilson JR, Kopjar B, Yoon ST, Arnold PM, Massicotte EM, Vaccaro AR, Brodke DS, Shaffrey CI, Smith JS, Woodard EJ, Banco RJ, Chapman JR, Janssen ME, Bono CM, Sasso RC, Dekutoski MB, Gokaslan ZL (2013) Efficacy and safety of surgical decompression in patients with cervical spondylotic myelopathy: results of the AOSpine North America prospective multi-center study. J Bone Joint Surg Am 95(18):1651-1658. https://doi.org/10.2106/JBJS.L.00589

7. Kato S, Fehlings M (2016) Degenerative cervical myelopathy. Curr Rev Musculoskelet Med 9(3):263-271. https://doi.org/10.1007/s12178-016-9348-5

8. Nouri A, Tetreault L, Singh A, Karadimas SK, Fehlings MG (2015) Degenerative Cervical Myelopathy: Epidemiology, Genetics, and Pathogenesis. Spine (Phila Pa 1976) 40(12):E675-693. https://doi.org/10.1097/BRS.0000000000000913

9. Goel A (2018) Ossification of posterior longitudinal ligament and cervical spondylosis: Same cause - Same treatment. J Craniovertebr Junction Spine 9(1):1-2. https://doi.org/10.4103/jcvjs.JCVJS_34_18

10. Nouri A, Tessitore E, Molliqaj G, Meling T, Schaller K, Nakashima H, Yukawa Y, Bednarik J, Martin AR, Vajkoczy P, Cheng JS, Kwon BK, Kurpad SN, Fehlings MG, Harrop JS, Aarabi B, Rahimi-Movaghar V, Guest JD, Davies BM, Kotter MRN, Wilson JR (2022) Degenerative Cervical Myelopathy: Development and Natural History [AO Spine RECODE-DCM Research Priority Number 2]. Global Spine J 12(1_suppl):39S-54S. https://doi.org/10.1177/21925682211036071

11. Wilder FV, Fahlman L, Donnelly R (2011) Radiographic cervical spine osteoarthritis progression rates: a longitudinal assessment. Rheumatol Int 31(1):45-48. https://doi.org/10.1007/s00296-009-1216-9

12. Northover JR, Wild JB, Braybrooke J, Blanco J (2012) The epidemiology of cervical spondylotic myelopathy. Skeletal Radiol 41(12):1543-1546. https://doi.org/10.1007/s00256-012-1388-3

13. Choi SH, Kang CN (2020) Degenerative Cervical Myelopathy: Pathophysiology and Current Treatment Strategies. Asian Spine J 14(5):710-720. https://doi.org/10.31616/asj.2020.0490

14. Dolan RT, Butler JS, O'Byrne JM, Poynton AR (2016) Mechanical and cellular processes driving cervical myelopathy. World J Orthop 7(1):20-29. https://doi.org/10.5312/wjo.v7.i1.20

15. Karadimas SK, Gatzounis G, Fehlings MG (2015) Pathobiology of cervical spondylotic myelopathy. Eur Spine J 24 Suppl 2:132-138. https://doi.org/10.1007/s00586-014-3264-4

16. Pope DH, Davies BM, Mowforth OD, Bowden AR, Kotter MRN (2020) Genetics of Degenerative Cervical Myelopathy: A Systematic Review and Meta-Analysis of Candidate Gene Studies. J Clin Med 9(1). https://doi.org/10.3390/jcm9010282

17. Wilson JR, Patel AA, Brodt ED, Dettori JR, Brodke DS, Fehlings MG (2013) Genetics and heritability of cervical spondylotic myelopathy and ossification of the posterior longitudinal ligament: results of a systematic review. Spine (Phila Pa 1976) 38(22 Suppl 1):S123-146. https://doi.org/10.1097/BRS.0b013e3182a7f478

18. Patel AA, Spiker WR, Daubs M, Brodke DS, Cannon-Albright LA (2012) Evidence of an inherited predisposition for cervical spondylotic myelopathy. Spine (Phila Pa 1976) 37(1):26-29. https://doi.org/10.1097/BRS.0b013e3182102ede

19. Singh A, Tetreault L, Fehlings MG, Fischer DJ, Skelly AC (2012) Risk factors for development of cervical spondylotic myelopathy: results of a systematic review. Evid Based Spine Care J 3(3):35-42. https://doi.org/10.1055/s-0032-1327808

20. Singh S, Kumar D, Kumar S (2014) Risk factors in cervical spondylosis. J Clin Orthop Trauma 5(4):221-226. https://doi.org/10.1016/j.jcot.2014.07.007

21. Tetreault L, Kopjar B, Nouri A, Arnold P, Barbagallo G, Bartels R, Qiang Z, Singh A, Zileli M, Vaccaro A, Fehlings MG (2017) The modified Japanese Orthopaedic Association scale: establishing criteria for mild, moderate and severe impairment in patients with degenerative cervical myelopathy. Eur Spine J 26(1):78-84. https://doi.org/10.1007/s00586-016-4660-8

22. Sterling M, Rebbeck T (2005) The Neck Disability Index (NDI). Aust J Physiother 51(4):271. https://doi.org/10.1016/s0004-9514(05)70017-9

23. Nurick S (1972) The pathogenesis of the spinal cord disorder associated with cervical spondylosis. Brain 95(1):87-100. https://doi.org/10.1093/brain/95.1.87

24. Bednarik J, Kadanka Z, Dusek L, Kerkovsky M, Vohanka S, Novotny O, Urbanek I, Kratochvilova D (2008) Presymptomatic spondylotic cervical myelopathy: an updated predictive model. Eur Spine J 17(3):421-431. https://doi.org/10.1007/s00586-008-0585-1

25. Smith SS, Stewart ME, Davies BM, Kotter MRN (2021) The Prevalence of Asymptomatic and Symptomatic Spinal Cord Compression on Magnetic Resonance Imaging: A Systematic Review and Meta-analysis. Global Spine J 11(4):597-607. https://doi.org/10.1177/2192568220934496

26. Chang V, Ellingson BM, Salamon N, Holly LT (2015) The Risk of Acute Spinal Cord Injury After Minor Trauma in Patients With Preexisting Cervical Stenosis. Neurosurgery 77(4):561-565; discussion 565. https://doi.org/10.1227/NEU.0000000000000888

27. Houten JK, Shahsavarani S, Verma RB (2022) The Natural History of Degenerative Cervical Myelopathy. Clin Spine Surg 35(10):396-402. https://doi.org/10.1097/BSD.0000000000001405

28. Fehlings MG, Kwon BK, Tetreault LA (2017) Guidelines for the Management of Degenerative Cervical Myelopathy and Spinal Cord Injury: An Introduction to a Focus Issue. Global Spine J 7(3 Suppl):6S-7S. https://doi.org/10.1177/2192568217701714

29. Rao RD, Gourab K, David KS (2006) Operative treatment of cervical spondylotic myelopathy. J Bone Joint Surg Am 88(7):1619-1640. https://doi.org/10.2106/JBJS.F.00014

30. Karadimas SK, Laliberte AM, Tetreault L, Chung YS, Arnold P, Foltz WD, Fehlings MG (2015) Riluzole blocks perioperative ischemia-reperfusion injury and enhances postdecompression outcomes in cervical spondylotic myelopathy. Sci Transl Med 7(316):316ra194. https://doi.org/10.1126/scitranslmed.aac6524

31. Moon ES, Karadimas SK, Yu WR, Austin JW, Fehlings MG (2014) Riluzole attenuates neuropathic pain and enhances functional recovery in a rodent model of cervical spondylotic myelopathy. Neurobiol Dis 62:394-406. https://doi.org/10.1016/j.nbd.2013.10.020

32. Fehlings MG, Badhiwala JH, Ahn H, Farhadi HF, Shaffrey CI, Nassr A, Mummaneni P, Arnold PM, Jacobs WB, Riew KD, Kelly M, Brodke DS, Vaccaro AR, Hilibrand AS, Wilson J, Harrop JS, Yoon ST, Kim KD, Fourney DR, Santaguida C, Massicotte EM, Kopjar B (2021) Safety and efficacy of riluzole in patients undergoing decompressive surgery for degenerative cervical myelopathy (CSM-Protect): a multicentre, double-blind, placebo-controlled, randomised, phase 3 trial. Lancet Neurol 20(2):98-106. https://doi.org/10.1016/S1474-4422(20)30407-5

33. Wilson JRF, Badhiwala JH, Moghaddamjou A, Martin AR, Fehlings MG (2019) Degenerative Cervical Myelopathy; A Review of the Latest Advances and Future Directions in Management. Neurospine 16(3):494-505. https://doi.org/10.14245/ns.1938314.157

34. Jannelli G, Nouri A, Molliqaj G, Grasso G, Tessitore E (2020) Degenerative Cervical Myelopathy: Review of Surgical Outcome Predictors and Need for Multimodal Approach. World Neurosurg 140:541-547. https://doi.org/10.1016/j.wneu.2020.04.233

35. Nouri A, Martin AR, Mikulis D, Fehlings MG (2016) Magnetic resonance imaging assessment of degenerative cervical myelopathy: a review of structural changes and measurement techniques. Neurosurg Focus 40(6):E5. https://doi.org/10.3171/2016.3.FOCUS1667

36. Ellingson BM, Salamon N, Holly LT (2015) Advances in MR imaging for cervical spondylotic myelopathy. Eur Spine J 24 Suppl 2(Suppl 2):197-208. https://doi.org/10.1007/s00586-013-2915-1

37. Nouri A, Martin AR, Kato S, Reihani-Kermani H, Riehm LE, Fehlings MG (2017) The Relationship Between MRI Signal Intensity Changes, Clinical Presentation, and Surgical Outcome in Degenerative Cervical Myelopathy: Analysis of a Global Cohort. Spine (Phila Pa 1976) 42(24):1851-1858. https://doi.org/10.1097/BRS.0000000000002234

38. Alafifi T, Kern R, Fehlings M (2007) Clinical and MRI predictors of outcome after surgical intervention for cervical spondylotic myelopathy. J Neuroimaging 17(4):315-322. https://doi.org/10.1111/j.1552-6569.2007.00119.x

39. Morio Y, Teshima R, Nagashima H, Nawata K, Yamasaki D, Nanjo Y (2001) Correlation between operative outcomes of cervical compression myelopathy and mri of the spinal cord. Spine (Phila Pa 1976) 26(11):1238-1245. https://doi.org/10.1097/00007632-200106010-00012

40. Nouri A, Tetreault L, Zamorano JJ, Dalzell K, Davis AM, Mikulis D, Yee A, Fehlings MG (2015) Role of magnetic resonance imaging in predicting surgical outcome in patients with cervical spondylotic myelopathy. Spine (Phila Pa 1976) 40(3):171-178. https://doi.org/10.1097/BRS.0000000000000678

41. Mummaneni PV, Kaiser MG, Matz PG, Anderson PA, Groff M, Heary R, Holly L, Ryken T, Choudhri T, Vresilovic E, Resnick D, Joint Section on Disorders of the S, Peripheral Nerves of the American Association of Neurological S, Congress of Neurological S (2009) Preoperative patient selection with magnetic resonance imaging, computed tomography, and electroencephalography: does the test predict outcome after cervical surgery? J Neurosurg Spine 11(2):119-129. https://doi.org/10.3171/2009.3.SPINE08717

42. Mastronardi L, Elsawaf A, Roperto R, Bozzao A, Caroli M, Ferrante M, Ferrante L (2007) Prognostic relevance of the postoperative evolution of intramedullary spinal cord changes in signal intensity on magnetic resonance imaging after anterior decompression for cervical spondylotic myelopathy. J Neurosurg Spine 7(6):615-622. https://doi.org/10.3171/SPI-07/12/615

43. Ellingson BM, Salamon N, Holly LT (2014) Imaging techniques in spinal cord injury. World Neurosurg 82(6):1351-1358. https://doi.org/10.1016/j.wneu.2012.12.004

44. Demir A, Ries M, Moonen CT, Vital JM, Dehais J, Arne P, Caille JM, Dousset V (2003) Diffusion-weighted MR imaging with apparent diffusion coefficient and apparent diffusion tensor maps in cervical spondylotic myelopathy. Radiology 229(1):37-43. https://doi.org/10.1148/radiol.2291020658

45. Ellingson BM, Salamon N, Grinstead JW, Holly LT (2014) Diffusion tensor imaging predicts functional impairment in mild-to-moderate cervical spondylotic myelopathy. Spine J 14(11):2589-2597. https://doi.org/10.1016/j.spinee.2014.02.027

46. Budzik JF, Balbi V, Le Thuc V, Duhamel A, Assaker R, Cotten A (2011) Diffusion tensor imaging and fibre tracking in cervical spondylotic myelopathy. Eur Radiol 21(2):426-433. https://doi.org/10.1007/s00330-010-1927-z

47. Jones JG, Cen SY, Lebel RM, Hsieh PC, Law M (2013) Diffusion tensor imaging correlates with the clinical assessment of disease severity in cervical spondylotic myelopathy and predicts outcome following surgery. AJNR Am J Neuroradiol 34(2):471-478. https://doi.org/10.3174/ajnr.A3199

48. Wen CY, Cui JL, Mak KC, Luk KD, Hu Y (2014) Diffusion tensor imaging of somatosensory tract in cervical spondylotic myelopathy and its link with electrophysiological evaluation. Spine J 14(8):1493-1500. https://doi.org/10.1016/j.spinee.2013.08.052

49. Hori M, Aoki S, Okubo T, Ishigame K, Kumagai H, Araki T (2005) Line-scan diffusion tensor MR imaging at 0.2 T: feasibility study. J Magn Reson Imaging 22(6):794-798. https://doi.org/10.1002/jmri.20440

50. Kerkovsky M, Bednarik J, Dusek L, Sprlakova-Pukova A, Urbanek I, Mechl M, Valek V, Kadanka Z (2012) Magnetic resonance diffusion tensor imaging in patients with cervical spondylotic spinal cord compression: correlations between clinical and electrophysiological findings. Spine (Phila Pa 1976) 37(1):48-56. https://doi.org/10.1097/BRS.0b013e31820e6c35

51. Mamata H, Jolesz FA, Maier SE (2005) Apparent diffusion coefficient and fractional anisotropy in spinal cord: age and cervical spondylosis-related changes. J Magn Reson Imaging 22(1):38-43. https://doi.org/10.1002/jmri.20357

52. Uda T, Takami T, Tsuyuguchi N, Sakamoto S, Yamagata T, Ikeda H, Nagata T, Ohata K (2013) Assessment of cervical spondylotic myelopathy using diffusion tensor magnetic resonance imaging parameter at 3.0 tesla. Spine (Phila Pa 1976) 38(5):407-414. https://doi.org/10.1097/BRS.0b013e31826f25a3

53. Sato T, Horikoshi T, Watanabe A, Uchida M, Ishigame K, Araki T, Kinouchi H (2012) Evaluation of cervical myelopathy using apparent diffusion coefficient measured by diffusion-weighted imaging. AJNR Am J Neuroradiol 33(2):388-392. https://doi.org/10.3174/ajnr.A2756

54. Wyss PO, Hock A, Kollias S (2017) The Application of Human Spinal Cord Magnetic Resonance Spectroscopy to Clinical Studies: A Review. Semin Ultrasound CT MR 38(2):153-162. https://doi.org/10.1053/j.sult.2016.07.005

55. Kendi AT, Tan FU, Kendi M, Yilmaz S, Huvaj S, Tellioglu S (2004) MR spectroscopy of cervical spinal cord in patients with multiple sclerosis. Neuroradiology 46(9):764-769. https://doi.org/10.1007/s00234-004-1231-1

56. Holly LT, Freitas B, McArthur DL, Salamon N (2009) Proton magnetic resonance spectroscopy to evaluate spinal cord axonal injury in cervical spondylotic myelopathy. J Neurosurg Spine 10(3):194-200. https://doi.org/10.3171/2008.12.SPINE08367

57. Ellingson BM, Salamon N, Hardy AJ, Holly LT (2015) Prediction of Neurological Impairment in Cervical Spondylotic Myelopathy using a Combination of Diffusion MRI and Proton MR Spectroscopy. PLoS One 10(10):e0139451. https://doi.org/10.1371/journal.pone.0139451

58. Salamon N, Ellingson BM, Nagarajan R, Gebara N, Thomas A, Holly LT (2013) Proton magnetic resonance spectroscopy of human cervical spondylosis at 3T. Spinal Cord 51(7):558-563. https://doi.org/10.1038/sc.2013.31

59. Woodworth DC, Holly LT, Mayer EA, Salamon N, Ellingson BM (2019) Alterations in Cortical Thickness and Subcortical Volume are Associated With Neurological Symptoms and Neck Pain in Patients With Cervical Spondylosis. Neurosurgery 84(3):588-598. https://doi.org/10.1093/neuros/nyy066

60. Jutten K, Mainz V, Schubert GA, Fabian Gohmann R, Schmidt T, Ridwan H, Clusmann H, Mueller CA, Blume C (2021) Cortical volume reductions as a sign of secondary cerebral and cerebellar impairment in patients with degenerative cervical myelopathy. Neuroimage Clin 30:102624. https://doi.org/10.1016/j.nicl.2021.102624

61. Zhou Y, Shi J (2022) Brain Structural and Functional Dissociated Patterns in Degenerative Cervical Myelopathy: A Case-Controlled Retrospective Resting-State fMRI Study. Front Neurol 13:895348. https://doi.org/10.3389/fneur.2022.895348

62. Yang Q, Xu H, Zhang M, Wang Y, Li D (2020) Volumetric and functional connectivity alterations in patients with chronic cervical spondylotic pain. Neuroradiology 62(8):995-1001. https://doi.org/10.1007/s00234-020-02413-z

63. Kuang C, Zha Y, Liu C, Chen J (2020) Altered Topological Properties of Brain Structural Covariance Networks in Patients With Cervical Spondylotic Myelopathy. Front Hum Neurosci 14:364. https://doi.org/10.3389/fnhum.2020.00364

64. Liu M, Tan Y, Zhang C, He L (2021) Cortical anatomy plasticity in cases of cervical spondylotic myelopathy associated with decompression surgery: A strobe-compliant study of structural magnetic resonance imaging. Medicine (Baltimore) 100(4):e24190. https://doi.org/10.1097/MD.0000000000024190

65. Grabher P, Mohammadi S, Trachsler A, Friedl S, David G, Sutter R, Weiskopf N, Thompson AJ, Curt A, Freund P (2016) Voxel-based analysis of grey and white matter degeneration in cervical spondylotic myelopathy. Sci Rep 6:24636. https://doi.org/10.1038/srep24636

66. Wang C, Laiwalla A, Salamon N, Ellingson BM, Holly LT (2020) Compensatory brainstem functional and structural connectivity in patients with degenerative cervical myelopathy by probabilistic tractography and functional MRI. Brain Res 1749:147129. https://doi.org/10.1016/j.brainres.2020.147129

67. Bernabeu-Sanz A, Molla-Torro JV, Lopez-Celada S, Moreno Lopez P, Fernandez-Jover E (2020) MRI evidence of brain atrophy, white matter damage, and functional adaptive changes in patients with cervical spondylosis and prolonged spinal cord compression. Eur Radiol 30(1):357-369. https://doi.org/10.1007/s00330-019-06352-z

68. Wang C, Holly LT, Oughourlian T, Yao J, Raymond C, Salamon N, Ellingson BM (2021) Detection of cerebral reorganization associated with degenerative cervical myelopathy using diffusion spectral imaging (DSI). J Clin Neurosci 86:164-173. https://doi.org/10.1016/j.jocn.2021.01.011

69. Wang C, Ellingson BM, Salamon N, Holly LT (2022) Recovery of Supraspinal Microstructural Integrity and Connectivity in Patients Undergoing Surgery for Degenerative Cervical Myelopathy. Neurosurgery 90(4):447-456. https://doi.org/10.1227/NEU.0000000000001839

70. Kowalczyk I, Duggal N, Bartha R (2012) Proton magnetic resonance spectroscopy of the motor cortex in cervical myelopathy. Brain 135(Pt 2):461-468. https://doi.org/10.1093/brain/awr328

71. Zhao R, Guo X, Wang Y, Song Y, Su Q, Sun H, Liang M, Xue Y (2022) Functional MRI evidence for primary motor cortex plasticity contributes to the disease's severity and prognosis of cervical spondylotic myelopathy patients. Eur Radiol 32(6):3693-3704. https://doi.org/10.1007/s00330-021-08488-3

72. Zhou FQ, Tan YM, Wu L, Zhuang Y, He LC, Gong HH (2015) Intrinsic functional plasticity of the sensory-motor network in patients with cervical spondylotic myelopathy. Sci Rep 5:9975. https://doi.org/10.1038/srep09975

73. Woodworth DC, Holly LT, Salamon N, Ellingson BM (2018) Resting-State Functional Magnetic Resonance Imaging Connectivity of the Brain Is Associated with Altered Sensorimotor Function in Patients with Cervical Spondylosis. World Neurosurg 119:e740-e749. https://doi.org/10.1016/j.wneu.2018.07.257

74. Holly LT, Wang C, Woodworth DC, Salamon N, Ellingson BM (2019) Neck disability in patients with cervical spondylosis is associated with altered brain functional connectivity. J Clin Neurosci 69:149-154. https://doi.org/10.1016/j.jocn.2019.08.008

75. Duggal N, Rabin D, Bartha R, Barry RL, Gati JS, Kowalczyk I, Fink M (2010) Brain reorganization in patients with spinal cord compression evaluated using fMRI. Neurology 74(13):1048-1054. https://doi.org/10.1212/WNL.0b013e3181d6b0ea

76. Cronin AE, Detombe SA, Duggal CA, Duggal N, Bartha R (2021) Spinal cord compression is associated with brain plasticity in degenerative cervical myelopathy. Brain Commun 3(3):fcab131. https://doi.org/10.1093/braincomms/fcab131

77. Wang C, Ellingson BM, Oughourlian TC, Salamon N, Holly LT (2022) Evolution of brain functional plasticity associated with increasing symptom severity in degenerative cervical myelopathy. EBioMedicine 84:104255. https://doi.org/10.1016/j.ebiom.2022.104255

78. Wang C, Ellingson BM, Islam S, Laiwalla A, Salamon N, Holly LT (2021) Supraspinal functional and structural plasticity in patients undergoing surgery for degenerative cervical myelopathy. J Neurosurg Spine:1-9. https://doi.org/10.3171/2020.11.SPINE201688

79. Young WF (2000) Cervical spondylotic myelopathy: a common cause of spinal cord dysfunction in older persons. Am Fam Physician 62(5):1064-1070, 1073

80. Yonenobu K, Abumi K, Nagata K, Taketomi E, Ueyama K (2001) Interobserver and intraobserver reliability of the japanese orthopaedic association scoring system for evaluation of cervical compression myelopathy. Spine (Phila Pa 1976) 26(17):1890-1894; discussion 1895. https://doi.org/10.1097/00007632-200109010-00014

81. Fischl B, Sereno MI, Dale AM (1999) Cortical surface-based analysis. II: Inflation, flattening, and a surface-based coordinate system. Neuroimage 9(2):195-207. https://doi.org/10.1006/nimg.1998.0396

82. Desikan RS, Segonne F, Fischl B, Quinn BT, Dickerson BC, Blacker D, Buckner RL, Dale AM, Maguire RP, Hyman BT, Albert MS, Killiany RJ (2006) An automated labeling system for subdividing the human cerebral cortex on MRI scans into gyral based regions of interest. Neuroimage 31(3):968-980. https://doi.org/10.1016/j.neuroimage.2006.01.021

83. Gupta A, Mayer EA, Sanmiguel CP, Van Horn JD, Woodworth D, Ellingson BM, Fling C, Love A, Tillisch K, Labus JS (2015) Patterns of brain structural connectivity differentiate normal weight from overweight subjects. Neuroimage Clin 7:506-517. https://doi.org/10.1016/j.nicl.2015.01.005

84. Taki Y, Kinomura S, Sato K, Inoue K, Goto R, Okada K, Uchida S, Kawashima R, Fukuda H (2008) Relationship between body mass index and gray matter volume in 1,428 healthy individuals. Obesity (Silver Spring) 16(1):119-124. https://doi.org/10.1038/oby.2007.4

85. Whitfield-Gabrieli S, Nieto-Castanon A (2012) Conn: a functional connectivity toolbox for correlated and anticorrelated brain networks. Brain Connect 2(3):125-141. https://doi.org/10.1089/brain.2012.0073

86. Rolls ET, Huang CC, Lin CP, Feng J, Joliot M (2020) Automated anatomical labelling atlas 3. Neuroimage 206:116189. https://doi.org/10.1016/j.neuroimage.2019.116189

87. Donofry SD, Stillman CM, Erickson KI (2020) A review of the relationship between eating behavior, obesity and functional brain network organization. Soc Cogn Affect Neurosci 15(10):1157-1181. https://doi.org/10.1093/scan/nsz085

88. Figley CR, Asem JS, Levenbaum EL, Courtney SM (2016) Effects of Body Mass Index and Body Fat Percent on Default Mode, Executive Control, and Salience Network Structure and Function. Front Neurosci 10:234. https://doi.org/10.3389/fnins.2016.00234

89. Park BY, Seo J, Yi J, Park H (2015) Structural and Functional Brain Connectivity of People with Obesity and Prediction of Body Mass Index Using Connectivity. Plos One 10(11):e0141376. https://doi.org/10.1371/journal.pone.0141376

90. Calamante F, Tournier JD, Smith RE, Connelly A (2012) A generalised framework for super-resolution track-weighted imaging. Neuroimage 59(3):2494-2503. https://doi.org/10.1016/j.neuroimage.2011.08.099

91. Martin AR, De Leener B, Cohen-Adad J, Cadotte DW, Nouri A, Wilson JR, Tetreault L, Crawley AP, Mikulis DJ, Ginsberg H, Fehlings MG (2018) Can microstructural MRI detect subclinical tissue injury in subjects with asymptomatic cervical spinal cord compression? A prospective cohort study. Bmj Open 8(4). https://doi.org/ARTN e019809

10.1136/bmjopen-2017-019809

92. Shabani S, Kaushal M, Budde MD, Wang MC, Kurpad SN (2020) Diffusion tensor imaging in cervical spondylotic myelopathy: a review. J Neurosurg Spine:1-8. https://doi.org/10.3171/2019.12.SPINE191158

93. Cao JM, Zhang JT, Yang DL, Yang YP, Xia HH, Yang L (2017) Imaging Factors that Distinguish Between Patients with Asymptomatic and Symptomatic Cervical Spondylotic Myelopathy with Mild to Moderate Cervical Spinal Cord Compression. Med Sci Monit 23:4901-4908. https://doi.org/10.12659/msm.906937

94. Soares JM, Marques P, Alves V, Sousa N (2013) A hitchhiker's guide to diffusion tensor imaging. Front Neurosci 7:31. https://doi.org/10.3389/fnins.2013.00031

95. Wycoco V, Shroff M, Sudhakar S, Lee W (2013) White matter anatomy: what the radiologist needs to know. Neuroimaging Clin N Am 23(2):197-216. https://doi.org/10.1016/j.nic.2012.12.002

96. George K, J MD (2022) Neuroanatomy, Thalamocortical Radiations. In: StatPearls. Treasure Island (FL),

97. Jimsheleishvili S, Dididze M (2022) Neuroanatomy, Cerebellum. In: StatPearls. Treasure Island (FL),

98. Huff T, Mahabadi N, Tadi P (2022) Neuroanatomy, Visual Cortex. In: StatPearls. Treasure Island (FL),

99. Chen Z, Zhao R, Wang Q, Yu C, Li F, Liang M, Zong Y, Zhao Y, Xiong W, Su Z, Xue Y (2020) Functional Connectivity Changes of the Visual Cortex in the Cervical Spondylotic Myelopathy Patients: A Resting-State fMRI Study. Spine (Phila Pa 1976) 45(5):E272-E279. https://doi.org/10.1097/BRS.0000000000003245

100. Doble A (1996) The pharmacology and mechanism of action of riluzole. Neurology 47(6 Suppl 4):S233-241. https://doi.org/10.1212/wnl.47.6_suppl_4.233s

101. Harrison JK, Jiang Y, Chen S, Xia Y, Maciejewski D, McNamara RK, Streit WJ, Salafranca MN, Adhikari S, Thompson DA, Botti P, Bacon KB, Feng L (1998) Role for neuronally derived fractalkine in mediating interactions between neurons and CX3CR1-expressing microglia. Proc Natl Acad Sci U S A 95(18):10896-10901. https://doi.org/10.1073/pnas.95.18.10896

102. Fumagalli S, Perego C, Ortolano F, De Simoni MG (2013) CX3CR1 deficiency induces an early protective inflammatory environment in ischemic mice. Glia 61(6):827-842. https://doi.org/10.1002/glia.22474

103. Abode-Iyamah KO, Stoner KE, Grossbach AJ, Viljoen SV, McHenry CL, Petrie MA, Dahdaleh NS, Grosland NM, Shields RK, Howard MA, 3rd (2016) Effects of brain derived neurotrophic factor Val66Met polymorphism in patients with cervical spondylotic myelopathy. J Clin Neurosci 24:117-121. https://doi.org/10.1016/j.jocn.2015.07.016

104. Wang ZC, Hou XW, Shao J, Ji YJ, Li L, Zhou Q, Yu SM, Mao YL, Zhang HJ, Zhang PC, Lu H (2014) HIF-1alpha polymorphism in the susceptibility of cervical spondylotic myelopathy and its outcome after anterior cervical corpectomy and fusion treatment. PLoS One 9(11):e110862. https://doi.org/10.1371/journal.pone.0110862

105. Yu HM, Chen XL, Wei W, Yao XD, Sun JQ, Su XT, Lin SF (2018) Effect of osteoprotegerin gene polymorphisms on the risk of cervical spondylotic myelopathy in a Chinese population. Clin Neurol Neurosurg 175:149-154. https://doi.org/10.1016/j.clineuro.2018.09.013

106. Nishida N, Kato Y, Imajo Y, Kawano S, Taguchi T (2012) Biomechanical analysis of cervical spondylotic myelopathy: the influence of dynamic factors and morphometry of the spinal cord. J Spinal Cord Med 35(4):256-261. https://doi.org/10.1179/2045772312Y.0000000024

107. Yue WM, Tan SB, Tan MH, Koh DC, Tan CT (2001) The Torg--Pavlov ratio in cervical spondylotic myelopathy: a comparative study between patients with cervical spondylotic myelopathy and a nonspondylotic, nonmyelopathic population. Spine (Phila Pa 1976) 26(16):1760-1764. https://doi.org/10.1097/00007632-200108150-00006

108. Pavlov H, Torg JS, Robie B, Jahre C (1987) Cervical spinal stenosis: determination with vertebral body ratio method. Radiology 164(3):771-775. https://doi.org/10.1148/radiology.164.3.3615879

109. Tierney RT, Maldjian C, Mattacola CG, Straub SJ, Sitler MR (2002) Cervical Spine Stenosis Measures in Normal Subjects. J Athl Train 37(2):190-193

110. Prasad SS, O'Malley M, Caplan M, Shackleford IM, Pydisetty RK (2003) MRI measurements of the cervical spine and their correlation to Pavlov's ratio. Spine (Phila Pa 1976) 28(12):1263-1268. https://doi.org/10.1097/01.BRS.0000065570.20888.AA

111. Tempest-Mitchell J, Hilton B, Davies BM, Nouri A, Hutchinson PJ, Scoffings DJ, Mannion RJ, Trivedi R, Timofeev I, Crawford JR, Hay D, Laing RJ, Kotter MRN (2019) A comparison of radiological descriptions of spinal cord compression with quantitative measures, and their role in non-specialist clinical management. PLoS One 14(7):e0219380. https://doi.org/10.1371/journal.pone.0219380

112. Wilson JR, Barry S, Fischer DJ, Skelly AC, Arnold PM, Riew KD, Shaffrey CI, Traynelis VC, Fehlings MG (2013) Frequency, timing, and predictors of neurological dysfunction in the nonmyelopathic patient with cervical spinal cord compression, canal stenosis, and/or ossification

of the posterior longitudinal ligament. Spine (Phila Pa 1976) 38(22 Suppl 1):S37-54. https://doi.org/10.1097/BRS.0b013e3182a7f2e7

113. Lin T, Wang Z, Chen G, Liu W (2021) Predictive effect of cervical spinal cord compression and corresponding segmental paravertebral muscle degeneration on the severity of symptoms in patients with cervical spondylotic myelopathy. Spine J 21(7):1099-1109. https://doi.org/10.1016/j.spinee.2021.03.030

114. Fischl B (2012) FreeSurfer. Neuroimage 62(2):774-781. https://doi.org/10.1016/j.neuroimage.2012.01.021

115. Crandall PH, Batzdorf U (1966) Cervical spondylotic myelopathy. J Neurosurg 25(1):57-66. https://doi.org/10.3171/jns.1966.25.1.0057

116. Ellingson BM, Salamon N, Woodworth DC, Holly LT (2015) Correlation between degree of subvoxel spinal cord compression measured with super-resolution tract density imaging and neurological impairment in cervical spondylotic myelopathy. J Neurosurg Spine 22(6):631-638. https://doi.org/10.3171/2014.10.SPINE14222

117. Seif M, David G, Huber E, Vallotton K, Curt A, Freund P (2020) Cervical Cord Neurodegeneration in Traumatic and Non-Traumatic Spinal Cord Injury. J Neurotrauma 37(6):860-867. https://doi.org/10.1089/neu.2019.6694

118. Vallotton K, David G, Hupp M, Pfender N, Cohen-Adad J, Fehlings MG, Samson RS, Wheeler-Kingshott C, Curt A, Freund P, Seif M (2021) Tracking White and Gray Matter Degeneration along the Spinal Cord Axis in Degenerative Cervical Myelopathy. J Neurotrauma 38(21):2978-2987. https://doi.org/10.1089/neu.2021.0148

119. Gohmann RF, Blume C, Zvyagintsev M, Mainz V, Clusmann H, Wiesmann M, Brockmann MA, Mueller CA (2019) Cervical spondylotic myelopathy: Changes of fractional anisotropy in the spinal cord and magnetic resonance spectroscopy of the primary motor cortex in relation to clinical symptoms and their duration. Eur J Radiol 116:55-60. https://doi.org/10.1016/j.ejrad.2019.04.009

120. Gao SJ, Yuan X, Jiang XY, Liu XX, Liu XP, Wang YF, Cao JB, Bai LN, Xu K (2013) Correlation study of 3T-MR-DTI measurements and clinical symptoms of cervical spondylotic myelopathy. Eur J Radiol 82(11):1940-1945. https://doi.org/10.1016/j.ejrad.2013.06.011

121. Golash A, Birchall D, Laitt RD, Jackson A (2001) Significance of CSF area measurements in cervical spondylitic myelopathy. Br J Neurosurg 15(1):17-21. https://doi.org/10.1080/02688690020024337

122. Dobkin BH (2000) Spinal and supraspinal plasticity after incomplete spinal cord injury: correlations between functional magnetic resonance imaging and engaged locomotor networks. Prog Brain Res 128:99-111. https://doi.org/10.1016/S0079-6123(00)28010-2

123. Ito T, Oyanagi K, Takahashi H, Takahashi HE, Ikuta F (1996) Cervical spondylotic myelopathy. Clinicopathologic study on the progression pattern and thin myelinated fibers of the

lesions of seven patients examined during complete autopsy. Spine (Phila Pa 1976) 21(7):827-833. https://doi.org/10.1097/00007632-199604010-00010

124. Tan S, Faull RLM, Curtis MA (2022) The tracts, cytoarchitecture, and neurochemistry of the spinal cord. Anat Rec (Hoboken). https://doi.org/10.1002/ar.25079

125. Al-Chalabi M, Reddy V, Alsalman I (2022) Neuroanatomy, Posterior Column (Dorsal Column). In: StatPearls. Treasure Island (FL),

126. Ellingson BM, Salamon N, Woodworth DC, Yokota H, Holly LT (2018) Reproducibility, temporal stability, and functional correlation of diffusion MR measurements within the spinal cord in patients with asymptomatic cervical stenosis or cervical myelopathy. J Neurosurg Spine 28(5):472-480. https://doi.org/10.3171/2017.7.SPINE176

127. Ellingson BM, Salamon N, Holly LT (2015) Advances in MR imaging for cervical spondylotic myelopathy. Eur Spine J 24 Suppl 2:197-208. https://doi.org/10.1007/s00586-013-2915-1

128. Henning A, Schar M, Kollias SS, Boesiger P, Dydak U (2008) Quantitative magnetic resonance spectroscopy in the entire human cervical spinal cord and beyond at 3T. Magn Reson Med 59(6):1250-1258. https://doi.org/10.1002/mrm.21578

129. Wang L, Yu B, Li Q, Qi F, Guo Q (2018) Sensorimotor cortex atrophy in patients with cervical spondylotic myelopathy. Neuroreport 29(10):826-832. https://doi.org/10.1097/WNR.0000000000001039

130. Ellingson BM, Mayer E, Harris RJ, Ashe-McNally C, Naliboff BD, Labus JS, Tillisch K (2013) Diffusion tensor imaging detects microstructural reorganization in the brain associated with chronic irritable bowel syndrome. Pain 154(9):1528-1541. https://doi.org/10.1016/j.pain.2013.04.010

131. Salat DH, Buckner RL, Snyder AZ, Greve DN, Desikan RS, Busa E, Morris JC, Dale AM, Fischl B (2004) Thinning of the cerebral cortex in aging. Cereb Cortex 14(7):721-730. https://doi.org/10.1093/cercor/bhh032

132. Nakajima R, Kinoshita M, Shinohara H, Nakada M (2020) The superior longitudinal fascicle: reconsidering the fronto-parietal neural network based on anatomy and function. Brain Imaging Behav 14(6):2817-2830. https://doi.org/10.1007/s11682-019-00187-4

133. Cho SH, Kim DG, Kim DS, Kim YH, Lee CH, Jang SH (2007) Motor outcome according to the integrity of the corticospinal tract determined by diffusion tensor tractography in the early stage of corona radiata infarct. Neurosci Lett 426(2):123-127. https://doi.org/10.1016/j.neulet.2007.08.049

134. Jang SH (2009) A review of corticospinal tract location at corona radiata and posterior limb of the internal capsule in human brain. NeuroRehabilitation 24(3):279-283. https://doi.org/10.3233/NRE-2009-0479

135. Holly LT, Dong Y, Albistegui-DuBois R, Marehbian J, Dobkin B (2007) Cortical reorganization in patients with cervical spondylotic myelopathy. Journal of Neurosurgery-Spine 6(6):544-551. https://doi.org/DOI 10.3171/spi.2007.6.6.5

136. Kovesdi E, Szabo-Meleg E, Abraham IM (2020) The Role of Estradiol in Traumatic Brain Injury: Mechanism and Treatment Potential. Int J Mol Sci 22(1). https://doi.org/10.3390/ijms22010011

137. Elkabes S, Nicot AB (2014) Sex steroids and neuroprotection in spinal cord injury: A review of preclinical investigations. Experimental Neurology 259:28-37. https://doi.org/10.1016/j.expneurol.2014.01.008

138. Byers JS, Huguenard AL, Kuruppu D, Liu NK, Xu XM, Sengelaub DR (2012) Neuroprotective Effects of Testosterone on Motoneuron and Muscle Morphology Following Spinal Cord Injury. J Comp Neurol 520(12):2683-2696. https://doi.org/10.1002/cne.23066

139. Sengelaub DR, Han Q, Liu NK, Maczuga MA, Szalavari V, Valencia SA, Xu XM (2018) Protective Effects of Estradiol and Dihydrotestosterone following Spinal Cord Injury. Journal of Neurotrauma 35(6):825-841. https://doi.org/10.1089/neu.2017.5329

140. Zendedel A, Monnink F, Hassanzadeh G, Zaminy A, Ansar M, Habib P, Slowik A, Kipp M, Beyer C (2018) Estrogen Attenuates Local Inflammasome Expression and Activation after Spinal Cord Injury. Molecular Neurobiology 55(2):1364-1375. https://doi.org/10.1007/s12035-017-0400-2

141. Aminmansour B, Asnaashari A, Rezvani M, Ghaffarpasand F, Amin Noorian SM, Saboori M, Abdollahzadeh P (2016) Effects of progesterone and vitamin D on outcome of patients with acute traumatic spinal cord injury; a randomized, double-blind, placebo controlled study. J Spinal Cord Med 39(3):272-280. https://doi.org/10.1080/10790268.2015.1114224

142. Garcia-Ovejero D, Gonzalez S, Paniagua-Torija B, Lima A, Molina-Holgado E, De Nicola AF, Labombarda F (2014) Progesterone reduces secondary damage, preserves white matter, and improves locomotor outcome after spinal cord contusion. J Neurotrauma 31(9):857-871. https://doi.org/10.1089/neu.2013.3162

143. Wagner AK, McCullough EH, Niyonkuru C, Ozawa H, Loucks TL, Dobos JA, Brett CA, Santarsieri M, Dixon CE, Berga SL, Fabio A (2011) Acute serum hormone levels: characterization and prognosis after severe traumatic brain injury. J Neurotrauma 28(6):871-888. https://doi.org/10.1089/neu.2010.1586

144. Golz C, Kirchhoff FP, Westerhorstmann J, Schmidt M, Hirnet T, Rune GM, Bender RA, Schafer MKE (2019) Sex hormones modulate pathogenic processes in experimental traumatic brain injury. J Neurochem 150(2):173-187. https://doi.org/10.1111/jnc.14678

145. Sarkaki AR, Khaksari Haddad M, Soltani Z, Shahrokhi N, Mahmoodi M (2013) Time- and dose-dependent neuroprotective effects of sex steroid hormones on inflammatory cytokines after a traumatic brain injury. J Neurotrauma 30(1):47-54. https://doi.org/10.1089/neu.2010.1686

146. Zhong YH, Wu HY, He RH, Zheng BE, Fan JZ (2019) Sex Differences in Sex Hormone Profiles and Prediction of Consciousness Recovery After Severe Traumatic Brain Injury. Front Endocrinol (Lausanne) 10:261. https://doi.org/10.3389/fendo.2019.00261

147. Stewart AN, MacLean SM, Stromberg AJ, Whelan JP, Bailey WM, Gensel JC, Wilson ME (2020) Considerations for Studying Sex as a Biological Variable in Spinal Cord Injury (vol 11, 802, 2020). Frontiers in Neurology 11. https://doi.org/ARTN 597689

10.3389/fneur.2020.597689

148. Imaging Data Parkinson's Progression Markers Initiative (PPMI). Accessed 2021

149. Desikan RS, Segonne F, Fischl B, Quinn BT, Dickerson BC, Blacker D, Buckner RL, Dale AM, Maguire RP, Hyman BT, Albert MS, Killiany RJ (2006) An automated labeling system for subdividing the human cerebral cortex on MRI scans into gyral based regions of interest. Neuroimage 31(3):968-980. https://doi.org/10.1016/j.neuroimage.2006.01.021

150. Lemaitre H, Goldman AL, Sambataro F, Verchinski BA, Meyer-Lindenberg A, Weinberger DR, Mattay VS (2012) Normal age-related brain morphometric changes: nonuniformity across cortical thickness, surface area and gray matter volume? Neurobiol Aging 33(3):617 e611-619. https://doi.org/10.1016/j.neurobiolaging.2010.07.013

151. Good CD, Johnsrude I, Ashburner J, Henson RN, Friston KJ, Frackowiak RS (2001) Cerebral asymmetry and the effects of sex and handedness on brain structure: a voxel-based morphometric analysis of 465 normal adult human brains. Neuroimage 14(3):685-700. https://doi.org/10.1006/nimg.2001.0857

152. Chen XH, Sachdev PS, Wen W, Anstey KJ (2007) Sex differences in regional gray matter in healthy individuals aged 44-48 years: A voxel-based morphometric study. Neuroimage 36(3):691-699. https://doi.org/10.1016/j.neuroimage.2007.03.063

153. Fjell AM, Westlye LT, Amlien I, Espeseth T, Reinvang I, Raz N, Agartz I, Salat DH, Greve DN, Fischl B, Dale AM, Walhovd KB (2009) Minute Effects of Sex on the Aging Brain: A Multisample Magnetic Resonance Imaging Study of Healthy Aging and Alzheimer's Disease. Journal of Neuroscience 29(27):8774-8783. https://doi.org/10.1523/Jneurosci.0115-09.2009

154. Smith CD, Chebrolu H, Wekstein DR, Schmitt FA, Markesbery WR (2007) Age and gender effects on human brain anatomy: A voxel-based morphometric study in healthy elderly. Neurobiology of Aging 28(7):1075-1087. https://doi.org/10.1016/j.neurobiolaging.2006.05.018

155. Sanchis-Segura C, Ibanez-Gual MV, Adrian-Ventura J, Aguirre N, Gomez-Cruz AJ, Avila C, Forn C (2019) Sex differences in gray matter volume: how many and how large are they really? Biology of Sex Differences 10. https://doi.org/ARTN 32

10.1186/s13293-019-0245-7

156. Dong Y, Holly LT, Albistegui-Dubois R, Yan XH, Marehbian J, Newton JM, Dobkin BH (2008) Compensatory cerebral adaptations before and evolving changes after surgical

decompression in cervical spondylotic myelopathy. Journal of Neurosurgery-Spine 9(6):538-551. https://doi.org/10.3171/Spi.2008.10.0831

157. Durga A, Sepahpanah F, Regozzi M, Hastings J, Crane DA (2011) Prevalence of Testosterone Deficiency After Spinal Cord Injury. Pm&R 3(10):929-932. https://doi.org/10.1016/j.pmrj.2011.07.008

158. Bauman WA, La Fountaine MF, Spungen AM (2014) Age-related prevalence of low testosterone in men with spinal cord injury. J Spinal Cord Med 37(1):32-39. https://doi.org/10.1179/2045772313y.0000000122

159. Fomberstein K, Qadri S, Ramani R (2013) Functional MRI and pain. Curr Opin Anaesthesiol 26(5):588-593. https://doi.org/10.1097/01.aco.0000433060.59939.fe

160. Holly LT, Dong Y, Albistegui-DuBois R, Marehbian J, Dobkin B (2007) Cortical reorganization in patients with cervical spondylotic myelopathy. J Neurosurg Spine 6(6):544-551. https://doi.org/10.3171/spi.2007.6.6.5

161. Oughourlian TC, Wang C, Salamon N, Holly LT, Ellingson BM (2021) Sex-Dependent Cortical Volume Changes in Patients with Degenerative Cervical Myelopathy. J Clin Med 10(17). https://doi.org/10.3390/jcm10173965

162. LaCroix-Fralish ML, Tawfik VL, Spratt KF, DeLeo JA (2006) Sex differences in lumbar spinal cord gene expression following experimental lumbar radiculopathy. J Mol Neurosci 30(3):283-295. https://doi.org/10.1385/JMN:30:3:283

163. Sipski ML, Jackson AB, Gomez-Marin O, Estores I, Stein A (2004) Effects of gender on neurologic and functional recovery after spinal cord injury. Arch Phys Med Rehabil 85(11):1826-1836. https://doi.org/10.1016/j.apmr.2004.04.031

164. Xiao J, Zhang J, Zhao Y, Huang W, Guo Z, Su B, Guo Q (2017) Sex differences of steroid receptor coactivator-1 expression after spinal cord injury in mice. Neurol Res 39(11):1022-1027. https://doi.org/10.1080/01616412.2017.1367077

165. Wang J, Zuo X, He Y (2010) Graph-based network analysis of resting-state functional MRI. Front Syst Neurosci 4:16. https://doi.org/10.3389/fnsys.2010.00016

166. Stam CJ, Jones BF, Nolte G, Breakspear M, Scheltens P (2007) Small-world networks and functional connectivity in Alzheimer's disease. Cereb Cortex 17(1):92-99. https://doi.org/10.1093/cercor/bhj127

167. Rocca MA, Valsasina P, Meani A, Falini A, Comi G, Filippi M (2016) Impaired functional integration in multiple sclerosis: a graph theory study. Brain Struct Funct 221(1):115-131. https://doi.org/10.1007/s00429-014-0896-4

168. Anderson A, Cohen MS (2013) Decreased small-world functional network connectivity and clustering across resting state networks in schizophrenia: an fMRI classification tutorial. Front Hum Neurosci 7:520. https://doi.org/10.3389/fnhum.2013.00520

169. Peng XJ, Tan YM, He LC, Ou YT (2020) Alterations of functional connectivity between thalamus and cortex before and after decompression in cervical spondylotic myelopathy patients: a resting-state functional MRI study. Neuroreport 31(5):365-371. https://doi.org/10.1097/Wnr.0000000000001346

170. Bhagavatula ID, Shukla D, Sadashiva N, Saligoudar P, Prasad C, Bhat DI (2016) Functional cortical reorganization in cases of cervical spondylotic myelopathy and changes associated with surgery. Neurosurg Focus 40(6):E2. https://doi.org/10.3171/2016.3.FOCUS1635

171. van Wijk BC, Stam CJ, Daffertshofer A (2010) Comparing brain networks of different size and connectivity density using graph theory. Plos One 5(10):e13701. https://doi.org/10.1371/journal.pone.0013701

172. Liu J, Li M, Pan Y, Lan W, Zheng RQ, Wu FX, Wang JX (2017) Complex Brain Network Analysis and Its Applications to Brain Disorders: A Survey. Complexity. https://doi.org/Artn 8362741

10.1155/2017/8362741

173. Rubinov M, Sporns O (2010) Complex network measures of brain connectivity: uses and interpretations. Neuroimage 52(3):1059-1069. https://doi.org/10.1016/j.neuroimage.2009.10.003

174. Zhao R, Su Q, Chen Z, Sun HR, Liang M, Xue Y (2020) Neural Correlates of Cognitive Dysfunctions in Cervical Spondylotic Myelopathy Patients: A Resting-State fMRI Study. Front Neurol 11. https://doi.org/ARTN 596795

10.3389/fneur.2020.596795

175. Takenaka S, Kan S, Seymour B, Makino T, Sakai Y, Kushioka J, Tanaka H, Watanabe Y, Shibata M, Yoshikawa H, Kaito T (2019) Towards prognostic functional brain biomarkers for cervical myelopathy: A resting-state fMRI study. Sci Rep 9(1):10456. https://doi.org/10.1038/s41598-019-46859-5

176. Zhou F, Wu L, Liu X, Gong H, Luk KD, Hu Y (2015) Characterizing Thalamocortical Disturbances in Cervical Spondylotic Myelopathy: Revealed by Functional Connectivity under Two Slow Frequency Bands. Plos One 10(6):e0125913. https://doi.org/10.1371/journal.pone.0125913

177. Cao Y, Zhan Y, Du M, Zhao G, Liu Z, Zhou F, He L (2021) Disruption of human brain connectivity networks in patients with cervical spondylotic myelopathy. Quant Imaging Med Surg 11(8):3418-3430. https://doi.org/10.21037/qims-20-874

178. Li XS, Zhou SS, Zhu WQ, Li XH, Gao ZW, Li MQ, Luo SL, Wu XQ, Tian YH, Yu YQ (2021) Sex Difference in Network Topology and Education Correlated With Sex Difference in Cognition During the Disease Process of Alzheimer. Front Aging Neurosci 13. https://doi.org/ARTN 639529

10.3389/fnagi.2021.639529

179. Ingalhalikar M, Smith A, Parker D, Satterthwaite TD, Elliott MA, Ruparel K, Hakonarson H, Gur RE, Gur RC, Verma R (2014) Sex differences in the structural connectome of the human brain. Proc Natl Acad Sci U S A 111(2):823-828. https://doi.org/10.1073/pnas.1316909110

180. Stumme J, Jockwitz C, Hoffstaedter F, Amunts K, Caspers S (2020) Functional network reorganization in older adults: Graph -theoretical analyses of age, cognition and sex. Neuroimage 214. https://doi.org/ARTN 116756

10.1016/j.neuroimage.2020.116756

181. Gong GL, He Y, Evans AC (2011) Brain Connectivity: Gender Makes a Difference. Neuroscientist 17(5):575-591. https://doi.org/10.1177/1073858410386492

182. Duarte-Carvajalino JM, Jahanshad N, Lenglet C, McMahon KL, de Zubicaray GI, Martin NG, Wright MJ, Thompson PM, Sapiro G (2012) Hierarchical topological network analysis of anatomical human brain connectivity and differences related to sex and kinship. Neuroimage 59(4):3784-3804. https://doi.org/10.1016/j.neuroimage.2011.10.096

183. Tunc B, Solmaz B, Parker D, Satterthwaite TD, Elliott MA, Calkins ME, Ruparel K, Gur RE, Gur RC, Verma R (2016) Establishing a link between sex-related differences in the structural connectome and behaviour. Philos T R Soc B 371(1688). https://doi.org/ARTN 20150111

10.1098/rstb.2015.0111

184. Rosenthal CR, Andrews SK, Antoniades CA, Kennard C, Soto D (2016) Learning and Recognition of a Non-conscious Sequence of Events in Human Primary Visual Cortex. Curr Biol 26(6):834-841. https://doi.org/10.1016/j.cub.2016.01.040

185. Sherman SM, Guillery RW (2002) The role of the thalamus in the flow of information to the cortex. Philos Trans R Soc Lond B Biol Sci 357(1428):1695-1708. https://doi.org/10.1098/rstb.2002.1161

186. Unverdi M, Alsayouri K (2022) Neuroanatomy, Cerebellar Dysfunction. In: StatPearls. Treasure Island (FL),

187. Zhao R, Song Y, Guo X, Yang X, Sun H, Chen X, Liang M, Xue Y (2021) Enhanced Information Flow From Cerebellum to Secondary Visual Cortices Leads to Better Surgery Outcome in Degenerative Cervical Myelopathy Patients: A Stochastic Dynamic Causal Modeling Study With Functional Magnetic Resonance Imaging. Front Hum Neurosci 15:632829. https://doi.org/10.3389/fnhum.2021.632829

188. Rolls ET (2019) The cingulate cortex and limbic systems for action, emotion, and memory. Handb Clin Neurol 166:23-37. https://doi.org/10.1016/B978-0-444-64196-0.00002-9

189. Vogt BA, Laureys S (2005) Posterior cingulate, precuneal and retrosplenial cortices: cytology and components of the neural network correlates of consciousness. Prog Brain Res 150:205-217. https://doi.org/10.1016/S0079-6123(05)50015-3

190. van Wingen GA, van Broekhoven F, Verkes RJ, Petersson KM, Backstrom T, Buitelaar JK, Fernandez G (2008) Progesterone selectively increases amygdala reactivity in women. Mol Psychiatry 13(3):325-333. https://doi.org/10.1038/sj.mp.4002030

191. van Wingen G, Mattern C, Verkes RJ, Buitelaar J, Fernandez G (2010) Testosterone reduces amygdala-orbitofrontal cortex coupling. Psychoneuroendocrinology 35(1):105-113. https://doi.org/10.1016/j.psyneuen.2009.09.007

192. Volman I, Toni I, Verhagen L, Roelofs K (2011) Endogenous testosterone modulates prefrontal-amygdala connectivity during social emotional behavior. Cereb Cortex 21(10):2282-2290. https://doi.org/10.1093/cercor/bhr001

193. Ottowitz WE, Siedlecki KL, Lindquist MA, Dougherty DD, Fischman AJ, Hall JE (2008) Evaluation of prefrontal-hippocampal effective connectivity following 24 hours of estrogen infusion: an FDG-PET study. Psychoneuroendocrinology 33(10):1419-1425. https://doi.org/10.1016/j.psyneuen.2008.09.013

194. Ottowitz WE, Derro D, Dougherty DD, Lindquist MA, Fischman AJ, Hall JE (2008) FDG-PET analysis of amygdalar-cortical network covariance during pre- versus post-menopausal estrogen levels: potential relevance to resting state networks, mood, and cognition. Neuro Endocrinol Lett 29(4):467-474

195. Peper JS, van den Heuvel MP, Mandl RC, Hulshoff Pol HE, van Honk J (2011) Sex steroids and connectivity in the human brain: a review of neuroimaging studies. Psychoneuroendocrinology 36(8):1101-1113. https://doi.org/10.1016/j.psyneuen.2011.05.004

196. Martin AR, De Leener B, Cohen-Adad J, Cadotte DW, Nouri A, Wilson JR, Tetreault L, Crawley AP, Mikulis DJ, Ginsberg H, Fehlings MG (2018) Can microstructural MRI detect subclinical tissue injury in subjects with asymptomatic cervical spinal cord compression? A prospective cohort study. BMJ Open 8(4):e019809. https://doi.org/10.1136/bmjopen-2017-019809

197. Lee BC, Choi J, Martin BJ (2020) Roles of the prefrontal cortex in learning to time the onset of pre-existing motor programs. PLoS One 15(11):e0241562. https://doi.org/10.1371/journal.pone.0241562

198. Elkabes S, Nicot AB (2014) Sex steroids and neuroprotection in spinal cord injury: a review of preclinical investigations. Exp Neurol 259:28-37. https://doi.org/10.1016/j.expneurol.2014.01.008

199. Byers JS, Huguenard AL, Kuruppu D, Liu NK, Xu XM, Sengelaub DR (2012) Neuroprotective effects of testosterone on motoneuron and muscle morphology following spinal cord injury. J Comp Neurol 520(12):2683-2696. https://doi.org/10.1002/cne.23066

200. Sengelaub DR, Han Q, Liu NK, Maczuga MA, Szalavari V, Valencia SA, Xu XM (2018) Protective Effects of Estradiol and Dihydrotestosterone following Spinal Cord Injury. J Neurotrauma 35(6):825-841. https://doi.org/10.1089/neu.2017.5329

201. Stewart AN, MacLean SM, Stromberg AJ, Whelan JP, Bailey WM, Gensel JC, Wilson ME (2020) Considerations for Studying Sex as a Biological Variable in Spinal Cord Injury. Front Neurol 11:802. https://doi.org/10.3389/fneur.2020.00802

202. Bauman WA, La Fountaine MF, Spungen AM (2014) Age-related prevalence of low testosterone in men with spinal cord injury. J Spinal Cord Med 37(1):32-39. https://doi.org/10.1179/2045772313Y.0000000122